Electron Transport in Molecular Nanostructures



Alessandro Lodi

Trinity College

University of Oxford

A thesis submitted for the degree of

Doctor of Philosophy in Materials

Trinity Term 2022

To my parents and my little brother Jacopo, for their unconditional love & support, and to Cecilia, because she chooses me for Sunday night pizza.

Abstract

The past decades have seen huge efforts in trying to integrate carbon nanomaterials into electronic devices. Although microelectronic processors running on carbon nanotubes have demonstrated excellent performance and low power consumption, there are still limitations inherent to these materials, which restrict their applicability and integrability into devices. The lack of a bandgap in graphene, the mixture of metallic and semiconducting behaviours in carbon nanotubes, and tendency of nanotube to aggregate, are some examples of why it is necessary to devise alternative carbon nanostructures.

In this thesis, I investigate the electronic properties of nanodevices where molecularly defined graphene nanoribbons have been integrated as functional elements. These systems offer several advantages: they are intrinsically semiconducting, with atomically precise topology that guarantees, in principle, low scattering and ultra-clean behaviour, as well as access to topological states. On the other hand, their integration into devices is just in its infancy. After detailing the background of these systems, and of the most advanced devices that can be created out of them, I will describe the instrumentation and device architectures used to measure the electronic-transport properties. I then demonstrate a molecular quantum single-electron transistor that can work up to room temperature, and detail the transport regimes that appear in the different temperature regions. These findings are not only the first observation of quantum operation at room temperature in a molecular structure, but also clarify the physics of how such devices work.

I then address the second issue that has plagued devices based on carbon nanotubes: the presence of aggregates that can compromise, by intermolecular forces, device performance. I demonstrate how chemical functionalisation of the edges by the appropriate side groups can overcome these issues, allowing us to produce some the cleanest electronic nanodevices and features of single-electron transport, ever obtained. The clarity of the transport features is comparable of what has been seen for carbon nanotubes after more than 10 years of efforts, and allow us to address fundamental interactions that can regulate the transport, such as the electron–vibration coupling. I observe very strong vibronic coupling, with clear features of a Franck–Condon blockade.

Eventually I examine how to control the chemical potential of molecular nanoribbons, and dope them at will. This is first addressed by investigating

dopant groups attached to the ribbon edges. The energy shift induced in the nanoribbons by the dopant is, however, weak and impractical at the device level. I then present measurements in the first field-effect transistor of a unique class of materials, where dopants and metal atoms are inserted directly into the honeycomb lattice, and I propose possible improvements.

These results offer a first step towards the realisation of practical and extremely clean electronic devices based on molecular nanoribbons. They thus open the path to the use of electronics for the investigation of spin states, topological effects, and the physics of quantum systems at high temperatures. They offer a picture of the transport mechanisms at play, and, from the practical level, offer the first recipes to overcome longstanding issues that have hindered the development of carbon-based electronic devices, and may thus be instrumental in the development of the first nanoribbon-based microprocessors.

Declaration

I hereby affirm that the present thesis is exclusively my original work, and no portion of it has been previously submitted for examination at the University of Oxford or any other institution. The copyright for this thesis remains with the author, except where explicitly stated otherwise. The total word count for this document is 38,967 words.

The data incorporated within this thesis have been securely stored across multiple locations to ensure their total protection. Low-temperature data obtained through the Triton instrumentation are preserved locally on the Triton-3 desktop machine, which, at the time of writing, was situated in the Hume-Rothary building at the University of Oxford. Additionally, a complete copy of the dataset can be accessed in the Microsoft Teams storage space designated for the OxNanoSpin group. Room temperature field-effect transistor data are stored on a hard disk located on the ground floor (Philly lab) during the time of writing, as well as in the dedicated workstation detailed in Chapter 3. Furthermore, a comprehensive copy of the dataset is also maintained within the shared folders of the OxNanoSpin Microsoft Teams storage space.

All experiments and data analysis presented in this thesis were performed by myself, with the exception of what I will delineate here below.

In chapter 3 the graphene substrates utilized in this and all subsequent chapters for fabricating graphene nanogaps were supplied by Graphenea.

In chapter 4 Dr. Alex Gee was responsible for fabricating the gold and graphene micro-Hall sensors.

In chapter 5 Dr. Wenhui Niu synthesized the graphene nanoribbons (GNRs) with maleimide groups. Dr. Simen Sopp conducted the Franck-Condon analysis on the temperature data I gathered. Mr. Fanmiao Kong performed the phonon dispersion calculations. The numerical code used for simulating the stability diagram and vibrational states through the rate-equation model was adapted from a code provided by Dr. Jakub Sowa. Dr. Alex Gee assisted in collecting additional data when I was unable to access the lab due to a Covid-19 infection.

Chapter 7

Dr. Alicia Gotz synthesized the GNRs-OMe, while Dr. Qiang Chen synthesized the porphyrin-GNR Ni hybrids. Mr. Fanmiao Kong provided support in setting up the electronic calculations on the ARC supercomputing centre.

Research Outputs

Publications

- Exceptionally Clean Single-Electron Transistors from Solutions of Molecular Graphene Nanoribbons [1].
- Porphyrin-Fused Graphene Nanoribbons [2].
- A Room-Temperature Single-Electron Transistor based on a Synthetic Molecular Graphene Nanoribbon (in preparation).

Relationship with thesis

This thesis and the associated appendices are based on the papers listed above. Elements from these papers are interspersed throughout this paper. In particular:

- Chapter 5 is based on the as-yet unpublished paper on a room-temperature single-electron transistor based on a molecularly-synthesised graphene nanoribbon,
- Chapter 6 is based on [1],
- Chapter 7 is based on the as-yet unpublished paper on porphyrin-fused within a molecular graphene nanoribbon

Acknowledgements

My thesis would not have been possible without the great support of many people.

First and foremost, I want to express my thanks to my supervisor Prof. Lapo Bogani for everything he has done for me over the last five years. He has not only fostered a stimulating environment, but has also encouraged me to pursue my own ideas even when others would seem more cool and trendy, to always verify at my best what I am claiming, and that, regardless of how many things he had on his desk, I could always knock on his door and ask for advice. Thank you also for not missing a single one-on-one meeting during the COVID-19 pandemic, which made me feel less alone.

In the past four years, I have measured molecular graphene nanoribbons that were sent to me by fantastic coworkers. Dr Wenhui Niu, Dr Junzhi Liu, Dr Ji Ma, and Prof. Xinliang Feng from the Centre for Advancing Electronics Dresden, Dr Alicia Götz and Prof. Akimitsu Narita from the Okinawa Institute of Science and Technology. I would like also to thank Dr Glenn Wagner for sharing his interest for the physics of one-dimensional systems with me.

The financial support of the Clarendon Foundation throughout the years has allowed me to pursue my DPhil, and I thank them.

I will be forever thankful to everyone in the group for all of their help and encouragement. All the postdocs: Alex, Dimitris, Iago, Michael, Ramon, Tian, and Xuelin, who are experts in nanofabrication, chemistry, EPR, and instrumentation development. Alex, in particular, I owe my gratitude for all the hours we spent working together in the lab and for sharing his enthusiasm for electronics.

Colleagues such as Federico, Ming-Yee, and Simen have been a source of motivation for me since the beginning of my master programme. You are amongst the smartest people I have ever encountered, and it has been a privilege to cross our paths. Thanks for sharing your passion for science, chess, football, and coding. A special thanks to Michael and Ming-Yee for patiently providing me feedback through multiple iterations of this thesis.

I would also like to thank Fanmiao, with whom I have spent countless evenings debating everything, from the most accurate pronounciation of Chinese words to the accuracy of numerical experiments. I am also really grateful for letting me crash at your place the week before I submitted this thesis.

I would like to thank Dr James Thomas and Dr Zhixin Chen for the stimulating discussion about molecular transport, for sharing your scientific passions, and for building a friendly environment in all the labs we have shared throughout these years.

Dinner with Angie, Dimitris, and Michael will forever be amongst my favourites. I appreciate all the times you hosted us, making us feel like home, the innumerable times you asked me for a caffe and Dimitri's Opera cake, which can definitely be listed as the eighth wonder of the world.

My time in Oxford would not have been the same without the people I spent the most time with, whether we were at Trinity or Exeter College, out for a run, gym, or a formal dinner. Aidan, Andreas, Jan, Neale, Prateek, Rujual, and Said. A special thanks to Andreas, who let me crash at his apartment when I needed to, and to Said, who came to visit me and my nonna in Italy.

What have become my family in Oxford will always have my undying gratitude. Kevin, Michał, Mrin, and Vinita. Oxford will always remind me of you. Thank you for the compassion, understanding, the laughs, and the many dinners we enjoyed together, from Diwali to pierogi, passing through Thanksgiving.

I want to express my gratitude to Cecilia's family, who lovingly embraced me into their home during my holiday visits. Your kindness has enriched my life and for that, I am truly thankful. Daniela, Fabrizio, Gaia - each one of you holds a special place in my heart.

The constant love and encouragement my family has given me has been the driving force in my dedication throughout the whole journey. To my parents, Daniele and Francesca, and my younger little brother, Jacopo.

Finally, to you, Ce. Because you were there for me all the time. Always.

Contents

List of Figures **xii**

Abbreviations **xv**

1 Motivations **1**

2 Theoretical Concepts and Experiments **5**

2.1 Graphene 6

2.1.1 Crystal and Band Structure 6

2.1.2 Graphene Transistors 9

2.1.3 High-Frequency Applications 13

2.2 Carbon Nanotube Electronics 16

2.2.1 Channel-Length Scaling 21

2.2.2 Contact-Length Scaling 25

2.3 Single-Electron Conduction 27

2.3.1 Energy Scales and Characteristic Lengths 27

2.3.2 Electronic-Transport Regimes 28

2.3.3 Experimental Evidences 35

2.4 Basics of One-dimensional Physics 38

2.4.1 A Succinct Primer of Fermi-Liquid Theory 39

2.4.2 Introduction to the Tomonaga–Luttinger Model 41

2.4.3 Derivation of the tunnelling Density of States 44

2.4.4 Experimental Evidence: Luttinger Liquid in Carbon Nanotubes 48

2.5 Graphene Nanoribbons 51

2.5.1 Crystal and Band Structure 52

2.5.2 Edge States 56

2.5.3 Graphene Nanoribbons Field-Effect Transistors 58

2.5.4 Bandgap Engineering 61

2.5.5 Graphene Nanoribbons Electronics 62

3 Experimental Details: Nanofabrication and Measurement Protocols 65
3.1 Introduction . . . 65
3.2 Sample Nanofabrication . . . 66
3.2.1 Graphene Patterning . . . 68
3.3 Room-Temperature Transport Setup . . . 69
3.4 Graphene Tunnel Junctions . . . 70
3.4.1 Gate-controlled Electroburning . . . 72
3.5 Contacting Graphene Nanoribbons . . . 75
3.6 Deposition Process and Related Phenomena . . . 77
3.7 Cryogenic-Temperature DC Transport Setup . . . 81

4 Instrumentation Development 86
4.1 Temperature-dependent Protocol . . . 87
4.2 AC Measurements . . . 88
4.2.1 Integration of Lock-in Amplifier with High-Sensitivity Electronics . . . 89
4.3 Micro-Hall Devices . . . 92
4.3.1 Technical Background . . . 92
4.3.2 Test Measurements . . . 95
4.4 Graphene Hall Bars . . . 97
4.4.1 Fabrication . . . 100
4.4.2 Test Measurements . . . 100
4.5 Concluding Remarks . . . 105
4.6 Project Overview . . . 106

5 Room Temperature Graphene Nanoribbon Single-Electron Transistor 107
5.1 Introduction . . . 107
5.2 Single-Electron Transistor Architecture . . . 110
5.3 Temperature-Dependent Coulomb-Blockade Spectroscopy . . . 111
5.3.1 MGNR Length Extraction from Coulomb Data . . . 117
5.4 Analysis of the Low-Bias Conductance . . . 117
5.5 Temperature-Dependent Integrated Conductance . . . 120
5.6 Discussion . . . 122
5.7 Outlook and Perspectives . . . 123
5.8 Project Overview . . . 123

6 Vibrational Effects in Graphene Nanoribbons 124
6.1 Introduction . . . 124
6.2 Coulomb-blockade Spectroscopy . . . 125
6.3 Analysis of the Franck–Condon Conductance Blockade . . . 129
6.4 Simulation of the Stability Diagram . . . 131
6.5 Role of the Maleimide Groups: *Ab-Initio* and Statistical Analysis . 132
6.6 Discussion . . . 137
6.7 Outlook and Perspectives . . . 139
6.8 Project Overview . . . 140

7 Chemical Doping of Graphene Nanostructures 141
7.1 Introduction . . . 141
7.2 Numerical Study of the Edge Doping . . . 143
7.3 Methoxy-Edge-Decorated MGNRFETs . . . 147
7.4 Heteroatoms-Doping-Embedment in MGNRs . . . 151
7.5 Discussion . . . 163
7.6 Outlook and Perspectives . . . 164

8 Conclusions and Perspectives 166

Appendices

A Graphene Nanoribbons Single-Electron Transistors 172

B Porphyrin-Fused Graphene Nanoribbons: Single-Electron and Field-Effect Transistors 184
B.1 Additional Data . . . 184

References 188

List of Figures

1.1 Moore's Law for Microprocessors 3

2.1 Honeycomb Lattice, Dirac Cones, and Graphene Density of States . 7
2.2 Graphene Device Architectures and Operating Schematic 11
2.3 Graphene MOSFET Band Structure 12
2.4 Carbon Nanotube Structure and Energy Dispersion 17
2.5 High-κ Carbon Nanotube Field-Effect Transistors 22
2.6 Contact-Length Scaling in CNTFETs 24
2.7 Sub-10 nm Channel-Length Scaling in CNTFETs 25
2.8 Single-Electron Transistor and its Equivalent Circuit 29
2.9 Coulomb Diamond Diagram 32
2.10 Schematic of a Single-Level Tunnelling-Transport Mechanism 34
2.11 Carbon Nanotube Single-Electron Transistors 37
2.12 Franc–Condon Blockade in Carbon Nanotubes 38
2.13 Schematic of a One-Dimensional System 39
2.14 Schematic of The Tomonaga–Luttinger-Liquid Model 43
2.15 Low-Energy Quasiparticles Excitations in One-Dimensional Systems 44
2.16 Luttinger Liquid in Ropes of Carbon Nanotubes 49
2.17 Luttinger Liquid in Metallic Carbon Nanotubes 50
2.18 Correlation Between Bandgap Energy and Graphene Nanoribbon Width 52
2.19 MGNR Edge Structure Canvas 54
2.20 Edge State in ZigZag Graphene Nanoribbons 57
2.21 Bandgap Energy vs. Graphene Nanoribbon Width 59

3.1 Schematic of Electrode Patterning 67
3.2 Room-Temperature Setup: Probe Station 69
3.3 Graphene Tunnel Junctions: The Simmons Model 71
3.4 Gate-Controlled Feedback Electroburning Algorithm 74
3.5 Probability Distribution of a Ribbon Landing Onto a Device 76
3.6 Dry-Cycling Deposition Method 78
3.7 mK Setup: ^{3}He/^{4}He Dilution Refrigerator 82

3.8 DC Electronics Setup, Digitizer Calibration Curve, and Current-to-Voltage Converter 83
3.9 Electronic Setup at mK 84
3.10 Breakout Box Connection, Chipholder Schematic, and DC Lines Frequency Test 85

4.1 Circuit Schematic of a Voltage-Biased Sample Thorough the Breakout Box 89
4.2 AC Electronics Setup 90
4.3 DC vs. AC Stability Diagram 91
4.4 Micro-Hall Sensor Operating Schematic 93
4.5 Optical and SEM Image of a Au-Fabricated Micro-Hall Sensor . . . 94
4.6 Driving-Current-Dependent Hall-Voltage Measurements 96
4.7 Angular Relation to Hall Voltage Response 98
4.8 Hall-Probe Magnetometry of Mn_{12}-ac Micro-Crystals 99
4.9 AC-GHB response of Mn_{12}-ac Micro-Crystals 101
4.10 DC-GHB response of Mn_{12}-ac Micro-Crystals 103

5.1 Room-Temperature Graphene Nanoribbon Single-Electron Transistor 109
5.2 Temperature-Dependent Stability Diagram for a MGNR ($T = 0.025 - -30\,\mathrm{K}$) 112
5.3 Temperature-Dependent Stability Diagram for a MGNR ($T = 60 - -270\,\mathrm{K}$) 113
5.4 Temperature-Dependet of Differently Biased Gate Traces 114
5.5 Temperature Evolution of Zero-Bias Conductance 118
5.6 Linear Dependence of the Peak Width with the Temperature 119
5.7 Zero-Bias Temperature Evolution of The Integrated Conductance . 121

6.1 Solubility Improved 2-Terminal Devices 126
6.2 Solubility Improved 3-Terminal Devices 128
6.3 Franck–Condon Bloackade in MGNR 130
6.4 Single-Mode and Phonon Bath Models for MGNR Vibrations 132
6.5 Phonon Dispersion MGNR: The Role of Anthracene Groups 134
6.6 Phonon Dispersion MGNR: The Role of Maleimide Groups 135
6.7 MGNR–Maleimide Statistics: A p-Value Argument 136

7.1 Cove-4 GNR structure and Length Distribution 144
7.2 DFT Band Structures and DOS of a 4-Cove GNR–H and a GNR–Anthracene 145
7.3 DFT Band Structures and DOS of Chemically-Functionalised MGNRs 146
7.4 Methoxy-Functionalised GNRFETs 148

7.5 Switching Behaviour of Methoxy-Functionalised GNRFETs 150
7.6 A Chemical Route to GNR-Porphyrin Hybrid. 152
7.7 GNR-porphyrin Hybrid Device: Low- and Room-Temperature Comparison 153
7.8 GNR-Hybrid Field-Effect Transistors at Room Temperature 154
7.9 MGNR–Ni Hybrid: Additional FETs (device b11, c4) 155
7.10 MGNR–Ni Hybrid: Additional FETs (device c6, c30) 157
7.11 GNR-Hybrid Stability Diagram and Addition Energies 159
7.12 GNR-Hybrid Coulomb Diamond 160
7.13 Tables Lorentzian fit parameters and vibrational modes. 161
7.14 Capacitance Measurements Device 162

A.1 MGNR with Alkyl Chains: Addition Data 172
A.2 GNR with Maleimide Groups: Additional Data 176
A.3 GNR with Maleimide Groups: Additional Temperature Data 183

B.1 MGNR–Ni Hybrid: Additional SETs (device 2) 184
B.2 MGNR–Ni Hybrid: Additional SETs (device 3) 185
B.3 MGNR–Ni Hybrid: Additional FETs (device d3, d5) 186
B.4 MGNR–Ni Hybrid: Additional FETs (device e5) 187

Abbreviations

AC alternating current. 90

ACE artificial concentrated evaporation. 78, 79

AFM atomic force microscope. 48, 77, 149

AGNR armchair graphene nanoribbon. 52, 53, 55, 59, 138

CMOS complementary metal-oxide semiconductor. 2, 9, 11, 13, 20, 21, 51

CNT carbon nanotube. 6, 16, 18, 19, 20, 21, 22, 23, 24, 25, 26, 27, 35, 36, 37, 38, 47, 48, 50, 51, 56, 63, 78, 79, 108, 119, 120, 122, 137, 139, 166

CNTFET carbon-nanotube field-effect transistor. 16, 17, 18, 19, 20, 21, 23, 150, 154

CVD chemical vapour deposition. 15, 66, 100, 161

DAC digital-to-analog converter. 81, 92, 97, 100

DC direct current. 14, 66, 81, 88, 89, 90, 92, 129

DFT density-functional theory. 59, 134, 138, 142, 148, 163

DIBL drain-induced barrier lowering. 20

DOF degree of freedom. 33, 35, 37

DOS density of states. 8, 9, 28, 35, 38, 47, 55, 56, 57, 144, 145

EBL electron-beam litography. 52, 101

EOT effective oxide thickness. 23, 64

ESD electronic discharge. 81

FET field-effect transistor. 10, 17, 50, 60, 147, 151, 153, 154, 155, 156, 157, 158, 159, 164, 165, 186, 187

FWHM full width at half maximum. 118

GGA generalised-gradient approximation. 143

GHB graphene Hall bar. 97, 100, 101, 103, 104, 106

GNR graphene nanoribbon. 3, 4, 6, 16, 20, 27, 38, 47, 50, 51, 53, 56, 57, 58, 59, 63, 64, 71, 75, 78, 79, 138, 139, 142, 144, 149, 151, 165

GNRFET graphene nanoribbon field-effect transistor. 58, 63, 64, 78, 148, 149, 163

GNRSET graphene-nanoribbon single-electron transistor. 4, 139

GTJ graphene tunnel junction. 65, 66, 68, 71, 73, 136

hBN hexagonal boron nitride. 11, 100, 105

HOMO highest occupied molecular orbital. 53, 141

IC integrated circuit. 1, 166

LDA local-density approximation. 143

LUMO lowest unoccupied molecular orbital. 53, 141

MGNR molecular graphene nanoribbon. 38, 47, 51, 58, 65, 108, 109, 110, 111, 113, 117, 118, 119, 120, 121, 123, 124, 125, 127, 131, 132, 133, 135, 136, 138, 139, 140, 141, 142, 143, 144, 163, 164, 165

MOSFET metal–oxide–semiconductor field-effect transistor. 11, 14, 16, 23, 24, 25

NEGF non-equilibrium Green's function. 26, 144

pGNR porphyrin–GNR. 142, 151, 152, 153, 154, 158, 159, 160, 164, 184

QD quantum dot. 28, 29, 30, 31, 32, 33, 35, 36, 37, 48, 50, 73

RF radiofrequency. 13

RT room temperature. 108, 110, 111, 113

SB schottky barrier. 12, 18, 19, 36, 62, 106, 110

SET single-electron transistor. 28, 29, 36, 65, 107, 108, 109, 110, 115, 119, 122, 127, 135, 136, 137, 139, 153

STM scanning tunnelling microscope. 53

TB tight-binding. 53, 59

TDOS tunnelling density of states. 44, 45, 47, 48, 57, 119

TLL Tomonaga–Luttinger liquid. 42, 43, 45, 119, 120, 121

ZGNR zigzag graphene nanoribbon. 52, 55, 57

1 Motivations

This thesis start from a fundamental, yet non-trivial question. Can we fabricate graphene and, more broadly, graphene-derived structures that offer a competitive advantage over ubiquitous silicon integrated circuits? In an attempt to answer this question, I will present an overview of the key all-carbon alternatives studied so far since the late 1990s.

For approximately six decades, silicon has maintained its status as the preeminent material employed in the fabrication of integrated circuits (ICs). Numerous constraints, however, including scaling limitations, power consumption, and escalating complexity in integrated circuit design, have prompted both prominent semiconductor manufacturers and the scientific community to investigate viable alternative materials and methodologies to either supplant or, more realistically, complement silicon. The intensification of manufacturing costs, partially instigated by global crises such as the COVID-19 pandemic in 2020 and the Ukrainian conflict in 2022, has exerted significant pressure on all chip manufacturers. Amid these circumstances, only industry leaders such as Intel, Samsung, and TSMC can counterbalance costs incurred in maintaining production facilities that operate at the requisite capacity to satisfy demand.

In 2021, Bloomberg reported that the fundamental costs of building a semicon-

ductor manufacturing are approximately $15 billion, with profit requirements of roughly $3 billion to maintain market competition and avoid obsolescence [3]. These findings are also backed by a study last year conducted by the Boston Consulting Group, which ranked investments in research and development (22% of annual semiconductor sales) and capital spending (26%) as the highest in all industries [4].

The first prototype of a point-contact transistor, developed at the beginning of the 1940s by Bardeen, Brattain and William Shockley at Bell Labs, and the realisation of complementary metal-oxide semiconductor (CMOS) techology by Atalla and Kahng ten years later, together marked the beginning of integrated components [5]. Arguably, the density-scaling capabilities of this technology has been one of the main reasons responsible for the constant technological development over a timespan of more than fifty years. In this scenario, Moore's law is considered both as a metric for estimating future numbers of transistors per integrated circuit and as a driver of innovation and competitiveness.

The search of new materials for integrated electronics is not only motivated by the desire to increase the number of transistors per chip. Fig. 1.1 displays five microprocessor figures of merit and their trends over the past five decades. The clock frequency is the number of clock cycles (number of electrical pulses) that a CPU can execute every second, measured in Hz. Within these electrical pulses, the CPU can conduct fundamental operations such as memory access, data writing, and instruction retrieval, but also generates heat. From Fig. 1.1, it is clear that a positive correlation exists between the clock speed and the power dissipated[†] per transistor, and this has been one of the main reasons that has motivated, for example, the research of materials with high thermoelectric-conversion efficiency [6, 7].

One of the major problematics with the CMOS-density scaling is that as the channel length is shortened, leakge current increases because of quantum tunnelling of the charge carriers through the channel. This issues has been mitigated over the

[†]This is typically referred as static power, i.e. power dissipated when the transistor is not switching. CMOS technology is well known for low static power for standard supply voltages (3–5 V)

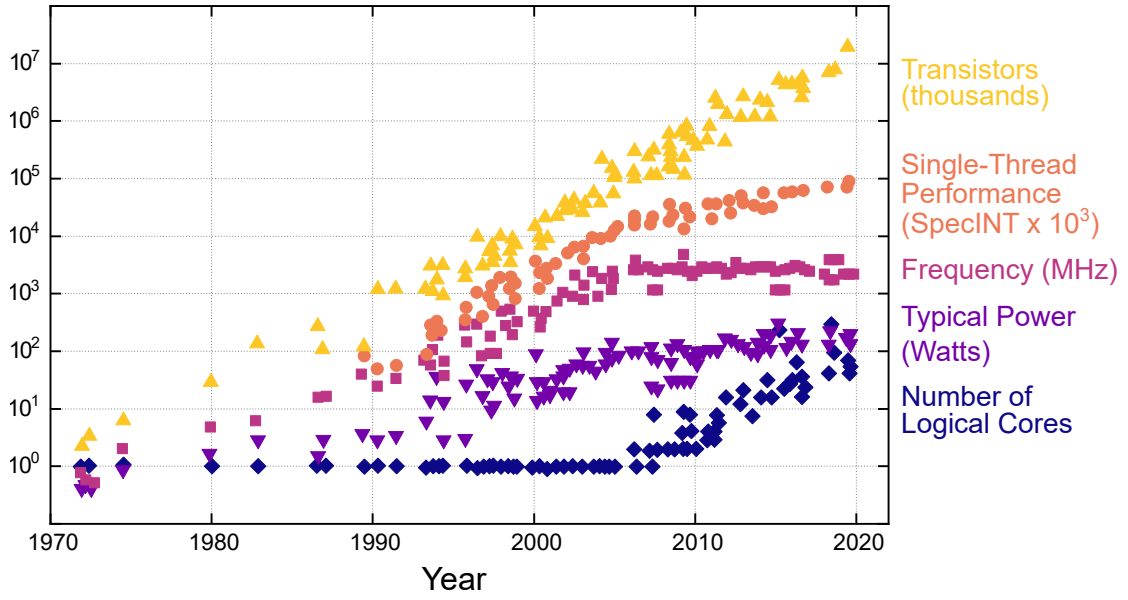


Figure 1.1: The arc of Moore's law over fifty years of microprocessor development. While the number of transistors have doubled about every two years, the same cannot be said for other key figures. In particular, clock frequency and power dissipated have plateaued out since 2003. The release in 2005 by Intel of the first dual-core processor (Pentium D), and the ability to perform hyper-threading have sparked reserach into the number of logical cores per CPU. This is the ability of a single core to carry out two or more processes simultaneously. Since then, the increase in multi-threading performance compared with stagnating single-thread performance has been one of the main driving factors for multi-core processors in modern laptops. Data collected by K. Rupp. Adapted from a talk given by Nvidia.

last few years by adopting non-planar transistor architectures such as FinFETs [8] and Gate-All-Around FETs [9], but fundamental problems still remains.

Several researchers have envisioned graphene as one of the most robust materials against short-channel effects [10–15] and have suggested that it will be possible to integrate graphene into semiconductor manufacturing cycles in the near future. Despite its remarkable electronic and mechanic properties, several fundamental problems such as the lack of bandgap have prevented a smooth integration within integrated circuits.

A candidate alternative material for this integration are graphene nanoribbons (GNRs). In contrast to graphene, GNRs are confined to one dimension, and this leads to a bandgap, making them interesting for semiconductor applications. From a theoretical point of view, GNRs have attracted much attention in the last twenty

years, yet experimental evidences have remained scarce because of insufficient purity. However, as a result of recent and novel developments in bottom-up synthesis, it is now possible to synthesise high-purity GNRs and atomically-precise topologies that guarantees, in principle, low scattering and high device performance, as well as access to topological states.

In this work, we tackle the question of how molecular graphene nanoribbons can be integrated in low-power electronic devices. To establish the groundwork for the thesis, we begin with a broad introduction, both theoretical and experimental: we discuss the electronic properties of graphene, carbon nanotubes, and graphene nanoribbons and how to use them to fabricate electronic devices for high-frequency, digital, and quantum applications. Since the 1D nature of graphene nanoribbons plays an important role in this research project, we also present an overview of the most important properties of 1D systems.

In consideration of the experimental techniques developed for this work, a chapter is dedicated to the experimental background: we explain the fabrication recipes we have optimised to fabricate nanoelectronic devices and the instrumentation apparatus for measurements at room and mK temperatures. We also explore several instrumentation developments we have undertaken and , partially or entirely, completed, with the goal of improving our current measurement setup. We then present in details three main research projects.

We begin with the investigation of a room-temperature-operating single-electron transistor made with molecular graphene nanoribbons. This represents the first study demonstrating the physics at play in such devices. We then progress to study a chemical strategy which produces ultra-clean graphene-nanoribbon single-electron transistor (GNRSET), allowing the first investigation of strong vibronic coupling in GNRs. Finally, we conclude by investigating two possible strategies for controlling the injection of dopants into molecular nanoribbons, i.e. by chemical functionalisation attached along the edges, and by insertion of porphyrin rings carrying transition-metal ions inside the GNR backbone.

2

Theoretical Concepts and Experiments

Contents

2.1 Graphene 6
2.1.1 Crystal and Band Structure 6
2.1.2 Graphene Transistors 9
2.1.3 High-Frequency Applications 13
2.2 Carbon Nanotube Electronics 16
2.2.1 Channel-Length Scaling 21
2.2.2 Contact-Length Scaling 25
2.3 Single-Electron Conduction 27
2.3.1 Energy Scales and Characteristic Lengths 27
2.3.2 Electronic-Transport Regimes 28
2.3.3 Experimental Evidences 35
2.4 Basics of One-dimensional Physics 38
2.4.1 A Succinct Primer of Fermi-Liquid Theory 39
2.4.2 Introduction to the Tomonaga–Luttinger Model 41
2.4.3 Derivation of the tunnelling Density of States 44
2.4.4 Experimental Evidence: Luttinger Liquid in Carbon Nanotubes 48
2.5 Graphene Nanoribbons 51
2.5.1 Crystal and Band Structure 52
2.5.2 Edge States 56
2.5.3 Graphene Nanoribbons Field-Effect Transistors 58
2.5.4 Bandgap Engineering 61
2.5.5 Graphene Nanoribbons Electronics 62

In this chapter, I will present an overview of the key all-carbon alternatives

studied so far since the late 1990s. This chapter begins with a concise overview of the fundamental properties of graphene, carbon nanotubes (CNTs), and GNRs. Since the last two materials are 1D, throughout the discussion we will present theoretical groundwork developed to better comprehend the physics and the functioning mechanisms of electronic and quantum devices made with CNTs and GNRs, followed by a selection of the most significant carbon-based proposals developed to date.

2.1 Graphene

2.1.1 Crystal and Band Structure

Graphene has a hexagonal structure, where the carbon atoms are hybridised as sp^2. In the International Table of Crystallography, graphene is included in the symmorphic space group #191, with symmetry D_{6h} ($P6/mmm$) [16].

As shown in Fig. 2.1a–b, the carbon atoms in graphene form a two-dimensional hexagonal lattice with two non-equivalent atoms per unit cell:

$$\mathbf{a}_1 = \frac{a}{2}(3, \sqrt{3}),\ \mathbf{a}_2 = \frac{a}{2}(3, -\sqrt{3}), \tag{2.1}$$

with $a \simeq 1.42\,\text{Å}$ the carbon–carbon bond length. Each atom belonging to one sublattice, called sublattice A, has three nearest neighbours belonging to the other sublattice, called sublattice B. With respect to one atom chosen from sublattice A as origin, the position of these first three neighbours in real space are given by:

$$\boldsymbol{\delta}_1 = \frac{a}{2}(1, \sqrt{3}),\ \boldsymbol{\delta}_2 = \frac{a}{2}(1, -\sqrt{3}),\ \boldsymbol{\delta}_3 = -a(1, 0), \tag{2.2}$$

while the reciprocal-lattice vectors may be written as:

$$\mathbf{b}_1 = \frac{2\pi}{3a}(1, \sqrt{3}),\ \mathbf{b}_2 = \frac{2\pi}{3a}(1, -\sqrt{3}). \tag{2.3}$$

whereas the Brillouin point are:

$$\mathbf{K} \equiv \mp\ \frac{2\pi}{3a}\left(\frac{1}{\sqrt{3}}, 1\right), \tag{2.4}$$

$$\mathbf{K'} \equiv \pm\ \frac{2\pi}{3a}\left(\frac{1}{\sqrt{3}}, -1\right), \tag{2.5}$$

$$\mathbf{M} \equiv \pm\left(0, \pm\ \frac{2\pi}{3a}\right). \tag{2.6}$$

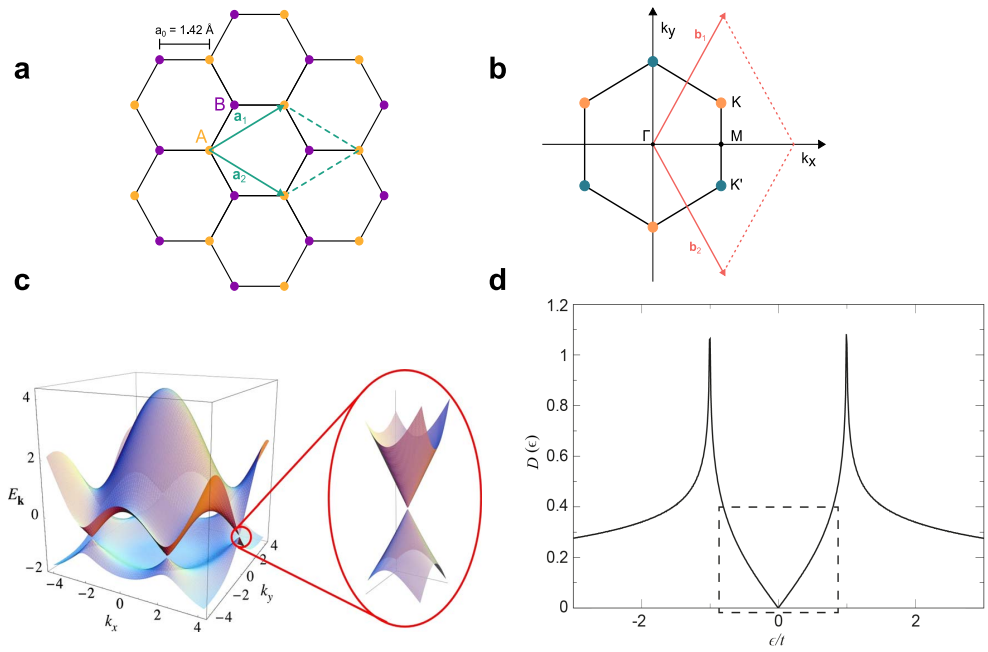


Figure 2.1: **a**, Honeycomb lattice of graphene. Two non-equivalent carbon atoms A and B in the primitive cells (direct space) are denoted in yellow and purple. The set of possible translations are shown by the lattice vectors $\mathbf{a}_1, \mathbf{a}_2$ (green arrows). **b**, The first Brillouin zone of graphene with vertices **K** (orange) and **K′** (green), and reciprocal-lattice vectors drawn in red. **c**, Graphene energy dispersion resulting from Eq. 2.7 (in units of the hopping parameter t). The magnification shows one of the Dirac cones, which are located at the **K** and **K′** points, emphasising the linear-dispersion relation. **d**, The electron states density as a function of t, showing pronounced van Hove singularities for $\varepsilon \simeq \pm t$. The dashed rectangle indicates the low-energy linear-dispersion region which is typically probed in transport experiments. Adapted from [18].

Based on the experimental evidence collected in the last 20 years, the model that best describe the properties of graphene is the Wallace model of the band structure, which dates back to 1947, and qualifies graphene as a semimetal with a linear dispersion of the electronic excitations close to the Fermi energy [17].

Within the second-quantisation formalism (with $\hbar = 1$), the tight-binding Hamiltonian may be written as

$$\mathcal{H}_{\mathrm{TB}} = -t \sum_{\langle ij \rangle, \sigma} \left(a^{\dagger}_{\sigma,i} b_{\sigma,j} + \mathrm{h.c.} \right) - t' \sum_{\langle\langle ij \rangle\rangle, \sigma} \left(a^{\dagger}_{\sigma,i} a_{\sigma,j} + b^{\dagger}_{\sigma,i} b_{\sigma,j} + \mathrm{h.c.} \right), \tag{2.7}$$

The notation $\langle ij \rangle$ means the sum runs over pairs of electrons that are nearest neighbours; similarly, the notation $\langle\langle ij \rangle\rangle$ specifies a summation over the next-nearest neighbours. The two operators $a^{\dagger}_{i,\sigma}$ ($a_{i,\sigma}$) and $b^{\dagger}_{i,\sigma}$ ($b_{i,\sigma}$) create (annihilate)

an electron with spin $\sigma = \uparrow, \downarrow$ for atoms on sublattices A and B, respectively. The value of t that best reproduces the experimental evidence is $t \simeq 2.8$ eV [18], and quantifies the nearest-neighbour hopping energy; similarly, t' denotes the next-nearest-neighbour hopping energy, and the experimental estimate is $t' \simeq 0.1\,\text{eV}$ [19].

By diagonalising the Hamiltonian in Eq. 2.7, it is possible to work out the energy dispersion of graphene,

$$E_{\pm}(\mathbf{k}) = \epsilon_p - t' f(\mathbf{k}) \pm t\sqrt{3 + f(\mathbf{k})}, \tag{2.8}$$

with $f(\mathbf{k})$ defined as:

$$f(\mathbf{k}) = 2\cos\left(\sqrt{3}k_y a\right) + 4\cos\left(\frac{\sqrt{3}}{2}k_y a\right)\cos\left(\frac{3}{2}k_x a\right). \tag{2.9}$$

Eq. 2.8 identifies an upper band (π^*) associated with the plus sign and a lower band (π) associated with the minus sign, and these bands are symmetric with respect to zero energy[‡]. If the system is undoped, there will be one electron per carbon atom, resulting in two electrons per cell: the lower band will be full, while the top band will be empty. Therefore, the system is semi-metallic.

When examining the trend close to the **K** and **K′** points, the peculiarities of the energy-band dispersion can be appreciated. By taking the positive components for the **K** point, as defined in Eq. 2.4, and expanding Eq. 2.8 as $\mathbf{k} = \mathbf{K} + \mathbf{q}$, with $|(\mathbf{q})| \ll |(\mathbf{K})|$, one obtains:

$$E_{\pm}(\mathbf{q}) = \epsilon_p \pm \frac{3at}{2}|\mathbf{q}|, \tag{2.10}$$

This remarkable result tells us that the dispersion close to the Fermi level is linear in $\mathbf{q}$. The Fermi velocity is defined by the usual relation $v_F = \frac{1}{\hbar}\left(\frac{\mathrm{d}E}{\mathrm{d}\mathbf{k}}\right)$, and in graphene $v_F \simeq 1 \times 10^6$ ms^{-1} [17]. An important consequence of this result is that while for a two-dimensional electron gas the density of states (DOS) is constant, the DOS in graphene close to the Fermi level is:

$$\rho(E) = \frac{2A_{\text{cell}}}{\pi}\frac{|E|}{v_F^2}. \tag{2.11}$$

[‡]The fact that the energy dispersion is symmetric to zero energy is a result of the particle–hole symmetry of the system.

This linear dependency of the electronic states density on the absolute value of the energy has important consequences on the particle velocity $c^* = v_F = 3ta/2\hbar$, which is constant and similar to the speed of light $E = pc = c^*\hbar|\mathbf{k} - \mathbf{K}|$ [20]. This similarity has led to the definition of *massless fermions* for electrons near the Fermi energy of graphene [21]. Furthermore, for undoped graphene, the DOS displays two Van Hove singularities at $\rho(\omega_{\mathrm{VH}}) = \pm 1\,\mathrm{eV}$ [22]. This behaviour is rather different to the conventional case of electrons in 2D metals, where they have energy dispersion $\epsilon = \hbar^2 q^2/2m^*$ in terms of the band mass m^*, and where one obtains a constant density of states $\rho^{2\mathrm{D}}(\epsilon) = gm^*/2\pi\hbar^2$.

Finally, the graphene conductivity may be computed semiclassically using the Einstein–Smoluchowski relation† and the DOS [23]:

$$\sigma_{\mathrm{sc}} = e^2 \rho v \ell_{\mathrm{el}}, \tag{2.12}$$

where v is the carrier velocity, ℓ_{el} the elastic mean free path (see Sec. 2.16), and e the elementary charge. From Eq. 2.12 and by knowing the charge density n, one can calculate the charge mobility, which at $T = 0\,\mathrm{K}$ reads:

$$\mu(E) = \frac{\sigma_{\mathrm{sc}}}{en}. \tag{2.13}$$

Close to the Dirac points, the experimental conductivities lie within $\sigma \simeq 2 - 5\ e^2/h$ [24], although several experiments have demonstrated a variation of more than an order of magnitude because of doping from the electrical contancts or the substrate [25, 26].

2.1.2 Graphene Transistors

The remarkable properties outlined in the last section are certainly amongst the reasons that motivates the great emphasis put on graphene in the 2021 International Roadmap for Devices and Systems [27], which in its *beyond CMOS* study analyses technologies and semiconductor materials that will supplement or replace silicon (Tab. 2.1). Initial interest for using graphene as a channel material in CMOS logic

†$D = k_{\mathrm{B}}T/\eta = \mu k_{\mathrm{B}}T$, where $k_{\mathrm{B}}T$ is the thermal energy of a flow of semiclassical charge carriers that experience an average friction coefficient η when diffusing in a medium with coefficient D.

	Indirect Gap		Direct Gap		
	Si	Ge	GaAs	InAs	Graphene
a_{lattice} (Å)	5.43	5.65	5.65	6.06	2.46
E_g (eV)	1.12	0.66	1.42	0.36	0
μ ($\text{cm}^2\text{V}^{-1}\text{s}^{-1}$) at 300 K	1400	3900	4600	16,000	200,000
v_{sat} (10^7 $\text{cm}\,\text{s}^{-1}$)	1	0.6	2.2	4.0	>5
DOS (m^*/m_0)	1.08	0.56	0.067	0.023	0
ϵ_r	11.9	16.0	13.1	14.6	2.4
κ ($\text{W}\,\text{m}^{-1}\,\text{K}^{-1}$)	150	60.2	46	27	5000

Table 2.1: Comparison between graphene and the most common materials in semiconductor electronics. The general interest in finding solutions for circumventing the absence of the bandgap in graphene is due to various graphene characteristics, including mobility, carrier velocity at saturation, low electrostatic shielding provided by a very low dielectric constant, and an excellent ability to conduct heat, as shown by thermal conductivity values. The last point is particularly pertinent to the design of graphene-based thermal sinks.

may have been fueled by its remarkable mobility [28]. In a standard CMOS gate, carriers are driven by a longitudinal electric field $\mathcal{E}_{\text{SD}}$ from the the source to the drain, and their motion is often limited by various scattering sources, such as collisions between electrons and phonons of the crystal lattice from which the gate is made. In their first graphene-based field-effect transistor (FET) prototype, Novoselov and colleagues measured an impressive intrinsic mobility μ_e^{in} at 290 K close to $\mu_e^{\text{in}} \simeq 10,000\ \text{cm}^2\text{V}^{-1}\text{s}^{-1}$ [21] using a single layer of graphene on a Si/SiO_2 substrate serving as a back gate. These results were explained by: (1) an assumption that graphene has electrons with negligible effective mass close to the Fermi energy, and (2) a lack of direct carrier backscattering because of graphene's lattice symmetry [20]. Although some believed scatterings due to charged impurities [29] or microscopic ripples [30] to be predominant at low temperatures, weak electron–phonon scattering

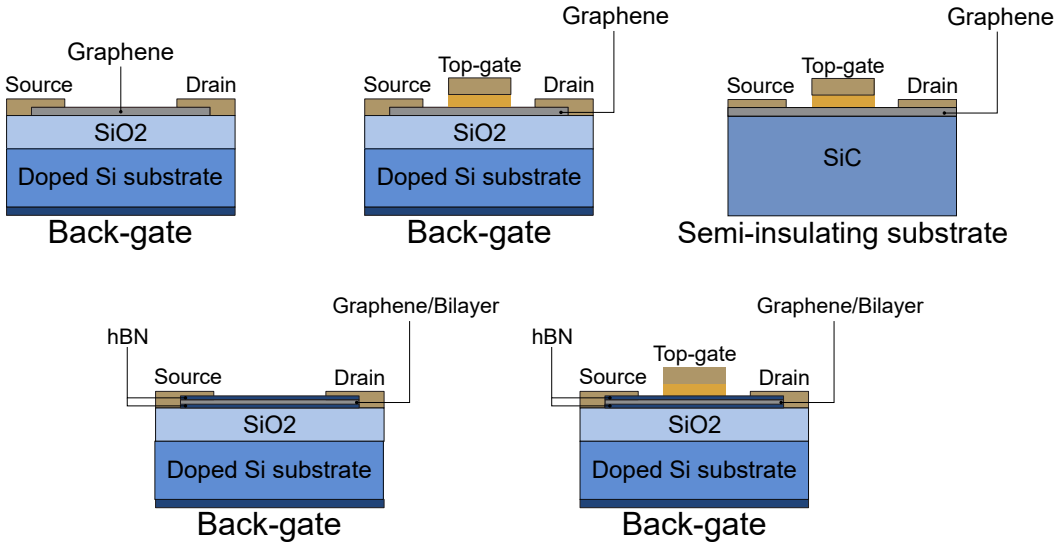


Figure 2.2: top, Architectures of graphene metal–oxide–semiconductor field-effect transistors (MOSFETs). Charge carriers can be modulated in a graphene channel (epitaxial, CVD-grown, or multi-layer) connecting two metal contacts by either a back-gate or a top-gate. SiC substrates have been used for growing in-situ thermally decomposed graphene, which has found successful radiofrequency applications. **bottom,** Same architectures can be now fabricated with graphene between two hexagonal boron nitride (hBN) layers. Adapted from [14].

even at room temperature is considered to be responsible for the extrordinary mobility $\mu^{\text{in}} \simeq 200\,000\,\text{cm}^2\,\text{V}^{-1}\,\text{s}^{-1}$ reported from graphene sandwiched between two hBN layers [31] (Fig. 2.2). Having a slight lattice mismatch (about 1.5% [32]) relative to graphene, $\varepsilon_{\text{hBN}} \simeq$3–4, and significant bandgap (5.9 eV), hBN is considered the best insulating to encapsulate graphene, and indeed hBN-sandwiched graphene devices have been recently used for groundbreaking results such as unconventional superconductivity in bilayer graphene [33] and Stoner ferromagnetism [34].

The high mobility alone is, however, insufficient. As we have mentioned earlier, one of the main motivations for engineering graphene-based transistors is that, because of the absence of electron backscattering, they should be robust against increases in off-state current when the CMOS channel is scaled down [35–37]. Furthermore, the device conductance must be regulated by the gate voltage V_{G}, and has to be robust against any voltage fluctuations. The figure of merit associated

with last requirement is the so-called I_{on}/I_{off}. The on–off ratio quantifies the ability of any circuit component in electrical contact with the transistor to distinguish between the transistor's on and off-states. A high on–off ratio corresponds, typically, to a low leakage current. It is possible to estimate the on–off ratio of a device using

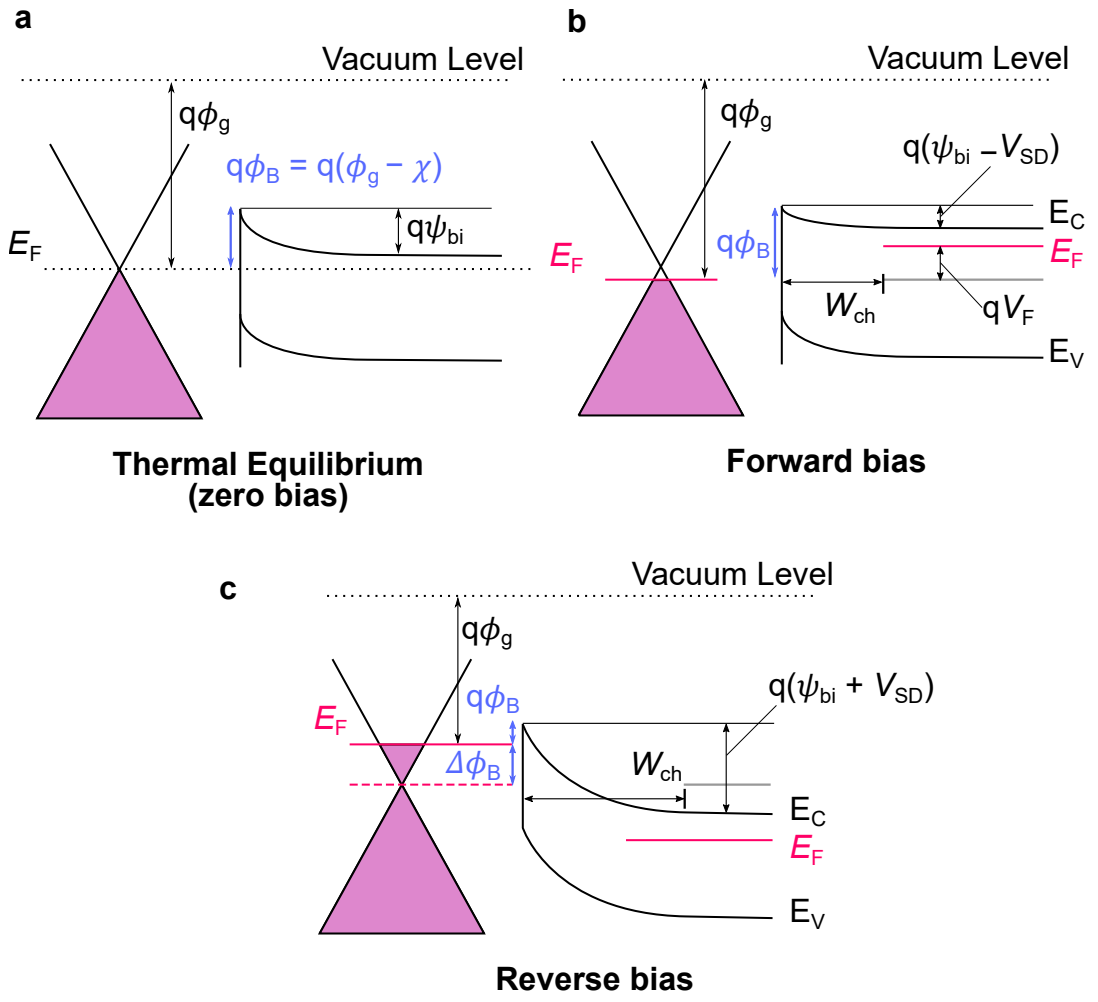


Figure 2.3: a–c, Energy-band diagrams of graphene–semiconductor contacts (a) in thermal equilibrium, (b) when a forward bias is applied, and (c) when a reverse bias is applied. χ is the electron affinity, ψ_{bi} is the built-in potential, and W_{ch} is the channel length [38].

the thermoionic-emission model for the drain current (Fig. 2.3). When graphene is in contact with silicon, the two work functions ϕ_{Si} and ϕ_g align accordingly based on the doping and the carrier concentrations. If $\phi_{Si} = \phi_g$, the schottky barrier (SB) formed at the Si–graphene junction may be written as $\phi_B = E_g/2$, where E_g is

the semiconductor bandgap, and the on–off ration is [39]:

$$\frac{I_{\text{on}}}{I_{\text{off}}} \propto \exp\left(\frac{E_g}{2k_{\text{B}}T}\right), \tag{2.14}$$

where $k_{\text{B}}T$ is the thermal energy. Some researchers suggest that bandgap values of 0.3–0.5 eV are ideal for CMOS applications [14, 40].

Despite considerable efforts, logic applications have been hindered by the metallic nature of graphene from producing CMOS architectures with high-resistance off-states, and have therefore deemed it unsuitable for logic applications. In contrast, graphene-based electronics are broadly useful in applications requiring high frequencies. For analogue applications, properties such as ballistic transport, linear current–voltage characteristics, high transconductance, and exceptionally high sustained currents ($> 10^8$ A cm^{-2}) have proven to be ideal [41, 42].

2.1.3 High-Frequency Applications

The frequency device performance are characterised in terms of two quantities, namely cutoff f_{T} and maximum of oscillations f_{max} frequencies. The former indicates how quickly a signal may travel from the gate to the drain of the device and is often measured when the small-signal current gain approaches unity, while the latter is the highest possible frequency at which there is a non-vanishing power gain [14]. The frequency response is inversely related to the length of the gate and proportional to the transconductance, which is approximately proportional to mobility[†]. Therefore, to achieve high cut-off frequencies in a transistor, researchers must maintain high carrier mobility when the channel length is scaled down [35]. In this regard, numerous research groups have demonstrated radiofrequency (RF) applications for graphene [43–45].

Late in 2008, it was claimed that the first device with a cutoff frequency in the gigahertz region was fabricated using exfoliated graphene placed on a high-resistivity silicon substrate, with a 30 nm-thick top-gate dielectric made of HfO_2 and a 500 nm-long gate [41]. Despite a reported cutoff frequency of about $f_{\text{T}} \simeq 14.7$ GHz, it was

[†]This is strictly valid if the mobilities are in the diffusive regime. If carriers approach ballistic values, then the transconductance is constant.

stated that excessive contact resistances and gate lengths were the primary causes of low ($f_{\max} < 1\,\mathrm{GHz}$) maximum frequency performance. The following year, Pd/Au contacts and a 12 nm-thick aluminum oxide were implemented in a 350 nm-long graphene gate, and although the cutoff frequency was increased to 50 GHz the maximum frequency was increased only to 2 GHz [46]. This poor performance was attributed to the organic contaminations on the graphene surface resulting from the use of poly(methyl methacrylate) (PMMA) as a supporting layer during the transfer process, as well as poor development of gate dielectrics [47].

After two years, a one-order-of-magnitude rise in the cutoff and the highest frequency of oscillation was demonstrated [48]. The device was realised with an epitaxially grown silicon-carbide–graphene MOSFETs with a 240 nm gate length, Ti/Pd/Au contacts, and HfO_2 10 nm-thick as top gate. Local gating is frequently preferred as gate-source, and gate-drain capacitances are inversely proportional to the channel length and minimised in this geometric configuration, hence improving the cut-off frequency that can be reached [44]. In addition to $f_{\mathrm{T}} \simeq 100\,\mathrm{GHz}$, the highest maximum frequency ever measured was $f_{\max} \simeq 100\,\mathrm{GHz}$, beyond the capabilities of any technology at the time. Xu et al. noticed that, since the maximum oscillation frequency significantly depends on device layout and parasitic resistances arising from the metallic contacts, partial passivation of the metal contacts and a multi-finger gate layout would be viable strategies to increase $f_{\max}$ [49].

Later the same year, a 144 nm-long gate device with $f_{\mathrm{T}} \simeq 300\,\mathrm{GHz}$ was developed using mechanically exfoliated graphene and Co_2Si–Al_2O_3 nanowire as self-aligned multi top-gates [50]. This result was also confirmed by comparison to the predicted value based on the relationship[†] between direct current (DC) transconductance, gate capacitance, and the cutoff frequency in the case where total input parasitic capacitance is negligible. The authors did not report the power $G_{\max}^{1/2}$, only the current gain $|h_{21}|$, making it difficult for others to assess the $f_{\max}$ of the device. A rough estimate might be extracted by looking at the

[†] $f_{\mathrm{T}} = g_{\mathrm{m}}/(2\pi C_{\mathrm{g}})$ [51]

results reported by Cheng and colleagues on a similar device, where the gate was built using a stack of $Au/Ti/Al_2O_3$ [52].

Improvements in the cutoff frequency response ($f_T \simeq 427\,GHz$ for a channel length of 67 nm) compared with that of chemical vapour deposition (CVD) graphene devices with similar gate length, however, were eclipsed by only minor improvements to the device maximum frequency response ($f_{max} = 8\,GHz$) when the gate length was lowered to 46 nm. As for the cutoff frequency, it is vital to minimise all parasitic resistances and capacitances in order to optimise f_{max}. In addition, the output conductance must be decreased in order to obtain the highest feasible operating speeds, which is often accomplished by operating the transistor when the drain current is saturated.

IBM researchers investigated the saturation behaviour of short-channel graphene transistors leveraging CVD graphene transferred to diamond-like and SiC substrates, in an attempt to improve the power gain [53]. These are particularly attractive possibilities since the substrates are commercially accessible on high-quality wafers, which makes it quite straightforward to scale up graphene arrays. Since the work function of graphene ($\phi^g = 4.5\,eV$) is greater than that of silicon carbide ($\phi^{SiC} = 3.7\,eV$), negative charges accumulate on the graphene side of the contact, leaving graphene n-doped [54]. The authors compensated this unwanted doping by using an innovative technique involving plasma-enhanced CVD silicon nitride as an intrinsic, p-type gate dielectric.

The transistors perform well at high speeds, not only because of their good cutoff frequencies ($f_T \simeq 350\,GHz$), but also because of their twofold increase in maximum oscillation frequency $f_{max} \simeq 40\,GHz$, suggesting undoped-graphene substrates as ideal for high-frequency applications. To the best of my knowledge, the current graphene transistor power-gain record is approximately 70 GHz, achieved by using a $(0\,0\,0\,\overline{1})$ carbon-terminated surface of silicon carbide instead of the conventional $(0\,0\,0\,1)$. This indicates that a low contact resistance between the gold contacts and graphene is the primary factor responsible for the high maximum frequency [55].

In terms of cutoff frequencies, the performance of graphene-based devices is comparable to that of the leading solid-state competitors, such as GaAs high-electron-mobility transistors (HEMT), InP HEMT, and Si MOSFETs. The performance in terms of maximum frequencies, however, is one or two orders of magnitude below the required values for a competing technology [56–58]. In the scientific literature, one of the most commonly cited underlying factors for this behaviour is the weak saturation in the drain current in graphene, which ultimately depends on the lack of a bandgap in the channel.

Because of their intrinsic semiconductivity, graphene-derived materials such as CNTs and GNRs-MOSFETs could be a viable solution to this problem. In the following sections, I will investigate some important aspects of the electronic response at the device level for each class of materials.

2.2 Carbon Nanotube Electronics

The literature on carbon nanotubes is vast and well documented. In the following, I have two primarily aims. Firstly, I will provide a comprehensive review of carbon-nanotube field-effect transistors (CNTFETs), highlighting crucial elements that have, in my opinion, played a significant role in enhancing the competitiveness of nanotube-based transistors. Secondly, I will quantify the performance in order to compare it to GNR-based transistors.

In contrast to graphene, CNTs have an electrical bandgap that varies according to the nanotube chirality and diameter [59], and may be defined in real space by two unit vectors $\mathbf{a_1}$ and $\mathbf{a_2}$ and any linear combination of these with integer coefficients, which are typically labelled m and n [60]. Depending on these coefficients, a CNT can be metallic, quasi-metallic, or semiconducting.

As depicted in Fig. 2.4, states resulting from quantisation in the circumferential direction may or may not pass through one of the $\mathbf{K}$ points in the first Brillouin zone of graphene, and the resulting CNT will be metallic when the electronic states cross a $\mathbf{K}$ point, else it will be semiconducting. Exceptions to this simple rule arise from to the strong curvature when the diameter of the tube is sufficiently small,

which leads to large spin–orbit interactions [61, 62]. The discovery of charge-carrier

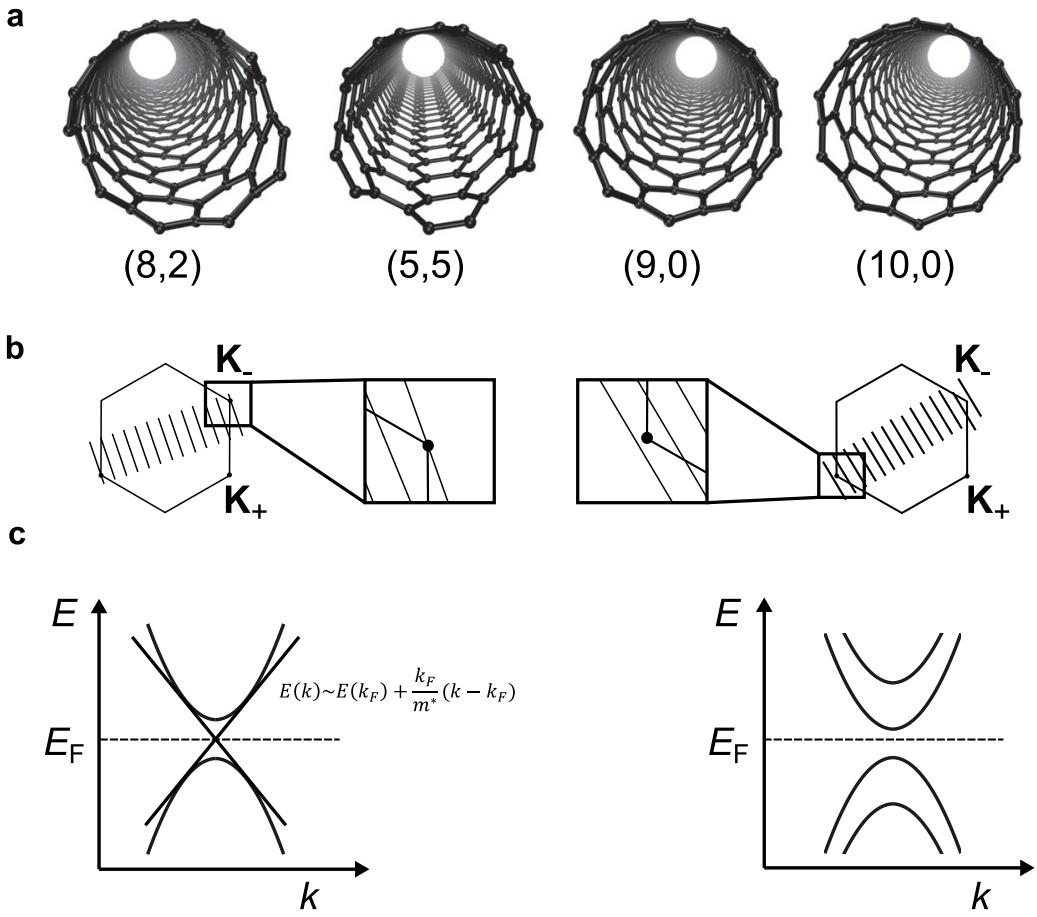


Figure 2.4: **a**, Cartoon structure of a chiral (8, 2), an armchair (5, 5), and a zigzag (10, 0) nanotube. **b**, Graphene Brillouin zone and allowed **k**-vectors for the (8, 2) and (10, 0) CNTs. A metallic tube (left) includes one of the **K** points among the set of allowed **k**-vectors. As shown in **c**, it is then possible to linearise the energy dispersion in the momentum space for low excitations (close to the Fermi energy E_{F}). Conversely, the **K** point is not an allowed vector for semiconducting nanotube, and this leads to an energy gap. Inspired by [63].

modulations within a nanotube produced by a gate-induced electric field was the first landmark which started the field [64]. These early FETs were fabricated using a doped silicon substrate as the gate to tune the energy bands, with thermally grown silicon dioxide acting as the dielectric between the nanotube and the substrate, and Au contacts to electrically contacting the nanotube.

Since then, several CNTFET designs have been put forward (Tab. 2.2), which

Table 2.2: Figures of merit for a few CNTFETs reported in the literature. *SS*: subthreshold swing; g_{m}: intrinsic transconductances; L_{ch}: channel length; μ: carrier mobility; f_T: cutoff frequency; f_{max}: maximum of oscillations frequency

Device type	$I_{\mathrm{on}}/I_{\mathrm{off}}$	*SS* (mV/dec)	g_{mt} ($\mu\mathrm{S\,cm^{-1}}$)	L_{ch} (nm)	f_T [f_{max}] (GHz)	Ref.
Bottom gate	10^4	94	$\simeq 40$	9	—	[65]
	10^5	$\simeq 85$	40	15	—	[66]
	10^5	$\simeq 85$	20	20	—	[66]
	10^5	60	20	200	—	[67]
	10^5	$\simeq 63$	—	200	—	[68]
	10^4	80	50	240	—	[69]
	—	—	143	800	—	[70]
	10^4	—	—	1500	1.5 – 3.0	[71]
	—	70	12†	2000‡	—	[72]
	10^8	—	—	$< 10\,000$‡	—	[73]
	—	—	−500	—	30	[74]
Top gate	10^6	—	20†	80	—	[75]
	2	—	$\simeq 50$	100	25	[76]
	50	—	310	100	$\simeq 70$ [80]	[77]
	—	—	0.3	210	—	[78]
	10^5	—	33.5	85 000	—	[79]

†Normalized by the tube width.
‡Referred to the gated length of a nanotube.

may be classified even more fundamentally as devices with or without a spacer. The length of the spacer L_{spr} is the gap between the channel and the metal contacts. Given that a certain class of nanotubes is intrinsically semiconducting, the flow of charge carriers in spacer-less devices is not generated by the electric field $\mathcal{E}_{\mathrm{SD}}$ in the conductive channel, but rather by the charge-concentration gradient that exists between the two ends of the nanotube.

The role of the gate is to lower the energy barrier between the metal and the semiconducting channel, thereby allowing electrons to tunnel from the source through the SB. In this case, both the metal ϕ^{M} and the CNT ϕ^{CNT} work functions are critical in the transistor performance: the lower their mismatch is, the more efficient is the injection of the carriers at the source, resulting in current densities that approach the Ohmic-contact case (Tab. 2.3). In contrast, CNTFETs with

Table 2.3: Comparative analysis of the most common electrical-contact types for connecting CNTFETs [81]. Applied drain voltage $V_{SD} = 0.5\,V$

Contact type	I_{on} (A)	I_{off} (A)	I_{on}/I_{off}	g_{mt} (µS)	SS (mV/dec)
Conventional	1.4×10^{-5}	4.1×10^{-10}	3.4×10^{4}	29	100
Partial S/D-doped	1.5×10^{-5}	2.3×10^{-8}	6.4×10^{2}	64	93
Schottky-Barrier	3.3×10^{-6}	2.3×10^{-8}	1.4×10^{2}	20	110
Tunnel	5.5×10^{-6}	1.2×10^{-8}	4.8×10^{2}	13	108

spacers are not limited by the at-the-source injection step, since the electric field $\mathcal{E}_{SD}$ drives the carriers flow, and indeed Javey and Kong produced a device with spacers where the mismatch between ϕ^{M} and CNT ϕ^{CNT} was large, and found that the device was more resistant to ambipolar conduction because of the substantial energy barrier at the drain [63, 80].

There is another reason to study how different work functions affect the transistor performance. Solid-state semiconductors have dangling bonds at the surface resulting in Fermi-level pinning, which means that the variation of the band bending is independent of the metal work function even when large [82]. Since, ideally, the CNT structure has no open bonds, the Fermi level of the metal will not be pinned to mid-gap states [83, 84].

For example, it has been shown that metals with high work functions, such as Pd ($\phi^{Pd} \simeq 5.2$–$5.6\,eV$), yields p-type behavior with high on state current for large-enough CNT diameter $d_{CNT} \geq 2\,nm$ [85], and that the SB height is inversely proportional to d_{CNT} [84]. The reason for this observation was explained within the SB framework, i.e. large work functions prevent the minority carriers to hop over the barrier back into the channel, resulting in low leakage current. Metals with large work functions are, however, more strongly associated with large contact resistances when their wettability is poor [86], suggesting mentals with good wettability such as Ti and Cr as ideal for low contact resistances.

Often, however, metals with low work functions and good wettability have a strong tendency to oxidise, especially in air. A possible workaround is to cap low-work-function contacts all-around with metals having high work functions,

such as Sc and Y [87]: the CNTFETs thus produced displayed high on-state currents ($I_{\mathrm{on}} \simeq 250\,\mu\mathrm{A}$), mobilities $\mu \geq 500\,\mathrm{cm\,V^{-2}\,s^{-1}}$, and drain-induced barrier lowering (DIBL) up to 105 mV/V, together with excellent switching behaviour $SS \simeq 73\,\mathrm{mV\ dec^{-1}}$ [87, 88].

The subthreshold swing SS measures the rate at which the gate voltage switches on the transistor, and it is a metric that quantifies the control the gate has on the conductive channel. It is also indirectly linked to heat dissipation, which is one the primary obstacles to miniaturising CMOS technology. Since the carriers are thermally injected, it is challenging to reduce the operating voltage while at the same time improving CPU operational speed and maintaining a low off-state power dissipation. The off-state power scales quadratically with the off-state current $P_{\mathrm{off}} = RI_{\mathrm{off}}^2$, thus the objective is to lower the I_{off} without sacrificing I_{on}. The process of thermally injecting charge carriers imposes a limit, called Boltzmann limit, on the subthreshold slope which for the is approximately $2.3k_{\mathrm{B}}T/q \simeq 60\,\mathrm{mV\ dec^{-1}}$ at room temperature.

One of the most promising approaches to overcoming the Boltzmann limit uses a different source–carrier injection mechanism based on Zener tunnelling rather than thermal means. If the transmission probability does not depend on the energy gap between the metal and the nanotube work functions, but instead depends on the interband tunnelling, the output current is temperature-independent. Several researchers have proposed both CNT- and GNR-based transistors with this operating mechanism [89–91].

Crucial is also the conduction type. The vast majority of the CNTFET transfer I_{SD}–V_{G} characteristics reported are p-doped [92], and this is largely because photochemical resists in the lithographic steps often leave p-type contaminations on the substrate [93]. Instead, n-type devices would be desirable.

As a result of the presence of electron-donating dopants, n-type doping assures that, in a heterojunction, CNTs do not have to pull electrons from the opposite side of the junction because this need is satisfied by the dopant atom [94]. Instead, the nanotube would preferentially donate electrons to the heterojunction p-type

side, leaving behind an electron vacancy (hole) that is stabilised by the excess of negative charge carriers provided by the dopant.

An interesting solution for fabricating n-type CNTFETs is by doping the nanotube-channel surface with elements of the first two groups of the periodic table, such as K^+ and Mg^{2+} [95, 96]. Precise control of the doping density per CNT unit length is, however, necessary, and this is often difficult because of the high tendency of CNTs to aggregate when dispersed in solution, often yielding uncontrolled doping levels [94, 97]. Additionally, ionised impurities, instability in air and to temperature fluctuations have hampered the applications of n-type CNTFETs.

2.2.1 Channel-Length Scaling

Whether Si could operate at channel lengths below 10 nm was a question for a long time, but recent scientific advances in FinFETs [8] and Gate-All-Around FETs [9] have demonstrated its viability and sparked a plethora of commercial uses (currently, modern devices employ the 4 nm technology). Nonetheless, CMOS scaling has always been a good-enough reason for investigating fabrication techniques and materials robust against short-channel effects[†].

In CNTFETs, two are the main device parameters that can be scaled down: the contact length L_c and the channel length L_{ch}. The L_{ch} scaling typically reduces the gate control over the channel, hence the ability of the electric field generated through the gate to bend the silicon band structure. Intuitively, as the channel length is reduced, the electric field created by the source–drain contacts will be felt by the charge carriers more and more. CNTs may provide a suitable platform for such scaling because of their ultrathin, hollow nature. This could be, however, a double-edged sword. Since the electron effective mass is smaller[§] compared to that of silicon, the tunnelling probability may be large enough to increase drastically the source–drain current. From a device performance point of view, this often means an increase in the SS and high I_{off}.

[†]Typicaly short-channel effects are threshold voltage roll-off, off-state leakage current, and channel length-modulation are just a few of the problems

[§]$m^*_{CNT} = (0.228 \pm 0.129)m_0$ [99]

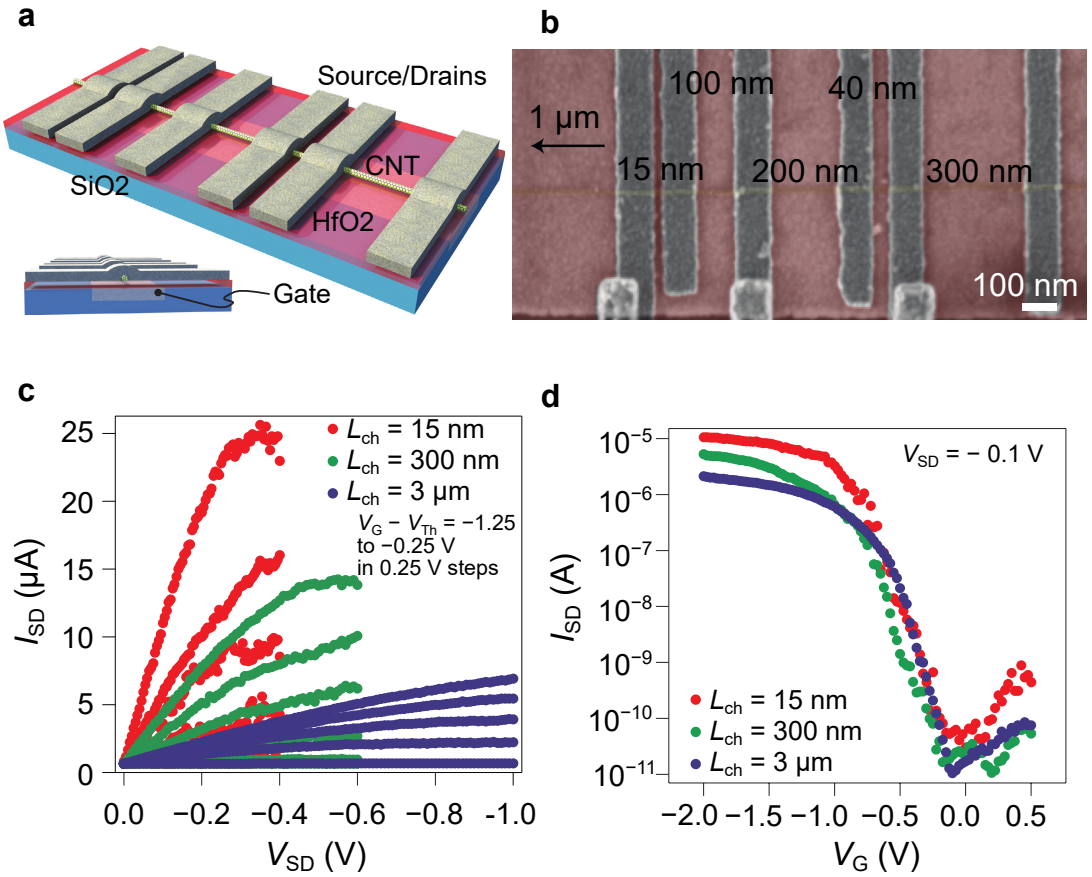


Figure 2.5: **a**, Schematic of the set of transistors used by Franklin and Chen. Cleverly, a single CNT was used with L_{ch} ranging from 1 µm downo to 15 nm. **b**, False-coloured SEM image. **c**, Output I_{SD}–V_{SD} characteristics, demonstrating improvement in the on-state current when L_{ch} is scaled from 3 µm down to 15 nm. **d**, Subthreshold I_{SD}–V_G transfer curves, showing the consistency of V_{Th} and SS when L_{ch} is reduced by more than two orders of magnitude. Adapted from [98].

Franklin and Chen conducted one of the earliest systematic studies on L_{ch} scaling, through a series of experiments on CNTs [98] (Fig. 2.5). When the channel length was reduced by more than two orders of magnitude (from 3 µm down to 15 nm), a consistent trend was found in both the threshold voltage ($V_{Th} \simeq (-0.5 \pm 0.2)$ V) and the subthreshold swing ($SS \simeq 90$ mV dec^{-1}). The threshold voltage is the gate voltage required to fully invert the semiconductor. It is typically measured by applying a small V_{SD} and measuring the I_{SD} as a function of V_G, provided that the drain current is at least one order of magnitude smaller than the applied gate voltage, scaled accordingly by the gate capacitance.

This, essentially, means that the gate-generated electric field controls the carriers flow even when the electric field between source and drain becomes non-neglibile. An aggressive reduction of the channel length, however, could in principle make the gate less effective in controlling the charge carriers, meaning that larger gate variations are required for pulling the same amount of current from the drain. This essentially implies that the gate-generated electric field controls the flow of carriers even when the electric gradient between source and drain is no longer negligible. However, an extreme reduction of the channel length might, in theory, reduce the current amplification (the gain), excluding the possibility of employing CNTs as molecular op-amp.

And indeed, at that time of Franklin and Chen's experiment part of the scientific community believed that the L_{ch} scaling could have had a negative impact on the CNTFETs gain, i.e. low transconductance g_{m} [80, 100, 101]. In a standard MOSFET, the transconductance g_{m} is defined as $g = \partial I_{\mathrm{SD}}/\partial V_{\mathrm{G}}$, and it is measured by applying a small, constant bias. Typical values lies in the range (1–30) $\mathrm{mS\,\mu m^{-1}}$ for a small-signal field-effect transistor [51]. However, Franklin and his colleagues measured transconductance values as high as $40\,\mathrm{\mu S\,\mu m^{-1}}$ for CNTFETs with $L_{\mathrm{ch}} \simeq 15\,\mathrm{nm}$ ((Fig. 2.6)), which corresponds to transconductance values of approximately (91–110) $\mathrm{mS\,\mu m^{-1}}$, thereby meeting the requirements for a technology compatible and competitive with the silicon. Two years after their findings, Franklin et al. shrank the channel length of a CNTFET to less than 10 nanometers [65]. Their technique involved the use of smaller tubes, and a reduction of the effective oxide thickness (EOT) to 0.65 nm: this was achieved by wrapping the nanotube in a all-around gate (Fig. 2.7). The rationale behind the use of all-around gates is that if the oxide is extremely thick, the gate control over the flow of carriers in the channel tends to weaken [51]. The length of the channel was successfully lowered from down to 9 nm, and the authors reported on-current values close the ballistic limit for transistors 41 nm [98]. Franklin and Chen advocated for decreasing the CNT diameter to reduce the subthreshold swing and off-current with minimum effect to the on-current, and in fact also the switching performance ($SS \simeq 94\,\mathrm{mV\ dec^{-1}}$)

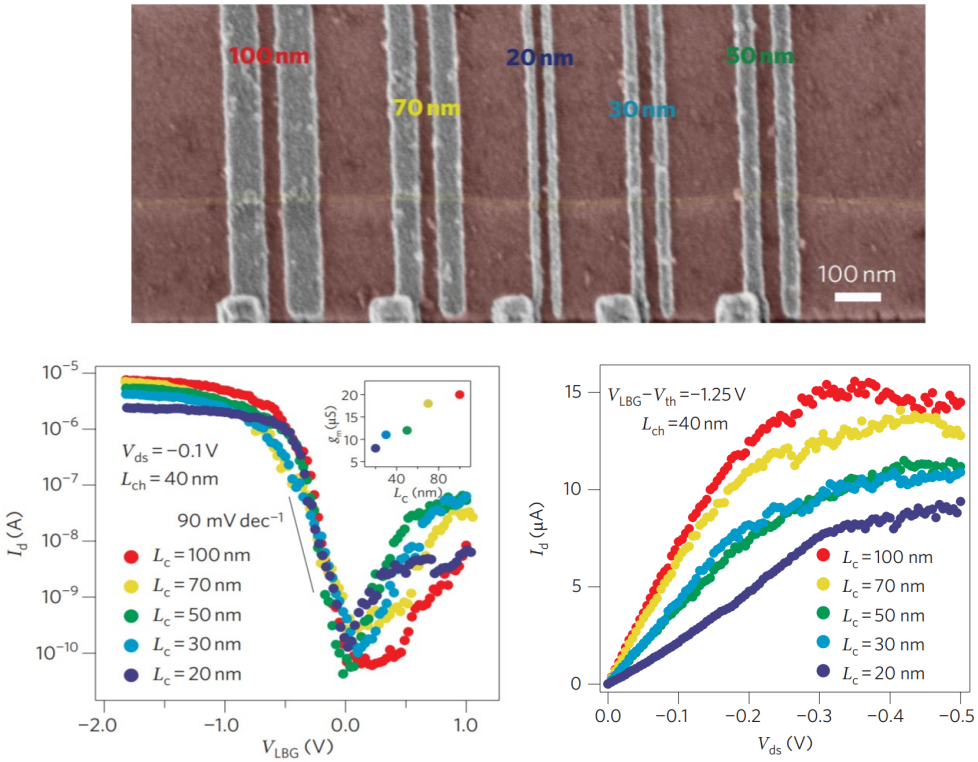


Figure 2.6: Top frame is the false-coloured SEM image of several transistors on the same nanotube but having different L_c, from 100–20 nm. Even for the smaller contacts the gate has complete control over the channel and the device switches quicker than most Si MOSFETs-based competitors. Small contact leghts, however, severly degrades the on-state current, although the saturation regime it is still well within the experimental accessible region. Adapted from [98]

generated great enthusiasm around the CNT technology, leading the year after to the first proposal of carbon nanotube computer [102].

As previously pointed out, in order to keep the off-current low, not only the channel width must be sufficiently wide to discourage quantum tunnelling across the barrier, but also has to be large enough to prevent thermal hopping above the barrier, limiting the back-injection of minority carriers into the channel. We have already seen one device parameter that may be used to adjust this value, namely the nature of the electrical connections. In the following part, we will briefly examine another other adjustable parameter, namely the contact length L_c.

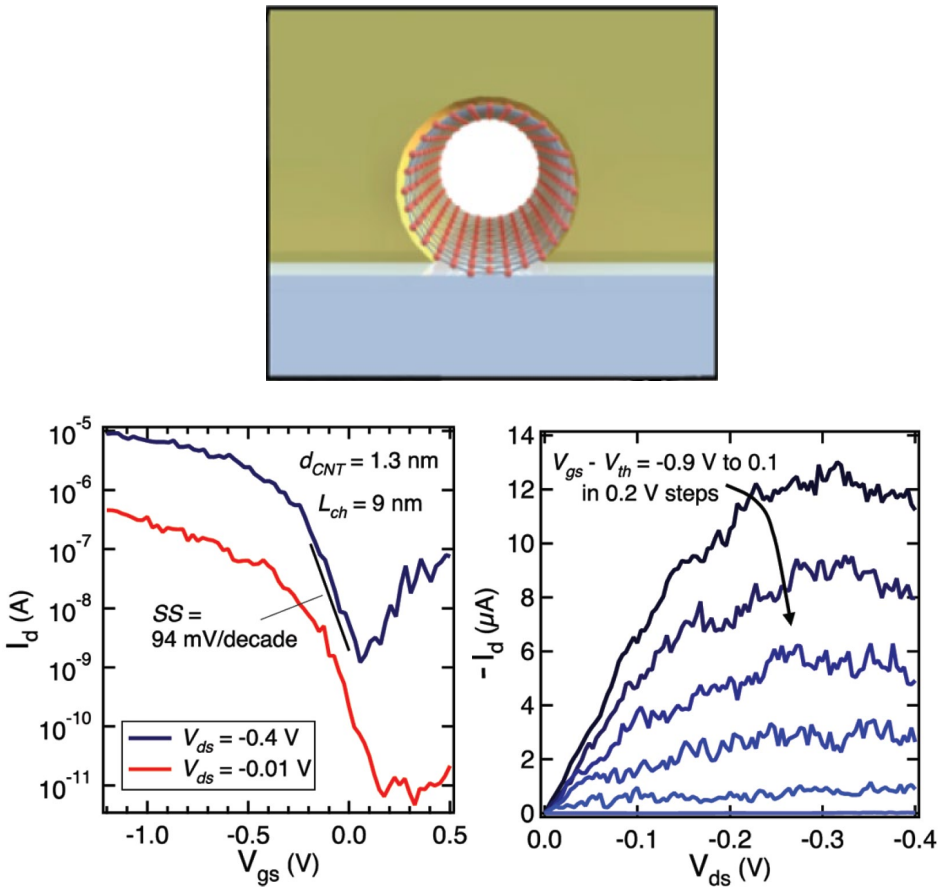


Figure 2.7: top, Visualisation of all-around gate and hollow CNT structures **bottom left**, Subthreshold (off-state) and, **bottom right** output (on-state) characteristics for a $L_{\mathrm{ch}} \simeq 9\,\mathrm{nm}$ demonstrates that the gate does not loose control over the channel. Adapted from [65].

2.2.2 Contact-Length Scaling

When MOSFETs are shrank down to the nanoscale, one must consider also the effect played by the overlap of the CNT with source and drain. Numerical investigations of this phenomenon have suggested that high contact transparencies might be obtained when the metal–CNT coupling is weak, meaning the electronic states of the tube are, more or less, unchanged after the formation of the lead–CNT junctions [103–105]. Especially for long contacts ($L_{\mathrm{c}} \simeq 30\,\mathrm{nm}$), one suggestion advanced by these studies was that in order to achieve high-transparency contacts

one should minimise the coupling while maximising the overlap region, and that the junction Pd–CNT might leads to quasi-Ohmic contacts [106].

By using the transfer length[†] model, experiments performed on small-diameter ($d_{\mathrm{CNT}} \simeq 1.5\,\mathrm{nm}$) CNTs highlighted inverse scaling of the contact length with the resistance between the nanotube and the electrodes, i.e. $L_{\mathrm{c}} \propto 1/R_{\mathrm{c}}$ [98, 108]. These observations were rationalised by considering dipole moments building up at the metal–CNT interface [85], which could be caused by interface states at the junction.

A large density of dipole charges should then translates into a large density of interface states, which could pin the Fermi level. Since, in a planar contact, the dipole in a metal–CNT junction is localised in all directions, the consequence of having interface states is that the CNT energy bands might be shifted away from the junction, inducing the formation of a narrow barrier responsible for the increased contact resistance [109]. Therefore, in order to limit the band shift from the junction, electrical contact with work functions close in value to the CNT one might reduce Fermi-level pinning caused by surface states.

More sophisticated computational methods have also been used in an attempt to clarify the nature (and the role) of the chemical bonds produced when the CNT interacts with the electrode crystal structure. By applying non-equilibrium Green's function (NEGF) numerical schemes, Fediai et al. suggested that the most unfavourable length scaling should be observed for weakly-interacting metals such as Cr, Pd, Pt, and, on the other hand, metals such as Au, Al, and Sc could be nearly insensitive to the scaling of L_{c} when it is decreased down to $\approx 15 - -20\,\mathrm{nm}$ [105]. Furthermore, the authors proposed a numerical criterion through which they projected a better contact resistance scaling for Rh in comparison to Au, Pt, and Pd. However they also simulated the metal–junction long limit and suggested that differences in the R_{c} resulted by adopting Pd instead of Rh

[†]The transfer length is the distance over which a fraction equal to $1 - \exp\{-1\}$ of the total current is *transferred* from the contact metal to the semiconducting channel (e is the Euler's number), and it is frequently used as a metric for quantifying the coupling between electrical contacts and conduction channel (small transfer lengths result in greater couplings, and, consequently, lower contact resistances) [107].

were neglibile, suggesting that the better scaling for the Rh–CNT junctions may be not worth the cost of the material.

2.3 Single-Electron Conduction

When only one single CNT connects source an drain, interesting phenomena arise. The interplay between the energy-level spacing δ and the capacitance per unit length has important consequences for the mechanism through which a current is generated. In particular, mesoscopic systems such as graphene, CNTs, and GNRs can manifest quantum transport phenomena when their sample size becomes comparable to the characteristic lengths of travelling electrons. As a result, physical properties such as the electrical conductivity depend on the specimen dimensionality.

2.3.1 Energy Scales and Characteristic Lengths

Typically, three characteristic lengths are investigated in mesoscopic transport experiments. The mean free path ℓ, the Fermi wavelength λ_F, and the phase-relaxation length L_φ. The first, ℓ, is the average distance an electron travels prior to being dispersed by a scattering centre, whereas $\lambda_F = 2\pi/k_F$ is the wavelength of an electron at the Fermi energy E_F. Finally, L_φ is the average distance over which an electron travels before its quantum-mechanical phase is randomised.

When the scattering of an electron is *elastic*, e.g. when there are no electronic transitions between the ground state and any excited states following the scattering event, the wavefunction essentially undergoes a phase shift following the event, and remains coherent. Elastic scattering, therefore, affects only ℓ and L_φ is unchanged.

In contrast, when the electronic wavefunction loses energy because of (1) electronic transitions, (2) spins associated with magnetic impurities or (3) phonons, both the ℓ and L_φ may be affected (*inelastic* scattering). Tab 2.4 summarises a few of these factors for various materials as a function of carrier concentration n. Because only electrons around the Fermi energy E_F affects the transport properties,

Table 2.4: Physical parameters relevant in transport phenomena. See also [63, 110]

Material type	n $(\mathrm{cm}^{-3})/[\mathrm{cm}^{-2}]$	λ_F (nm)	ℓ (nm)	L_φ (µm)
Metal	1×10^{23}	0.5	$1-10$	0.5
Graphene	1×10^{11}	$2\sqrt{\pi/n}$	50−3000	0.5
SW-CNT	1×10^{11}	0.74	1000	3
MW-CNT	–	–	$10-40$	0.1

both ℓ and L_φ are often scaled by the Fermi velocity:

$$t_m = \frac{L_m}{v_\mathrm{F}} \quad \text{and} \quad t_\varphi = \frac{L_\varphi}{v_\mathrm{F}}. \tag{2.15}$$

The t_m and t_φ are the momentum relaxation time and the phase-relaxation time, respectively, and are often compared to the time takes one electron take to travel through the whole length of the sample [60].

Several are the possible sources of scattering in a transport experiment. For example, by applying a magnetic field it is possible to induce or suppress pure-spin currents by localised magnetic moments in graphene [111, 112], whereas phonons excitations are typically suppressed by decreasing the thermal energy $k_\mathrm{B}T$ [113]. We will use a few of these concepts to give a phenomenological explanation for a few of the experiments we have performed, more specifically in Ch. 5, whereas in the next section we will take a look at how the energy scales introduced here can be captured within the quantum-transport framework.

2.3.2 Electronic-Transport Regimes

In charge-transport experiments, molecules are typically a few nanometers in size, orders of magnitude smaller than what any common manipulation tools could handle. Since the system is confined in 3D, the DOS approaches the Dirac delta distribution $\rho_\mathrm{0D} \sim \delta(E)$. An analogous platform where the density of state approaches the Dirac delta functions are quantum dots (QDs) embedded in single-electron transistor (SET), historically fabricated through lithography means on metallic substrate. In these devices, source and drain are electrically contactd to the central island, whereas one or more gates are just capacitatively coupled (Fig. 2.8).

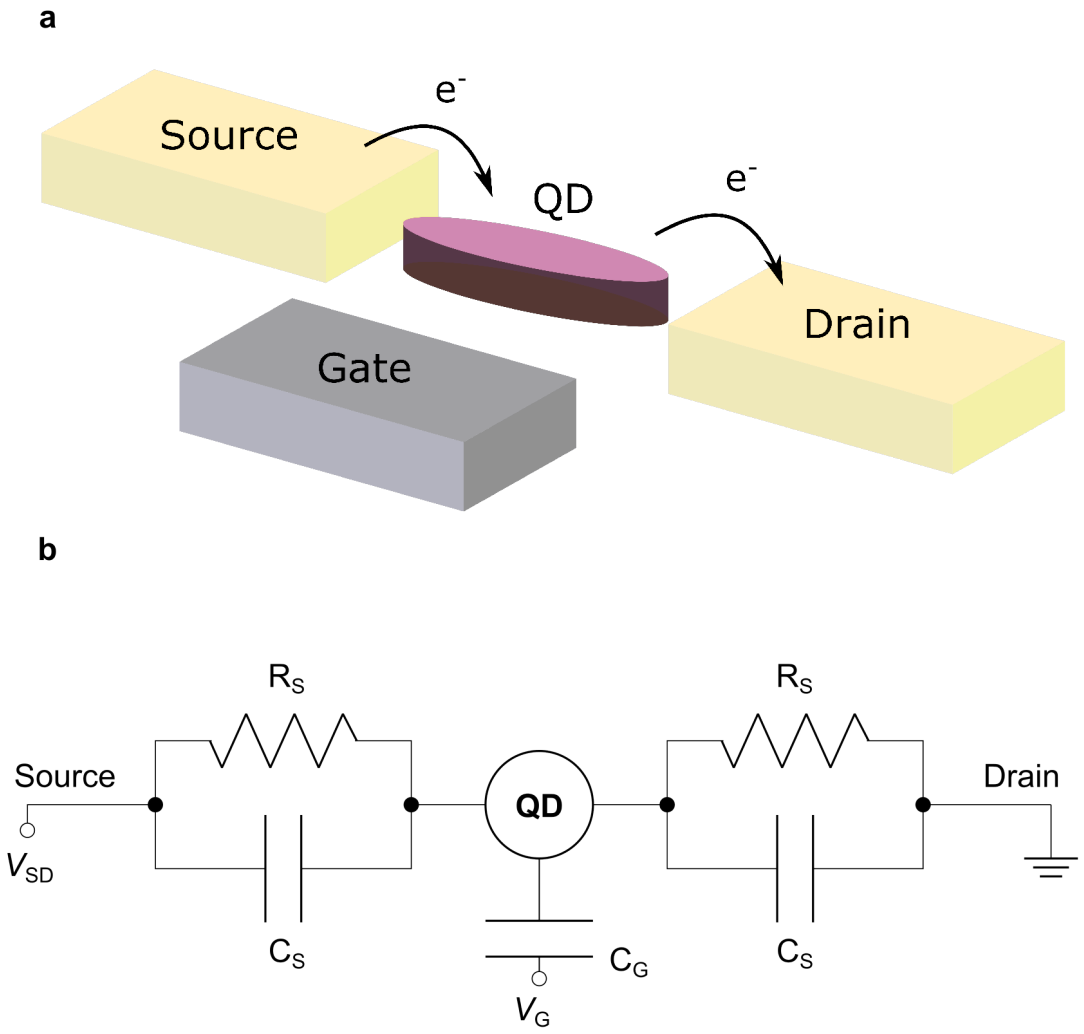


Figure 2.8: **a**, Schematic for a SET based on a QD. **b**, Equivalent circuit. Each tunnel barrier is represented by an RC circuit, and electrons tunnel from the source to the QD and then to the drain.

System such this one can be satisfactorily described by the constant interaction model [114]: Coulomb interactions between source–dot and dot–drain are described by a single capacitance C, which is assumed to be constant and given by the sum of the individual capacitances between the dot with any terminal i in the circuit:

$$C = \sum_{i=1}^{\text{terminals}} C_i, \tag{2.16}$$

The total Hamiltonian is also assumed to be modelled as a sum of single-particle Hamiltonians, meaning that the total energy of the system can be expressed as a

sum of single-particle energies $\Delta\varepsilon$ corresponding to the individual, non-interacting energy levels of the QD [62].

For a three-terminal device with N electrons, the QD energy becomes:

$$U(N) = \sum_{i=1}^{N} E_i + \frac{[e(N - N_0) + C_S V_S + C_D V_D + C_G V_G]^2}{2C}, \tag{2.17}$$

where eN_0 is the charge present on the QD when $V_{SD} = V_G = 0$, and may be because of background charges in the substrate. The chemical potential, central parameter to evaluate whether a current can flow through a dot, is the minimum energy required to add an extra electron to the dot, may be expressed as:

$$\begin{aligned} \mu_{dot}(N) &= E_{dot}(N) - E_{dot}(N-1), \\ &= \left(N - N_0 - \frac{1}{2}\right) E_C - \frac{E_C}{e}\left(C_S V_S + C_D V_D + C_G V_G\right) + E_N, \end{aligned} \tag{2.18}$$

where $E_C = e^2/C$ is the charging energy. In the simplest case as the one above, the overall transport regime is determined by the interplay between E_C, $\Delta\varepsilon$, the thermal energy $k_B T$, and how strongly coupled is the QD to the metallic contacts, quantified by the lifetime broadening Γ. In the following, we will briefly outline the different transport regimes at the nanoscale based on the relative magnitude of these energy scales.

Weak-Coupling Regime

In order to operate in the weak-coupling regime, the smallest energy scale in place must be the molecular-state lifetime broadening, i.e. $\Gamma \ll E_C, E_{add}(N), k_B T$, and this condition is often realised in electrical break junctions such as the ones used in this thesis [115].

In this regime, Coulomb blockade (Fig. 2.9) and single-electron (sequential) tunnelling prevails. This transport mechanism typically involves two steps. In the first step, an electron tunnels from one electrode into the molecule: this process is often captured by the notation $N \leftrightarrow N + 1$, where the double-ended arrow refers to the possibility of having an electron tunnelling back into the first electrode. Overall, the total-spin change is $\Delta S = \pm 1/2$. In the second step, the electron tunnels from the molecule to the second reservoir.

A necessary, and sufficient, condition for the charge transfer to take place is that the energy levels of the two leads $E_{\mathrm{F},(1,2)}$ and $E_{\mathrm{F},2}$ have, at least, an energy equal to the electrochemical potential of the molecule μ_N. This condition is often met by either applying a bias $eV_{\mathrm{SD}} = E_{\mathrm{F},1} - E_{\mathrm{F},2}$ between the leads or by tuning μ_N thorugh a gate electrode, thus allowing or blocking the current flow. The resulting device conductance may be visualised by plotting it as a function of the gate and bias voltages (*charge stability diagram*, Fig. 2.9a). The Coulomb blockade (grey regions) are characterised by noisefloor level of currents, and are referred to as Coulomb diamonds: in these regions transport is blocked because the energy cost to add an electron onto the QD exceeds the available energy.

Strong-Limit Regime

In this regime, Γ is greatest energy scale at play, i.e. $\Gamma \gg E_C, E_{\mathrm{add}}(N), k_{\mathrm{B}}T$, leading to a strong hybridisation QD states with those of the leads. Coulomb blockade is suppressed by quantum fluctuations of the electric charge, and the dominant transport mechanism is elastic coherent tunnelling. This mechanism is particurarly appealing because and the electrical conductance G can be well described by the Landauer formula $G \simeq \frac{2\exp 2}{h}\mathcal{T}(E)$, where $\mathcal{T}(E)$ is the transmission probability thorugh the dot for all the available conduction channels, and is often use as a starting point of many numerical routines [118].

As pointed out in [115], the crossover between the weak- and strong- coupling remains largely unstudied, and only a few experiments have been performed to probe this intermediate regime. Examples in the literature include the crossover induced by the high-energy vibrational modes (e.g. streching) in mechanical break junctions [119] and the one induced at high temperature whitin the inverted Marcus region, cause by nuclear tunnelling [120].

Intermediate Case

When there is no energy scale which dominates over the others, a combination of the weak-coupling and strong-coupling regimes occurs. QD retains a noticeable Coulomb blockade, while also exhibiting transport within the zero-conductance

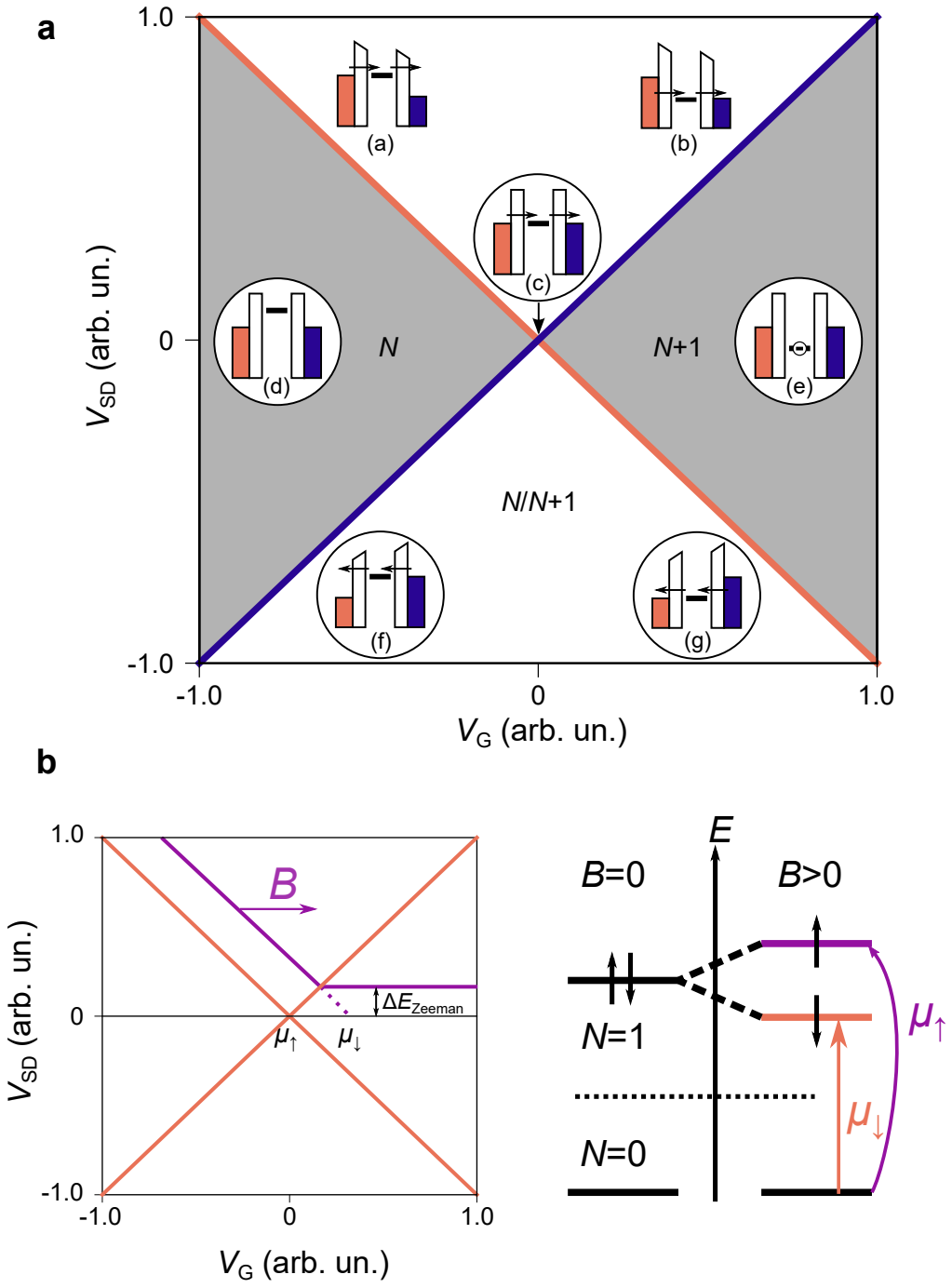


Figure 2.9: **a**, Stability charge map. Within the grey regions, the charge is fixed at N (d) or $N+1$ (e), which leads to Coulomb blockade. In the white area, electron tunnelling occurs in and out of the QD. The blue and orange line are observed if instead of the current I_{SD} one measure the differential conductance dI/dV_{SD}, e.g. through a lock-in amplifier (See Ch. 4) **b left**, Ground and excited state split induce by the Zeeman interaction. Conductance step may occur when $e|V_{SD}| = \Delta E_{Zeeman}$ in the blockade region [116]. **b right**, Two different charge states. Degeneracy between spin up and spin down is lifted by the external magnetic field B. Adapted from [117].

region. The two most common transport mechanisms of the intermediate coupling regime are elastic and inelastic cotunnelling. Compared to sequential single-electron tunnelling, these are higher-order transport mechanisms that involve the tunnelling of two electrons at the same time.

In the first step, the QD chemical potential lies lower in energy than the electrochemical potentials of both leads. When an electron tunnels from the source into the drain through the QD, and a virtual state lies within the bias window, two are the main possible scenarios. Another electron may tunnel from the source to QD, while simultaneously an electron leave the dot and tunnels into the drain. This process, does not involve any energy exchange and is therefore called *elastic cotunnelling* (Sec. 2.3.1); experimental signatures are horizontal lines in the zero-conductance region touching a slanted diamond line on the Coulomb edge [116]. In the second scenario, an electron tunnels into the virtual state positioned at an energy δ away from E_{F} in the electrodes, and, as we saw in Sec.2.3.1, results in an exchange of the total energy (*inelastic cotunnelling*).

In the case of cotunnelling, an electron tunnels into one of the leads as long as another electron tunnels back into the dot within a short time. This process briefly violates energy conversation, which is quantum-mechanically allowed within a timescale $\tau_{\mathrm{COT}} \sim \hbar/\delta$ [121]. Cotunnelling currents are often tiny and difficult to detect, but their features have been used in quantum dot spectroscopy to explore cotunnelling-mediated transport in single quantum dots [122] or spin effects in double quantum dots [123].

Accounting for the Vibrational Degrees of Freedom: the Rate-Equation Model

The inclusion of vibrational degree of freedom (DOF) within the picture drawn so far is not a trivial task. In the recent years, the rate-equation model have become widely used for modeling, through the use of a kinetic description of the electrode–dot junction, the scenarios where an electron can also use QD vibrational states [124, 125] (Fig. 2.10). One of the most important assumption the model

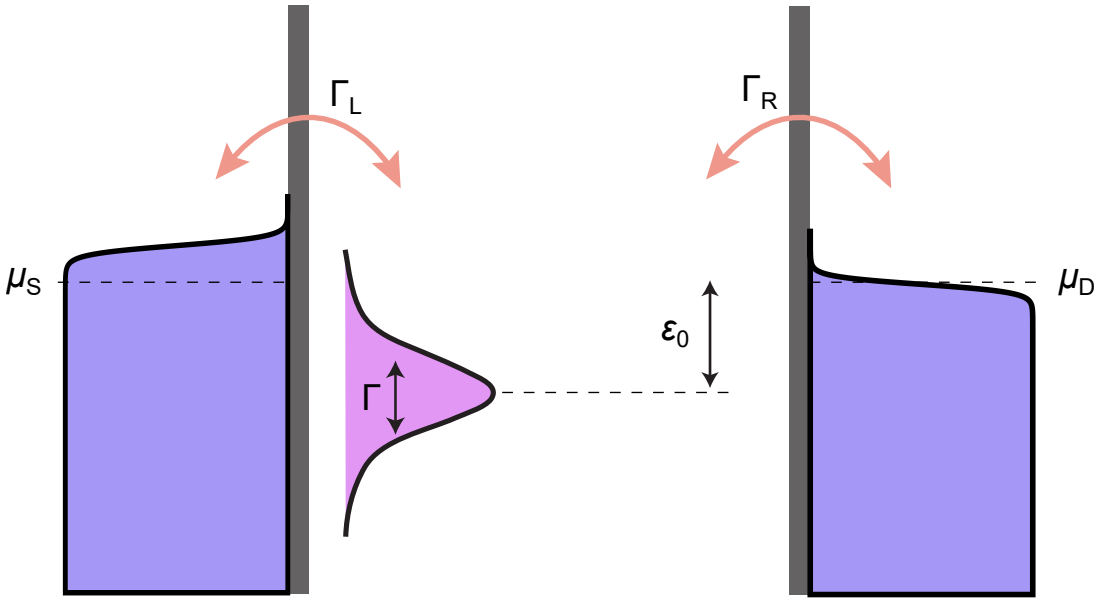


Figure 2.10: Schematic for a single-level transport model. The single-particle state with energy ε_0 and lifetime Γ contributes to the total current flowing across the junction. Γ_{L} and Γ_{R} are the tunnelling coupling with the left and right electrode, respectively.

makes is that the total current is uniquely determine by how fast an electrons tunnels in and out in the weak-coupling regime [126, 127].

Here we will adopt the description reported in references where the electronic degrees of freedom interact with an unstructured environment modelled by a superohmic bath having an exponential cut-off:

$$\mathcal{J}(\omega) = \frac{\lambda}{2}\frac{\omega^3}{\omega_{\mathrm{c}}}\exp\{-\omega/\omega_{\mathrm{c}}\}, \tag{2.19}$$

where λ is the reorganisation energy as defined by the Marcus model [120] for an electron transfer in solution, and ω_{c} is a cut-off frequency. The kinetic description allows us to write the total current as:

$$I = |e|\frac{\gamma^{\mathrm{S}}_{\mathrm{ox}}\gamma^{\mathrm{D}}_{\mathrm{red}} - \gamma^{\mathrm{S}}_{\mathrm{red}}\gamma^{\mathrm{D}}_{\mathrm{ox}}}{\gamma^{\mathrm{S}}_{\mathrm{red}} + \gamma^{\mathrm{D}}_{\mathrm{red}} + \gamma^{\mathrm{S}}_{ox} + \gamma^{\mathrm{D}}_{ox}}, \tag{2.20}$$

where $\gamma^{\mathrm{S/D}}_{\mathrm{red/ox}}$ are the electron-transfer rates at each electrode and corresponds to a reduction or an oxidation, respectively. When the charge transition from N to

the $N+1$ is considered, the electron-transfer rates are given by:

$$\gamma_{\mathrm{red}}^{\mathrm{S,D}} = 2\frac{\Gamma_{\mathrm{S,D}}}{\hbar}\int f_{\mathrm{S,D}}(\epsilon)\ k_{\mathrm{red}}(\epsilon)\mathrm{d}\epsilon, \tag{2.21}$$

$$\gamma_{\mathrm{ox}}^{\mathrm{S,D}} = \frac{\Gamma_{\mathrm{S,D}}}{\hbar}\int [1 - f_{\mathrm{S,D}}(\epsilon)]\ \ k_{\mathrm{ox}}(\epsilon)d\epsilon, \tag{2.22}$$

where $\Gamma_{\mathrm{S,D}}$, as we have already seen, is the coupling between the QD and the electrodes, which have a Fermi–Dirac distributions $f_{\mathrm{S,D}}(\epsilon)$. The DOS for the reduced and oxidized can be written as:

$$k_{\mathrm{red/ox}}(\epsilon) = \frac{1}{\pi}\,\mathrm{Re}\int_0^\infty \exp\{\sigma i(\varepsilon - \varepsilon_0)t/\hbar\}\exp\{-t/\tau\}B(t)dt, \tag{2.23}$$

where $\sigma = 1(-1)$ for reduction (oxidation) process, ε_0 is the dot energy level and which corresponding state (assuming non-degenerate) has lifetime $\tau = 2\hbar/\left(\Gamma_{\mathrm{S}} + \Gamma_{\mathrm{D}}\right)$.

The term $B(t)$ is the phononic correlation function used to model the vibrational DOFs and may be written as the product between a single-mode term $D_q(t)$ and a mean-field contribution $D_{\mathrm{bath}}(t)$ given by the environment:

$$B(t) = \exp\{D_q(t)\}\cdot\exp\{D_{\mathrm{bath}}(t)\}, \tag{2.24}$$

and the two terms can be expressed as [128]:

$$D_q(t) = \left(\frac{g_q}{\omega_q}\right)\left[(\cos\omega_q t - 1)\cdot\coth\left(\frac{\omega_q}{2k_BT}\right) - i\sin\left(\omega_q t\right)\right], \tag{2.25}$$

$$D_{\mathrm{bath}}(t) = \int\frac{J(\omega)}{\omega^2}\left[(\cos\omega t - 1)\cdot\coth\left(\frac{\omega}{2k_BT}\right) - i\sin(\omega t)\right]d\omega, \tag{2.26}$$

where g_q is the electron–vibration coupling, ω is the vibronic frequency, $J(\omega)$ the phonon-bath spectral density associated to a reorganisation energy λ. We will use this model in Chapter 6 to reproduce the low temperature transport features of a molecular graphene nanoribbon with a strong electron–vibron coupling.

2.3.3 Experimental Evidences

The platform most commonly used in quantum transport experiments is an electronic device made by CNT embedding a QD (Fig. 2.11a). The exact position of the QD inside CNT has been object of scientific debate, but it is now considered to

be the nanotube portion between the large SB barriers arising at the metal–CNT junctions, where electrons can be trapped by the electric fields induced by local gates located beneath the tube [62]. A QD (or, more generally, a SET) can be realised if the contact resistances at the junctions source–QD and QD–drain exceed a certain limit, i.e. $R_c \geq 26\,\mathrm{k}\Omega$ [129]. Contacts that opaque are often called *tunnelling barriers*, given that the main transport mechanism through which current can flow is quantum tunnelling. In this setting, the CNT energy levels can then be studied by measuring the I_{SD} through as a function of V_{SD}, V_G, and other parameters such as magnetic field B, temperature T, etc. At cryogenic temperatures, the smearing of $k_B T$ makes a number of quantum phenomena observables. Examples of such are the conductance blockage due to strong Coulomb interactions [132], interference effects [133], periodic shell-filling signatures related to the tunnelling through energy levels [130], and Kondo effects originated from the hybridisation of CNT spin states with the continuum of states in the metallic leads [134].

Since the introduction of tunnelling barriers add a longitudinal confinement, the impact that the CNT mechanical motion have on the electronic transport has been studied both theoretically and experimentally. Particularly interesting were the experimental evidences collected by [131] on suspended CNT by using a slightly modified architecture compared to the one reported in Fig. 2.11. The QD was precisely embedded between the source and the drain by using a second, top gate combined with a standard Si/SiO_2 backgate.

The exceptional quality of the samples allowed the researchers the unambiguous observation of several features, such as (1) excited vibronic states as lines running paralles to the edges of the Coulomb diamonds, (2) the appearance of absorption sideband peaks within the Coulomb blockaded regions when T was increased, and (3) an aggressive suppression of the current at the edge of the diamonds. Since the current at the edges was suppressed by an amount comparable with the current magnitude for the excited vibronic states, the researchers hypothesised the Franck–Condon conductance blockade [135, 136].

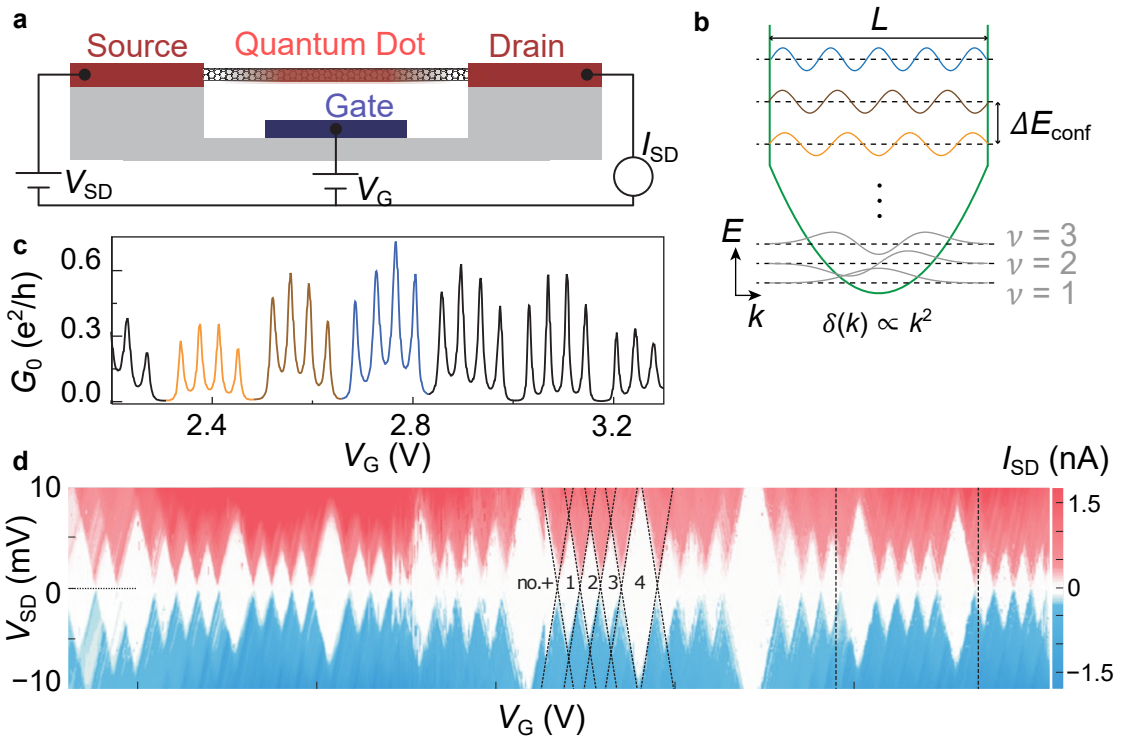


Figure 2.11: **a**, QD device schematic. A CNT is contacted by source and drain electrodes and capacitively coupled to a gate. The current I_{SD} through the device is measured as a function of V_{SD} and V_G. Through V_G, one may control the number of electrons N on the island and tune the dot energy levels. **b**, QD energy levels schematic (electron–electron interactions are ignored). Electronic wave function envelopes $\psi(k)$ are superimposed on the level diagram for several electron shells. With ν we indicate the mode index for the first three shells. Adapted from [62]. **c**, Coulomb blockade peaks sequence measured in QD whose length is $L \simeq 750\,\text{nm}$. Peaks corresponding to three successive shells are colored to illustrate the connection to different wave functions. Although the four electrons that fill each shell occupy states of similar energy, an extra energy δ is needed to populate a higher shell, leading to fourfold periodic peak spacing. Adapted from [130]. **d**, Experimental device that confirmed the fourfold periodicity. White diamonds are regions where the I_{SD} is suppressed because of Coulomb blockade. Adapted from [131].

On top of the study of the role of vibrational DOFs, CNTs have been proven an invaluable platform for shading some light on important 1D-physics problems. In the next section, we will provide an brief theoretical overview on the physics of 1D systems followed by some of the most significant experimental evidences

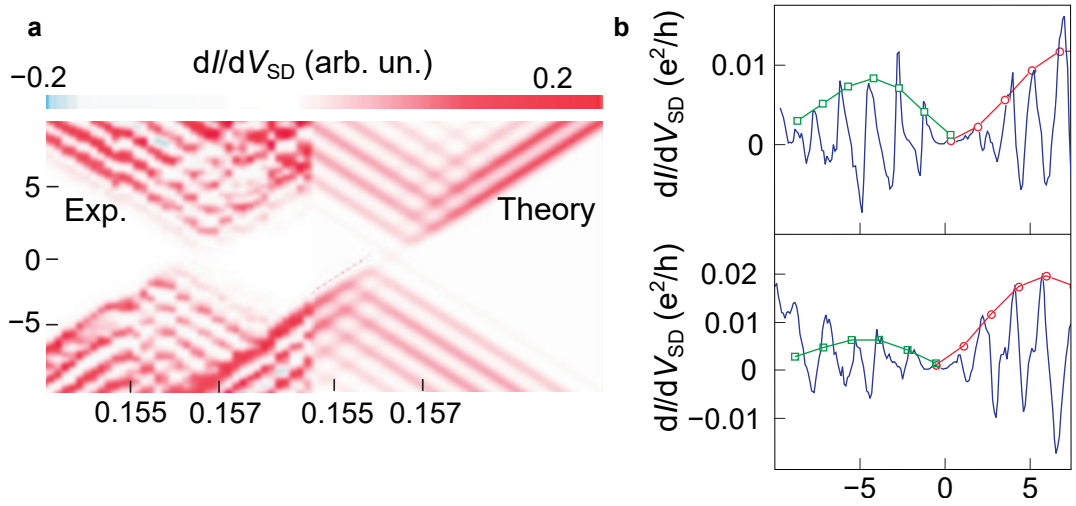


Figure 2.12: **a**, Experimental and theoretical zoom into a part of CNT Coulomb diamonds, showing the suppression of the low-bias conductance. In order to reproduce the experimental evidence, Leturcq et al. used $\gamma = 3.3$ for the electron–vibron coupling. **b**, Differential conductance measured at $V_{TG} = 0.068\,V$ (top) and $V_{TG} = 0.157\,V$ (bottom). Solid lines are fits of the conductance maxima using the Franck–Condon progression. **top**, $g = 3.5$ (negative bias voltage, green squares) and $g = 5.0$ (positive bias voltage, red circles). Deviations from the progression were explained by the researchers as due to electronic excited states within the V_{SD} window. **bottom**, $g = 3.0$ (green squares) and $g = 4.5$ (red circles). Adapted from [131].

2.4 Basics of One-dimensional Physics

In this section, we will very briefly review some of the concepts related to the Fermi liquid theory and its failure in describing 1D systems. As a result of the lateral confinement of the charge carriers, GNRs are indeed a quasi-1D system. The *quasi* refers to the fact that not until the recently-developed bottom-up techniques [137–139] the fabrication of atomically-precise molecular graphene nanoribbons (MGNRs) has become possible.

The topics introduced here draw the peculiarities in the DOS for 1D fermionic systems and the role of long-range Coulomb interactions within them. We believe these concepts are highly relevant in order to provide an explanation to the experimental evidences exposed in Chapter 5. A more exhaustive treatment of the following concepts are reviewed in [140–143].

2.4.1 A Succinct Primer of Fermi-Liquid Theory

The Fermi liquid theory was advanced by Lev Landau in 1956 as a phenomenological explanation to decribe the low-temperature behaviour of the heat capacity of liquid ^{3}He, which is surprisingly similar to that of the ideal gas one. Since then, the theory has been used and extended to describe electrons in metallic systems.

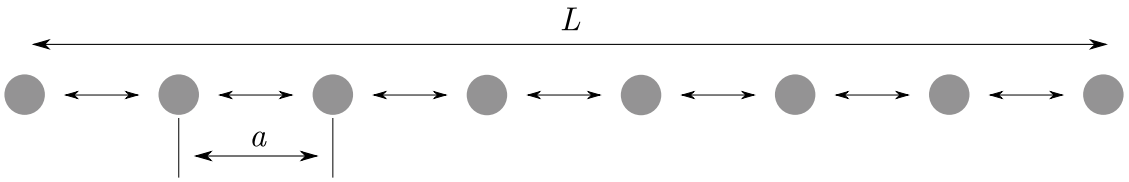


Figure 2.13: Pictorial representation of a 1D electron system. The density of the system is defined as the number of atoms N confined in a 1D box of length L, i.e. $\rho = N/L = 1/a$, where a is the spacing between two atoms.

The ground state of a non-interacting gas can be fully captured by statistical mechanics. In this framework, a key quantity for calculating macroscopic quantities is the momentum-distribution function for a gas $n^0_{\vec{k}}$, which depends on the wavevector $\vec{k}$. More generally, the ground state also depends on the spin occupation number σ, but we will drop the spin subscript for the moment. The zero-temperature limit of a fermionic gas $n^0_{\vec{k}}$ is the well-known step function, which equals to:

$$n^0_{\mathbf{k}} = \begin{cases} 1 & k \leq k_{\mathrm{F}}, \\ 0 & k > k_{\mathrm{F}}. \end{cases} \tag{2.27}$$

At finite temperatures, the momentum-distribution function coincides with the well known Fermi–Dirac distribution. The energy of a free particle follows the well-known parabolic dispersion, $\epsilon_{\vec{k}} = \hbar k^2/m$, and the total-energy change of the fermionic gas δE caused by an arbitrary excitation may be expressed as a functional of the energy deviation from the ground-state energy E_0:

$$\delta E[\delta n] = E[n] - E_0 = \sum_{\vec{k}} \epsilon_{\vec{k}}\ \delta n_{\vec{k}} \tag{2.28}$$

The single-particle energy can then be written as a functional derivative of the total-energy change caused by a variation of the number of gas particles within

a specified $\vec{k}$ vector:

$$\epsilon(\vec{k}) = \frac{\delta E[n]}{\delta n_{\vec{k}}} \tag{2.29}$$

In general, an elementary excitation can be thought as the process of adding (or removing) a particle to (from) the ground state and an arbitrary-excitated state. Close to the Fermi surface, $\vec{k} = k_{\mathrm{F}}$, the energy dispersion is sufficiently linear for applying a Taylor-series expansion:

$$\epsilon_{\vec{k}} = \epsilon_{\mathrm{F}} + \upsilon_{\mathrm{F}}\hbar(\mathbf{k} - k_{\mathrm{F}}) + \mathcal{O}((\mathbf{k} - k_{\mathrm{F}})^2) \tag{2.30}$$

where $\upsilon_{\mathrm{F}} = \boldsymbol{\nabla}_{\vec{k}}\epsilon|_{\vec{k}=k_{\mathrm{F}}}$ is the Fermi velocity. Landau's assumption was that low-lying eigenstates of the non-interacting Fermi gas continuously evolve into the eigenstates of the (real) multi-body system as the interaction is adiabatically switched on. This construction allows one to recovery individual excitations, called *quasiparticles*, that are the starting point of the Fermi-liquid theory.

Pictorially, a quasiparticle can be visualised as a fermion surrounded by a cloud of disturbance arising from the interactions with other particles. The Fermi-liquid theory predicts that this interaction decay as $\sim 1/\vec{r}^2$, where with $\vec{r}$ we denote the three spatial coordinates [140]. The mass is also rescaled to an effective mass $m^* = \hbar k_{\mathrm{F}}/\upsilon$ which value is determined by the interaction strength.

In order to quantify the quasiparticle-excitation energies, we can expand the energy functional with a Taylor's series up to the second order:

$$\delta E[\delta n] = \sum_{\vec{k}} \epsilon_{\vec{k}}\ \delta n_{\vec{k}} + \frac{1}{2V}\sum_{\vec{k}} f(\vec{k},\vec{k'})\ \delta n_{\vec{k}}\delta n_{\vec{k'}}, \tag{2.31}$$

where the quantity:

$$\frac{f(\vec{k},\vec{k'})}{V} = \frac{\delta^2 E[n]}{\delta_{\vec{k}}\delta_{\vec{k'}}}, \tag{2.32}$$

is known as Landau the function, which quantifies the interaction strength between quasiparticles. In a similar fashion, quasiparticle energies can defined as:

$$\tilde{\epsilon}_{\vec{k}} = \frac{\delta E[\delta n]}{\delta n_{\vec{k}}} = \epsilon_{\vec{k}} + \frac{1}{V}\sum_{\vec{k'}} f(\vec{k},\vec{k'})\delta_{\vec{k'}}. \tag{2.33}$$

. Why does the Fermi liquid theory fail to capture 1D systems? Essentially, that is because the Landau function is treated by mean-field approximation, but a mean-field-kind description breaks down in 1D [140]. This is caused by several reasons.

Firstly, for a system arranged in a linear chain fashion, only collective excitations exist. Pictorially, one might covince themselves by thinking of an electron which oscillates around its equilibrium position. Due to strong electron–electron interactions, the motion is fastly trasmitted all along the chain, resulting in a collective excitation. Secondly, in high dimensions we have seen that even if the particles interact with each other one can still recover an individual excitation description, where the interactions result in the concept of quasiparticles. In the next section we will take a look at how all these issues have been rationalised in 1D by studying the Tomonaga–Luttinger model.

2.4.2 Introduction to the Tomonaga–Luttinger Model

The absence of efficient charge screening in 1D results in the presece of long-range interactions, which cause strong correlations and the breakdown of an independent-particle description. These correlations are the main reason for the necessity of computing correlation functions for calculating any quantity of interest, hence the wide employment of Green's function methods (propagators).

One consequence of this uniqueness is that, conveniently, it is often sufficient to conduct an asymptotic analysis for capturing the physical insights about a 1D system. In particular, one has to provide two parameters: the wave velocity u and the interaction streght K (also called g), a dimensionless number that controls the decay of all the correlation functions, as well as the thermodynamic quantities [141].

The first model proposed in 1950 by Tomonaga aimed to describe the ground state of an interacting Fermi gas, and its excitations, as sound waves to field equations [144]. The model was later extended by Luttinger in 1963 in an attempt to include interaction of arbitrary strengths [145]. The correct solution was firstly advanced by Mattis and Lieb in 1965 [146] and finalised by a genius intuition from Haldane in 1981 [147].

A key techniques required to arrive to Haldane's solution is bosonisation, a mathematical tool which maps fermionic excitations to bosonic modes of spin-density and charge-density waves, and which prerequisite is the possibility of linearise the energy dispersion close to the Fermi level [148]. This linear approximation is subjected to a more stringent requirement in the Tomonaga–Luttinger liquid (TLL) model, meaning that fermions occupy the linearised energy spectrum all the way down to $-\infty$ on the energy scale (also called Dirac sea, Fig. 2.14). In order to apply this assumption, clearly the density of states has to be constant. The TLL Hamiltonian might be written as the sum between kinetic and interaction contributions:

$$\mathcal{H}_{\mathrm{TLL}} = \mathcal{H}_0 + \mathcal{H}_{\mathrm{int}}. \tag{2.34}$$

Using the second quantisation formalism, the kinetic part may be written as [140]:

$$\mathcal{H}_0 = \sum_{k;r=R,L} \upsilon_{\mathrm{F}}(\epsilon_r k - k_{\mathrm{F}}) c^{\dagger}_{k,r} c_{k,r}, \tag{2.35}$$

where we have dropped the arrow notation for the wavevector as we are now dealing only with one dimension. Here, $c^{\dagger}_{k,r}(c_{k,r})$ is the creation (annihilation) operator acting in corresponding Fock space. Because the Fermi surface in 1D consists of just two points at $k = \pm k_{\mathrm{F}}$, we can distinguish states in the right branch ($\epsilon_R = +1$) from those in the left branch ($\epsilon_L = -1$), and the corresponding dispersion relations are:

$$\epsilon_{k,R} = \epsilon_0 + \hbar \upsilon_{\mathrm{F}} k \tag{2.36}$$

$$\epsilon_{k,L} = \epsilon_0 - \hbar \upsilon_{\mathrm{F}} k \tag{2.37}$$

$$\epsilon_0 = \epsilon_{\mathrm{F}} + \hbar \upsilon_{\mathrm{F}} k_{\mathrm{F}} \tag{2.38}$$

Since states in the $\epsilon_R = +1$ branch have positive velocities they are also referred to as *right movers*; conversely, states in the left branch are referred as *left movers*.

In order to write the interaction term down, we shall first introduce a key quantity which is the *density operator*. Because the system is subject to quantum fluctuations, even at zero-temperature, low-energy processes, i.e. close to the

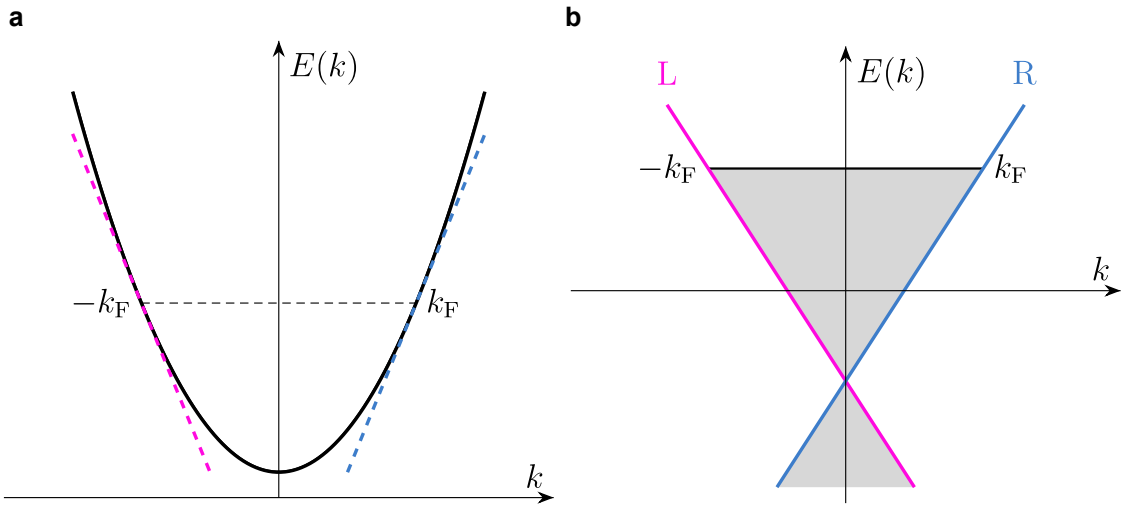


Figure 2.14: The Tomonaga–Luttinger-liquid (TLL) model. **a**, Free electron parabolic dispersion (black solid curve) and the linearisation carried out according to the TLL model for excitations close the Fermi level (pink and blue dashed lines). **b**, The linear dispersion used in the TLL model. Pink and blue solid lines correspond, to left-(L) and right (R)-moving electrons, respectively. Shaded area shows the Dirac sea below the Fermi energy. Figure adapted from [149].

Fermi surface, will drive the total system response [150]. These processes are well described by the density operator[§]:

$$\rho^{\dagger}(q) = \sum_{k} c^{\dagger}_{k+q,r} c_{k,r}, \tag{2.39}$$

and the interaction term can be expressed as:

$$\mathcal{H}_{\text{int}} = \frac{1}{2V} \sum_{k,k',q} V(q) c^{\dagger}_{k+q} c^{\dagger}_{k'-q} c_{k'} c_{k}, \tag{2.40}$$

As illustrated in Fig. 2.15, k and $k-q$ are restricted to be close the two points at $\pm k_{\text{F}}$, therefore there are only two possible values of q depending on the sign of k and $k-q$. When k and $k-q$ have the same sign, $|q| \sim 0$. This corresponds to a scattering term for fermions moving in the same direction and is interpreted as a *forward scattering*. When k and $k-q$ have opposite sign, $|q| \sim 2k_{\text{F}}$, meaning that fermions exchange sides (*backward scattering*). A problem with Eq. 2.40

[§]A technicality here. Since the model includes all of the negative states, the density operator as in Eq. 2.39 is infinite and the number of fermions too. One has to introduce the *normal ordering* of operators, meaning that what matters are deviations in the density with respect to the ground-state density [148].

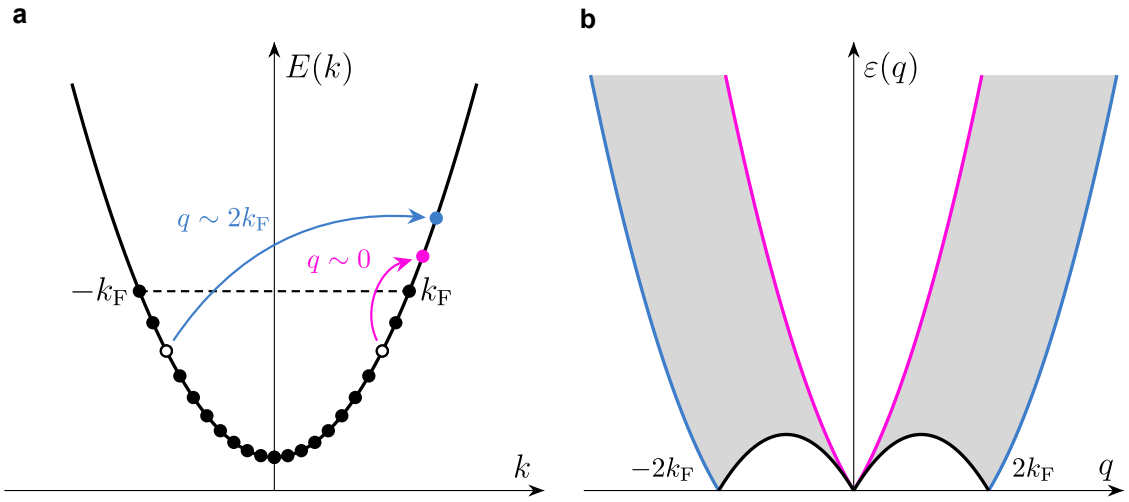


Figure 2.15: **a**, The Fermi surface consists of only two points, corresponding to wavevector $\pm k_{\mathrm{F}}$. Low-energy single-particle excitations such asforward (pink) and backward (blue) scattering for small momentum. The $q \sim 0$ component switches on particle-hole excitations on the same branch, whereas the $q \sim 2k_{\mathrm{F}}$ carries a particle across the two sides of the Fermi surface. Black dots are filled (occupied) states, holes are empty circles. **b**, Particle–hole excitation spectrum. Accessible energies are the one shaded in grey, whereas the forbidden regions indicated by the white gaps are unique to the 1D nature of these systems and find no correspondece in higher dimensions. The position of the spectral edges, separating accessible from forbidden regions, are marked by a solid-black curve. Experimental observations of the magnetic response for certain classes of solid-state materials (Heisenberg antiferromagnetic chains such as $KCuF_3$) through inelastic neutron scattering have confirmed these regions [151, 152]. Adapted from [153].

can be found in the product between the two density operators. When these are expressed in the fermion operator basis, these will expand to be a quartic function of the fermion operators. Consequently it is not trivial to diagonalise such quartic Hamiltonian. Haldane's intuition [147] was to map the problem, through a change of the basis, into the bosonic-operator domain, where the interaction is reduced to a quadratic form, so that a closed-form solution is attainable. This process will be briefly outlined in the next section when I will derive the tunnelling density of states in case for a fermion tunnelling through a Luttinger liquid.

2.4.3 Derivation of the tunnelling Density of States

Here, we will briefly sketch the derivation of the tunnelling density of states (TDOS) for a Luttinger liquid [154–156]. We will use the second quantisation

formalism, in which both the wavefunctions and the operators are expressed as operators (more generally, fields) acting in the Fock space. This formalism greatly simplifies the description of multi-electron interacting systems in situations where single-particle interactions fail to capture all the features. The short and medium correlations between different parts of the system, well captured by the Green's function (propagator) between operators associated with a certain observable between different time frames, are central to this formalism.

The TDOS may be written as

$$\rho_{\text{dos}}(\omega) = \int_{-\infty}^{\infty} \frac{dt}{2\pi} \exp\{i\omega t\} \left\langle \psi_e(t)\psi_e^{\dagger}(0) \right\rangle, \tag{2.41}$$

where $\psi_e(t)$ is the time-dependent fermionic operator (field), ω is an energy scale, and the brackets indicate the propagator (Green's function) as introduced in Sec. 2.4. The mapping between fermionic and bosonic operators takes place through bosonization [148], which allows writing fermionic operators in terms of bosonic fields. We then may write the bosonised form of the fermionic operator as:

$$\psi_e = \psi_L + \psi_R, \tag{2.42}$$

where $\psi_{L/R}$ are the left/right fermionic operators for left-moving and right-moving carriers*, which may be written in terms of a bosonic operator $\exp\{-i\varphi_{L/R}\}$ normalized by the inter-particle spacing a when particles are confined along a 1D chain $\psi_{L/R} = \exp\{-i\varphi_{L/R}\}/\sqrt{a}$.

In order to diagonalise the TLL Hamiltonian, it may be convenient to introduce the following fields:

$$\phi_{\pm} = \frac{1}{\sqrt{2}} g^{\mp\frac{1}{2}} \left(\varphi_L \mp \varphi_R\right), \tag{2.43}$$

where $g > 0$ (for free electrons $g = 1$) is a dimensionless parameter which quantifies the electron–electron interactions in a 1D quantum wire. These fields are canonically

*This argument, as will be explained later, assumes that chirality symmetry is respected. As a result, applying a strong magnetic field that could cause chiral-symmetry breaking compel this argument to be adjusted [157].

conjugated to the displacement field $\theta(x)$, whose derivative models the electron-density fluctuations:

$$\delta n(x) = n(x) - n_0 = \frac{\partial_x \theta(x)}{\pi}, \tag{2.44}$$

where n_0 is the average density. This expression is obtained by considering that if $\theta(a) - \theta(0) = -\pi$, then there is only one extra electron between two particles separated by a distance a.

The two fermionic fields thus read:

$$\begin{aligned} \psi_L &= \frac{1}{\sqrt{a}} \exp\left\{ -\frac{i}{\sqrt{2}} \left(\frac{1}{\sqrt{g}} \phi_- + \sqrt{g}\phi_+ \right) \right\}, \\ \psi_R &= \frac{1}{\sqrt{a}} \exp\left\{ -\frac{i}{\sqrt{2}} \left(\frac{1}{\sqrt{g}} \phi_- - \sqrt{g}\phi_+ \right) \right\}, \end{aligned} \tag{2.45}$$

while the fermionic propagator may be written as

$$\begin{aligned} \left\langle \psi_e(t) \psi_e^+(0) \right\rangle &= \langle \psi_L(t)\psi_L(0) \rangle + \langle \psi_R(t)\psi_R(0) \rangle \\ &= \langle \psi_L(t)\psi_L(0) \rangle + \text{h.c.} \end{aligned} \tag{2.46}$$

Cross terms such as $\left\langle \psi_L^\dagger \psi_R \right\rangle$ cancel each other since we assume chirality is conserved. For the remaining terms the sum can be opened such as:

$$\begin{aligned} \left\langle \psi_L^\dagger(t)\psi_L(0) \right\rangle &= \frac{1}{a} \left\langle \exp\left\{ \frac{i}{\sqrt{2}} \left(\frac{1}{\sqrt{g}} \phi_-(t) \sqrt{g}\phi_+(t) \right) \right\} \exp\left\{ \frac{i}{\sqrt{2}} \left(\frac{1}{\sqrt{g}} \phi_-(0) \sqrt{g}\phi_+(0) \right) \right\} \right\rangle, \\ &= \frac{1}{a} \left\langle \exp\left\{ \frac{i}{\sqrt{2g}} \phi_-(t) \right\} \exp\left\{ \frac{-i}{\sqrt{2g}} \phi_-(0) \right\} \right\rangle \times \\ &\times \left\langle \exp\left\{ \frac{i}{\sqrt{2g}} \phi_+(t) \right\} \exp\left\{ \frac{-i}{\sqrt{2g}} \phi_+(0) \right\} \right\rangle, \end{aligned} \tag{2.47}$$

By using the Baker–Campbell–Hausdorff identity, which is valid for exponential operators and is obeyed by free bosonic fields

$$\langle \exp\{B_1\} \exp\{B_2\} \rangle = \exp\left\{ \frac{1}{2} \right\} \left\langle B_1^2 + 2B_1B_2 + B_2^2 \right\rangle, \tag{2.48}$$

and time-translational symmetry, we obtain:

$$\begin{aligned} \left\langle \exp\left\{ \frac{i}{\sqrt{2g}} \phi_-(t) \right\} \exp\left\{ -\frac{i}{\sqrt{2g}} \phi_-(0) \right\} \right\rangle &= \exp\left\{ \frac{1}{2g} \left\langle \phi_-(t)\phi_-(0) - \phi_-(0)\phi_-(0) \right\rangle \right\} \\ &= \left(1 + \frac{i\upsilon_F t}{a} \right)^{-\frac{1}{2g}} \end{aligned}$$

where we introduce the Fermi velocity v_{F} and used the relation

$$\langle \phi_-(t)\phi_-(0)\rangle = -\ln\!\left(1+\frac{i\upsilon_F t}{a}\right) \tag{2.49}$$

Similarly

$$\left\langle \exp\!\left\{i\sqrt{\frac{g}{2}}\phi_+(t)\right\}\exp\!\left\{-i\sqrt{\frac{g}{2}}\phi_+(0)\right\}\right\rangle = (1+i\upsilon_F t/a)^{-\frac{g}{2}} \tag{2.50}$$

and by combining the two terms, the fermionic propagator reads:

$$\langle \psi_e(t)\psi_e(0)\rangle = \frac{1}{a}(1+\frac{i\upsilon_{\mathrm{F}} t}{a})^{\frac{1}{2}(g+g^{-1})} \tag{2.51}$$

Incorporating this expression into the TDOS yields:

$$\begin{aligned}\rho_{\mathrm{dos}}(\omega) &= \int_{-\infty}^{\infty}\frac{\mathrm{dt}}{2\pi}\exp\{i\omega t\}\left\langle \psi_e(t)\psi_e^{\dagger}(0)\right\rangle \\ &= \frac{1}{2\pi a}\int_{-\infty}^{\infty}\mathrm{dt}\exp\{i\omega t\}\left(1+\frac{i\upsilon_{\mathrm{F}} t}{a}\right)^{-\frac{1}{2}\left(g+g^{-1}\right)}\end{aligned} \tag{2.52}$$

Since we are interested in the low-energy behavior of the TDOS, we look at the limit for which $\omega \to 0$, which in the time-domain corresponds to look at the behavior for $t \to \infty$:

$$\begin{aligned}\rho_{\mathrm{dos}}(\omega) &\sim \int_{-\infty}^{\infty}\mathrm{dt}\frac{\exp\{i\omega t\}}{t^{1/2(g+g^{-1})}} \\ &\sim \omega^{\frac{1}{2}(g+g^{-1})-1} = \omega^{\alpha}\end{aligned} \tag{2.53}$$

For the process associated with a tunnelling event into the bulk of a CNT the exponent of Eq. 2.53 is expected to be $\alpha \simeq 0.4$ [156]. As we have seen in Sec. 2.4.2, this exponent can be phenomenologically interpreted as the strength of the electron–electron interactions, which lead to a suppression of the conductance when an excess of energy (thermal or electric) is pumped into the system.

The approach detailed in this chapter is, as we have mentioned, applicable to any 1D. As such, it should be possible to describe GNRs, and in particular MGNRs, within this framework, especially in the $l_{\mathrm{GNR}} \gg w_{\mathrm{GNR}}$ limit. Furthermore, in MGNRs, the graphene band structure allows us to label both the valley and the spin DOSs, amounting to a total four-fold degeneracy of the band structure: this should lead to a TDOS whose tunnelling exponent into one of the MGNR ends is $\alpha \simeq \frac{1}{4}(g^{-1}-1)$ [158, 159]. In Ch. 5 we will outiline the experiment we have setup in order to confirm this theoretical estimate.

2.4.4 Experimental Evidence: Luttinger Liquid in Carbon Nanotubes

In interacting 1D systems such as CNT, the electrons behaviour cannot be captured within the Fermi liquid theory, but by Luttinger-liquid models [154–156]. In these models, spin and charge excitations are described as bosonic modes, are separable, and propagate at different velocities. Furthermore, the electron–electron interaction leads to a TDOS suppression and interaction-dependent power laws for transport quantities (Sec. 2.4.2). The experimental evidence of such interactions was revealed through a series of remarkable experiments first on individual CNT bundle (also called *rope*), i.e. multiples tubes closely packed together, and later on single CNTs.

One of such experiments, for instance, was performed by Bockrath et al. on carbon nanotubes ropes contacted either from the top (end-contact) or from below (contacting the tube along its bulk) [160]. In both cases, researchers found a power-law scaling of the conductance measured at zero bias as the temperature was increased, i.e. $G(T) \sim T^{\alpha}$. The phenomenological interpretatio the author gave was that, depending on the fabrication details, the power-law exponent may change. In particular, they reported an $\alpha_{\text{end}} \simeq 0.6$, whereas in the case of bulk contact the suppression of the TDOS is weaker, setting an $\alpha_{\text{bulk}} \simeq 0.3$. Comparing these values with the expected electron–electron interaction predicted by the theory yielded a $g \simeq 0.28$.

The Luttinger parameter, g, which characterizes the strength and sign of the electron interaction, can be related to readily measured nanotube parameters E_{C}, the charging energy, and δ the mean orbital level spacing by $g = (1 + 2E_{\text{C}}/\delta)^{-1/2}$. Further experimental evidences, however, demonstrated that the interpretation of the tunnelling exponent may be not that trivial. Postma et al. measured the conductance of electrons tunnelling inside a carbon-nanotubes QD, where the tunnelling barriers were induced by mechanically bending the nanotube with an atomic force microscope (AFM) tip. Since the QD was not end-contacted, they explained the conductance-suppression exponent as the result of a tunnelling event from a Tomonaga–Luttinger liquid (the nanotube) into a Luttinger island

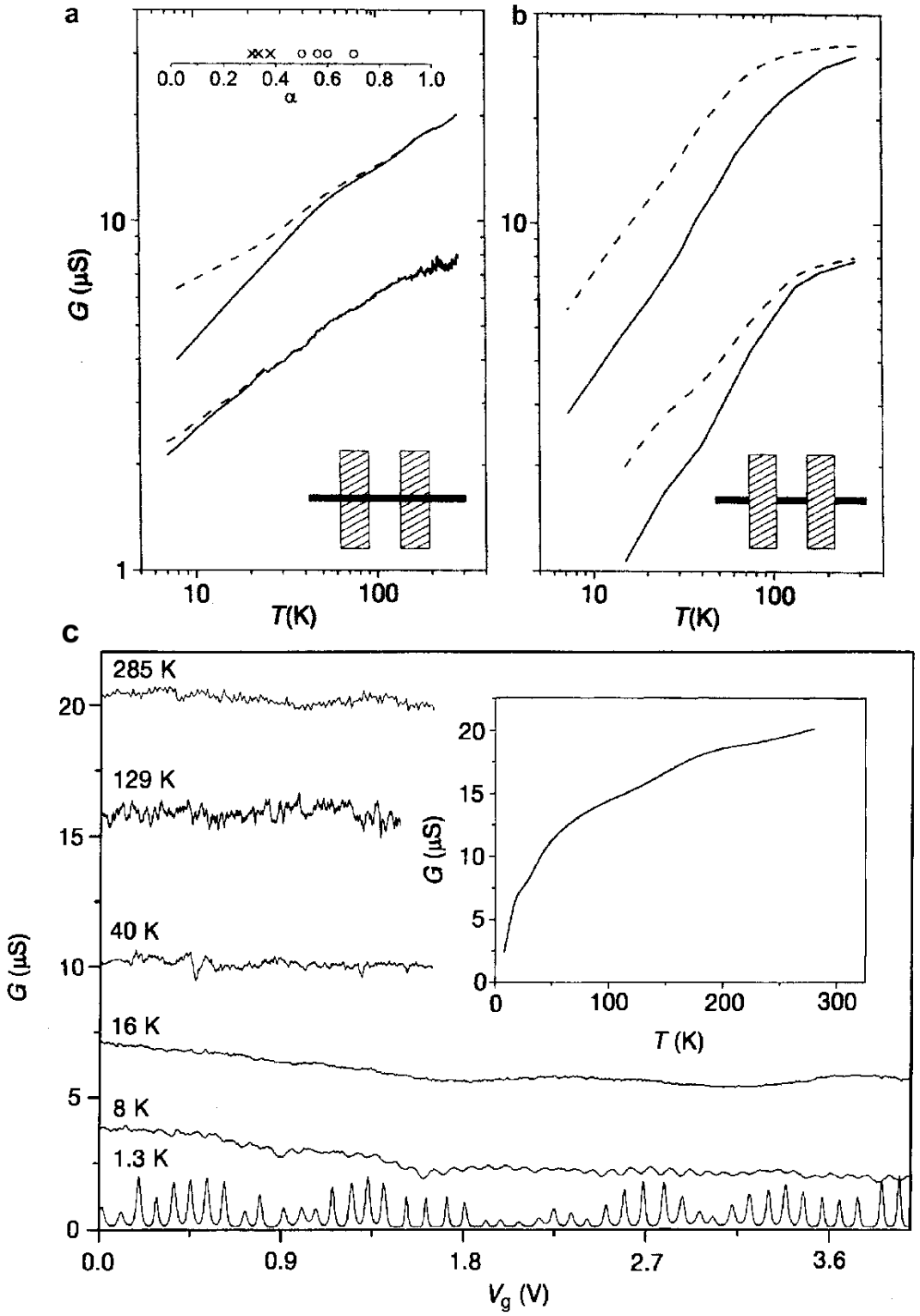


Figure 2.16: **a**, Bulk-contacted and **b**, end-contacted nanotube ropes, showing raw data (solid line) and data scaled by the temperature dependence expected from the Coulomb blockade model (dashed line). **c**, Two-terminal temperature-dependent conductance for metallic bulk-contacted ropes. Adapted from [160].

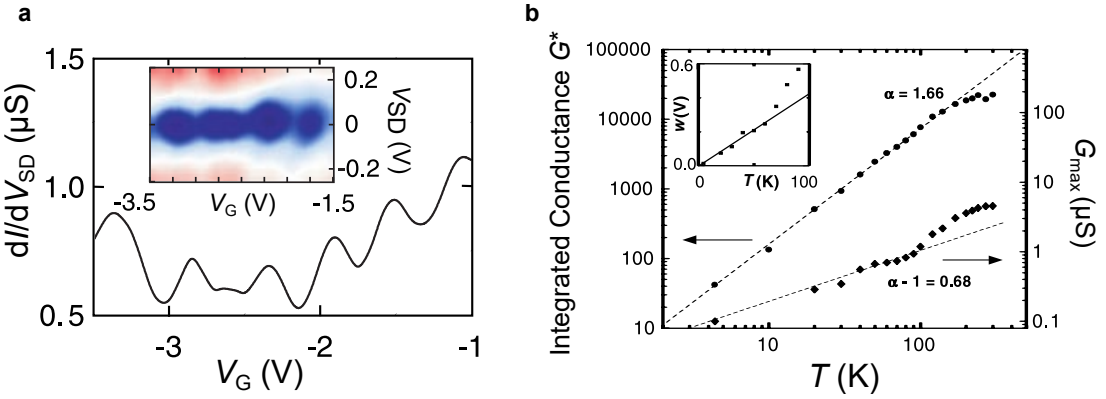


Figure 2.17: **a**, Oscillations in G at 260 K, showing Coulomb bloackade. (Inset) Differential conductance map. Blue regions represents low conductance, red regions high conductance. The authors did not report the colorbar. **b**, Temperature-dependent conductance G (right axis) and integrated conductance G^* (left axis) reveal a power law scaling for the tunnelling through the nanotube, explained within the Luttinger-liquid framework. (Inset) At low temperature, the peak width w correlates linearly with T. Adapted from [161].

(the quantum dot hosted inside the tube). In this case, the conductance was strongly suppressed, reporting an $\alpha_{\text{bulk}} \sim 0.64$, and rationalised by strong electron–electron interactions $g \sim 0.23$, supported also by theoretical predictions [155]. This observation was hypothesised to be the consequence of a different kind of tunnelling mechanism called *correlated sequential tunnelling* [162]. Briefly, in this mechanism once the electron tunnel on the QD it does not immediately tunnels onto the drain but there is a dephasing due to interaction with plasmon excitations.

To summarise, CNTs can host a variety of intriguing 1D phenomena while also being used to fabricate high-performance FETs. However, the fabrication of all-semiconducting devices is frequently challenging because, even when modern separation and growth protocols are used, mixtures of semiconducting and metallic nanotubes arise. In this regard, narrow GNR are advantageous, and we will begin to investigate their electronic properties in the following section.

2.5 Graphene Nanoribbons

The graphene band structure described in Ch. 2 shows that it is a semimetal, and that many electronics applications rely on the employment of a semiconductor with a finite band gap, through which one can modulate the charge transfer. Similar to CNTs, GNRs[†] are described in terms of an energy gap caused by the lateral quantum confinement of the carriers [163]: the bandgap, in particular, depends on the width w_{GNR} and length l_{GNR} of the ribbon [164].

Fig. 2.18 shows various ribbon widths and their corresponding bandgaps, as reported by theoretical and experimental studies. Moreover, this graph illustrates the paucity of ribbons with suitable widths when CMOS-suitable bandgap range ((0.1–1) eV) is considered [35, 165]. One of the key reasons for the scarcity of appropriate GNRs is that the bottom-up process for the synthesis of graphene ribbons was still in its infancy at the time this graph was created. The *bottom-up* methodology is a technique for synthesising MGNRs where the ribbon structure is created from molecular precursors using reaction patterns inherited from the chemistry of polymers and pericyclic reactions. Pioneered by two seminal papers by Hongjie Dai [167] and Klaus Müllen [171], it is now deemed the ideal technique to produce high-quality, atomically-precise ribbons. With these class of techniques, hundred nanometer-long MGNRs with widths less than 5 nm have been synthesised [172], which may be appropriate for interconnection applications where high-current density have to be maintained without causing any voltage drops.

Secondly, important nano-and- opto-electronics properties such as electronic bandgap, charge-carrier mobility, and optical absorption have become tunable by either varying GNRs chemical structures or by introducing opportune decorations along the ribbon edges [139, 173]. Fig.2.19 gives a glimpse on the vast variety of edge structures generated by bottom-up techniques, suggesting the effectiveness and versatility of this approach over early *top-down* approaches. These were typically

[†]Throughout the thesis, we will use the abbreviation GNR to qualify any graphene nanoribbons. When we use the abbreviation MGNR is because we are identifing ribbon synthesised through *bottom-up* strategies.

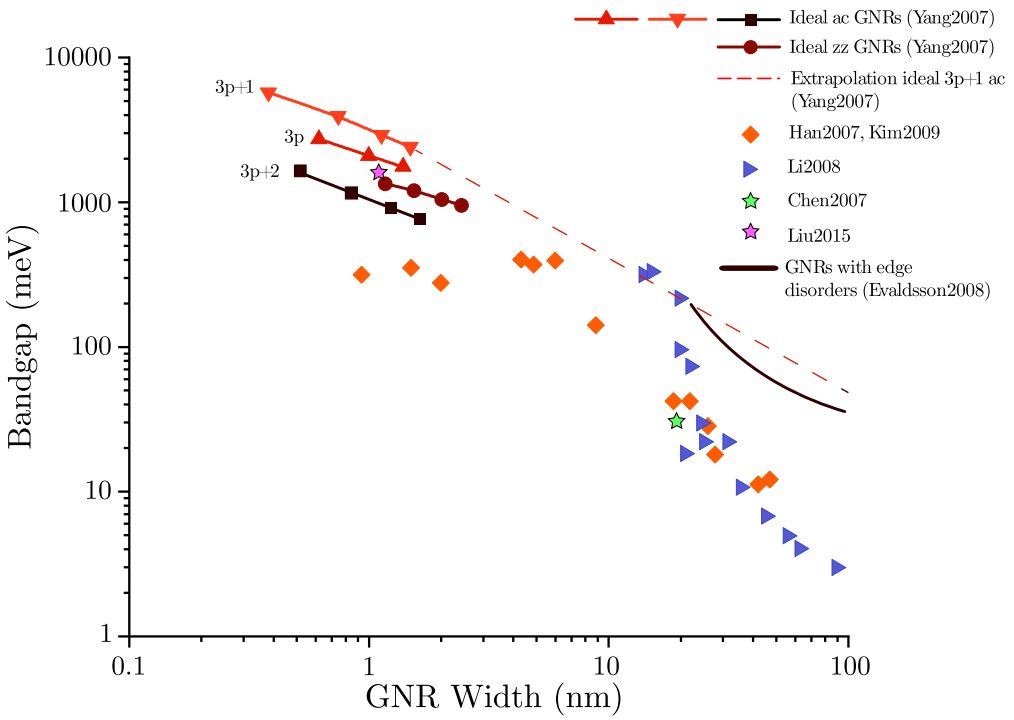


Figure 2.18: Bandgap versus nanoribbon width as reported both in experimental [164, 166–168] and theoretical works [169, 170]. ac stands for *armchair*, while zz for *zigzag*. See main text. Adapted from [35].

accomplished by either patterning ribbons through lithography with electron-beam litography (EBL) [164, 174] or by longitudinal unzipping of single-walled nanotubes [175], or by cutting graphene sheets with metallic nanoparticles [176]. These methods, however, frequently produced wide widths and uncontrollable structural defects [170, 177]. Finally, bottom-up technology has made it possible to synthetically control the kind of defects injected into the carbon lattice, and this technological superiority is considered by many to be a substantial advantage compared to graphene and carbon nanotubes [178, 179].

2.5.1 Crystal and Band Structure

Armchair graphene nanoribbons (AGNRs) and zigzag graphene nanoribbon (ZGNR) (Fig. 2.19) are the two main ribbon geometries that were first investigated, and the different connectivity the atoms have at the edges has a significant impact on the

Table 2.5: Prediction of AGNR electronic properties based on TB.

N	Type	E_g (eV)
$3p$	Semiconductor	$0.1 - 2.5$
$3p+1$	Semiconductor	$0.1 - 2.5$
$3p+2$	Metallic	0

respective band structures [180–183]. In general, the energy spectrum of a GNR with length l_{GNR} and width w_{GNR} may be approximately written as:

$$E_{n,m} = \pm\hbar v_{\mathrm{F}}^{*} \sqrt{\left(\frac{n\pi}{l_{\mathrm{GNR}}}\right)^{2} + \left(\frac{m\pi}{w_{\mathrm{gnr}}}\right)^{2}} \tag{2.54}$$

where v_{F}^{*} is the group velocity for an energy band indexed by the pair of quantum numbers n, m [184].

Steven Louie's group was one of the first to characterise the band structure properties of AGNRs based on the number of carbon dimer lines N perpendicular to the ribbon width using tight-binding (TB) calculations [181]. This seminal work revealed that, when N is a multiple of three of an integer p, resulting ribbons feature large bandgaps that scale inversely with the width of the ribbon[§] (Tab. 2.5), and, even when the criterion $N = 3p + 1$ is met, this trend persists qualitatively. On the other hand, if $N = 3p + 2$, AGNRs are metallic [186]. When the width of the ribbon falls below 10 nm, electron–electron interactions cannot be no longer excluded, and corrective terms must be included (Tab.2.6) [185].

These theoretical estimates were for the first time observed and quantified experimentally on surface-synthesised 5-atom wide AGNRs through scanning tunnelling microscope (STM), reporting bandgaps of $E_g \simeq 100\,\mathrm{meV}$ [187–189]. Kimouche et al. experiment aimed, in particular, at quantifying the orbital energy size as a function of l_{GNR} by measuring the differential conductance of increasingly longer ribbons, and to shed some light on the implication that finite-size effects have on the bandgap scaling with l_{GNR}. As expected, the energy difference between highest occupied molecular orbital (HOMO) and lowest unoccupied molecular orbital (LUMO) rapidly narrows l_{GNR} increases. In addition, while the energy gap may

[§]The $E_g \propto 1/w_{\mathrm{gnr}}$ relation holds when $15\,\mathrm{nm} \leq w_{\mathrm{gnr}} \leq 90\,\mathrm{nm}$ [185]

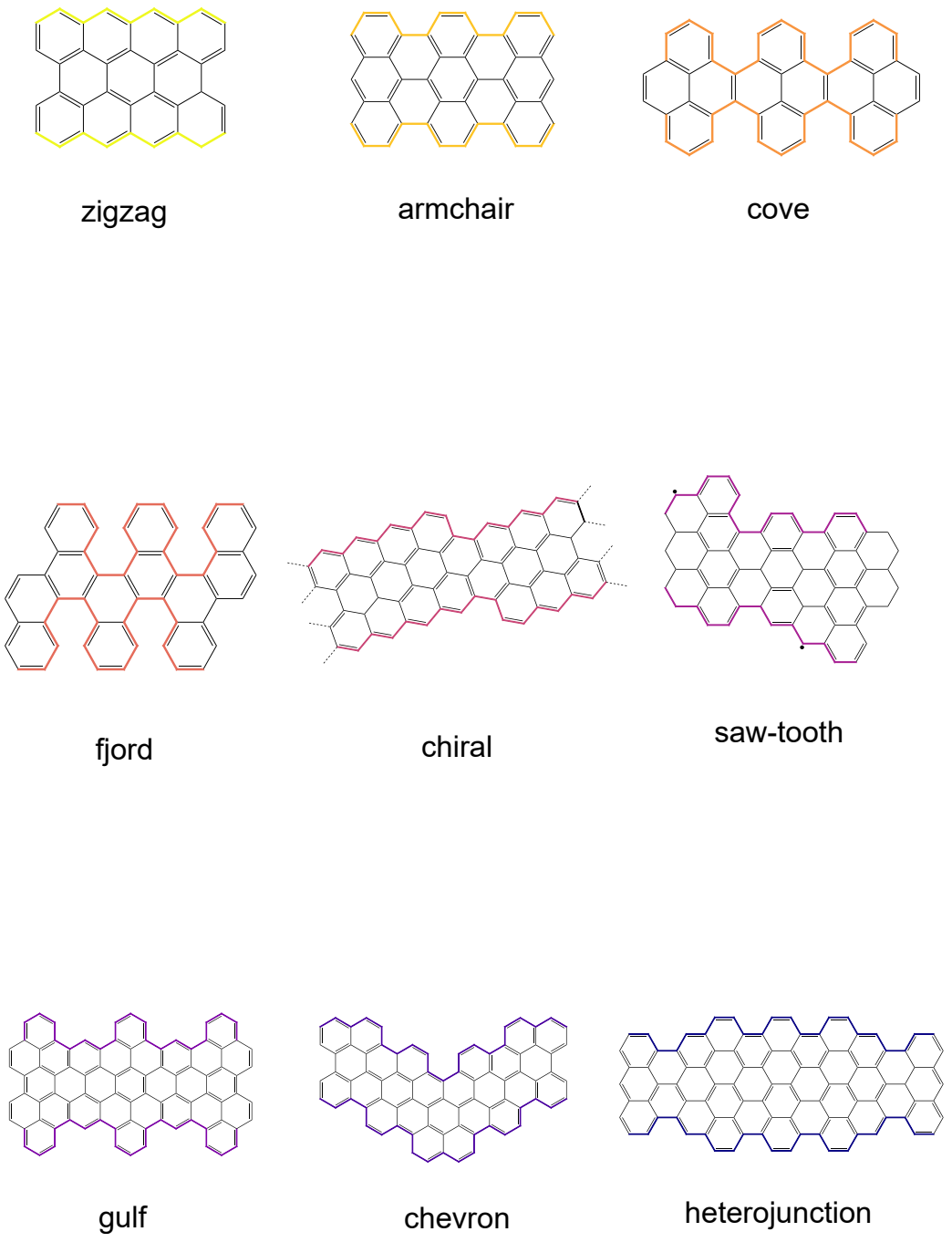


Figure 2.19: Different geometries and edge structures of graphene nanoribbons.

Table 2.6: Prediction of AGNR electronic properties based on the Green's function formalism within the GW approximation.

N	Type	E_g (eV)
$3p$	Semiconductor	$2.5 - 5.5$
$3p+1$	Semiconductor	$0.1 - 2.5$
$3p+2$	Semiconductor	$1 - 2$

vary quadratically with the ribbon length $E_g \propto 1/l_{\mathrm{GNR}}^2$, the energy spacing between electronic states that belong to the same band scaled inversely with the ribbon length $E_g \propto 1/l_{\mathrm{GNR}}$, as predicted by models which assume linear dispersions. The electronic properties of ZGNR are qualitatively and quantitatively distinct from those of AGNRs. In order to define the unit cell of a ZGNR, $2 \times 4 = 8$ atoms per unit cell are required, as opposed to $4 \times 3 + 2 = 14$ atoms for an AGNR (Fig. 2.19). The positions of the two non-equivalent atoms in the unit cell and the translation symmetry of the lattice give rise to a 2_1 screw axis along the width direction. Most notably, the presence of glide planes and screw axes in nonsymmorphic space groups[‡], which include also the wavevector group, causes energy bands to converge along certain high symmetry points and axes in the Brillouin zone [16]. This *flat band* region is positioned at wavevectors $2\pi/3 \leq k \leq \pi$, and the electronic states in this region have been interpreted as localised states along the zigzag edges by looking at charge distribution maps [180].

In one-dimensional systems, these electronic states are known as *edge states*, and their contribution to the entire wavefunction becomes minimal when w_{GNR} approaches the micrometre range, other than exhibiting an exponential decay of their DOS with distance from the ribbon centre [181, 190]. When the wavevector is between $\left[-\frac{\pi}{d_z}, -\frac{2\pi}{3d_z}\right]$ and $\left[\frac{2\pi}{3d_z}, \frac{\pi}{d_z}\right]$, where d_z is the unit cell distance, a bandgap is opened in the band structure (Fig. 2.20c).

It has been proven by spin-polarized ab-initio calculations that two distinct magnetic orderings are distinguishable in the ground state: a ferromagnetic (↑↑,

[‡]Nonsymmorphic groups are space groups that are not uniquely defined by the lattice translations repeating of a point-group motif. Te and α-quartz are examples of nonsymmorphic groups.

FM) configuration for spins aligned along a single edge and an antiferromagnetic ($\downarrow\downarrow$, AFM) condition for spins belonging to two distinct edges [191]. Numerical studies have also suggested that GNR could display *half metallicity*, i.e. to undergo a phase transition from an AFM configuration (semiconducting) to an FM state (metallic) when a transverse electric field is applied perpendicular to the ribbon plane [191, 192].

Similar to CNTs, GNRs can have chiral edges. Typically, chirality may be described by a chiral angle θ which may be defined as:

$$\theta = \arcsin\sqrt{\frac{3}{4}\left(\frac{m^2}{n^2+nm+m^2}\right)} \tag{2.55}$$

where the nanoribbon edge orientation is determined by translation vector (n, m) of the graphene lattice. Zigzag and armchair are characterised by $\theta = 0°$ and $\theta = 30°$, respectively, while chiral edges have θ in the range between.

2.5.2 Edge States

In an attempt to solve the DOS for chiral GNRs, Yazyev, Capaz, and Louie employed a mean-field Hubbard Hamiltonian for modelling the GNR dispersion relation, assuming the on-site Coulomb repulsion U comparable to the hopping integral t between two adjacent sites ($U/t \sim 1$):

$$\begin{aligned}\mathcal{H}_{\mathrm{MF}} = &- t \sum_{\langle ij\rangle,\ \sigma} \left(a^{\dagger}_{\sigma,i} a_{\sigma,j} + \mathrm{h.c.}\right) \\ &+ U \sum_{i} \left(n_{i\uparrow}\langle n_{i\downarrow}\rangle + \langle n_{i\uparrow}\rangle n_{i\downarrow} - \langle n_{i\uparrow}\rangle\langle n_{i\downarrow}\rangle\right),\end{aligned} \tag{2.56}$$

whereby the second summation is performed over spin-polarised densities $n_{i\sigma} = a^{\dagger}_{i\sigma} a_{i\sigma}$. This Hamiltonian preserves the electron–hole symmetry, which means that the density of states is symmetric with respect to the Fermi level. The experimental evidence is captured by the solutions of the associated eigenvalue problem, which predict the origin of two peaks splitting in the DOS, which have been interpreted as manifestation of two opposite magnetic orderings. One peak split caused by the AFM correlation between opposite edges, whereas the second, greater peak split should be caused by FM ordering along a single edge (Fig. 2.20b,c). The energy difference between the two magnetic orderings was estimated to be of order of tens

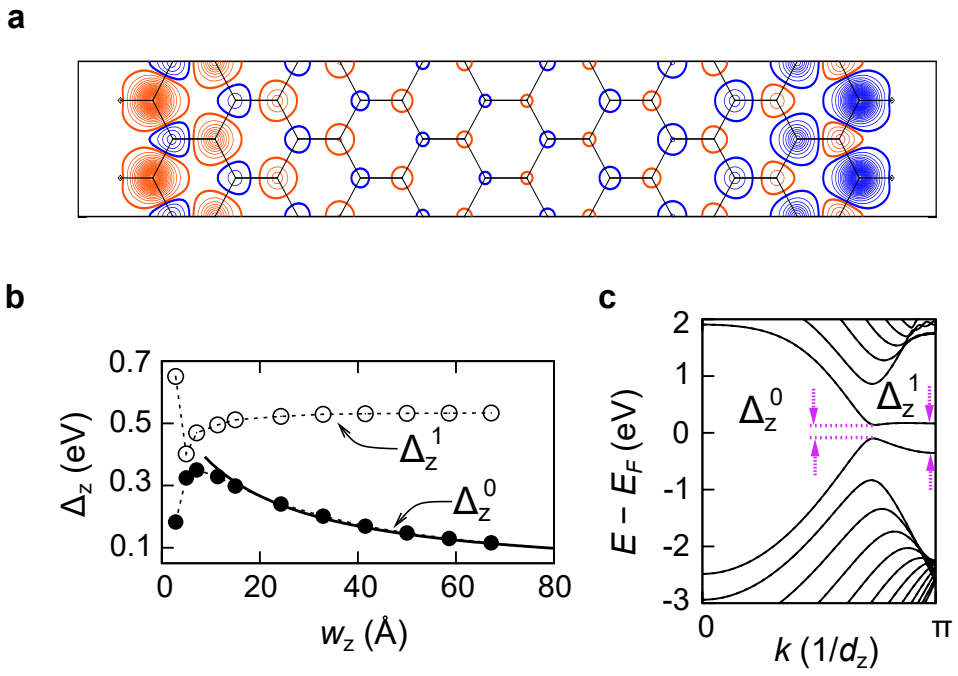


Figure 2.20: **a**, Contour plot representing the difference between spin-polarised *ab-initio* DOS of a 12-ZGNR. The high density of $\rho_\alpha(r)$ red lines ($\rho_\beta(r)$, blue line) to the left backbone edge demonstrates the delocalisation of edge states. **b**, Direct bandgap Δ_z^0 and the energy splitting Δ_z^1 as a function of the width w_z of the ribbon. For $N_z \geq 8$, the fit is shown as a solid line, whereas dotted lines are just visual guides. **c**, Band structure for the same ribbon plotted as a function of the normalised wavevector. Adapted from [181].

of meV per edge atom and to decrease as the ribbon width increases, eventually becoming negligible when the width is significantly larger than the exponential decay length of spin-polarised states ($\lambda \simeq$2–5 nm) [194]. In theory, it should then be possible to probe this energy difference by either studying the TDOS or by using high-frequency-resonance techniques.

Although the experimental evidence for the edge states[†] of ZGNRs and chiral GNRs still remains elusive, Slota et al. have demonstrated, using electron-spin resonance techniques, that magnetic edge states can be induced in cove GNRs. Stable nitronil-nitroxide radicals were grafted along the edges as spin injectors, allowing to separate the magnetic edge fingerprint from the signal of the radical. In addition, their study shown that the edge state has longer coherence times than the majority

[†]The peculiarities of these edge states is that they are instrinsically magnetic

of π-extended organic systems, even at room temperature and in powder, which makes graphene nanoribbons particularly interesting for spintronic applications.

2.5.3 Graphene Nanoribbons Field-Effect Transistors

One of the first graphene nanoribbon field-effect transistor (GNRFET) fabricated using MGNR was developed back in 2008 by the group of Honjie Dai [137]. The ribbon was synthesised through sonochemistry methods, and deposited on a Si/SiO_2 substrate, with electrical contacts realised in Pd. As previously discussed, the large work function of Pd should reduce the back-injection of the minority carriers in the conductive channel. Wang et al. examined the impact of ribbon widths as small as $w_{\mathrm{GNR}} \simeq 2.0(5)\,\mathrm{nm}$ on the device performance, while the ribbon lengths were kept roughly constant $l_{\mathrm{GNR}} \simeq 236\,\mathrm{nm}$.

Despite a few remarkable transistor key numbers such as $I_{\mathrm{on}} \simeq 2000\,\mu\mathrm{A}\,\mu\mathrm{m}^{-1}$, $I_{\mathrm{on}}/I_{\mathrm{off}} \simeq 10^6$, $SS \simeq 210\,\mathrm{mV\ dec}^{-1}$, and $g_{\mathrm{m}} = 900\ \mu\mathrm{S}\,\mu\mathrm{m}^{-1}$, lower carrier mobilities $\mu \simeq 50\text{–}200\,\mathrm{cm}^2\,\mathrm{V}^{-1}\,\mathrm{s}^{-1}$ were measured for narrower ribbons. These results led the researchers to two conclusions. Firstly, narrow GNRs entail higher bandgaps, leading to lower mobilities [196]. Secondly, scattering at the edge effects may dominate carrier transport in narrow $w_{\mathrm{GNR}} \leq 5\,\mathrm{nm}$ ribbons. Wang et al. proposed a phenomenological model in which edges, defects, and phonons were regarded as independent factors in order to link the mean freee path ℓ with the w_{GNR} and E_g [137]:

$$\frac{1}{\ell} = \frac{1}{\ell_{\mathrm{edge}}} + \frac{1}{\ell_{\mathrm{phonon}}} + \frac{1}{\ell_{\mathrm{defect}}}. \tag{2.57}$$

From the definition of mean free path (see also Sec. 2.3.1), the likelihood P of a scattering event to happen may be phenomenologically conceived as the inverse of the average time between two consecutive collisions:

$$\ell_{\mathrm{edge}} = \frac{k_{\parallel} w_{\mathrm{gnr}}}{P k_{\perp}}, \tag{2.58}$$

As we saw in the previous section, when $w_{\mathrm{GNR}} < 20\,\mathrm{nm}$, it is possible to approximate the ribbon energy gap as inversely proportional to the ribbon width, provided electron–electron correlations are neglected [197]:

$$E_g \simeq \frac{\hbar v_{\mathrm{F}}}{w_{\mathrm{gnr}}}. \tag{2.59}$$

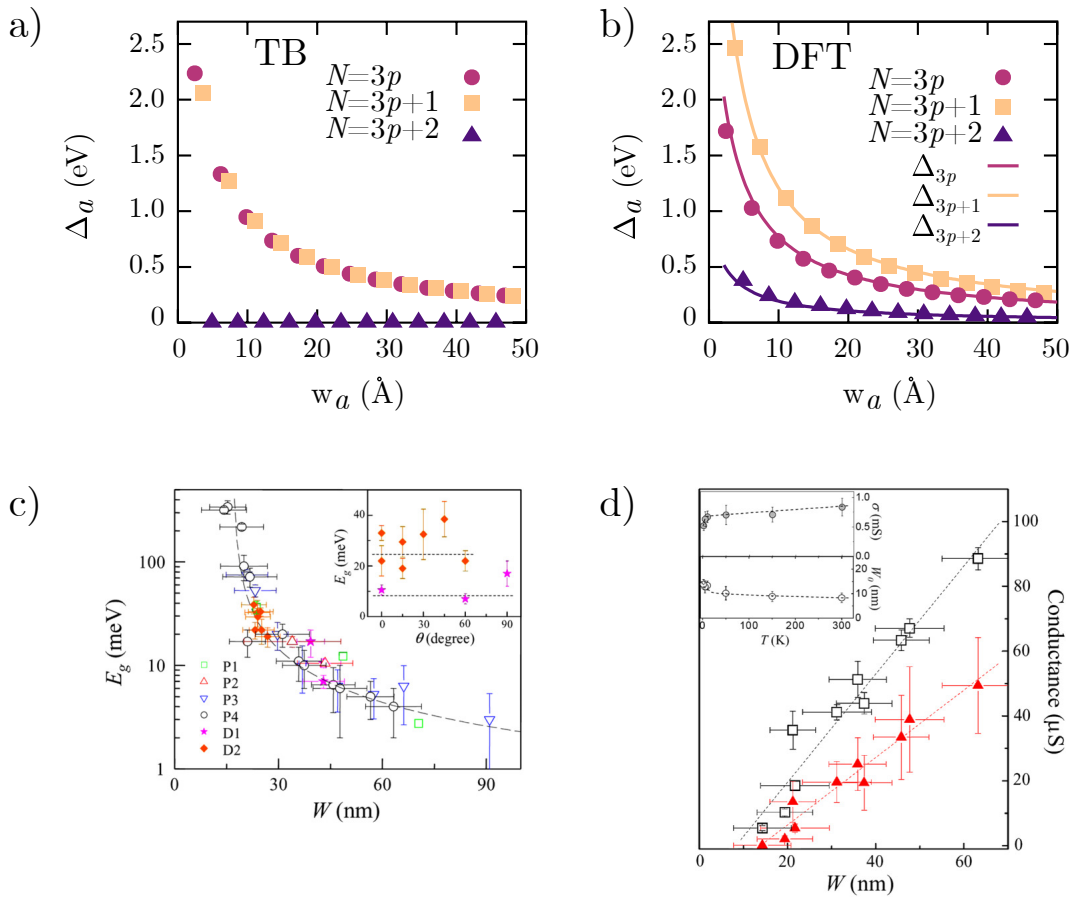


Figure 2.21: **a**, Bandgaps Δ_a calculated at TB level for three families of AGNRs as a function of the GNR width w_{GNR} [181]. **b**, Same as in **a**, but using density-functional theory (DFT). **c**, Experimental bandgaps measured for lithographic nanoribbons as a function of w_{GNR}. Contrary to early predictions, Han et al. investigated various crystallographic orientations for the ribbon and found no dependence on the direction. **d**, As expected, larger GNRs conduct more than narrow ones. Squares are values measured at 300 K whereas triangles correspond to 1.6 K. The insets show the conductivity (upper) and the inactive GNR width (lower) obtained from the linear fit of the conductance with the temperature. Adapted from [164].

By inserting Eq. 2.59 and the dispersion relation E_k into Eq. 2.58, an expression for the dependence on the width of the mean free path can be written as:

$$\ell_{\mathrm{edge}} = \frac{w}{P}\sqrt{\left(1+\frac{E_k}{E_g}\right)^2 - 1} \tag{2.60}$$

According to Eq. 2.60, both a wider width and well-defined edges should improve the ℓ. These hypotheses were experimentally confirmed by higher mobilities when GNRs as wide as 10 nm were measured [137, 165].

Table 2.7: Comparison amongst different FET realised with graphene nanoribbon as conducting channel. Top and bottom.

	Structural Parameter			Device Parameter	
Fabrication Approach	Edge Structure	Width (nm)	E_g (meV)	I_{on}/I_{off}	Mobility ($cm^2V^{-1}s^{-1}$)
Top-Down	—	5	145	47; 10^5 (5.4 K)[198]	—
	—	5	489.4 ± 19.0	$> 10^4$ (290 K)[199]	—
	—	15	120 ± 23	—[199]	—
	Mixed	10	140	10^5 (4 K)[200]	—
	—	12	100	10; 10^6 (4 K)[201]	—
	—	sub-10	200	—[91‡]	—
	—	10 – 20	10 – 15	4.5; 10 (20 K)[202]	—
	Closed	2.8	494	10^5	2443_{μ_h}
	Closed[203]	9.9	$891/[w_{gnr} - 1.0]$	$< 10^2$	3776_{μ_h}
	—	100 – 400	18 – 1	20 – 3.5[204]	—
Bottom-up	Cove	0.69 – 1.13	1,880	$>^{\dagger} 10^{10}$	
	AGNR	0.95	2,100	$^{\dagger}10^5$	
	Chevron	1.73	3,100 ± 400	—	
	—	2	—	$> 10^6$	
	AGNR	0.63	1,690 ± 100	$>^{\dagger} 10^10$	
	AGNR	0.95	1,690 ± 70	—	
	AGNR	1.27	1,130 ± 50	$^{\dagger}10^9$	
	AGNR	1.37	1,600 ± 400	—	
	AGNR	1.58	1,030 ± 40	$^{\dagger}10^8$	
	AGNR	5 – 9	≤ 400	$10^5 - 10^6$	
	ZGNR	6	1,400	—	
Epitaxial	—	900	—	—	
	AGNR	2 – 40	> 500	—	
	—	40	—	10; > 25 (4 K)	

2.5.4 Bandgap Engineering

The theoretically predicted relationship between ribbon width and energy gap was confirmed experimentally in 2007 by Philip Kim's team (Fig. 2.21) and shed lights on the difference between a true energy gap and the transport gap typically measured in an electron transport experiment [164, 177].

The experiments they perfomed suggested that edge disorders may produce charge localisations, and this effect becomes greater as the ribbon length increases [205–207]. This evidence was later combined with a detailed analysis that demonstrates how electron–electron interactions cannot be neglected when the ribbon width is reduced below 5 nm [208]. Moreover, the conductance is likely to be suppressed by Coulomb blockade, which also explained the deviation of larger energy gaps for small ribbons compared to theoretical studies [206, 208].

In an attempt to solve this conundrum, Kim's group suggested an explanation in between. Charge transfer via hopping through localised states will lead to a transport gap rather than a single energy gap when the distance between these state is of the order of magnitude of the ribbon size [177]. Through electrical transport experiments, Han, Brant, and Kim advanced the explanation that the gate voltage region ΔV_{G} where the conductance is suppressed may be related to the single-particle energy gap via [18]:

$$E_g = \hbar v_{\mathrm{F}} \sqrt{2\pi C_{\mathrm{G}} \Delta V_{\mathrm{G}} / |e|}, \tag{2.61}$$

where C_{G} is the capacitive coupling between the ribbon and the gate.

In addition, Han, Brant, and Kim measured the conductance temperature-dependence, reporting a strong suppression of the minimum of conductance G_{min}, which they interpreted by considering a thermally-activated process of the carriers, in contrast to first earlier suggestions which explained the observation within the Coulomb blockade theory [209]. Even with different ribbon widths, the scientists discovered a linear scaling of the conductance $G = \sigma(w_{\mathrm{GNR}} - w_0)/l_{\mathrm{GNR}}$ when this was normalised across an active transport region $(w_{\mathrm{GNR}} - w_0)$, being $\sigma \simeq$

1.7 mS for the sheet conductivity. Comparing similar trends reported for SB-restricted junctions led to the conclusion that the graphene nanoribbons-metal connection may have been limited by the formation of a Schottky barrier that dominates the charge injection [38].

2.5.5 Graphene Nanoribbons Electronics

Utilising pure carbon nanotubes and compressing them under high pressure to make graphene nanoribbons has recently yielded excellent device performance [203]. The nanotube samples were loaded and sealed in a sample chamber positioned in the centre of a pre-indented tungsten gasket, which was then compressed between two diamond anvils from ambient pressure to 22.8 GPa while the structural evolution was monitored by in-situ Raman spectroscopy through the diamond window.

The authors observed a resonant radial breathing mode peak at 116 cm^{-1}, corresponding to a nanotube with a diameter $\simeq 2.1\,\mathrm{nm}$, dropping in peak intensity as the pressure climbed, and finally becoming practically invisible when the pressure surpassed 5.5 GPa. The peak position shift and absence of the radial breathing mode were attributed to an irreversible structural transition in nanotubes that occurs at high pressure and affects their sub-band energy gaps.

The authors found a remarkable on–off ratio of approximately four orders of magnitude at extremely low bias (Tab. 2.7). Moreover, Chen et al.'s device showed a p-type on-state conductivity of about:

$$\sigma = \frac{G_{\mathrm{sd}} L_{\mathrm{ch}}}{w_{\mathrm{gnr}}} = 7.42\ \mathrm{mS} \tag{2.62}$$

for a channel of width of ($w_{\mathrm{gnr}} \simeq 2.8\,\mathrm{nm}$). They further test the relationship between the carrier mobilities for increasingly wider ribbon widths up to 10 nm. The experiments reported hole mobilities[†] of about $\mu \simeq 2.443\,\mathrm{cm}^2\,\mathrm{V}^{-1}\,\mathrm{s}^{-1}$ for the 2.8 nm wide and $\simeq 3.776\,\mathrm{cm}^2\,\mathrm{V}^{-1}\,\mathrm{s}^{-1}$ for the 10 nm wide, which are currently among the highest values observed, despite possible uncontrolled scattering events of the carriers with the non-spherical bulb-like ends cross at the two sides.

[†]Calculated according to standard FET theory $\mu = \frac{g_{\mathrm{m}} L_{\mathrm{ch}}}{C_{\mathrm{G}} V_{\mathrm{SD}}}$ [51]

Another issue in creating reproducible devices is transferring ribbon onto a substrate to measure its electrical characteristics. Because stamping methods that rely on mechanical contact of the ribbon growth and transfer substrate frequently result in poor-performing or irreproducible GNRFETs [171], Michael Crommie's group developed a robust transfer employing a stack of PMMA/GNR/Au/Mica [210]. Poly-methyl methacrylate (PMMA) was first spun-cast onto GNRs and baked to generate a PMMA/GNR/Au/Mica stack, which was then floated on concentrated HF (40%), causing the mica substrate to delaminate from the Au growth layer. The leftover PMMA/GNR/Au film stack was then rinsed twice in water before being put to Au etchant. Finally, the PMMA/GNR film was washed and drawn onto a silicon substrate before being baked to eliminate any remaining water. Finally, acetone was used to remove PMMA, leaving GNRs on an insulating surface.

At $V_{\mathrm{SD}} = 1\,\mathrm{V}$, the resultant transistor displayed gate-modulated conductance with on-currents ranging from tens of pA to a few nA. The authors reported that the electrical transport was mostly dominated by a significant Schottky barrier $\phi_{\mathrm{B}} \simeq 1.25\,\mathrm{eV}$, which was caused by adopting a much narrower ribbon with a wider bandgap. They also reported that, despite the fact that the contact between the ribbons and Pd must have been only a few to perhaps ten nanometers long, they were able to measure $I_{\mathrm{on}}/I_{\mathrm{off}} \simeq 10^3$ at $V_{\mathrm{SD}} = 1\,\mathrm{V}$, even if experiment on nanotube transistors have demonstrated resistance increases as contact length is reduced past the electron mean free path[§]. The off-state leakage was attributed to the holes tunnelling through the drain barrier, and therefore being largely temperature independent but strongly sensitive on the bias, as larger ones will significantly shrink the width of the Schottky barrier.

The authors also proposed a certain number of measures to mitigate the device shortcomings. Reducing the contact work function ($\phi^{\mathrm{Pd}} \simeq 5.2$–$5.6\,\mathrm{eV}$) would decrease the barrier height of the source conduction band and increase the barrier height of the drain valence band, resulting in enhanced on- and off-state performance. As effective mass and Schottky barriers are projected to be lower for smaller

[§]In graphene and CNTs this value is often referenced at $\ell \simeq 200\,\mathrm{m}$ [98, 211]. See also Sec. 2.2

bandgaps, the usage of wider GNRs with bandgaps $E_g \simeq 1.4\,\mathrm{eV}$ could also result in a further enhancement of band alignment. In conclusion, the researchers hypothesised that longer GNRs could also lower contact resistance by increasing L_c [212].

Using high-κ dielectrics is another viable method for enhancing the properties of transistors. The usage of such dielectrics is necessitated by the fact that, when scaling down the geometrical dimensions of a transistor, the oxide thickness cannot be scaled in the same manner as the other geometrical parameters, as this would result in leakage currents through the oxide. This phenomenon could also result in a field that exceeds the breakdown field of silicon dioxide. By raising the permittivity of the dielectric, one can afford a thicker dielectric while still achieving the same capacitance as with a thinner silicon dioxide dielectric.

Llinas et al. investigated the output characteristics of GNRFETs 9- and 13-atoms wide fabricated using two distinct gate dielectrics [213]. They compared the output response of a 50 nm-thick back-gated silicon dioxide substrate to that of a high-κ dielectric local gate (HfO_2, EOT$\simeq$1.5 nm). For the latter device at room temperature, current densities $I_\mathrm{on} > 1\,\mu\mathrm{A}$ measured at $V_\mathrm{SD} = -1\,\mathrm{V}$ with the narrower ribbon were amongst the highest ever reported, combined with an excellent $I_\mathrm{on}/I_\mathrm{off} \simeq 10^5$.

Through a temperature-dependent experiment, however, the authors noted that Schottky barriers generated at the contacts again dominated transport. While the high-κ dielectric lowers the carrier tunnelling, the Au/Pd–GNR junction leads to the formation of Schottky junctions partly due to the mismatch between the work functions of the metal and the ribbon. In order to lessen the mismatch and prevent the Schottky-dominated transport regime, adopting graphene as a contacting material could be one feasible approach [214, 215].

3

Experimental Details: Nanofabrication and Measurement Protocols

Contents

3.1 Introduction 65
3.2 Sample Nanofabrication 66
3.2.1 Graphene Patterning 68
3.3 Room-Temperature Transport Setup 69
3.4 Graphene Tunnel Junctions 70
3.4.1 Gate-controlled Electroburning 72
3.5 Contacting Graphene Nanoribbons 75
3.6 Deposition Process and Related Phenomena 77
3.7 Cryogenic-Temperature DC Transport Setup 81

3.1 Introduction

In this thesis, a substantial amount of effort was devoted to the investigation of graphene-based SETs, where bottom-up graphene nanoribbons (MGNRs) are essentially extended delocalized molecules connecting the two leads. To do this, electrodes separated by only a few nanometres are necessary, as well as mK temperatures and extremly high sensistivity in the electronic measurement.

In this chapter, I will describe the room temperature setup I used to fabricate graphene tunnel junctions (GTJs), the development of a new feedback electroburning

protocol that increases the chances of having quantum-dot-free GTJs, ideas for improving the deposition process, and a brief overview of the cryogenic setup and the electronic apparatus for performing DC measurements.

The fabrication procedure employed for producing GTJs was based on a standard laboratory protocol. The candidate, however, meticulously refined the recipe through an iterative process of trial and error based on the quality of the electroburning experiments based through experience. Furthermore, it is worth noting that the feedback electroburning protocol had been previously developed by other members of the research group. The contribution of the candidate to this body of work lies in the development and implementation of the gate-controlled feedback electroburning approach, thereby advancing the state of the art in the field.

3.2 Sample Nanofabrication

An ideal fabrication recipe is one in which small changes in the fabrication process have no substantial effect on the fabrication outcome. A robust fabrication recipe was achieved for the metallic contacts and a satisfactory electron-beam exposure protocol for the graphene leads.

Metal pads (Cr 5 nm/ Au 65 nm) were fabricated via standard lithography means (Fig. 3.1). Graphene leads, on the other hand, were fabricated through a modified wet transfer recipe [216] here below detailed.

1. A $1 \times 1\,\mathrm{cm}^2$ piece of graphene is manually cut from a 6 inch sheet of CVD graphene, purchased from Graphenea, which is backed with copper foil and coated with a thin protective layer of PMMA on top. The layer thickness I found to work best for our application (i.e. less level of graphene surface contamination) was 300 nm.

2. The graphene squares are placed into an oxygen plasma cleaner copper side up and etched at 50% power for 60 s with 25 sccm of oxygen to remove residual backside graphene.

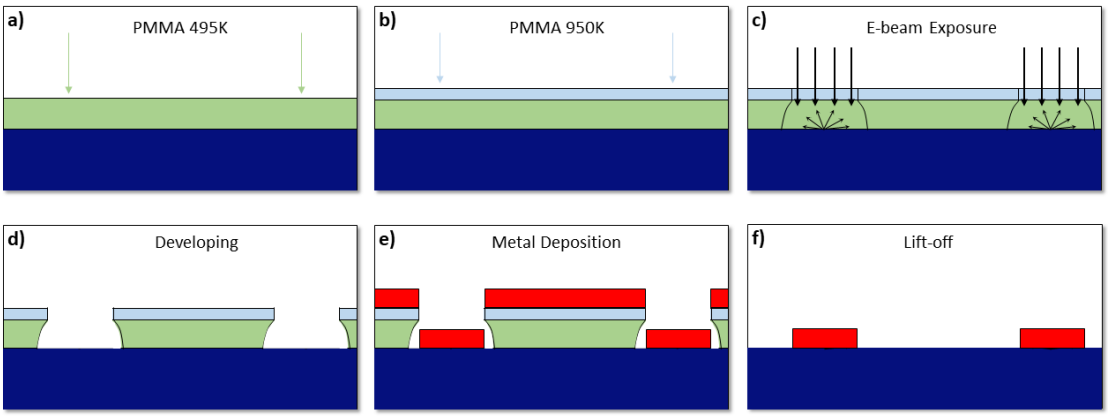


Figure 3.1: Schematic of Metal Deposition. **a**, The first photoresist covers the SiO_2 substrate. **b**, A second layer of photoresist is applied. **c**, Exposure to electron-beam lithography with secondary electron scattering from the substrate highlighted. **d**, Development of the resist, resulting in an undercut. **e**, Metal deposition using a thermal evaporator. **f**, Lift-off aided by the undercut, with the final metal structure remaining on the substrate.

3. A 0.4 mol solution of ammonium persulfate (APS) in deionised water is prepared in a clean beaker and sonicated to remove any air bubbles.

4. The graphene pieces are floated on top of the APS solution copper side down and left overnight for the copper to dissolve.

5. $1 \times 1\,\mathrm{cm}^2$ chips of a pre-patterned doped silicon wafer with a 300 nm layer of thermal oxide are cleaned by sonicating in acetone, washing in IPA and drying under nitrogen. The chips are patterned with an array of 851 electrode pairs, formed of 60 nm Au evaporated on top of a 5 nm -thick adhesion layer made by Cr. The electrode pairs are separated by 5 µm at the narrowest point, between which the graphene will be patterned.

6. The etched graphene pieces are transferred three times to clean beakers of deionised water using a clean glass slide to remove residual APS.

7. Graphene is transferred from the water directly onto the pre-patterned chips, using an IPA dip to remove any trapped air bubbles or smooth small creases, and is left to air dry for several hours.

8. Chips are baked at $T = 180\,^{\circ}\mathrm{C}$ for 1 hour to re-flow the protective PMMA layer and remove residual solvents.

9. The chips are submerged in acetone and heated to $180\,^{\circ}\mathrm{C}$ for at least 2 hours to remove the protective PMMA. The chips are then washed in fresh acetone and IPA and dried with nitrogen.

One of the recipe biggest flaws was the unreliability of graphene wet transfer [217]. Bubbles trapped beneath the water meniscus frequently cause ripples on the graphene surface, compromising the electroburning process [218]. In essence, ripples localise current-density increases, which lead to strong Joule heating increments in the graphene lattice. When this happens, I frequently observed an abrupt drop voltage drop beween the leads during the electroburning cyle (Sec. 3.4), and the resulting GTJs were often unsuitable for further transport experiments. To minimise these incoveniences, I later opted to outsource graphene transfers at the wafer size to Graphenea. This significantly enhanced graphene quality and electroburning yields.

3.2.1 Graphene Patterning

Once the Si/SiO_2 substrates were prepared, graphene was deposited onto them following the procedure detailed below.

1. Each graphene coated chip is loaded into a spin coater and 100 µL of Allresist AR-N 7500.18 negative resist is deposited onto the bare graphene.

2. The chip is spun at 5000 rpm for 60 s in order to achieve a resist thickness of $\simeq 3.5\,\mu\mathrm{m}$.

3. The coated chip is baked at $85\,^{\circ}\mathrm{C}$ for 60 s to cure the resist.

4. The chip is loaded into an electron-beam lithography (EBL) where constrictions with a nominal width of approximately 100 nm are patterned using a beam current of 500 pA and a dose of $300\,\mu\mathrm{C\,cm^{-2}}$.

5. The development step is carried out in DuPont MF-CD-26 developer for 45 s, removing the unexposed resist, before being washed in deionised water and dried under nitrogen.

6. The chips are loaded into an oxygen plasma cleaner and etched at 50% power, 25 sccm of oxygen for 60 s to remove the exposed graphene.

7. The chips are then submerged in Microresist MR-REM 660 at 50 °C for 2 hours to remove the remaining exposed negative resist.

8. The chips are washed in acetone and IPA and dried using nitrogen.

3.3 Room-Temperature Transport Setup

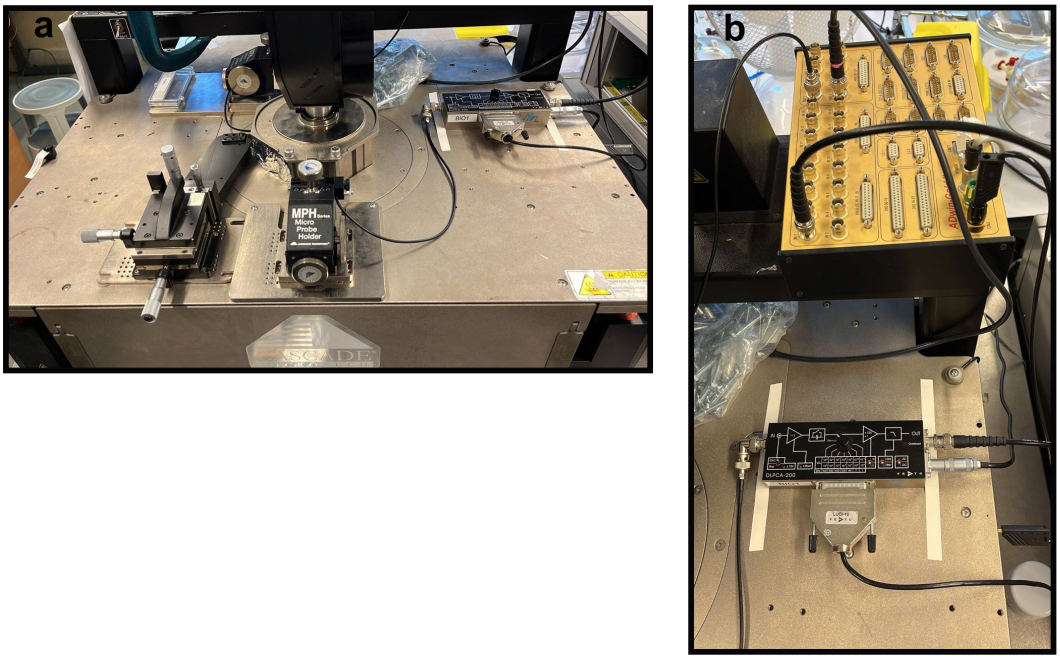


Figure 3.2: **a**, Probe Station setup. In **b**, the ADwin-Gold II, current amplifier and respective connection for a standard 3T measurement.

Electrical measurements at room temperature are performed on a fully automated Cascade Summit^{TM} 12000 M probe station, fitting three micro-manipulators (Fig. 3.2a). To ensure good electrical contacts, Copper beryllium probes by Lambda photometrics (tip diameter = 25 µm, length = 30 mm) were used for contacting Au (source/drain) pads, Tungesten (tip diameter = 10 µm, length = 30 mm) for HfO_2 (local) pads. Thanks to this automation system, I was able to address approximately 800 devices per chip.

Typically, currents flowing through a quantum device are within the $pA - nA$ range. To detect signals with enough accuracy, a Femto DLPCA-200 low-noise current amplifier with adjustable gain was used to convert currents to voltages (Fig. 3.2b). The bandwidth of the amplifier filters varies based on the gain settings and operates solely on the pure analogue signal: the internal low-pass-filter (LPF) is approximately 10 Hz to eliminate wide band noise for low-frequency applications, and at the highest trans-impedance gain settable of $1 \times 10^{11}\,\mathrm{V\,A^{-1}}$ guarantees a 3 dB bandwidth of 1.1 kHz. If the gain is not set correctly, the amplifier will overload, and block the passage of more current.

Through an Adwin-Gold II (Fig. 3.2b), voltages are applied and read. The system is equipped with 16 analogue inputs, 2 analogue outputs, 32 digital I/O, and a maximum output voltage range of ±10 V with a 16-bit resolution. During the feedback electroburning programme, a timer with a resolution of 3.3 ns is necessary for ramping back the voltage at the beginning of each burning cycle. The incoming data stream was sampled at a constant rate of $300\,\mathrm{MHz\,s^{-1}}$.

3.4 Graphene Tunnel Junctions

Due to the sp^2 covalent network of bonds between carbon atoms, electroburning does not occur through the migration of single atoms, as it does in gold electromigrated junctions, but rather through more dramatic chemical changes in which the final structure may be significantly different from the initial structure [219, 220]. In contrast to the pristine nanogaps that can be obtained by using metallic nanogaps, control over and knowledge of the final atomic structure of graphene

nanogaps are limited, and the relationship between this structure and the electrical transport capabilities of the device is largely unknown. GTJs were fabricated

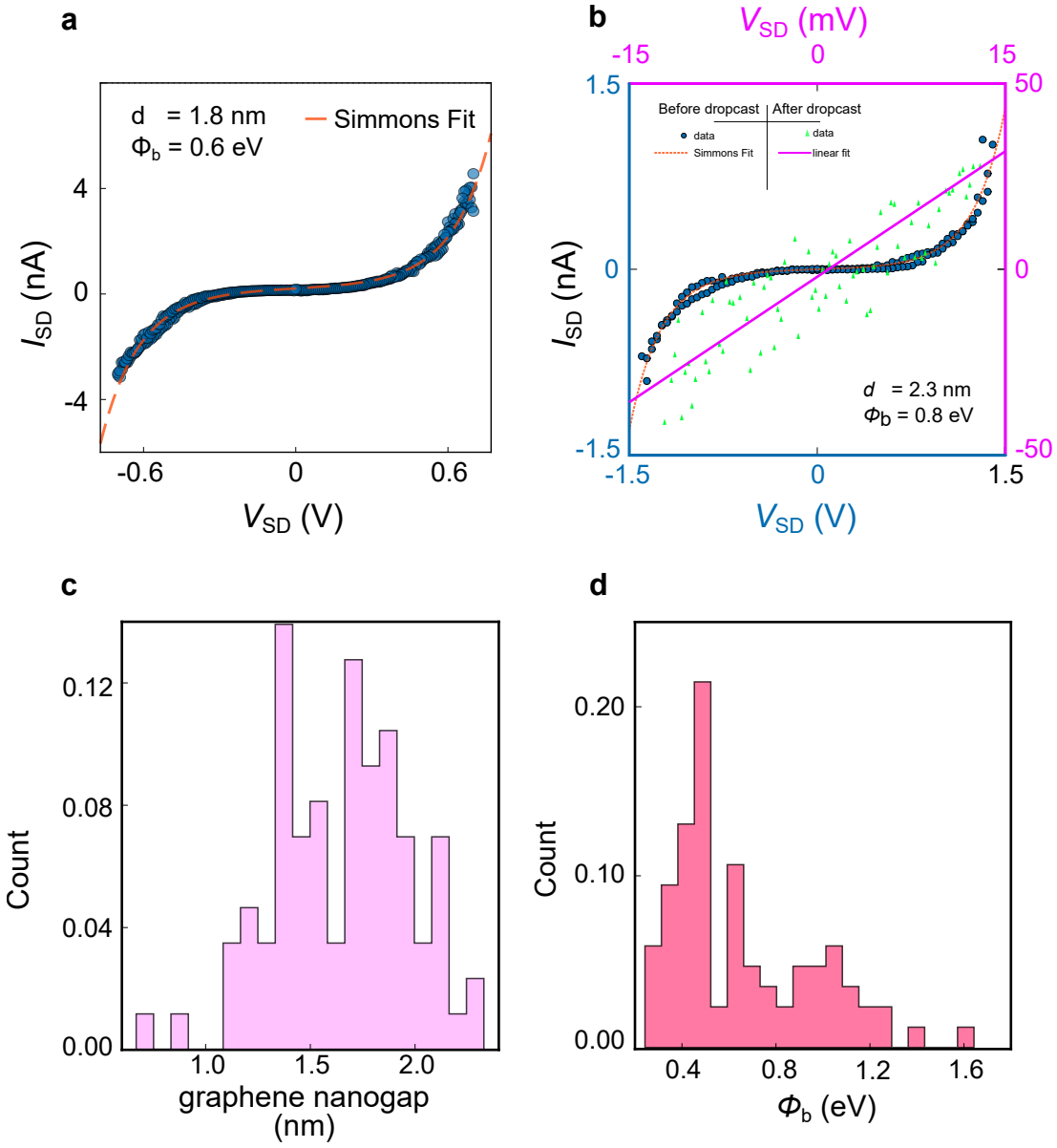


Figure 3.3: **a**, Typical GTJ measured at zero gate at the end of the electroburning. **b**, Source drain current I_{SD} pre (blue) and post (purple) depositing a solution of GNRs. **c**, Histrogram of the nanogap size resulting by fitting I_{SD} with the Simmons model as explained in the main text. **d**, A Poisson distribution-like histogram of the energy barrier fitting parameter.

using by the feedback-controlled electroburning protocol detailed in literature [221, 222]. In a typical electroburning experiment, the voltage across the graphene

constriction is ramped up at a rate of 5–8 $\mathrm{V\,s^{-1}}$ to a maximum of 10 V while the current is continuously sampled by the ADWin. Possible inflection points in the first few electroburning traces indicating negative differential conductance might be due to thermal cleaning of the graphene surface from residual litography contaminations [222].

When the current decreases as a result of removal of carbon atoms from the graphene lattice due to Joule heating, the feedback protocol responds by ramping the voltage back to 0 V at a rate of about 2500–5000 $\mathrm{V\,s^{-1}}$. The process is repeated until the junction resistance exceeds a specified threshold, which has been modified to optimise the process. Typical threshold values ranged between 0.5–2.4 GΩ, yielding a clean-junction percentage of roughly 18–24 %.

Fitting the $I - V_{\mathrm{SD}}$ trace of a device (Fig. 3.3a,b) to the Simmons model with an asymmetric barrier:

$$I_{\mathrm{SD}}(V_{\mathrm{SD}}) = I_0 + \frac{Ae}{(2\pi h d^2)}\left[(\Phi_{\mathrm{b}} - eV_{\mathrm{SD}}/2)\exp\left(\frac{-4\pi d}{h}\sqrt{2m\,(\Phi_{\mathrm{b}} - eV_{\mathrm{SD}}/2)}\right)\right.$$
$$\left. - (\Phi_{\mathrm{b}} + eV_{\mathrm{SD}}/2)\exp\left(\frac{-4\pi d}{h}\sqrt{2m\,(\Phi_{b} + eV_{\mathrm{SD}}/2)}\right)\right]$$

allows us to retrieve several fitting parameters. I_0 is an offset current accounting for possible shifts along the y-axis, A is the contact area of the two electrodes (cross-sectional area), d the gap size and Φ_{b} is the potential barrier expressed within a WKB approximation for transmission probability of an electron to tunnel through a an insulating barrier.

Fig. 3.3c,d shows the histograms for gap widths, which has mean gap size of approximately $\bar{d} = (1.7 \pm 0.3)\,\mathrm{nm}$, and for the energy barrier of $\overline{\Phi_{\mathrm{b}}} = (0.7 \pm 0.4)\,\mathrm{eV}$.

3.4.1 Gate-controlled Electroburning

When molecules are deposited on graphene leads, the tunnel coupling resulting from the anchoring to the honeycomb lattice frequently results in systems with in the weak-coupling regime (see Ch. 2.3.2). This indicates that Coulomb blockade characteristics can (and typically are) seen at gate voltages other than zero. This is

Table 3.1: Comparison between tradition and gate-controlled electroburning.

Device	Normal Electroburning	Gate-Controlled Electroburning
Spurious QDs	85	43
Clean	15	57
Yield	15%	57%

problematic because these features, which originate from contaminations formed during electroburning, can obscure molecular ones. To mitigate this problem, a novel electroburning procedure was created. The computational flowchart that was subsequently implemented within the Python measurement framework QTlab [223] is seen in Fig.3.4. Essentially, the protocol runs a first electroburning cycle and then determines if the probability distribution of the source–drain current values recorded via a gate trace at a fixed bias differs from a Gaussian distribution.

The null-hypothesis is evaluated using the Shapiro–Wilk test, and is rejected if the p-value is $p \leq 0.05$: in this case, there is a 95% chance that the source–drain current values do not follow a normal distribution, hence there must be a residual quantum dot at finite gate voltage. Visual inspection typically supports this conclusion by observing the progressive disappearing of current peaks in a gate trace (Fig. 3.4). Subsequently, the gate is automatically set to the maximum current value in the gate trace, and a second electroburning cycle begins. The loop is performed a predefined number of times, which is often set to 3. By leveraging this experimental GTJ fabrication protocol the percentage of clean junctions increased up to 52%–66%. Despite the fact that this procedure has increased the overall yield of clean junctions, several refinements are still possible. A future improvements of this approach should accommodate for situations in which significant signal spikes induced by frequency pickup could be identified as the maximum current point even though there is no coulomb diamond present. For instance, to distinguish the current steps from the background noise, an iterative median filter might be applied to the data to filter away transient spikes in the conductance while keeping even modest conductance steps caused by charging effects. After normalising the

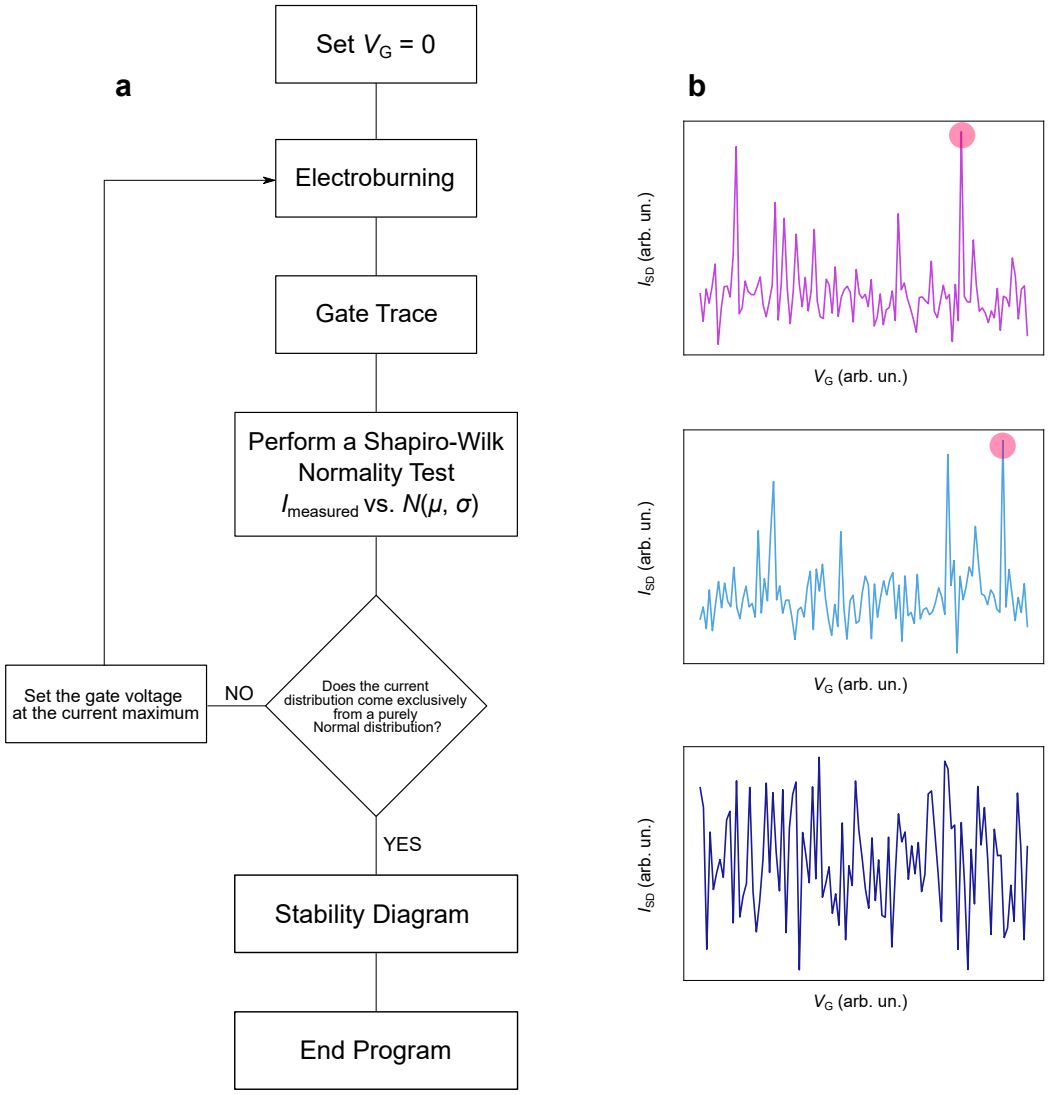


Figure 3.4: Gate-controlled feedback electroburning routine. **a**, Block diagram for the program as implemented. **b**, Gate trace examples as they are extracted at various stages of the routine. Usually a 0.4 V bias is applied during during the gate trace scan. Top graph reports an average gate trace taken at the end of a first electroburning cycle. The program then reads the maximum of the current (red circle), set the gate output channel of the ADwin to that corresponding potential, and starts a second electroburning protocol. When the distribution of the current data passes the Shapiro–Wilk statistics test (bottom graph), the null-hypothesis of the test is accepted (H_0 = the population of the current data is normally distributed), and the program performs a final stability diagram and save all the data in suitable format.

data, it is possible to separate the relevant steps from the background noise by evaluating the null-hypothesis for a normality test and counting only if the heights of the related conductance steps exceed a predetermined threshold.

3.5 Contacting Graphene Nanoribbons

The problem of connecting GNRs, or any molecular adduct, to a pair of electrodes is one of the greatest challenges to the development of reliable and robust electronics. As described in Ch. 2, when graphene is contacted with metals, the large difference between the two work functions would produce huge Schottky barriers at the metal–graphene interface.

Liquid-processable GNRs offer a step forward in terms of structural integrity and edge shape. One of the major hurdles to the usage of ribbons in solutions is the positioning of such structures on top of a device. When a drop of solution, even if poorly concentrated, is deposited on a chip, a number of competing events occur.

To begin, while still suspended in the solvent, GNRs will be subjected to two opposing forces. The solvent molecules will try to maximise the number of electrostatic contacts, and hence the number of solvent molecules adsorbed on ribbon surface, thus resulting in a flat strand, but intramolecular forces will bend up the nanoribbon. Furthermore, when a ribbon tries to fall on top of the electrode pairs, two conflicting mechanisms are at work. The anchoring of the ribbon with the leads will be preferred from a thermodynamic aspect if the free energy released after the creation of the anchoring bonds is larger than the energy required to keep the ribbon in solution. Second, if the solvent evaporation rate is too quick, the thermodynamic regime will not be achieved, and it will be more likely that molecular aggregates will be formed on top of the device surface, resulting in poor device yields (see al Sec. 3.6).

The problem of a graphene nanoribbon landing on a pair of electrodes separated by a gap is analogous to a well-known problem is geometric probability called the Buffon's needle. The Buffon's needle problem, first proposed in the eighteenth century, estimates the likelihood that by randomly tossing a needle of length l this will touch at least one line of a group of parallel lines separated by a distance $d > l$.

Even if no interactions between the needle and the grid are assumed, the problem captures the core of our experiment. The probability that the needle intersects at least one line can be computed analytically in the limit where $\lambda = l/d > 1$ [224]

$$P(\lambda) = \begin{cases} \frac{2\lambda}{\pi} & \lambda \leq 1 \\ \frac{2}{\pi}\left(\lambda - \sqrt{\lambda^2 - 1} + \sec^{-1}(\lambda)\right) & \lambda > 1 \end{cases} \tag{3.1}$$

When λ is smaller than zero (Fig. 3.5), the coverage probability grows linearly with

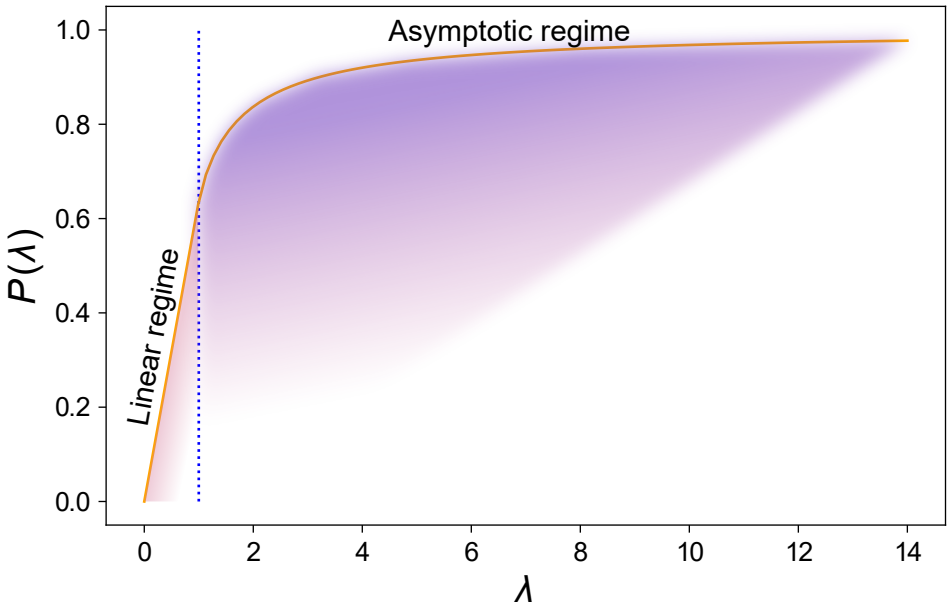


Figure 3.5: Probability distribution as a function of the parameter λ for a needle tossed onto a grid of equispaced parallel lines. When the needle is short ($\lambda < 1$), the coverage probability increases linearly with the length. When the needle becomes larger than the gap ($\lambda \geq 1$), the probability increases asymptotically to one and is independent of the parameter λ.

the length of the ribbon. This conclusion can be simply explained by observing that for a fixed grid-spacing distance, using increasingly longer ribbons increases our chances of successfully crossing a graphene nanogap. However, expanding the ribbon length forever is not recommended because the crossing probability drops below one for ribbons much longer than the grid spacing. This would result in a device surface covered in ribbons arranged in random directions, with many ribbons covering the same surface area, and increasing the odds of obtaining ribbon adducts and

aggregates. This regime may be sufficient for the fabrication of field-effect transistors, but it should be avoided if the goal is to produce single-electron transistors with only one ribbon bridging the nanogap. These straightforward and intuitive ideas have recently been confirmed by AFM and electrical transport measurements [225].

3.6 Deposition Process and Related Phenomena

A pivotal aspect of device fabrication pertains to the multifaceted interactions that ensue when a molecular adduct is translocated onto specific substrates [226, 227]. The expansive and intricate physics exhibited by graphene nanoribbons (GNRs) on substrates where they are directly grown are yet to be replicated when ribbons are transferred onto electronic devices. It is within this context that I submit the necessity for a more nuanced examination of the deposition landscape, a move I consider integral to the enhancement of device yield and reproducibility. To this end, I embarked on a qualitative exploration of the effects various deposition techniques have when a solution of liquid-processable nanoribbons is dropcasted onto the substrate. In this instance, the substrate is a chip adorned with shaped gold and graphene pads.

Prior to the dropcasting onto the substrate, GNRs were initially diluted in an organic apolar solvent. The choice of apolar solvents was driven by the desire to avoid unwanted charge-doping effects on graphene sheets. My preference veered towards toluene, chloroform, and tetrahydrofuran (THF) for this purpose, guided largely by suggestions from our collaborators who synthesised the GNRs I utilised and by the insights of Dr Xuelin Yao. I also ventured into using solvents with higher boiling points, such as 1-phenyloctane, grounded in the understanding that the deposition process is significantly influenced by the interactions formed between the ribbon and the diverse surfaces on top of the chip.

In order to foster favourable π–π^* interactions between the graphene leads and a singular GNR strand, a thermodynamic equilibrium should be encouraged. Specifically, this equilibrium exists between the amount of substance i adsorbed on the electrode per unit area, denoted as Γ_i, and its presence in the bulk, which is the

ribbon in the solvent. This equilibrium is preferable over kinetic-related processes, which include mass transfer by migration and diffusion.

An estimate of these interactions is provided by first-principle calculations where different anchoring groups such as pyrene and hexabenzocoronene were tested [222]. Approximately, the interaction between a graphene sheet and a pyrene molecule was calculated to be 26.3 meV/atom. The large-width limit for the binding interaction between two graphene sheet reports ranges within this estimate: 10–30 meV/atom for a stacking of type AA with an interlayer distance of 3.3 Å, and 18–23 meV/atom for AB-type stacking [228].

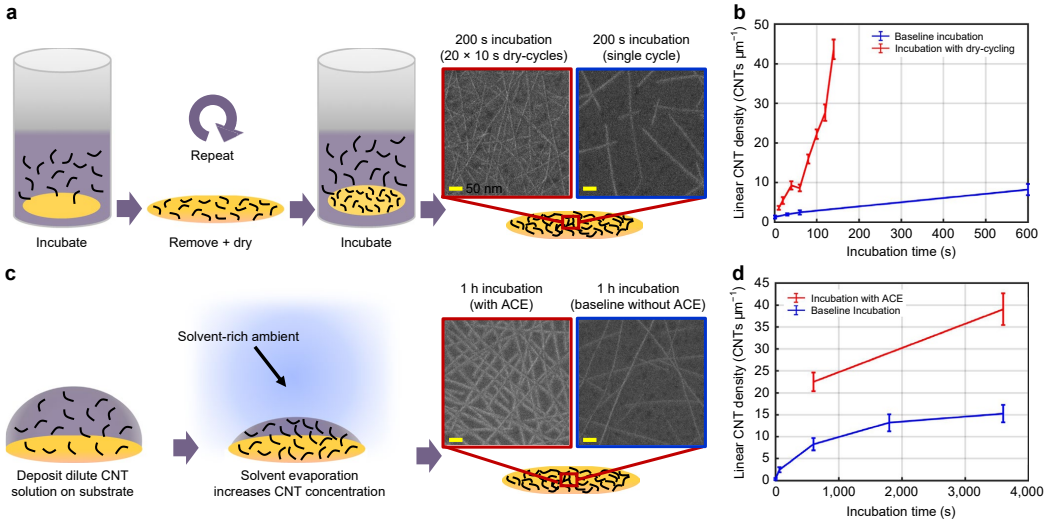


Figure 3.6: **a**, Cartoon of the dry-cycling process. After a short period of incubation (10 s), the substrate is removed, dried, and reintroduced into the CNT solution. This process is repeated for at least 10 times. **b**, Comparison of deposition rates for baseline incubation (single-cycle deposition) and dry-cycling incubation. This corresponds to a 1.5-fold increase in linear density and a $> 1,000$-fold increase in speed in comparison to the baseline incubation. Error bars indicate the 97.5% confidence interval. **c**, Cartoon of artificial concentrated evaporation (ACE). A low-concentrated GNR solution is deposited onto the substrate which is incubated in a solvent-rich environment. As the solvent evaporates, GNRs solution increases. **d**, Comparison of the linear density attained during ACE incubation versus the initial incubation. After $\simeq$ 1h, ACE achieves a 2.5-fold increase in density relative to the initial incubation at the same CNT stock concentration. Error bars depict the 97.5% confidence interval. Adapted from [229].

The deposition strategy we adopted to fabricate GNRFETs was inherited from the CNT literature and is known as *dry-cycling* incubation [229]. The technique

leverages the Frumkin isotherm to limit the GNR desorption in favour of a faster deposition rate. The substrate is submerged in a GNR solution and incubated for 10 s seconds, leveraging the fast, linear deposition regime outlined in Fig. 3.5. After removing it from the solution, it is washed with IPA and gently blowdry with nitrogen. This *single-cycle* incubation is repeated several times. Fig. 3.6b shows the CNT linear density together with control samples, and put in evidence the higher surface coverage ($\simeq$ 45 CNT/µm after 150 s).

In addition to slowing the desorption rate, increasing the rate of adsorption is complementary to the dry-cycling method. In order to achieve this, and according to the chemical equilibrium principle, evaporation of the solvent would be slowed down when this evaporates in a gas-phase-rich atmosphere. With this method, also known as ACE (Fig. 3.6c,d), the solvent evaporates gradually from the solution over time, increasing the concentration of GNRs above the initial concentration. Importantly, the rate of solvent evaporation is crucial for uniformity because sliding during rapid droplet evaporation generates *coffee ring* effect, resulting in non-uniform deposition throughout the substrate [230].

CNTs, lauded for their remarkable chemical and physical properties, have garnered significant interest across numerous fields of application. However, their potential is somewhat tempered by the considerable challenges associated with their processing. The hydrophobic nature of CNTs, their incompatibility with the majority of solvents, and a proclivity towards agglomeration underline these challenges (see also Ch. 2). The quality of CNT samples, contingent on the judicious selection and control of synthesis parameters, remains only partially within researchers grasp.

While the uniformity of CNTs, the integrity of their walls, and their purity are essential for harnessing their properties, these aspects necessitate further refinement. Persistent heterogeneities in CNT samples, encompassing carbonaceous species, impurities, defects, variations in diameter, chirality, morphology, and bundling, represent significant impediments to universal behaviours and efficient processing methods. The vast surface area of nano-scaled particles contributes to the CNTs'

tendency to form agglomerates, demanding innovative and optimised chemical treatments and processes.

Comparably, molecular graphene nanoribbons present their own unique set of processability challenges. Foremost amongst these is the need to work with low concentrations to avert aggregation, a delicate equilibrium as an excessive quantity of MGNRs can instigate clumping, thereby compromising their advantageous properties. Furthermore, the inability to ascertain the molecular weight of MGNRs complicates concentration measurements, necessitating the use of relative concentrations instead of molar concentrations, which introduces a further degree of uncertainty into the experimental design.

Dispersion of MGNRs presents an additional challenge, particularly for nanoribbons lacking bulky groups along their edges. Here, sonication at extremely low concentrations becomes a necessity as mere mechanical agitation often fails to achieve a desirable dispersion of the nanoribbons, necessitating the deployment of ultrasound to ensure a more uniform distribution within the solvent.

The deposition of MGNRs introduces a further set of challenges, notably the propensity of MGNRs to leave a distinctive "coffee ring effect" on the substrate, which can compromise device functionality. This issue was mitigated through the adoption of the dry-cycled approach, a strategy gleaned from the literature on carbon nanotubes.

Finally, the introduction of bulky groups is facilitated through a Diels–Alder reaction, which is reversible, as described by equation 3.2.

$$\mathrm{MGNR-Anthracene} + \mathrm{Maleimide} \underset{k_{-1}}{\overset{k_{+1}}{\rightleftharpoons}} \mathrm{MGNR-Maleimide}, \tag{3.2}$$

This reversibility necessitates careful temperature control to prevent the reaction from shifting in the reverse direction. Specifically, if the solution is heated to close to 100°C, the reaction rate accelerates significantly, while maintaining the temperature at approximately 80°C for a prolonged period encourages the reverse reaction. Therefore, to expedite solvent evaporation post-deposition while avoiding heating,

solvents with lower boiling points, such as tetrahydrofuran (THF) and toluene, were preferred over 1-phenyloctane or 1,3,5-trichlorobenzene. The meticulous management of these processability issues was thus key to optimising the synthesis and manipulation of MGNRs.

3.7 Cryogenic-Temperature DC Transport Setup

Transport experiments at mK temperatures were performed in a Triton 200 Oxford Instrument dilution refrigerator equipped with a 3D vector rotate magnet (VRM). The schematic of the instrumentation is outlined in Fig. 3.7. The operation principles can be found in the dedicated manual provided by the Oxford Instruments. The DC electronic system makes use of a low-noise home-made equipment, which is controlled using the Python interface QTlab (Fig. 3.8). Digital values from a desktop computer are sent into an optical signal generator, which produces a serial input for the digital-to-analog converter (DAC), which generates and reads voltages (bias V_{SD} and V_G). The four accessible DACs each have a 16-bit resolution and can read/write voltages between $\pm 2\,V$. Higher voltages are managed by using a high-impedance voltage source. The entire unit is battery-powered to provide complete isolation from the main source of electronic noise, and the switch box provides simple switching between different devices, as well as protection agains electronic discharge (ESD) that can permanently damage the sample (Fig. 3.10). Input signals from the switch board are routed through the measurement electronics before entering the fride. After passing through a series of low-pass filters (Fig. 3.9), the current is cooled by two sapphire heat sinks on the PT2 plate and two on the MC plate. An RC filter, a meandering-line copper powder filter, three LC filters, and another RC filter are included. The input signals are then routed to the sample through a 48-wire NanoD connection. The sample chip is wire-bonded to a 48-pin chip holder (Fig. 3.10b), which is mounted on a home-made printed circuit board.

The DUT source–drain current travels in reverse order via the specified components until it reaches the current amplifier (Fig. 3.8), which can amplify

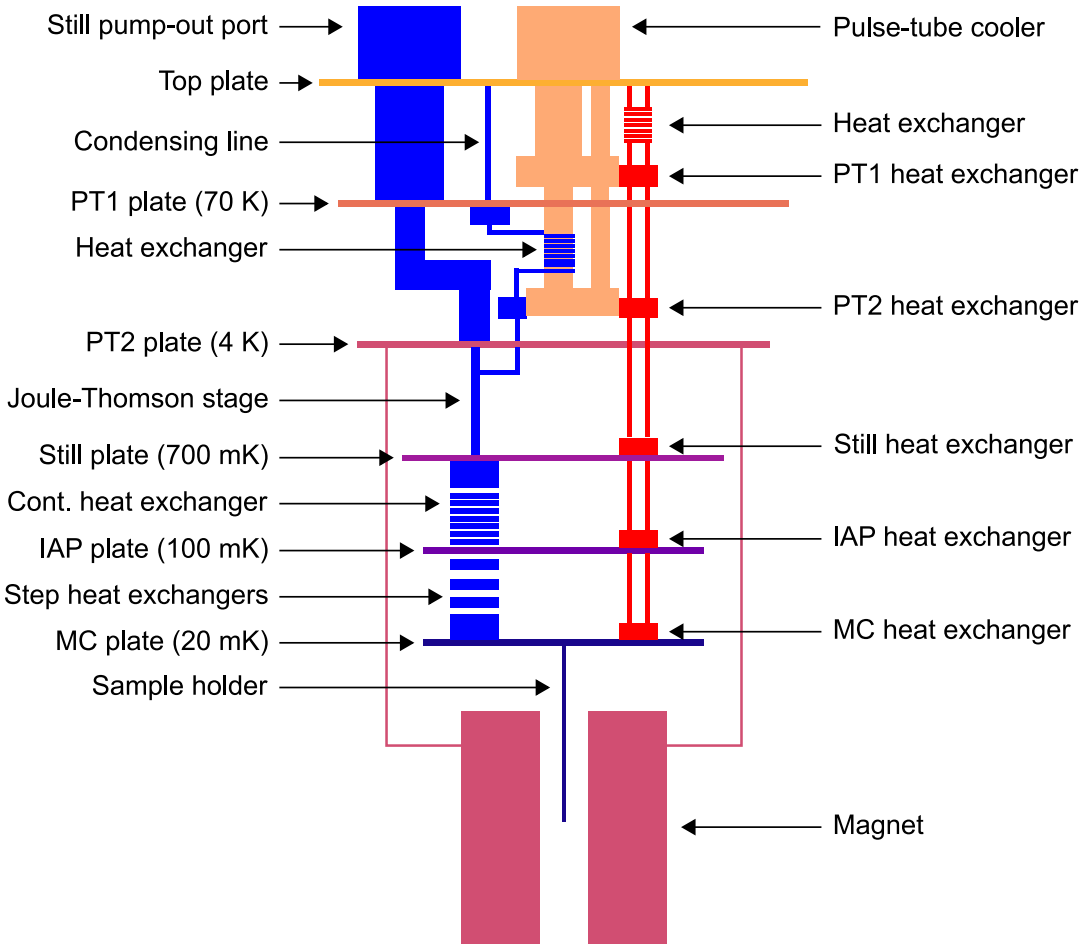


Figure 3.7: The Triton 200 schematics. The pulse-tube cooler is shown in orange, the pre-cool circuit in red, and the dilution circuit in blue. The different plates and their temperatures are also shown. The magnet (violet) is heated by the PT2 plate. Adapted from the Triton User Manual, courtesy of Oxford Instruments.

and monitor currents with noisefloors as low as $5\,\mathrm{fA\,Hz^{-0.5}}$ (at $1\,\mathrm{GV\,A^{-1}}$). The amplified output is then supplied into an Alazar data acquisition board (model ATS9440) via a coax wire, with the sampling rate set to 100 MS$^-$1 throughout the most portion of our experiment. The QTLab interface specifies an integration time t_{int} during which the Alazar card samples the source–drain current before computing and storing the average.

It is necessary to emphasize that the voltages read by the Alazar card are inaccurate. This is likely due to the input impedance setting, which causes the voltage to drop. To overcome this, a calibration curve (Fig. 3.8b) was constructed

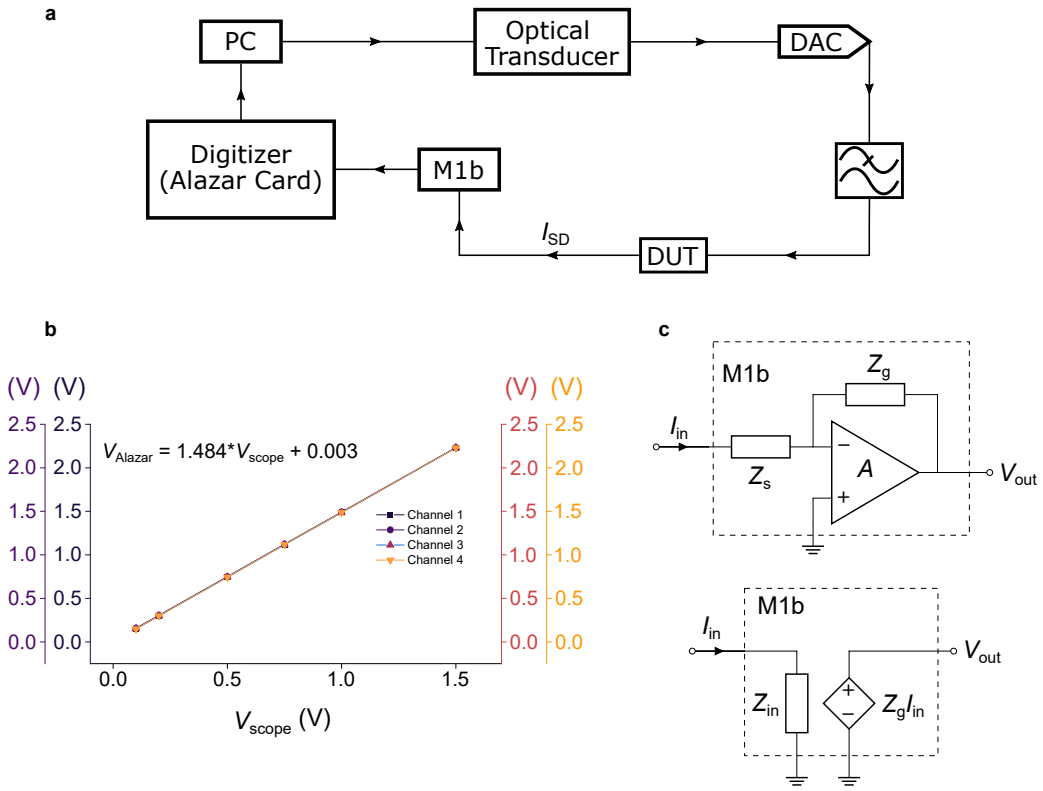


Figure 3.8: **a**, Schematic view of the DC electronics setup used in cryogenic transport. The low-pass filters before the DUT encompass RC with cutoff frequencies f_T between 5–11×10^3 Hz, Cu powder ($f_T \simeq 100$ kHz), and LC filters. **b**, The Alazar card four channels have been calibrated against known voltages output from an oscilloscpe (scope for short). **c,top** Current-to-voltage simplified schematic and its equivalent circuit **c,bottom**. For the M1b adopted in our setup, a manual dial allows changing Z_g between 1–1×10^3 MΩ.

by measuring known voltages with both the Alazar card and an oscilloscpe. All the numerical data presented in this thesis have been rescaled by using analogous calibration curves.

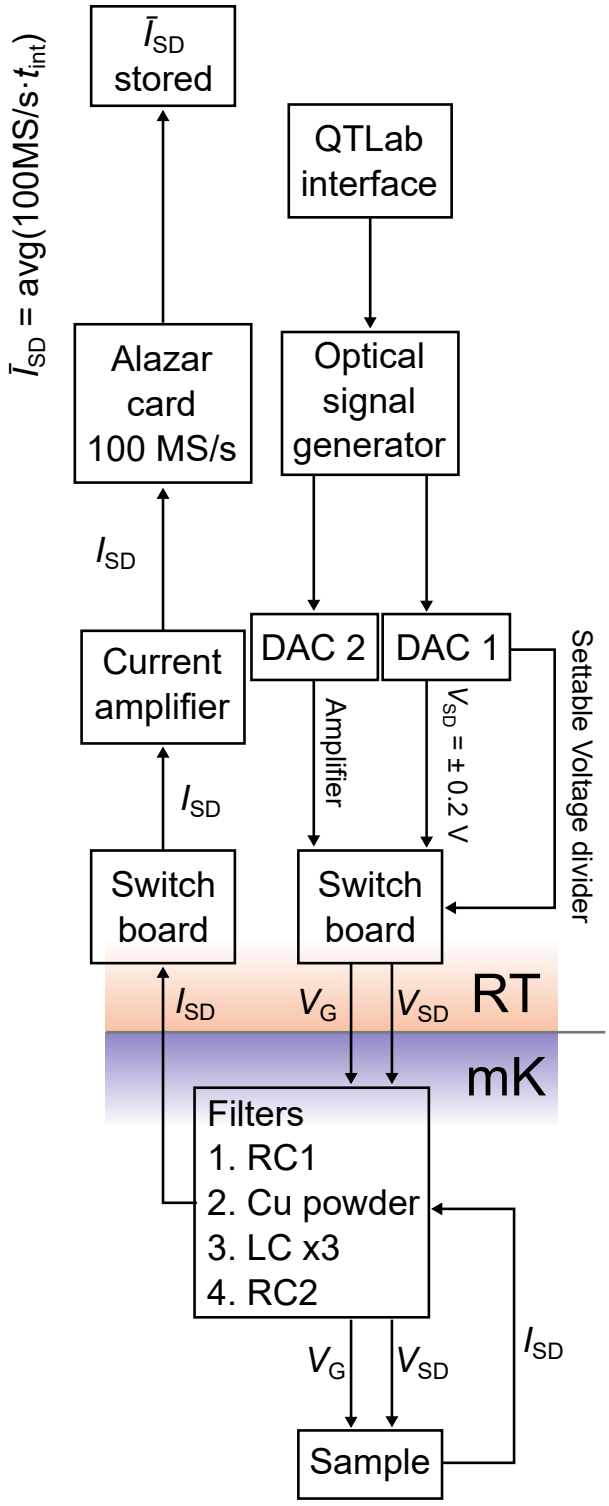


Figure 3.9: Schematic view of the DC electronics setup for mK transport spectroscopy. Adapted from [231].

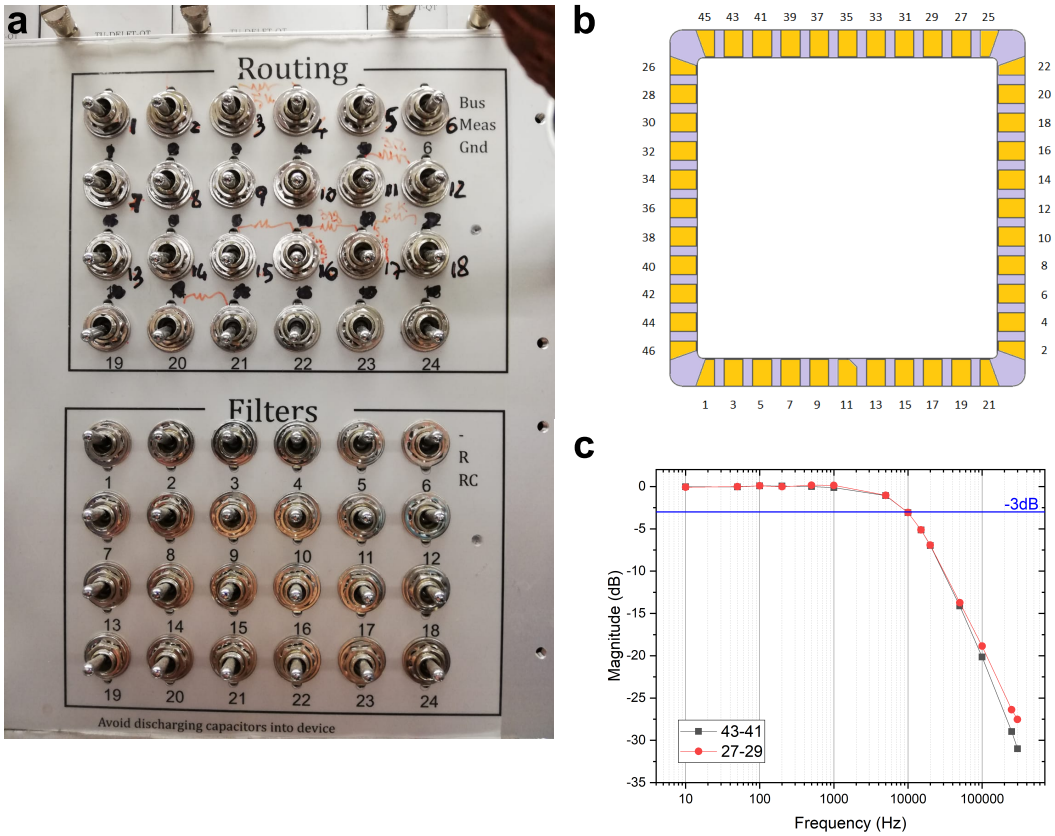


Figure 3.10: **a**, Breakout box of DC connections. A second breakout box is used for connections from 26 to 48. **b**, Chipholder schematic with each connection numbers: pin 11 is used to orientate the chip in the correct direction. **c**, Frequency test. Powder (Cu) and RC filters set frequency operation limit theoretically up to 10 kHz. In practice I experimentally observed a statistical significance degradation of the signal already at 5 kHz.

4

Instrumentation Development

In this chapter, I describe further improvements to the existing setup (Ch. 3) I have, partially or entirely, accomplished. I will first describe the measurement protocol implemented to continuously acquire data from mK to room temperature, and then take a look at how to integrate a lock-in amplifier with our electrics. I conclude the chapter with the fabrication and the testing of micro-Hall sensors made in gold and graphene.

I personally engineered and implemented through dedicated python code the temperature-dependent protocol. Additionally, I was responsible for the setup of the alternating current measurements, which included developing a custom driver for the SR 860 Lock-in amplifier.

The micro-Hall sensors made of gold and graphene were instead fabricated by Dr. Alex Gee. I took the initiative in devising both the experimental setup and the acquisition schemes. These were designed to accommodate experiments conducted with either dual lock-in amplifiers or a single amplifier, by adapating the measurement protocol I had already developed for differential conductance measurements.

4.1 Temperature-dependent Protocol

Although dilution refrigerators are mainly used for cryogenic measurements, it is possible to measure at temperatures outside the working temperatures of the still and mixing chamber heaters. This mode of operation is, however, highly non-trivial and at the same time essential to measure continuously the same device from mK ideally up to room temperature. Since there is no well-defined experimental procedure, I implemented a simple, but effective workaround.

Triton heaters are able to precisely control temperatures from base temperature ($T_{\text{base}} \simeq 20\,\text{mK}$) up to 30 K. To stabilise the temperature above this range, one must establish a thermal link between the sample and the surrounding environment. However, this thermal link must be not too strong or otherwise the fridge would warm up to quickly, hampering any reliable measurements to be taken.

Algorithm 4.1 Triton High Temperature Measurement

Require: Initialise Alazar, Triton and IVVI
Ensure: Alazar, Triton, and IVVI are global

```
Initialise Final Temperature
Initialise Bias Array
Initialise Target Temperatures Array
Current Temperature ← Read Temperature
Temperature Step ← 3
Temperature Channel ← RuO2
Precooled ← False
while Current Temperature < Final Temperature do
    Precooled ← True
    T ← Read Temperature
    if T > 1.5 then
        Temperature Channel ← Cernox
    end if
    for length Bias Array do
        Run Gate Trace Measurement
    end for
    T ← Read Temperature
    if T is in Target Temperatures Array then
        Precooled ← False
        Run Stability Diagram
    end if
end while
```

Once the temperature is brough to approximately 30 K by controlling the mixing chamber and the still heaters, these are turned off to prevent thermal energy to be excessively exchanged. Since the mixing chamber is extremely-well thermally isolated from the other fridge parts (operating pressure inside the fridge is $P_{\text{fridge}} \simeq 2.5 \times 10^{-4}$ mbar), temperature drift is slow: 24 hours after the heaters are turned off, temperature raises from 30 K to 32 K. The thermal link between the mixing chamber and the other fridge components is realised by filling the pre-cooling loop with the He_3/He_4 mixture: tipically, the fridge takes about 72h to reach room temperature.

The software application I implemented initialises the Alazar, Triton, and the electronic measurement drivers, and assigns them to global variables that retain their states during the execution of the application. Precool-loop variables are Triton-driver commands that enable direct control on the precool loop operation. Below 1 K, the RuO_2 thermometer is used to reliably measure the temperature, while the Cernox thermometer must be used when $T \geq 1$ K, hence the temperature-channel variable is set accordingly within the while loop if the threshold temperature $T = 1$ K is met. When a target temperature is reached, the thermal link between the sample chamber and the fridge is destroyed by emptying the precool loop; after the temperature is stabilised, the application acquires electrical measurements, such as I_{SD}–V_{SD} and I_{SD}–V_{G}. The algorithm designed and implemented in Python language is detailed in Alg. 4.1

4.2 AC Measurements

Although the measured cryogenic setup noisefloor level is a tenth of pA, the intrisic $1/f$ noise represents an instrinsic and important hurdle in any DC experiment. As I saw in Sec. 2.4.2, the central quantity in an electron transport experiment is the tunnelling density of states, which is ultimately related to the derivative of the current in a I_{SD}–V_{SD} experiment. Numerically retrieving the two-terminal conductance may introduce noise due to current fluctuations; this picture gets even further complicated in our devices, where abrupt shifts in the stability diagrams are

likely to happen becuase of charge jumps that occurs during the acquisition. A great

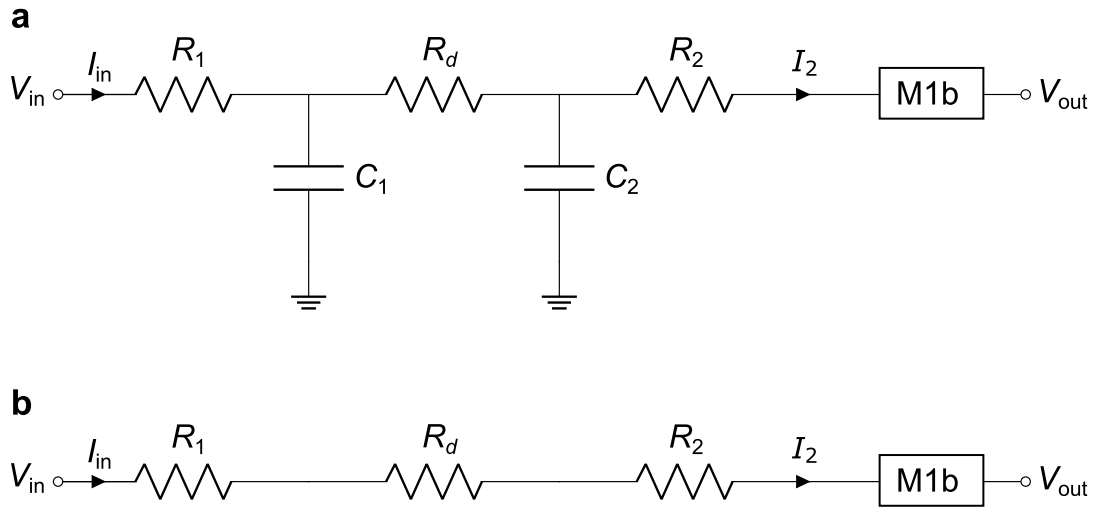


Figure 4.1: **a**, An example of circuit diagram of a voltage-biased sample R_d in series with two RC filters and measured by a current-to-voltage (M1b) converter. **b**, Because the device resistance is finite and the operating frequency is well below the DC lines bandwidth, it is assumed that capacitors' frequency response plays no role. Adapted from [232].

deal of information about the theory and tips of integrating a lock-in amplifier with low-noise electronic equipments can be found here [232] and in the setup developed here [233]. Here I briefly report and comment salient points that I have employed to successfully integrate a standard SR-830 lock-in with our electronics. Same concepts were later applied for integrating two Zurich Instruments lock-in amplifiers as well.

4.2.1 Integration of Lock-in Amplifier with High-Sensitivity Electronics

With a lock-in detection scheme, an oscillating voltage $V_{\mathrm{osc}}(f)$ is superimposed to a DC signal in order to produce an oscillating current $I_{\mathrm{tot}}(f) = I_{\mathrm{DC}} + I_{\mathrm{AC}}(f)$. The $1/f$ noise is suppressed outside a narrow band $f \pm \tau^{-1}$, where τ is the integration time. The lock-in frequency f must also not sit at a harmonic of the square wave of the main grid as this will also give an incorrect resistance value. Tipically, to check

a suitable lock in frequency, it is reccommended to run a power noise spectrum check over the entire frequency domain one intend to explore.

Compared with DC, alternating current (AC) conductance measurements can introduce errors on the scale of 10 points percent of the total signal, because the technique is susceptible to aberrations originating in the complex domain. Therefore, it is advisable to take extra caution if accurate conductance values are required. More loosen conditions can be considered, on the contrary, if qualitative features are desired, rather than accurate values. Fridge lines are filter with

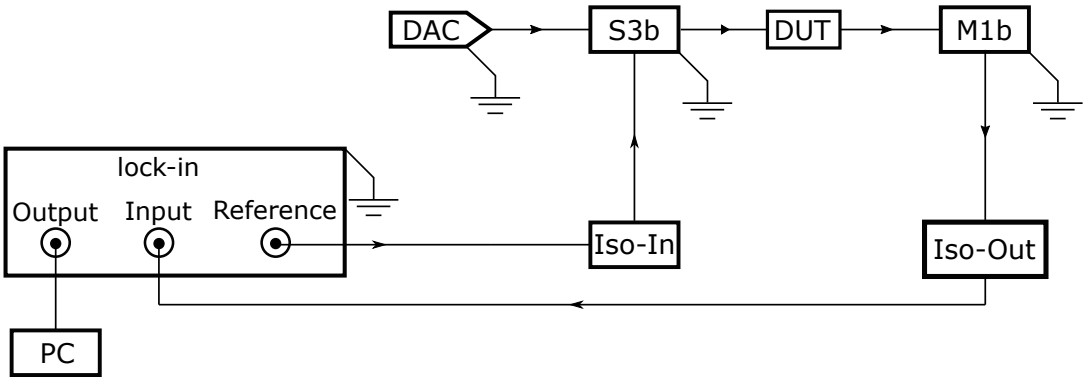


Figure 4.2: AC electronics setup. The oscillating signal is superimposed on a DC-only signal originating from the DAC and sent into the S3b voltage/current source module through the iso-amplifier input. Note that a 0.01 factor is introduced by the S3b control input to allow the superposition of a frequency-modulated signal on top of a dc-sweep. [234].

RC and Cu powder filter. At finite frequency $\omega = 2\pi f$, each circuit component response has to be modeled in the complex plane. As long as all the k capacitors active across all the stages within the fridge do not draw any current, i.e. $R_i \ll 1/(\omega C_k)$ where the subscript i denotes the number of resistance, it is safe to exclude any parasitic components when one attempts to recover the resistance value for the device under test.

This general rule might be thought as the requirement to work with oscillating voltages way below that the cut-off frequency imposed by the filters, namely:

$$f \ll f_{\text{cutoff}} = \frac{1}{2\pi R_i C_k} \tag{4.1}$$

As I have discussed previosuly (Fig. 3.10c in Ch. 3), the cut-off frequency set by our setup is around 1 kHz, even though the −3 dB point lies around one order of magnitude higher. The finite-frequency efficiency and response of the DC lines is, however, not the only factor that one has to take into account when adopting AC techiniques. Because of its narrow bandwidth of approximately 200 kHz, the

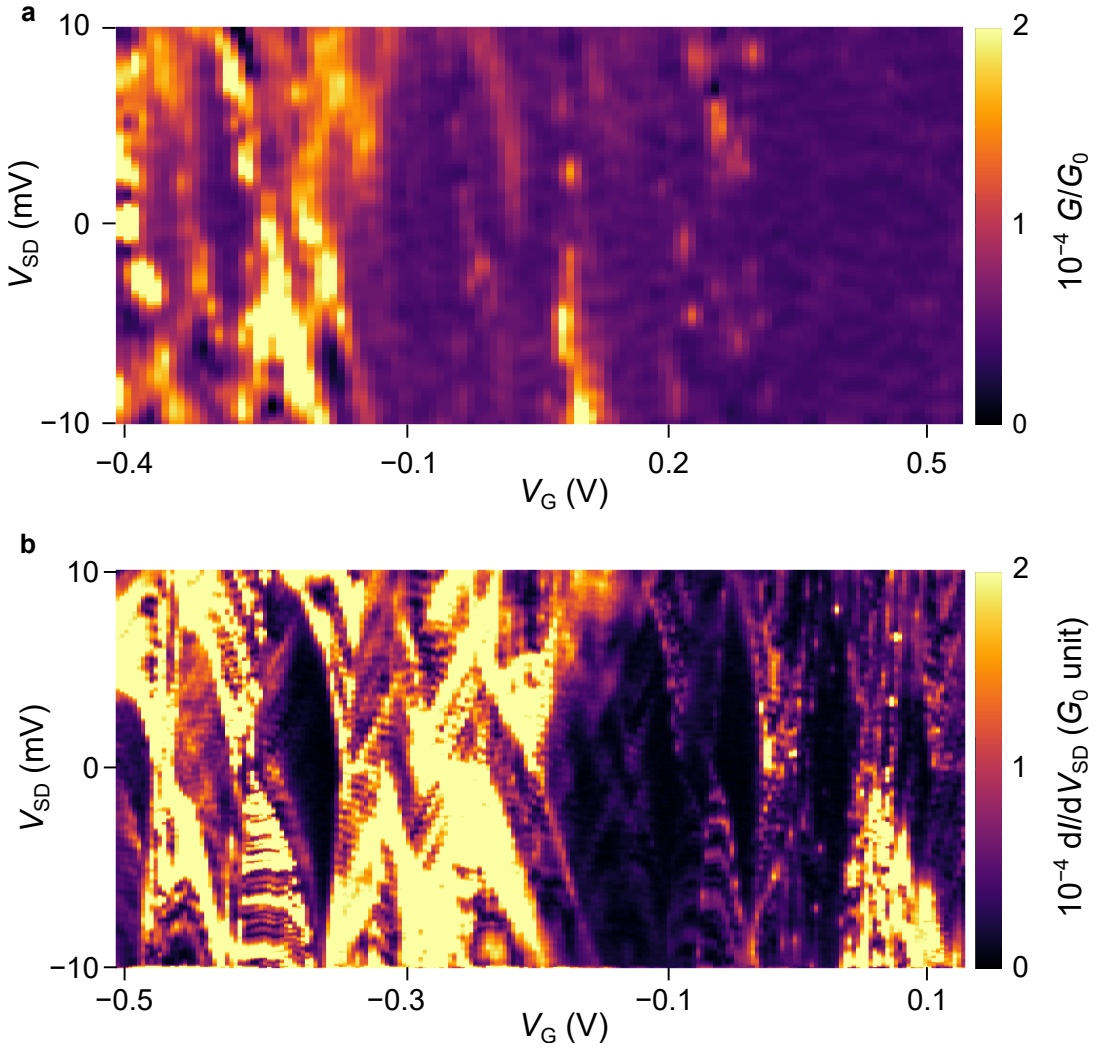


Figure 4.3: Comparison of **a**, DC and **b**, AC stability diagrams acquired for the same device at $T = 20$ mK. The lock-in excitation voltage felt by the device was $V_{osc} = 100\,\mu V$ whereas the sensistivity and the time constant were set at 200 mV and $\tau = 0.5$ s, respectively.

low-noise current amplifier used in our setup (Fig. 4.1) is especially susceptible to lock-in finite-frequency problems as well: the design objective is to minimise the

operating current, hence reducing risk of back-action into sample. Nonetheless, this constrains the operating frequency to approximately 30 kHz[†]. When this condition is not met, one must consider only the features of the measurement results and not their exact values.

In our setup Fig. 4.2, the isolated-amplifier input module is not coupled with the DAC by default. Thus, after having backwired that, the lock-in output is fed into the isolated amplifier of our electronics and and then fed to the sample. The signal was then locked at the proper frequency and phase-adjusted before being supplied to the desktop computer via usb or ethernet cable.

Experiment routines were implemented into the existing setup by instantiating a lock-in instance and integrating it into the superclass station, which contains instances for all the other required instruments. In Fig. 4.3 I compare the charge stability maps of the same device acquired in DC (top) and using the lock-in (bottom) using equivalent integration times.

4.3 Micro-Hall Devices

The ability to fabricate, control, and manipulate the properties of magnetic structures [235] has not only led to the discovery of several new physical phenomena [236–238], but also to the development of a large pool of experimental techniques for studying such structures [239, 240]. In this regard, micro-probe magnetometry based on the Hall effect is of particular interest. It offers high-field sensitivity even when the dimensionality shrinks down to the nanoscale, has excellent operating ranges in terms of temperature and magnetic field, and it is non-invasive.

4.3.1 Technical Background

In order to measure the conductivity σ of a semiconducting sample in presence of negligible gradients of carrier densities, one has to take into account both the

[†]The Zurich Instruments lock-in contains a built-in functionality that allows frequency sweep while monitoring the voltage noise calculated in $\mathrm{nV\,Hz^{-0.5}}$ for a given lock-in measurement bandwidth.

electrons concentrations n and mobility μ_e and the same quantities for holes, namely:

$$\sigma = |e|(n\mu_e + p\mu_h) = \frac{\vec{J}_{\text{drift}}}{\vec{E}}. \tag{4.2}$$

For a sample on a plane, if a magnetic field B is applied along the $+z$ direction, while current is flowing along the $+x$ direction, charge carriers will experience an average force in the $(-y)$ direction, i.e.

$$\vec{F_e} = +|e|\vec{E}\mu_e B_z \quad \text{for electrons,} \tag{4.3}$$

$$\vec{F_h} = -|e|\vec{E}\mu_h B_z \quad \text{for holes} \tag{4.4}$$

Because electron ($\vec{v_e} = \vec{E}\mu_e$) and hole velocities are in opposite directions, the two forces are in the same direction. When these are unequal, the surfaces along the $\pm y$ of the sample become charged and a potential difference arise between them. The appearence of this voltage is the Hall effect, and was discovered in 1879 by Edwin H. Hall. The transverse electric field E_y builds up until the transverse force due to

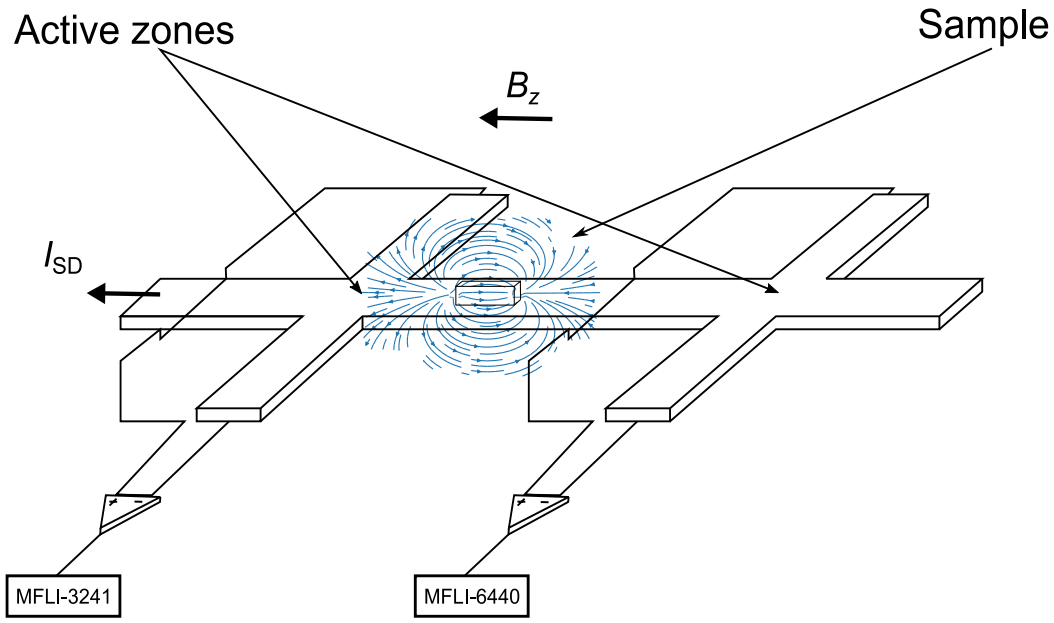


Figure 4.4: Cartoon of a micro-Hall sensor. Current flows along the central wires, while the sample sits on one of the two crosses. The sample is placed slightly offset compared to the crossposition as the magnetic field is less shielded by the gold surface. The signals are then measured in parallel by feeding first the voltage drops to two pre-amplifier and later to lock-in amplifiers.

it becomes equal and opposite to the force due to the magnetic field. When this happens, the stationary condition $eE_y = ev_xB_z$ allows to define the Hall voltage as:

$$V_{\mathrm{H}} = wE_y = v_xB_z = \frac{j_xB_z}{ne} \tag{4.5}$$

where w in this case is the width of the semiconducting material, j_x is the component along x of current density and n is the charge carrier density. Considering that $j = I_{\mathrm{SD}}/wd$ where d is the specimen thickness, the expression may be rewritten as:

$$V_{\mathrm{H}} = R_{\mathrm{H}}I_{\mathrm{SD}}B_z \quad \text{with} \quad R_{\mathrm{H}} = \frac{E_y}{j_xB_z} = \frac{1}{ned} \tag{4.6}$$

The quantity R_{H} is known as Hall resistance and can be regarded by all means to the magnetic sensistivity of a particular probe. Clearly, the higher this values is the smaller field variation could be in principle detected. To be more specific, the minimum detectable magnetic field for a given area is the Hall voltage net of the electrical noise present when the circuit is closed. The noise is predominantly given by Josephson and resistive (telegraph) noise. Due to the pandemic of Covid-19 it has

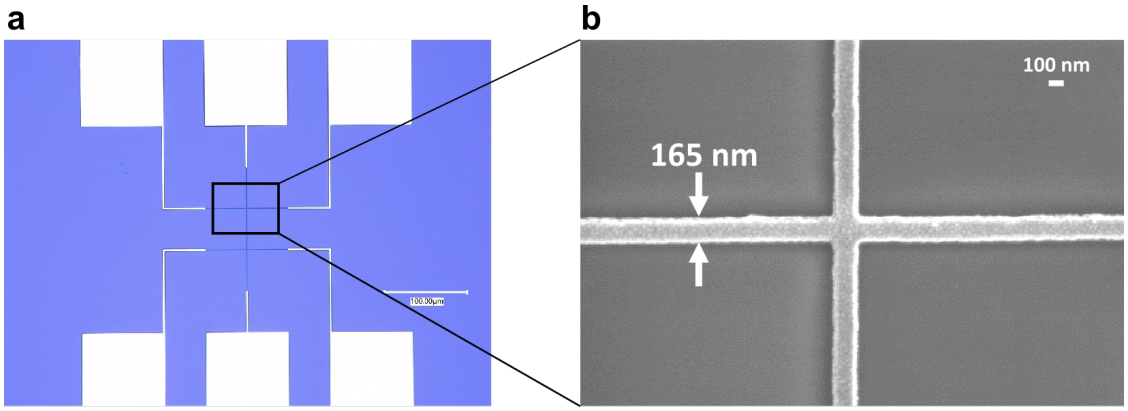


Figure 4.5: **a**, Optical microscope of a double-cross Hall bar fabricated with Au. The distance betwen the two crosses for this particular devices was 50 µm. **b**, Enlargment taken at the SEM of one of the two crosses, with the wire width displayed.

been impossible to find an adequate 2DEG substrate for this project. Nevertheless, I have tried to setup and detect the Hall signal from a Mn_12 microcrystals with a mesoscopic Hall made of Au. The Hall probe configuration with the simplest geometry is the Hall cross. When a magnetic object is placed close to the active

area of the probe, the Hall signal will be proportional to the sum of the external field B and the magnetic stray field that enters the active area from the sample.

4.3.2 Test Measurements

In order to prove the reliability of our apparatus and test its sensitivity, I have performed a few tests by measuring micro-crystals of Mn_{12}-acetate synthesised by Dr Dimitris Alexandropoulos. Mn_{12} is a molecular magnets whose magnetic response is well known in the literature. The coercive field of Mn_{12} at cryogenic temperature is about 6 T, therefore I had to operate and temperatures higher for checking its magnetic response. In order to minimise chances the magnet would increase the temperature while was swept, I have slow sweep rates ranging from 0.83–1.67 $\mathrm{mT\,s^{-1}}$.

We used SiO_2 as substrate where Hall devices with different spacing between the two crosses were used, ranging from 10 µm to 50 µm (Fig. 4.4). The deposition and the correct orientation of the crystals reavealed to be not a negligible challenge and so I choose to use crystal approximately of 50 µm. The transfer process was as follows.

We first spread the Mn_{12} crystals on top of a filter paper in order to remove big chunck of crystals. In particular, molecular monemers present a needle-shape whereas dimers comes in a bulky-ball shape form. I then deposited a few of these crystals on top of a bare silicon substrate, where I also deposited a thin film of high-vacuum grease. I then lowered one of the probe in the probe station setup as described in Sec. 3.3 thanks to the micropositioner. Tungesten probes with a nominal diameter of 10 µm worked best for this purpose. I then gently deposited the grease within the two crosses paying attention specifically to not to damage the electrical connections. The probe was then cleaned, and used to pick up a Mn_{12} crystal with the right lateral dimension, which was then gently lowered on top on the Hall bar device. In order to maximise the dipolar field generated by the sample, the crystal should be perfectly oriented along the central gold pads. The difficulty of aligning the crystal in the desired direction is one of the weaknesses of our approach. Adjusting it by rotating the probe chuck is a viable alternative, but care has to be taken in not damaging the electrical connections. Another source of problem is

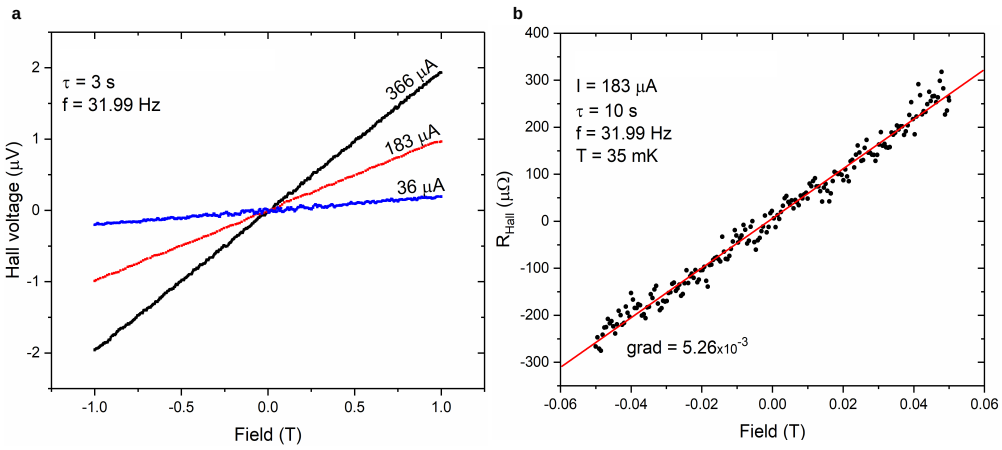


Figure 4.6: **a**, Hall voltage measured across one cross when the current driven is increased. The signal is proportional to the current as expected. The parameters f and τ are the lock-in operation frequency and integration time, respectively. The frequency in particular was optimised by taking a frequency scan the line response and set it to the point of minimum noise. **b**, From the linear fit of the resistance as a function of B I extract the Hall coefficient.

that often the crystal break upon touching the substrate. Although monemer of Mn_{12} should be relatively robust against the forces at play in this scenario, breaks might result as due to grains of crystals attached to each other.

The first test I did was to make sure that the Hall effect was present at varying measurement bias. From Eq. 4.6, the Hall voltage V_H is proportional to the current and the magnetic field and inversly proportional to the carrier density n of the conductor. The first test used only one lockin amplifier since only I was only intersted in the voltage built up across just one cross. Fig. 4.6 demonstrates that V_H is proportional to the current driven through the hall bar. In principle, this means that by increasing the current should lead to higher sensistivity. I report a Hall coefficient of approximately $R_H \simeq 1 \times 10^{-6}\,\Omega G^{-1}$, which is expected for a micro-sensor made by gold and having thickness $d \simeq 1\,\mu m$

Once this test was completed, I mounted a Mn_{12} crystal on the Hall-bar as previously outlined and measured the direction of maximum anisotropy at $T = 2\,K$ (Fig. 4.7). I recorded the voltage difference between the voltage drops at the two

crosses $\Delta_{\text{cross1}-\text{cross2}}$ while the field was rotated of $\theta = 360°$ in the the xy and zy planes. In both cases, the maximum voltage drop difference was found along the same (y) direction, suggesting that only voltage drop detected was the one from the *standard* Hall effect and not from the dipolar field generated by our sample. We further confirmed this hypothesis by measuring the voltage drop across the crosses in the transverse (y) and parallel (z) current directions independetly (Fig. 4.8). The response along y is the classical Hall voltage, whereas along z a well-know magnetotransport effect for Au film takes place. The quadratically dependence I observe for V_{H} means that the resistivity will depend linearly from B^2, as expected by the Kohler's rule [241, 242]. Since the minimum detectable field B_{min} is inversely proportional to the current $B_{\text{min}} \propto 1/I_{\text{SD}}$ (Fig. 4.6), and since it is was not possible to drive high-enough currents[†] through the Hall-bar with because of the Cu-powder and low-pass filters used in the DC lines, I concluded that, despite the successful fabrication and measurement setup, the presence of magnetic scattering in the gold substrate is dominant, preventing the detection of any signal from the crystal with this device.

The past decades have seen the emergence of graphene-Hall-sensor applications [240, 243]. Low-carrier densities and high mobilities should lead to remarkably high magnetic sensitivities and low electric noise. I therefore attempted to investigate the magnetic signal from Mn_{12} with a graphene Hall bar (GHB); I detail the process in the next section.

4.4 Graphene Hall Bars

The low sensistivities resulting from the Hall bars made films of gold depends, ultimately, on (1) the high charge-carrier concentration n, and (2) from the magnetoresistance effect produced when the gold atoms are placed in a magnetic field. Furthermore, misalignments in the sample orientation with respect to the

[†]Additionally, since the device resistance is extremely low, the voltage drop across it will be low too since the current through the wire is large. The result output voltage at the DAC to drop dramatically.

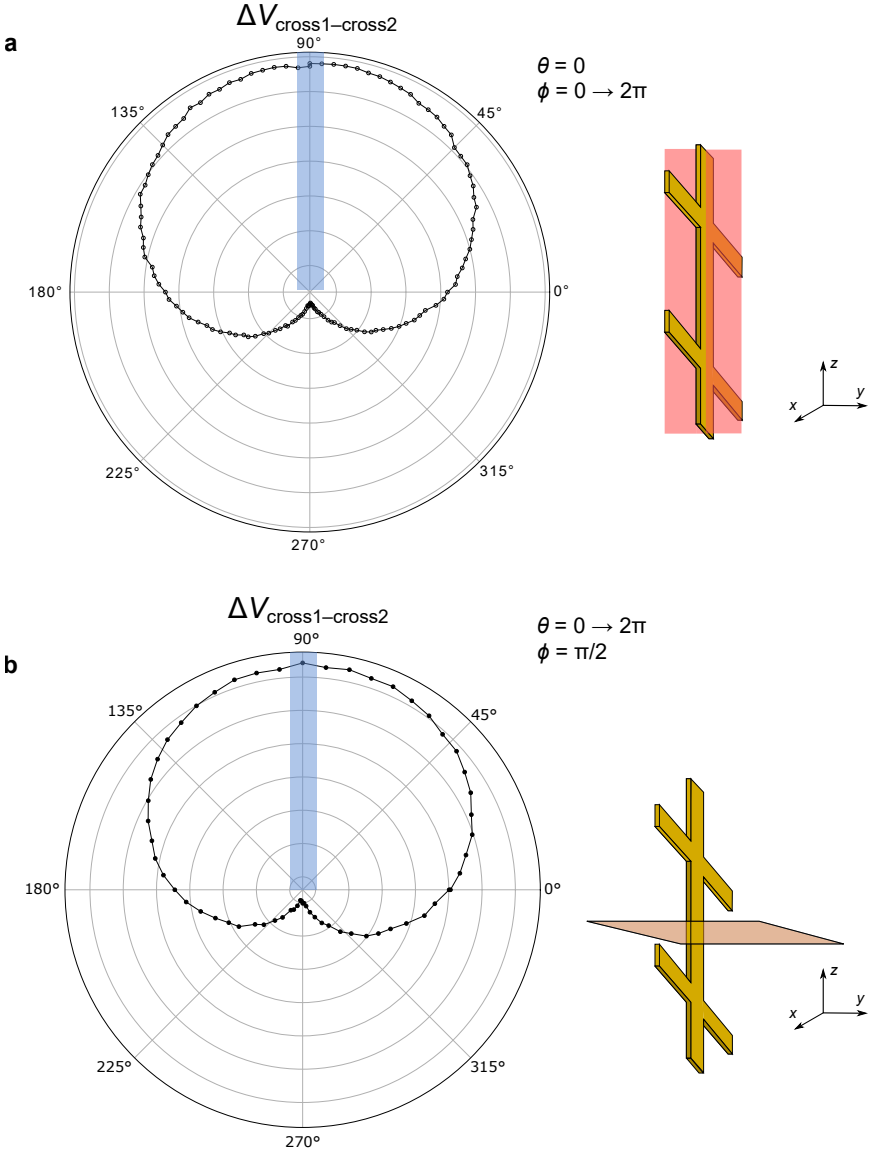


Figure 4.7: **a**, The difference between the voltages build up across the two crosses was recoded thorugh angle-resolved experiments. The direction of maximum signal is highlighted by the blue rectangle and along the y axis, as expected from the Hall effect. On the right, a schematic along which normal-plane the magnet was rotated along. θ and ϕ are the sperhical parameters to input in the routine I wrote. **b**, polar plot of the response for a x-oriented normal-plane. Once again, the region of maximum signal is found when the magnetic field component is perpendicular to the surface of the two crosses.

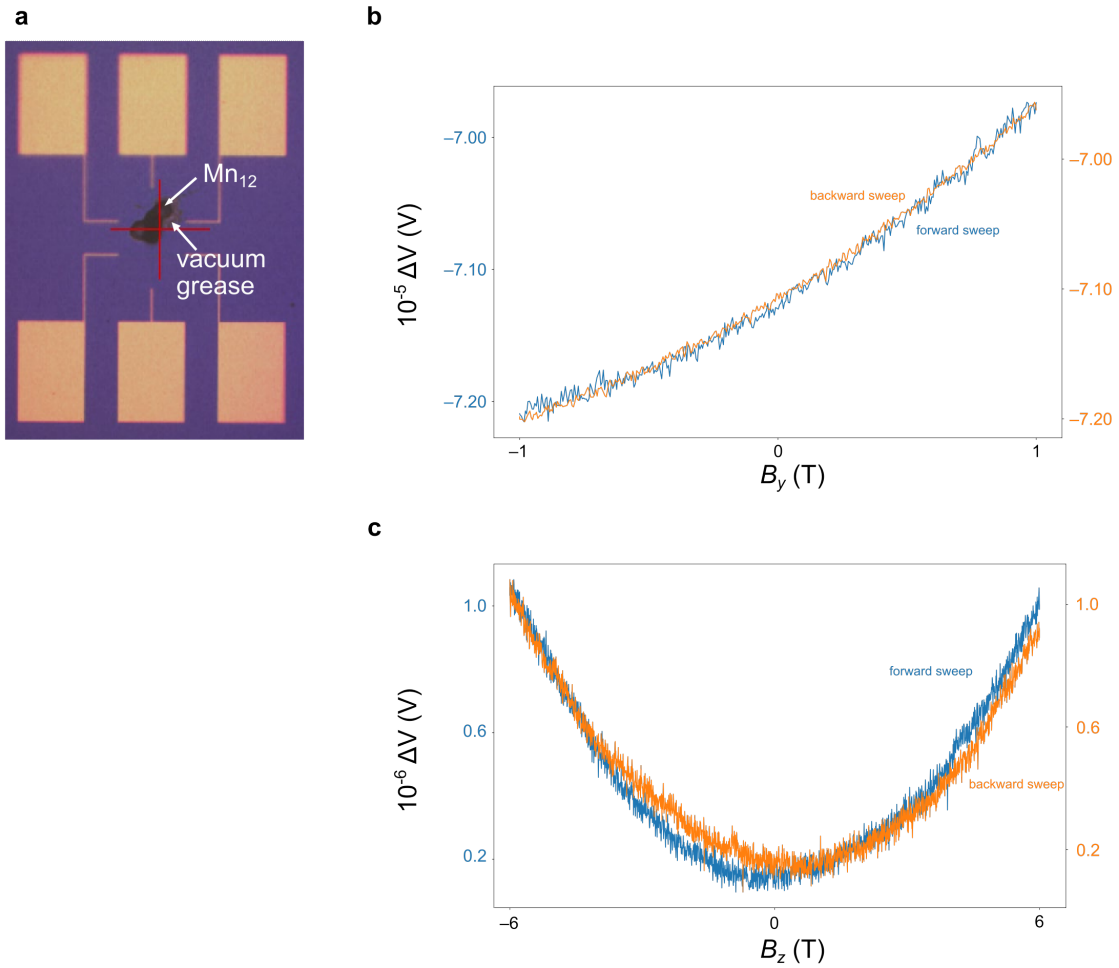


Figure 4.8: **a**, Optical lithography of a Au-based Hall-bar, placed on top of just one cross. **b**, Hall signal response as a function of the out-of-plane (y-direction) B field, demonstrating Hall effect. **c**, Same as in (b), but the field swept is the in-plane (z-direction) B field. I explain the observed magnetoresistance as the consequence of the diffusion of electrons, which is dampen when the spins inside the Au are well-oriented and act as a scattering centres.

magnetic field direction inside the dilution refrigerator cause the Hall effect induced by the dipolar field of the sample to be undetectable.

A workaround to this situation would be to use a material where the carrier concentration is minimum, such that the $1/n$ term in Eq. 4.6 is large enough to increase $B_{\min}$. One of such materials is a 2DEG, where concentrations $n \simeq 3 \times 10^{-11}\,\mathrm{cm}^{-2}$ and mobilities $\mu \simeq 1 \times 10^{6}\,\mathrm{cm\,V^{-2}\,s^{-1}}$ offer an best platform for this kind of measurements [244]. Unfortunately, the recent semiconductor crisis and the

scarcity of such substrates have made the production of such substrates hard.

Another suitable material for Hall probe is graphene. Thanks to its outstanding mobilities values (see Ch. 2) and the possibility to tune the carrier density n by gating the Fermi level, several architecture probes ranging from the epitaxially-grown graphene to fully encapsulated devices in hBN have been proposed [245, 246]. More challening has been proved to realised an adequate device by adopting CVD-grown graphene, as it is notoriously difficult to achieve good Hall coefficient since it depends, in first approximation, linearly with the eleastic mean free path $R_{\mathrm{H}} \simeq \ell_{\mathrm{el}}$, which is often due to edge and ripple scatterings.

4.4.1 Fabrication

GHB devices were fabricated by lithography means, reusing a typical two-terminal transistor architecture on 300 nm SiO_2 with n-doped Si as backgate and CVD-transferred graphene from Graphenea. The fabrication procedure begins with the removal of PMMA in acetone overnight, followed by a rinse in IPA and ebam exposure of negative resist ARN7500 at $300\,\mu\mathrm{C\,cm^{-2}}$. Etching was completed in oxygen plasma for 15 minutes, followed by 5 minutes of NMP, 30 minutes of acetone, a wash in IPA, and drying with a N_2 gun to remove the resist completely. Then, graphene was encapsulated in AlOx 100 nm via ALD with H_2O pre-treatment to promote nucleation. The chip was then put within a chip carrier. Backgate was secured by scraping the Si backside and using Ag paste for mechanical and electrical device mounting. High gate voltages up to $\pm 50\,\mathrm{V}$ were guaranteed by a bipolar high voltage source module wired to the DAC.

4.4.2 Test Measurements

Fig. 4.9 shows the GHB schematic and its electrical response when the gate voltage is swept, demonstrating graphene typical ambipolar field-effect-transistor behaviour. Hysteresis was observed both at 50 K and 2 K by repeatdly sweeping V_{G} and observing a shift in the Dirac point between forward and backward sweep; I believe hysteresis is due to the presence of water molecules adsorbed onto the graphene. A

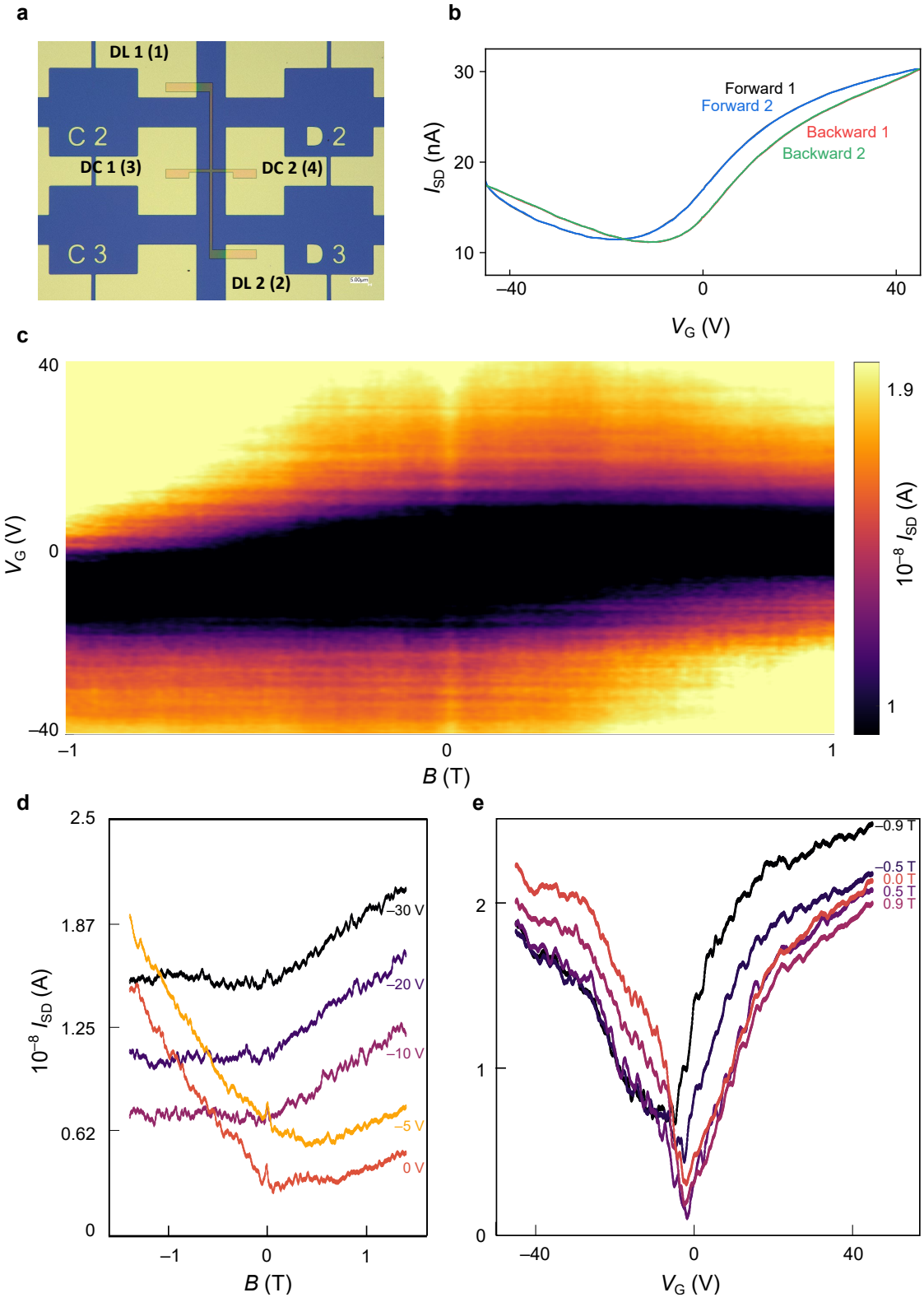


Figure 4.9: **a**, GHB after EBL showing the electrical connections. DL are direct lines. **b**, Gate response demonstrating the ambipolar behaviour typical of graphene. **c**, 1 kHz-frequency response after dropcasting a saturared solution of Mn_{12}. **d**, Hall bar signal as a function of the field along the y direction at various gates. **e**, The CNP shifts towards more positive gates as the field is increased, suggesting non-negligible magnetoresistivity present in our sample.

saturated solution of Mn_{12} is prepared (100 mg dissolved in 1 mL in acetonitrile). 5 µL are drop cast onto the Hall bar with all the lines grounded, and the solution is allowed to evaporate before loading the sample into the dilution fridge.

The 1 kHz-frequency response is shown in Fig. 4.9c. The magnetic field along the y axis in the laboratory frame system is the out-of-plane magnetic field, and the differential Hall voltage from the lock-in was recorded at a sweep rate of $0.05\,\mathrm{mT\,s^{-1}}$. When the gate voltage is positive, the response increases as the field grows more negative, however the opposite trends is observed when the voltage is close to the graphene charge neutrality point. This could be because charge carriers (holes and electrons) respond differently under a magnetic field (Fig. 4.9d,e). I was not able to measure the hysteresis cycle for Mn_{12} even with this setup.

One possible explanantion for the non-observation of the Mn_{12} hysteresis loop could lie in the preamplifier filters response to a frequency-varying signal. In this scenario, the frequency component from the lock-in output might be too fast for the filters, causing a delay in the quadrature component of the sigal, thus resulting in a delay of the reponse (Fig. 4.10b). However, I adjusted the frequency accordingly but found no qualitative differences compared with the graph Fig. 4.9c. In an attempt to circumvent this issue, I sought the Hall signal with a DC measurement. Firstly it is paramount to maximise the device's sensitivity while preserving acceptable linearity between carrier density and Hall response. A few studies suggest that this criterion is satisfied in graphene when the operating gate voltage is placed near to, but not exactly at, the Dirac point, whilst others claim that the charge neutrality point is optimal to this end [240, 243, 245].

It is necessary to emphasize that the voltages read by the Alazar card are inaccurate (see Fig. 3.8 in Ch. 3). This is likely due to the input impedance setting, which causes the voltage to drop at the digitiser input. To overcome this, a calibration curves were periodically constructed by measuring known voltages with both the Alazar card and a standard digital oscilloscpi. I used a Keithey 2450 as a constant current source. The compliance limit of 25 V restricted us to a maximum of 50 µA despite the fact that a higher current should have led to a greater sensitivity.

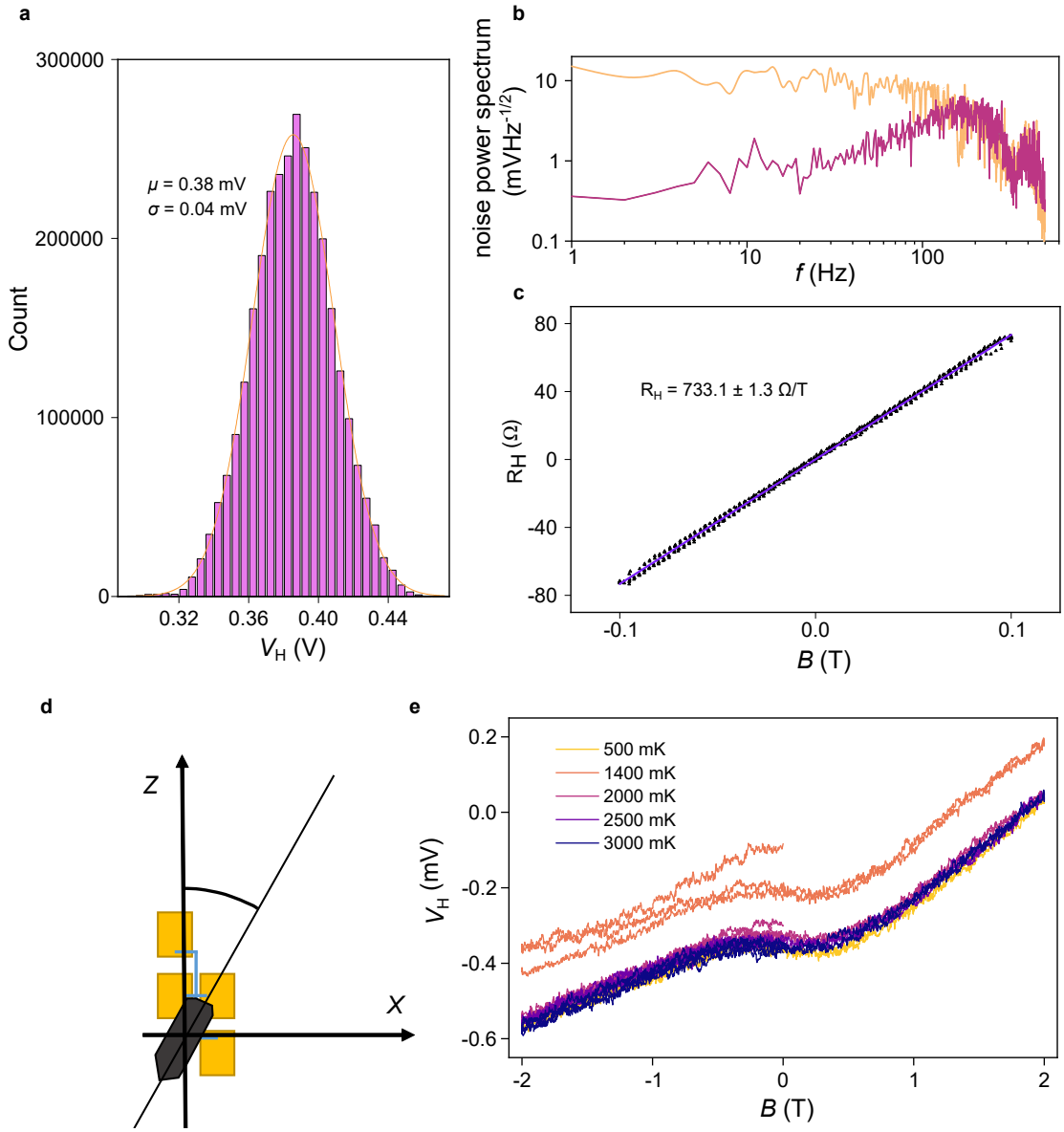


Figure 4.10: **a**, Histogram of Hall signals for an empty GHB. **b**, Noise power spectral densities with (purple) and without (yellow) band pass filters on the SR560 set to 10 Hz and 300 Hz. Roll off was set to 6 dB/Oct and lock-in excitation to $V_{\mathrm{pk}} = 0.5\,\mathrm{V}$. **c**, Hall coefficient estimated from a purely DC measurement. **d**, Mn_{12} crystal orientation with respect to the field directions, with a possible easy axis direction estimated. **e**, Temperature dependence of the Hall voltage when the field is applied along the easy axis direction.

Table 4.1: Operating parameters and performance of a few graphene-based micro-Hall magnetometers. A more complete overview can be found in [243]/

Graphene Source (Substrate)	R_H ($\Omega\,T^{-1}$)	I_H (µA)	f (kHz)	B_{min} ($\mu T\,Hz^{-0.5}$)
CVD (SiO_2)[247]	345	15	-	-
CVD (SiO_2)[248]	1800	30	20	1
CVD (SiO_2)[240]	140	12	0.531	59
CVD (PMMA)[249]	121	53	-	-
CVD (CVD hBN - encapsulated)[250]	97	90	1	400
Exfoliated (Exfoliated hBN - encapsulated)[251]	4100	-	3	0.05
This work (SiO_2)	824±1.8	50	-	16000

We first mesured the Hall voltage of the empty GHB at $T = 2\,K$. I estimate an Hall coefficient of $R_H = (733.0 \pm 1.3)\,\Omega\,T^{-1}$ when the gate voltage was set $V_G = 20\,V$ close to the Dirac cone, and an increment up to $R_H = (824.0 \pm 1.8)\,\Omega\,T^{-1}$ when the voltage was set exactly at the CNP ($V_D = 13\,V$). These values are in line with similar devices reported in literature [243]. In order to estimate the minimum detectable field, I recorded a time series of the Hall voltage (Fig. 4.10a) and measured the mean ($V_H = 0.38\,mV$) and peak-to-peak value ($V_{pk} \simeq 130\,mV$) and multiplied this value for the Hall coefficient. An estimate of about $B_{min} \simeq 16\,mT$ confirms the possibility of using our GHB for magnetometry measurements.

The placement of the crystal atop a device such this one is challenging. To transfer Graphene from graphenea wafer to our substrate, a protective layer must be employed: tipically this protection in realsed by any AlO_x layer. For the sample I report the measurments, I estimate the angle between the z direction and crystal ease axis to be $\theta \simeq 60°$. Therefore, I swept the field in this direction and recorded the Hall voltage generated by the sample. The form of the signal is qualitatively close to what would be expected from the reference sample, but no hysteresis loop was observed (Fig.4.10e). The chosen field direction, which may not have been the straightforward magnetization direction, could be a plausible cause for this. To resolve this issue, it may be necessary to scan the anisotropy of the Hall voltage as a function of field angle, as described in the previous section, and select the angle at which the response is greatest. Unfortunately, time constraints prevented us from testing this hypothesis. Another possible explanantion may be found in

the limited performance of our device. By using a standard 2DEG micro-Hall probe, Hall coefficient of $R_{\mathrm{H}} = 3000\,\Omega\,\mathrm{T}^{-1}$ and minimum detectable field of about $B_{\mathrm{min}} \simeq 2\,\mu\mathrm{T}$ can be easily reached [244].

4.5 Concluding Remarks

In this chapter, I have discussed the development of a measurement protocol which has enabled us to push the electrical measurements up to room temperature. I believe future experiments that can be possibly done with this protocol is a phase-diagram exploration of the two-terminal conductance G when the temperature T and the magnetic field B are varied simultaneously. This experiment could shed some light on quantum phase driven by strong correlations in carbon nanostructures [252–255]. The protocol can be directly integrated with the lock-in setup I have outlined in Sec. 4.2, which enables not only an unprecedent level of details, but also to measure fundamental quantifies, such as the differential conductance, which were previosuly extracted from noisier numerical procedures.

In the course of my research, I also undertook the task of testing micro-Hall sensors fabricated from gold and graphene. While this platform represented a marked advancement over torque magnetometry, primarily because with a micro-Hall platform the magnetic field B results to be less tediuous to calibrate compared to a cantilever probe, I regretfully encountered certain limitations. Specifically, I was unable to measure the hysteresis cycle of a Mn_{12} crystal.

However, this setback presents an opportunity for further improvements and optimization. First, I encountered significant challenges while working with gold-based Hall-bars. I found that the magnetoresistance effect arising from the gold atoms at high fields hampers the possibility to detect any weaker signal generated by the sample. Therefore, alternative materials such as 2DEG may need to be considered for future studies.

I believe graphene should be encapsulated within two layers of hBN to better preserve its electrical conductivity. I also suggest exploring larger Hall-bar widths.

This adjustment could potentially address the issue of the driving current in the bar often being limited by the output voltage, a factor which is dependent on the GHB width.

Additionally, I recommend improvements to the metal–graphene junctions, which currently produce high SB values. This could involve altering both the type of metal used and the geometry of the contact. In sum, although the initial tests of the micro-Hall sensors yielded inconclusive results, I am optimistic that these proposed improvements will enhance the functionality of the sensors and provide more promising outcomes in future investigations.

4.6 Project Overview

I thank Dr Alex Gee for his help and expertise in substrate fabrication, as well as his enthusiasm in all things electronic.

5

Room Temperature Graphene Nanoribbon Single-Electron Transistor

Contents

5.1 Introduction 107
5.2 Single-Electron Transistor Architecture 110
5.3 Temperature-Dependent Coulomb-Blockade Spectroscopy 111
5.3.1 MGNR Length Extraction from Coulomb Data 117
5.4 Analysis of the Low-Bias Conductance 117
5.5 Temperature-Dependent Integrated Conductance . . . 120
5.6 Discussion 122
5.7 Outlook and Perspectives 123
5.8 Project Overview 123

5.1 Introduction

Manipulating individual charges in nanostructured devices is of paramount importance for quantum technologies, and a fundamental step towards improved logic processing units and sensors. One of the possible fundamental building blocks are SETs (Sec. 2.3.2), in which the current can be tuned by adding electrons one-by-one to a nanoscopic element. Electrons would then flow only when quantized charged levels are shifted into the energy window of the applied bias V_{SD}, for

example by applying a gate voltage V_G, and this results in periodic regions of blocked conductance (Fig. 5.1a,b) [197].

One of the major hurdles of the SET technology is that its operability is often limited to cryogenic temperatures, while quantum transport at room temperature (RT) is necessary for many practical applications. To operate at RT, SETs need to simultaneously display a very low self-capacitance, C, charging energies (E_C) larger than the thermal energy ($k_B T$), and high tunnelling barriers that allow confining electrons on the nanoscale element. Carbon materials are a particularly appealing platform that have seen multiple scientific and technological breakthroughs, such as superconductivity [33], spin localization [179] and manipulation [256]. Furthermore, CNTs can display SET behaviour up to RT and have already been used to create low-power processing units [102]. On the other hand, their poly-dispersity still constitutes a major barrier to their large-scale integration.

MGNRs [167, 172, 202, 257] provide in this scenario unique opportunities since they can be chemically synthesised with a degree of edge and topological control far superior to what has been achieved with top-down nanofabrication [138, 171, 258, 259]. Most importantly, they display topologically non-trivial electronic quantum phases [260, 261], and offer edge magnetism [195] and long spin-coherence times at RT [178]. The missing ingredient to electrically control and read these topological and coherent spin states at high temperatures, if possible, is the observation of high-temperature SET behaviour in MGNRs.

This possibility seems within reach. Liquid-processable chemical strategies have recently opened up the path to ultra-clean single-MGNR devices directly created from solution [262, 263] (Ch. 6). Single-MGNR devices, because of their extremely-high length/width ratio, should display self-capacitances of $\simeq 1 \times 10^{-18}\,\mathrm{F}^{\dagger}$, thus being operable at bias voltages $V_{SD} < 100\,\mathrm{mV}$, while the extreme lateral electronic confinement should afford $E_C \gg k_B T$. MGNRs would thus offer excellent persective platforms for SETs at RT, but the evolution of their electronic behaviour with T, and the underlying phsyics, is still unknown.

[†]Because graphene electrodes have little electrostatic screening, the capacitive coupling of the ribbom to the back gate contributes the most to the overall capacitance.

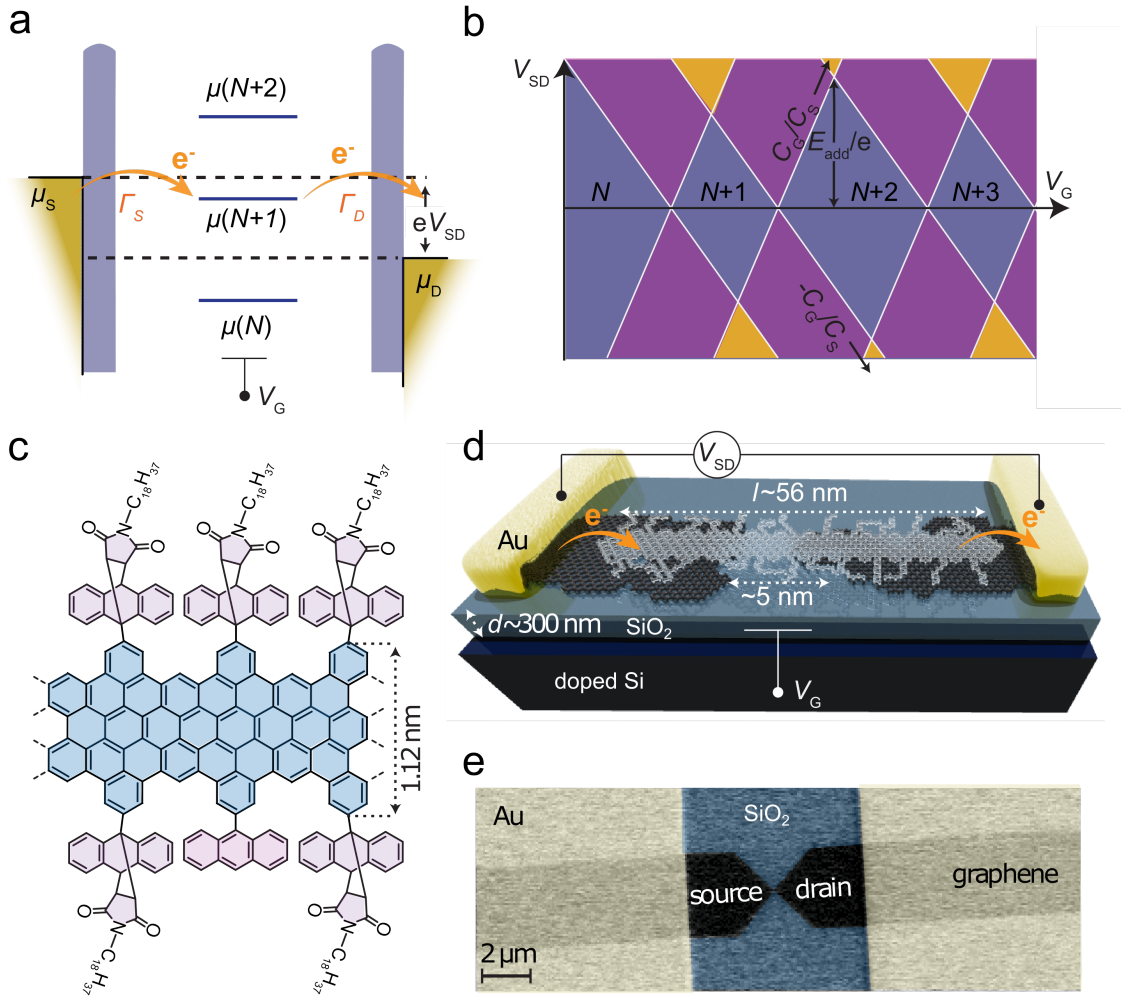


Figure 5.1: **a,** Scheme of the SETs, with electron reservoirs in yellow and barriers in blue. **b,** Resulting diamond diagram, showing regions of blocked conductance (blue) and regions of quantized conductance (violet). N indicates the single electrons being added. **c,** Structure of the liquid-processable MGNRs (aromatic backbone in blue, maleimide solubilizing groups in violet). **d,** Scheme of a SET device, with the MGNR depicted in white and side groups simplified for clarity. Terminals for gate V_G and bias V_{SD} voltages are indicated. **e,** False-color scanning-electron-microscope image of a typical back-gated junction.

This chapter describes, to the best of my knowledge, the first realisation of a SET built with MGNRs at RT. We shall explore the conduction regimes as T is increased from cryogenic to RT by using a variety of source–drain and gate voltages in a two-terminal back-gated device. The measurements were conducted using the apparatus described in Ch. 3 and Ch. 4.

The research, data analysis, interpretation, and writing presented in this chapter were conducted by myself and represent original work. The one aspect of this work for which I did not directly contribute is the synthesis of the graphene nanoribbons. These materials were prepared by Wenhui Liu, Ji Ma, and Prof. Xinliang Feng at the TU Dresden University. Their significant expertise and contributions in the area of graphene nanoribbon synthesis were essential for enabling the research presented in this chapter.

5.2 Single-Electron Transistor Architecture

Ultra-clean devices are obtained from MGNRs designed with bulky 3D side-groups that enhance solubility (Fig. 5.1c) in organic solvents, synthesised from diene and dienophile in three steps as previously reported [262]. These groups have here an additional function: by suppressing π-stacking interactions between the GNR and graphene electrodes, they contribute crucially to the presence of high tunnelling barriers, as necessary for high-T performance. Furthermore, the edges carry also optically-active anthracene groups which may be used to monitor the dispersion quality with fluorescent spectroscopy.

The aromatic backbone has width of precisely $w = 1.1\,\mathrm{nm}$, leading to a bandgap of $\pi\hbar v_F^* w_{\mathrm{GNR}}^{-1} \simeq 1.8\,\mathrm{eV}$ [180] which should be associated with a reduced effective mass, thus reducing the contribution to the overall conductance from SB [264], and an improvement of the band alignement with the graphene leads [210].

The nanodevices were fabricated as described in Ch. 3 (Fig. 5.1d,e). The junction energy barrier between the MGNRs and graphene is estimated to be $\phi \simeq 0.5\,\mathrm{eV}$ from the Simmons fit (Sec. 3.4) of the tunnelling current prior to

Table 5.1: Lever arms and addition energies extracted from the Coulomb diamonds slopes and heights for the different charge transitions. The addition energies reported here are obtained by averaging the height read both at positive and negative polarities.

Charge Transition	Lever Arm β ($\mathrm{meV\,V^{-1}}$)	E_{add} (meV)
$N \leftrightarrow N+1$	21	152
$N+1 \leftrightarrow N+2$	23	156
$N+2 \leftrightarrow N+3$	25	160
$N+3 \leftrightarrow N+4$	28	168
$N+4 \leftrightarrow N+5$	33	160
$N+5 \leftrightarrow N+6$	25	149
$N+6 \leftrightarrow N+7$	23	151
Mean	25 ± 4	157 ± 7

depositing the MGNRs, which guarantees enough transparency to observe single-electron tunnelling events.

Overall, we measured at low temperatures 5 devices (see Appendix A) that showed clear, periodic, and qualitatively similar single-electron features. Two out of five devices have been warmed up: one at 35 K, and the other at room temperature. The forthcoming experimental findings and discussion are solely based on the latter device.

5.3 Temperature-Dependent Coulomb-Blockade Spectroscopy

We explore the electronic behaviour by measuring the two-terminal conductance G as a function of V_{SD} and V_{G}, from 25 mK to RT (Fig. 5.2 and 5.3). Seven charge transitions are visible within the experimentally accessible V_{G} range (Fig. 5.2 and 5.3), and they remain clearly distinguishable upon increasing T, with a periodic peak spacing of $\Delta V_{\mathrm{G}} \simeq 4\,\mathrm{V}$. We assign the leftmost diamond having N electrons in the ground state with the charge transition $N \leftrightarrow N+1$, and the rightmost diamond as the $N+6 \leftrightarrow N+7$ transition, so we assume the ribbon is n-doped. The periodicity and cleanliness of the Coulomb oscillations excludes that electron transport occurs through multiple quantum dots in series, formed by intraribbon

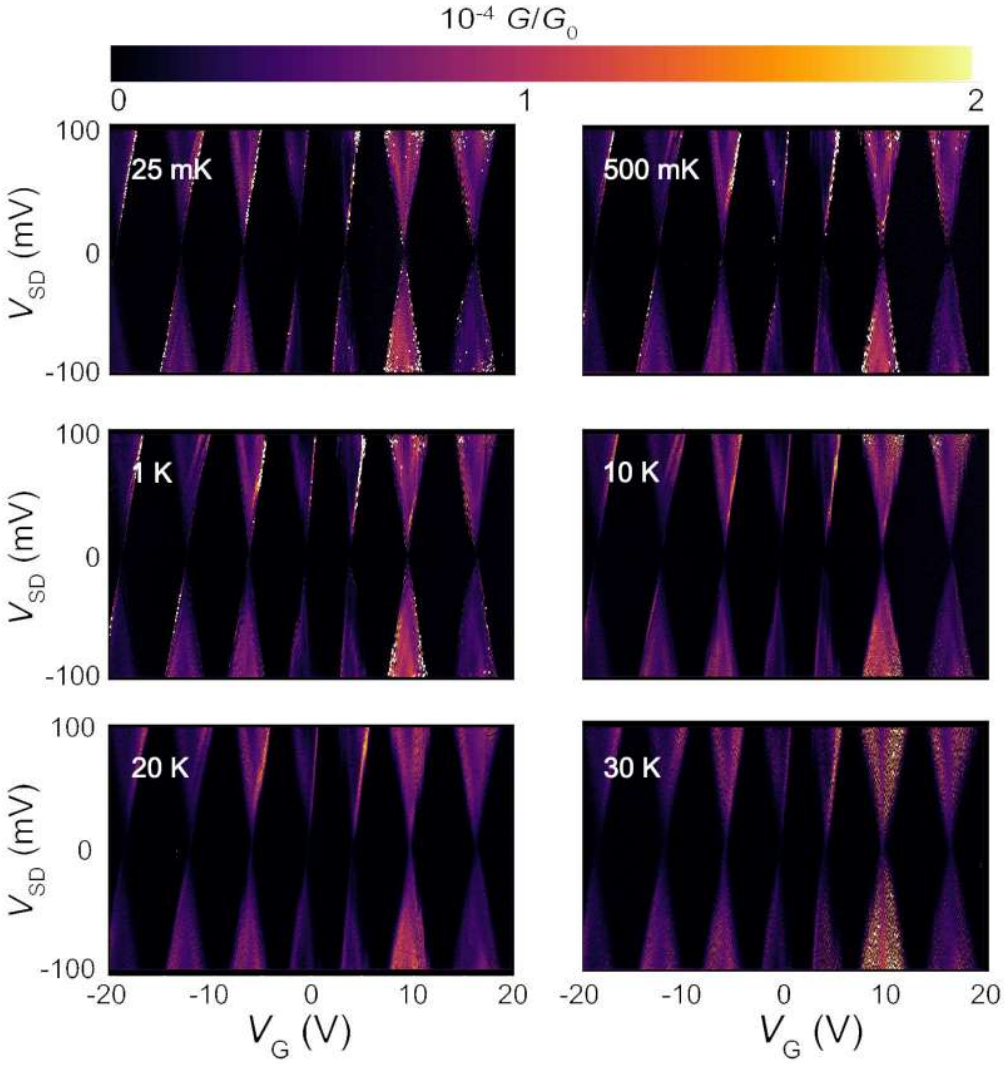


Figure 5.2: Stability diagrams of the DC conductance G in units of the conductance quantum G_0. Coulomb diamonds are periodic, with nearly symmetrical peak spacings centered at $V_G \simeq 0\,V$ and similar slopes and sizes. This reveals a regular, highly structured energy spectrum, indicative of a high-quality quantum system, which we assign to a single MGNR bridging the graphene electrodes. The observation that the device is n-doped is also noteworthy, as this suggests a specific directionality to the charge transport, with electrons being the primary charge carriers. Inspection of the zero-bias conductance around the diamond tip reveals that Coulomb diamonds are closed even at low temperatures.

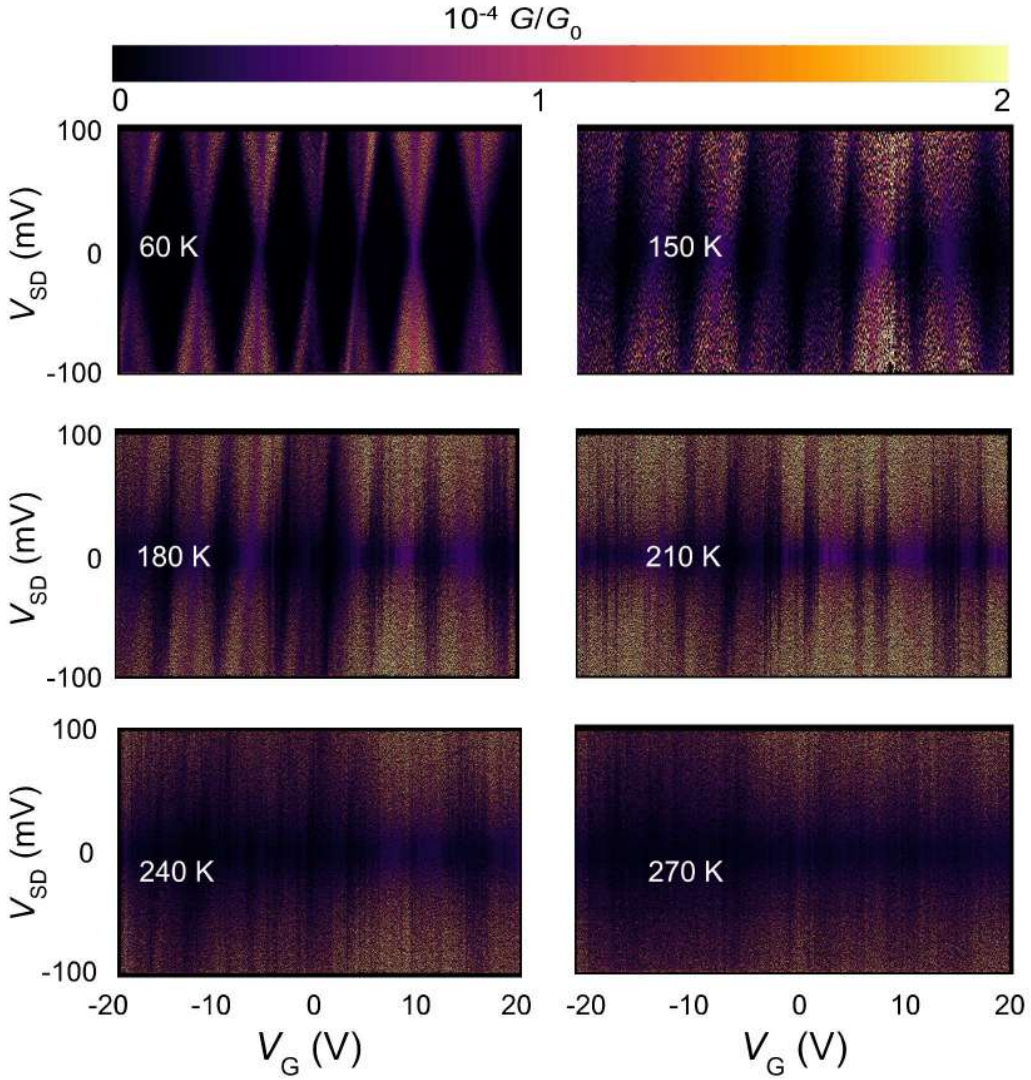


Figure 5.3: Stability diagrams of the DC conductance G in units of the conductance quantum G_0 at high temperatures. Since the Coulomb charging energy E_C as well as the energy separation δE between consecutive quantum energy levels exceed $k_\mathrm{B}T$ at RT ($\simeq 25\,\mathrm{meV}$), single-electron tunnelling in the MGNR device is still observable up to 240 K.

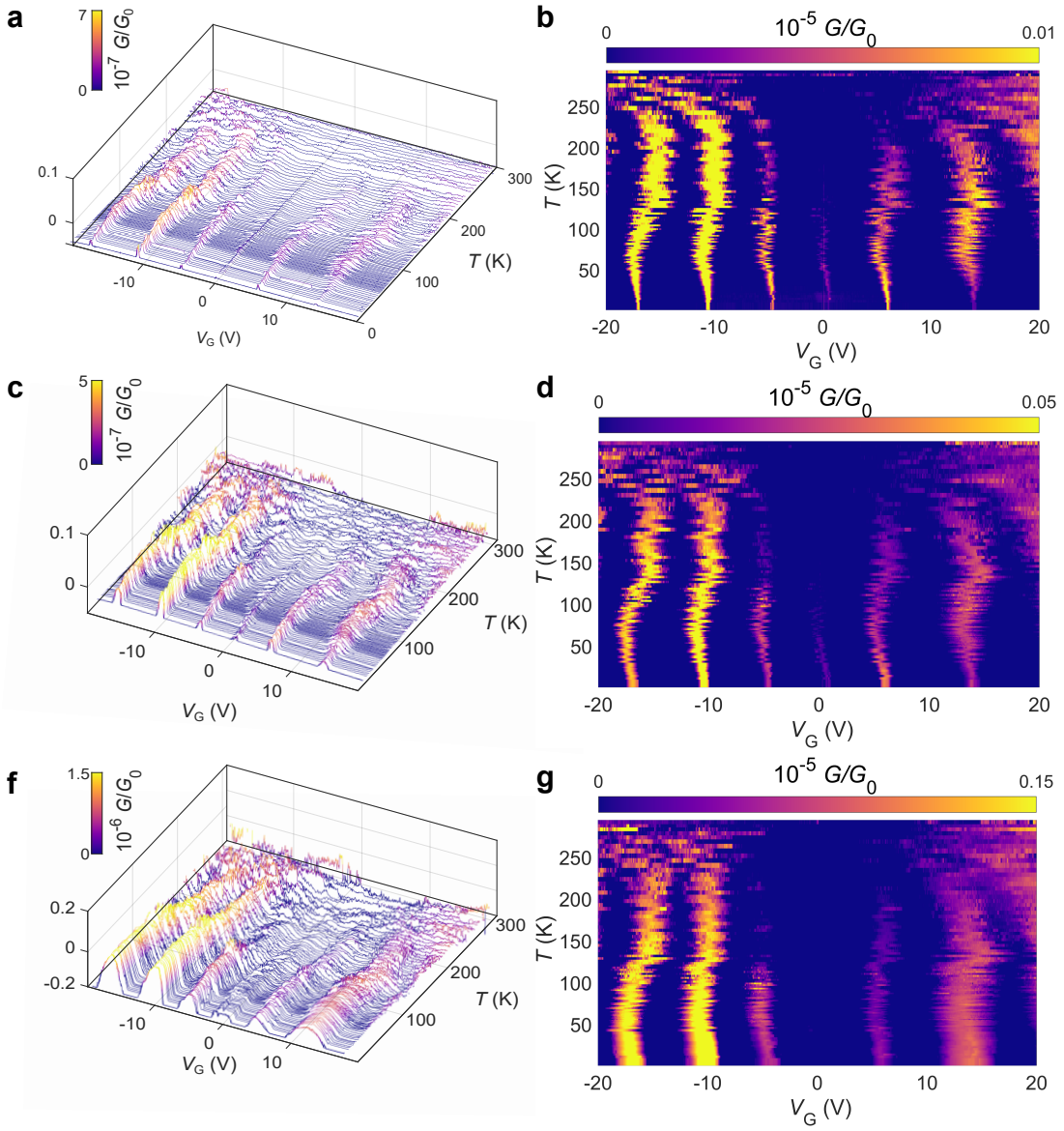


Figure 5.4: **(a, b)** Resonance levels probed when applied a polarity of 10 mV. **(c, d)** Energy levels involved in the tunnelling process at 30 mV. **(e, f)** Gate traces taken at 0.1 V. Interestingly, the peaks are subject to a shift towards the left for temperature below 100 K, for then being shifted towards the right.

defects, such as edge roughness [265, 266] and aromatic-core defects [179]. For each transition, it is possible to extract the gate coupling β (also knwon as *lever arm*) and the addition energy E_{add} from the Coulomb diamond heights (Tab. 5.1).

We observe a nonlinear increase in β for diamonds at negative gate voltages, peaking at the greatest values for diamonds at zero gate voltage and then decreasing practically linearly as we move towards more positive gate voltages, with a mean value of $\overline{\beta} = (25 \pm 4)\,\text{meV}\,\text{V}^{-1}$. This symmetric and non-linear gate dependence could be caused by electrostatic forces in the dioxide substrate [267].

Similarly, the charge-state addition enegies lie between 149 and 168 meV, with an average value of about $\overline{E_{\text{add}}} = (157 \pm 7)\,\text{meV}$, which is comparable to other GNRs [215] and CNT-embedded metal nanoparticles [268], and approximately five times larger than previously-reported values for CNT-based [161] or CMOS-integrable [269] SETs.

Conductance Peaks Features

Remarkably, Coulomb peaks show comparable heights indicating an equal participation of the same number of levels within the bias window. In fig. 5.4, I plot the temperature dependence of MGNR quantum states read off at various V_{SD}. The bias voltage essentially determines the energy window within which electronic states can contribute to the current, and controls the range of energies available for the electrons to tunnel through the device [120, 270]. Thus, the energy window is increased by increasing the bias, and more electronic states (both in the quantum system and the leads) can participate in transport.

Also, increasing the bias voltage also affects the tunneling rates into and out of the quantum device. This is because the tunneling rate depends on the available states in both the device and the leads, and these available states are directly affected by the bias voltage. This pattern reveals certain properties of the electronic structure and transport phenomena within the device. A possible interpretation of the experimental data could be as follow.

At negative gate voltages, the two charge transitions having the highest heights suggest that the electrons' transmission probability through the device is maximum in this regime [209]. This could be due to the alignment of the Fermi level of the leads with favorable electronic states in the GNR, leading to optimal resonant tunneling conditions. It could also imply that at these negative gate voltages, the device is optimally n-doped, with the Fermi level falling in the conduction band of the GNR, maximizing electron transport.

The lower charge transition observed right before zero gate voltage could correspond to the Fermi level moving through the bandgap of the GNR. In this region, fewer electronic states are available for transport, leading to a lower tunneling probability and hence a smaller charge transition peak.

The faint charge transition at zero gate voltage is particularly interesting. The fact that it is visible, but very small, might indicate the presence of midgap states, possibly due to defects or edge states, that can weakly contribute to electron transport [164, 271]. Alternatively, this could reflect a small degree of p-type doping at zero gate voltage, with the Fermi level only slightly penetrating the valence band.

Finally, the pattern of charge transitions at positive gate voltages mirroring those at negative gate voltages, but with smaller intensities, suggests a similar electron transport mechanism but with lower overall transmission probabilities [184]. This might be due to the device becoming p-doped as the gate voltage becomes positive, shifting the Fermi level into the valence band. The lower transmission probabilities could then be attributed to a lower density of available states for transport in the valence band as compared to the conduction band, possibly due to the unique band structure of GNRs [181, 197].

In summary, these observations underscore the sensitivity of quantum transport properties in GNRs to the gate voltage and provide insights into the device's electronic structure and transport phenomena. They also highlight the potential role of defects or edge states in contributing to transport, particularly around zero gate voltage.

Thermal Shift of the Conductance Peaks

The observed thermal shifts of conductance peaks below 100 K in the conductance spectroscopy map can resul from a range of factors. When we consider high temperatures, we must account for the potential shifts in electron energy levels caused by increased thermal fluctuations. As the kinetic energy of electrons increase, it can lead to noticeable shifts in peak positions [272]. Moreover, heating generally leads to the expansion of materials, which can affect the confinement conditions in nanostructures such as graphene nanoribbons [273]. The resulting subtle shifts in energy levels can give rise to the observed peak shifts.

As we increase the temperature further, the impact of electron–phonon interactions – the interactions of electrons with lattice vibrations – grows. These interactions can lead to broadening and shifts in electronic states, influencing peak positions. In higher temperature regions, the Fermi-Dirac distribution, which indicates the likelihood of an electron occupying a state at a particular energy level, begins to broaden [124]. This broadening can lead to wider and shifted peaks in the conductance spectrum.

5.3.1 MGNR Length Extraction from Coulomb Data

In a MGNR of length l_{GNR}, confinement produces an energy spacing given by $\delta_n = \pi\hbar v_F^* l_{\mathrm{GNR}}^{-1}$ [180], while, for a rectangular-shaped MGNR $E_C = \frac{e^2}{C} = \frac{e^2 \ln(4d/w)}{2\pi\varepsilon_0\varepsilon_r l_{\mathrm{GNR}}}$, where e is the electron charge, d is the ribbon–gate distance, w is the ribbon width, and ε_0 and ε_r are the dielectric permittivities of vacuum and SiO_2, respectively [274].

From $E_{\mathrm{add}} = \delta_n + 2E_C$, we thus extract $l_{\mathrm{GNR}} = 58 \pm 6$ nm[†].

5.4 Analysis of the Low-Bias Conductance

At $T = 25$ mK analysis of the low-bias ($V_{\mathrm{SD}} = 1$ mV) conductance peaks allows us to extract the graphene–MGNR coupling $\Gamma = 180\,\mu$eV by fitting with a Breit–

[†]For a ribbon with $w_{\mathrm{GNR}} \simeq 1.12$ nm and $l_{\mathrm{GNR}} \simeq 56$ nm the $E_{0,1}/k_{\mathrm{B}} \simeq 37$ meV, hence we include the single-particle level spacing contribution in E_{add}

Wigner model $G(\mu) = \frac{\Gamma/2\pi}{(\mu-\mu_N)^2+(\Gamma/2)^2}$ the resonances. In the model, μ is the chemical potential and μ_N is the chemical potential of the N^{th}-MGNR state. This energy scale identifies a first conduction regime at $T_C < \Gamma/k_B \sim 2$ K, and plot of the conductance peak maximum $G_{\max}$ against T on a double logarithmic scale indeed shows that the behaviour changes drastically around T_C (Fig. 5.5c). At

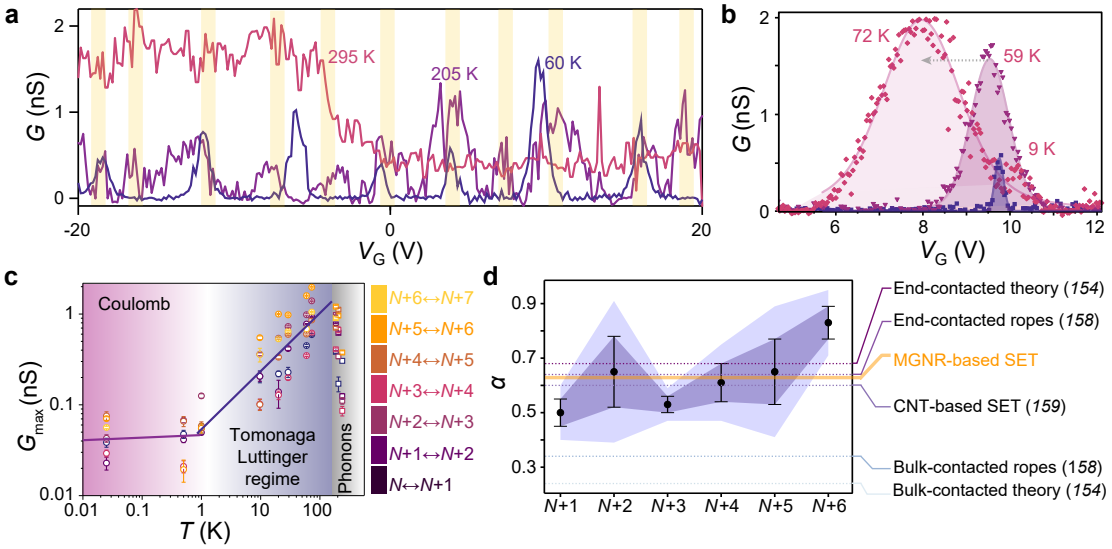


Figure 5.5: a, Comparison of low-bias traces acquired at $V_{SD} = 1$ mV for various T. **b,** Typical evolution of a G vs. V_G peak, shown here for the $N+5 \leftrightarrow N+6$ transition acquired at $V_{SD} = 1$ mV, with solid lines fits to the data (see text). **c,** Bilogaritmic plot of the evolution of the peak height $G_{\max}$ vs. T for all transitions (colour bar), and fits to the data. Shaded areas highlight different regimes. **d,** Power-law exponents for the 1–72 K region, for each transition, with comparison to the literature. Darker and lighter shaded regions are the 1σ and 2σ fitting error bands, respectively.

temperatures greater than T_C, we reproduce the low-energy excitations with a thermally-broaded model [161, 209]:

$$G(T) \sim \frac{G_{\max}(T)}{\cosh^2\left[\frac{2\text{arccosh}(\sqrt{2})V_G}{w(T)}\right]}, \tag{5.1}$$

being $G_{\max}$, V_G, and $w(T)$ the fitting parameters representing peak height, position and full width at half maximum (FWHM), respectively. Fit results for the peak height are reported in Tab. 5.2. Moreover, the thermal broadening of the peaks follows a linear T-dependence (Fig. 5.6), and we extract from the best-fit model $w_{\text{peak}} = (1.7 \pm 0.3) \times 10^{-1} + T(1.1 \pm 0.1) \times 10^{-2}$. For $T < T_C$, the only transport

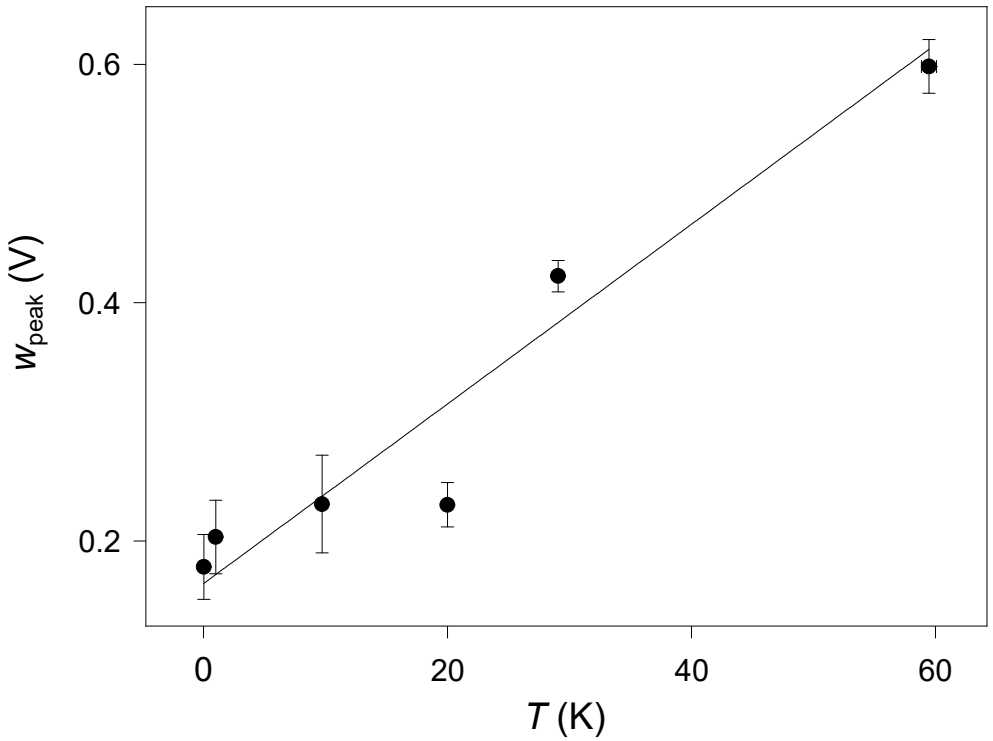


Figure 5.6: Peak width for the transistion $N + 4 \leftrightarrow N + 5$.

mechanism is pure Coulomb blockade, modulated by the strong spin-phonon coupling present in MGNRs, which leads to Franck–Condon blockade (Ch. 6). In this region, G is essentially constant, and this indicates that the MGNR states are independent on ϕ, as thermally-activated transport with law $G(T) \propto e^{-\phi/k_{\mathrm{B}}T}$ would otherwise be observed [275].

For $T > T_C$, up to 180 K, the conductance follows a power-law behaviour $G_{\max} \sim T^{\alpha}$, and the extracted exponents show values between $\alpha = 0.50 \pm 0.06$ and $\alpha = 0.83 \pm 0.06$ for all N states (Fig. 5.5c,d and Tab. 5.2). This power-law behaviour of the TDOS might be associated with the formation of TLL [154–156] in MGNRs, showing that correlated one-dimensional electronic states may be produced by electron–electron interactions.

Comparison of exponent values for MGNRs with those of single nanotube [276] and ropes of bundled CNTs [160] shows excellent agreement only with SETs based on single CNTs. The extracted average $\alpha = 0.63 \pm 0.08$ is in excellent agreement with the theoretical value for electron tunnels coherently at the ends of a TLL

Table 5.2: Power-law exponents for the conductance G and integrated conductance G^* across two different temperature ranges. Errors on the single charge transition are standard fitting errors, whereas error on the averages are estimated through error propagation formula.

Charge Transition	$G \sim T^{\alpha}$ ($1\,\mathrm{K} < T < 205\,\mathrm{K}$)	$G \sim T^{\alpha}$ ($1\,\mathrm{K} < T < 72\,\mathrm{K}$)	$G^* \sim T^{\xi}$ ($1\,\mathrm{K} < T < 72\,\mathrm{K}$)
$N \leftrightarrow N+1$	0.31 ± 0.11	0.51 ± 0.06	1.56 ± 0.2
$N+1 \leftrightarrow N+2$	0.54 ± 0.09	0.65 ± 0.08	1.76 ± 0.2
$N+2 \leftrightarrow N+3$	0.32 ± 0.12	0.54 ± 0.03	1.65 ± 0.1
$N+3 \leftrightarrow N+4$	0.60 ± 0.11	0.62 ± 0.07	1.43 ± 0.3
$N+4 \leftrightarrow N+5$	0.57 ± 0.08	0.65 ± 0.12	1.35 ± 0.2
$N+5 \leftrightarrow N+6$	0.57 ± 0.13	0.83 ± 0.06	1.61 ± 0.2
$N+6 \leftrightarrow N+7$	0.36 ± 0.2	0.45 ± 0.09	1.36 ± 0.3
Mean	0.47 ± 0.02	0.64 ± 0.01	1.53 ± 0.05

thorugh correlated sequential tunnelling [161, 162], $\alpha = 0.68$, and not into its bulk ($\alpha = 0.23$), as expected from the device geometry. The TLL phase allows exploring electron–electron interaction strength through the Luttinger parameter g, which is $g = 1$ for the non-interacting case and $\ll 1$ for strong repulsive interactions (Sec. 2.4.2). Given the four-fold degeneracy of the graphene band structure, it is possible to recover the expression for the tunnelling exponent of four conducting modes at Fermi energy E_F [160], as $g = (4\alpha + 1)^{-1} = 0.28 \pm 0.04$, or from the expression $g = (1 + 2E_C/\delta)^{-1/2} = 0.41 \pm 0.08$ [154, 155].

These values are well below $g = 1$, confirming the importance of finite long-range Coulomb interactions in MGNRs, but are interestingly weaker than those active in CNTs. This might be explained with the hypothesis that electron–electron interactions depend significantly on the curvature radius of the conjugated carbon sheet [62, 156].

5.5 Temperature-Dependent Integrated Conductance

Because peak broadening can obscure features and alter the power-law dependence, we also analyzed the integrated conductance, G^* (Fig. 5.7). A power law, $G^* \propto T^{\xi}$

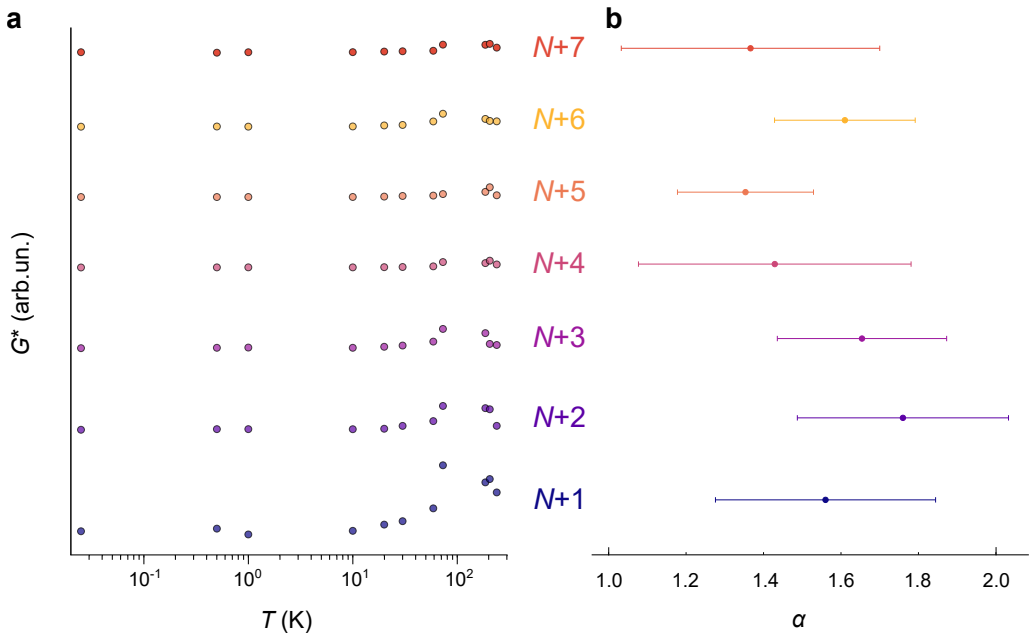


Figure 5.7: a, Integrated conductance G^* temperature trends, offset along the y direction for clarity. **b,** Power-law exponents α for each transition. Error bars are fitting errors.

is observed, where $\xi = \alpha + 1$ in the case of end-tunnelling [161, 162]. The extracted $\xi = 1.5 \pm 0.1$ is in overall agreement with the values extracted from originating from $G_{\max}$, which also confirms a more screened interaction picture for MGNRs [275].

MGNRs could display TLL only as long as electrons can tunnel coherently from one end to another via a single MGNR state, so that the whole MGNR acts as a single electronic structure. This condition is fulfilled when the electron thermal length $L_T = v_F/k_\mathrm{B}T$ is larger than the MGNR geometric length l_GNR, with deviations from the TLL behaviour expected when $L_T \ll l_\mathrm{GNR}$. This regime crossover is indeed observed above $T = 180\,\mathrm{K}$ (Fig. 5.5c), for which $L_T < 43\,\mathrm{nm} < l_\mathrm{GNR}$, using $v_F \simeq 1.6 \times 10^5\,\mathrm{m\,s^{-1}}$ for the group velocity.

Beyond 180 K, flexural phonons dominate the electronic behaviour by introducing phonon scattering [277, 278], and are responsible for a rapid increase of g, which approaches the non-interacting limit above 240 K.

5.6 Discussion

Using the temperature protocol developed in Ch. 4, we have presented the first experimental evidence of a molecular SET that can work up to room temperature based on a molecularly-defined graphene nanoribbons. The charging energy E_C overcomes the thermal fluctuations even at $T = 290\,\mathrm{K}$, leading to the observation of Coulomb oscillations.

We then revelead three major transport regimes for the low-energy excitations. At cryogenic temperatures, Coulomb-oscillation heights are essentially invariant, and we believe this is due to Coulomb blockade. Power-law scaling in T are found from 1 K to approximately 80 K, while Coulomb-oscillation widths are proportional to T. Similar scalings have been reported in the literature, and explained with the presence of finite-range Coulomb interactions in 1D systems. Because we do not observe an exponential decay of the conductance $G \sim T^{-\beta\phi}$, even when plotted against the reciprocal of the temperature (not shown), we exclude thermally-activated transport [275], supported by the evidence that Coulomb diamonds are closed at low ($T \simeq 20\,\mathrm{mK}$) temperatures.

From the diamond height, we estimate the device single-particle level spacing $\delta_n \simeq 38\,\mathrm{meV}$, which is in overall agreement with a single-electron transistor defined in a metallic CNT by two kinks which are separated by approximately 25 nm [279]. We interpret the power-law scaling as the tunnelling through a Luttinger liquid weakly coupled to a Luttinger island. Plasmon-mode excitations following the tunnelling event might rationalise the different power-law exponents reported for each charge transistion. We estimate the tunnelling exponent from $\alpha_{\mathrm{end}} = 2R/R_Q$ [280], where R is the impedance of a transmission line associated to plasmon oscillations and R_Q is the resistance quantum. For our device $R \simeq 7\,\mathrm{k\Omega}$, leads to an $\alpha_{\mathrm{end}} \simeq 0.5$, in good agreement with the average scaling exponent reported in Tab. 5.2.

Since the Coulomb-oscillation widths increase linearly with T, we measured the integrated conductance G^*, and observed a power-law scaling $G \sim T^{\alpha+1}$, in agreement with theoretical predictions [162]. We were then able to clarify the tunnelling mechanism involved in the process, which we interpreted within the

correlated-sequential-tuneling framework through a Tomonaga–Luttinger liquid within a weakly-coupled MGNR. Graphene flexural phonons, as well as plasmon excitations, start to become important from $T > 80\,\mathrm{K}$, introducing two main scattering channels that dominate the electron transport, leading to a deviation from the power-law scaling. These results are in overall agreement with a non-linear dispersion of the low-energy excitations, in contrast to metallic carbon nanotubes.

5.7 Outlook and Perspectives

The 1D nature, combined with the versatility of bottom-up chemical techniques, are likely to open up in the future a plethora of investigations using electronic devices such as the one presented here. In order to control electrically [281] and magnetically [179] spins in systems in graphene nanostructures, numerical many-body schemes would be necessary to clarify the energy ladder [282], especially when a magnetic field B is applied. In this regard, experimental studies have been already started from our group [231], which suggest a possible Stoner instability induced by spin–sping exchange interactions, leading to the emergence of spin-polarised states in MGNRs [283]. This result, combined with the one exposed in this chapter, offer an enthusiastic starting point that could lead to the exploration of spintronic devices [235] realised with MGNR and to one of the first all-carbon molecular qubit, where long coherence times are expected, owing to the topological nature of the energy states at low energies [260, 261].

5.8 Project Overview

MGNRs were synthesised in Dresden by Dr Wenhui Niu and the group of Xinliang Feng. Dr Simen Sopp helped me in collecting the high temperature data. Dr Glenn Wagner is thanked for the fruitful discussions about the physics of 1D systems.

6

Vibrational Effects in Graphene Nanoribbons

Contents

6.1 Introduction 124
6.2 Coulomb-blockade Spectroscopy 125
6.3 Analysis of the Franck–Condon Conductance Blockade 129
6.4 Simulation of the Stability Diagram 131
6.5 Role of the Maleimide Groups: *Ab-Initio* and Statistical Analysis 132
6.6 Discussion 137
6.7 Outlook and Perspectives 139
6.8 Project Overview 140

6.1 Introduction

As we saw in the last chapter, MGNRs cn provide a platform to electrically manipulate electronic states at high temperatures. Since spin coherence times up to µs have been measured in a comparable temperature range [179, 195], circumstances appear to be ideal for using single MGNRs to exploit spin and topological phenomena for quantum applications; however, only devices with sharp features, where all the quantum states can be accessed properly, can be used for quantum experiments.

Because of the strong $\pi - \pi$ interactions between their large conjugated sp^2-carbon planes, MGNRs can easily aggregate in the solid state and in solution, making the integration of MGNRs into electronic nanodevices challenging. For improving liquid-phase MGNR dispersion, both physical techniques (i.e., sonication exfoliation [137]) and chemical treatment with a strong acid [284] have been used. These approaches, however, have limited dispersion effects and, often, MGNRs clusters persist.

To date, two basic techniques for producing liquid-phase-dispersible MGNRs have been proposed. The first approach involves the addition of alkyl substituents along the edges. For example, dodecyl-decorated MGNRs with lateral widths of 0.7–1.1 nm and lengths of more than 200 nm are often the go to choice [138], but strong sonications are unfortunately still necessary, which may be detrimental to the honeycomb lattice, as carbon nanotubes have indicated in the past [285, 286].

The other approach involves the addition of bulky 3D groups at the periphery of the MGNRs. The dimensions of these substituents are typically greater than the graphite interlayer distance $\simeq 0.34$ nm, hence they should dramatically disrupt the $\pi - \pi$ interactions, and aid the dispersion of individual ribbons in the liquid phase. A little shaking or very mild sonication in common organic solvents such as THF, dichloromethane, and toluene is reported to yield homogeneous dispersions [262].

In this chapter, I will attempt to demonstrate that attaching 3D substituents with a high degree of steric hindrance along the ribbon edges can improve the solubility of graphene nanoribbons in common apolar solvents.

6.2 Coulomb-blockade Spectroscopy

In order to verify the hypothesis that bulky 3D groups enhance the de-bundling of MGNRs in solution and may lead to superior quantum properties, I tested two different nanoribbons, each decorated with different edge functionalizations. The first nanoribbon was decorated with dodecyl alkyl chains (MGNR**1**), while the second utilised maleimide groups (MGNR**2**) (Refer to Fig. 6.1). Moreover, to

explore potential disparities in device performance, I incorporated these ribbons into two different device architectures (Refer to Fig. 6.2).

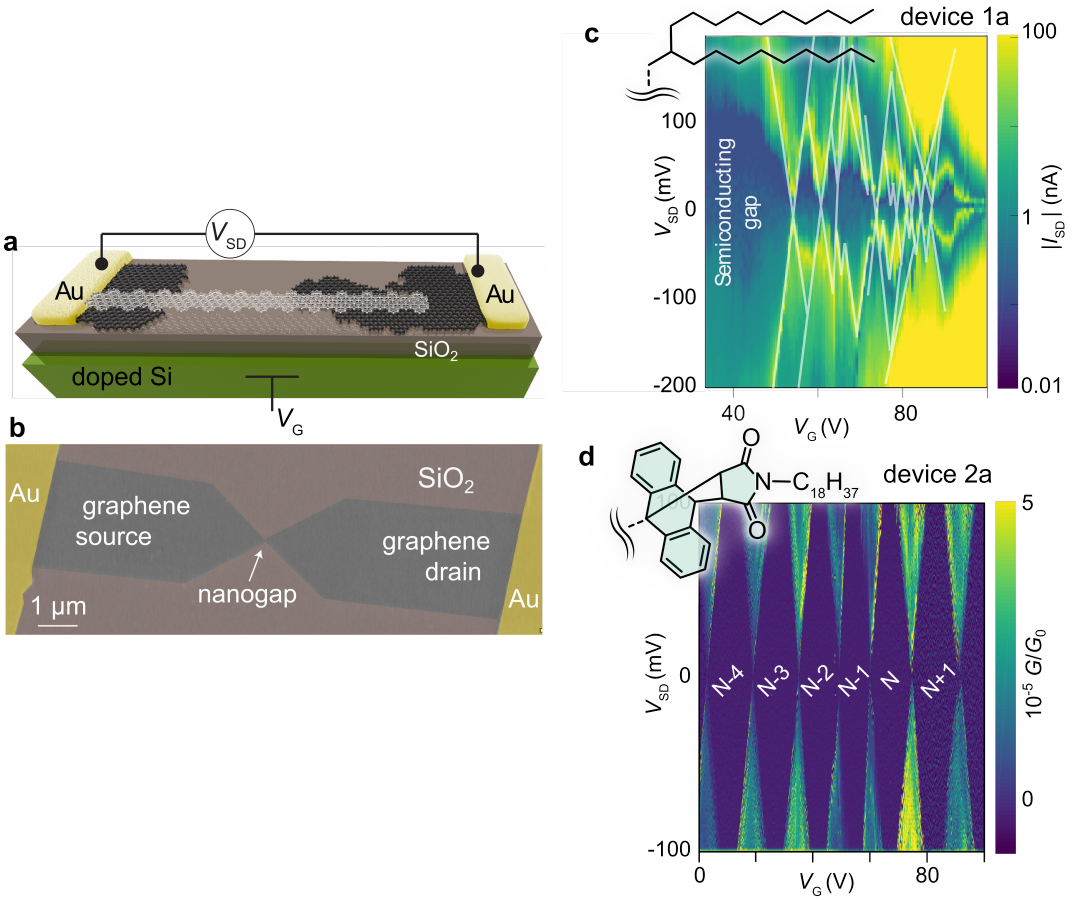


Figure 6.1: **a,** Scheme of the 2T-SET device, with the MGNR depicted in white and side groups simplified for clarity. Graphene leads (dark grey) are onto to Au pads. The gate is an n-doped Si wafer with a 300 nm SiO_2 insulating layer on top. Terminals for gate V_G and bias V_{SD} voltages are indicated. **b,** False-color scanning electron microscope image of a typical junction. **c,** A typical stability diagram measured at $T = 20\,\mathrm{mK}$ with MGNR**1**, showing diamonds of irregular sizes, a lack of periodicity, and a semiconducting gap where the conductance is heavily suppressed. **d,** Typical stability diagram for a MGNR**2**-made SET. The conductance between source and drain is given in units of the conductance quantum G_0. To my knowledge, the periodicity and clarity of these transport features rank amongst the most distinct, laying a crucial foundation for comprehensive studies.

The gate is provided by either an n-doped Si/SiO_2 backgate wafer ($t_{ox} \simeq 300\,\mathrm{nm}$) or a local Pd electrode etched into undoped Si and covered by HfO_2 ($t_{ox} \simeq 10\,\mathrm{nm}$);

reference for the former is Fig. 6.1a, where for the latter is Fig. 6.1b. The distinction between the two devices can be discerned from the accessible gate voltage range. With a 2T architecture, the gate coupling with the MGNR is low, thus necessitating high gate voltage ($V_G = \pm 80\,V$) values to encompass a sufficient number of electronic states for a given bias window. In contrast, the gate coupling in a 3T geometry is significantly higher, facilitating similar energy ladders at an order of magnitude lower voltage values ($V_G = \pm 4\,V$).

As mentioned in Ch.3, MGNRs are added by drop casting from solutions, with a yield of about 5 devices out of 100 electroburned gaps, and the existence of a nanoribbon connecting the two leads is identified as a sharp increase of the conductance $G = \partial I_{SD}/\partial V_{SD}$ from $G < 1\,nS$ to $\simeq 100\,nS$.

In a SETs, an electron tunnels through a single channel (quantum transport level). The energy associated with this level is governed by V_G, and can be brought in resonance with the leads Fermi levels. Because of Coulomb repulsion, an electron already in the conduction channel would block the influx of more electrons, thus suppressing the device conductance.

The anticipated high degree of bundling for MGNR**1** hindered the production of SETs with only one ribbon spanning the nanogap; typical stability diagram manifests a substantial region of suppressed conductance (Fig. 6.1c and Fig. 6.2c), corresponding to the bandgap of semiconducting MGNRs, followed by multiple overlapping Coulomb diamonds of varying sizes. From the height of the diamonds, and knowing the ribbon width and length [274], some of the most discernible diamonds yield $l_{MGNR} \simeq 28$, 90, 40, 17, 108, 60, 50, and 38 nm, and no sharp features inside the diamonds could be distinguished.

In stark contrast, SETs produced with MGNR**2** exhibit very clean conduction characteristics and a level of detail equivalent to ultra-clean CNTs (Fig. 6.1d and Fig. 6.2d). The diamonds are distinctly periodic, have identical slopes and diameters, and well-defined edges, indicating that each device has a single nanoribbon. Parallel to the Coulomb edges, the excited states are observable as intense, conductance

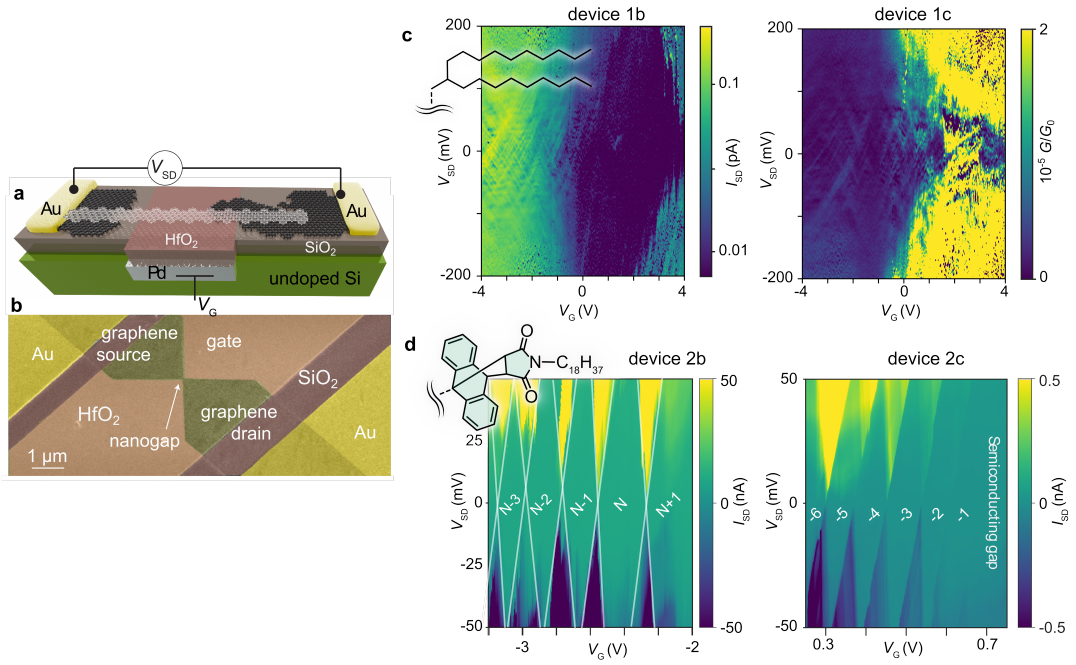


Figure 6.2: **a,** Scheme of the 2T-SET device, with the MGNR depicted in white and side groups simplified for clarity. Graphene leads (dark grey) are onto to Au pads. The gate is a Pd electrode buried in undoped Si with a $\simeq 10\,\mathrm{nm}$-thick HfO_2 layer on top (bottom). **b,** False-color scanning electron microscopy images of typical junction. **c,** Two typical stability diagrams measured at $T = 20\,\mathrm{mK}$ with MGNR**1**. Large regions were the conductance is suppressed and the lack of well-defined Coulomb diamonds have been reported for poorly-defined nanoribbons [177, 266]. **d,** Stability diagrams for MGNR**2** devices displaying ultra-clean features similar to those obtained with best performing CNTSETs [131]. Diamonds are labelled with regard to an arbitrary number of electrons, N, whenever possible.

lines running parallel to the diamonds. The high contact-impedances observed are likely influenced by contact lengths limited by the MGNR length [287], which is less than the transfer length.

Overall, across various production batches and cooldown processes, I assessed 10 devices with MGNR1 and 10 devices with MGNR2 at cryogenic temperatures. Of the 10 devices using MGNR1, none displayed clear periodic features, discernible Coulomb diamonds, or demonstrated stable repeatability in measurements. On the contrary, I successfully measured as many as 6 devices with MGNR2, each of them qualitatively exhibiting similar Coulomb diamond sizes and gate voltage periodicity.

Delving deeper into one of the diamonds reveals outstanding clarity of the fea-

tures, facilitating comprehensive characterisation of transport phenomena. Diamond edges are muted, and a cascade of multiple excited states becomes distinctly visible (Fig. 6.3a), with a common attribute of $\hbar\omega_\nu = (7.5 \pm 0.1)\,\mathrm{meV}$ across all devices. An observed suppression of edge-conductance at higher T is presented in Fig. 6.3d. Reminiscent of the Franck–Condon principle in molecular spectroscopy, the coupling of electron and vibron might hinder transport for lower vibronic states, as electrons are preferentially transmitted when nuclear positional shifts are at a minimum.

6.3 Analysis of the Franck–Condon Conductance Blockade

I shall now attempt to explain the suppression of conductance lines parallel to diamond edges within the Franck–Condon blockade framework. According to standard electronic absorption theory, the spectrum resulting from the excitation with wavelenths within the vibrational region is a progression of absorption peaks rising separated by multiples of the vibrational quanta, and with the intensity lines of the spectrum that follows a Poisson distribution [288]. The amplitude of each peak in the vibrational progression is governed by the Franck–Condon factors, which are defined as transition probabilities, according to standard quantum theory, between the vibrational states of two different electronic states (ground and excited states) over many vibrational modes.

If I assign the vibrational-state excitations to the equispaced parallel conductance lines within a Coulomb diamond, I might be able to link the Franck–Condon factor to the DC conductance maxima. Thus, by extracting and averaging within a bias window parallel lines to the Coulomb edges, I observed that the conductance peaks follows a known progression [131].

Franck–Condon theory describes the coupling electron–vibron γ, i.e. how an addition of an electron changes the electronic wave function and produces a shift in the equilibrium coordinate of a molecule. If γ is large, then charge transport may be suppressed through low-lying vibronic MGNR states (Fig. 6.3b). Furthermore,

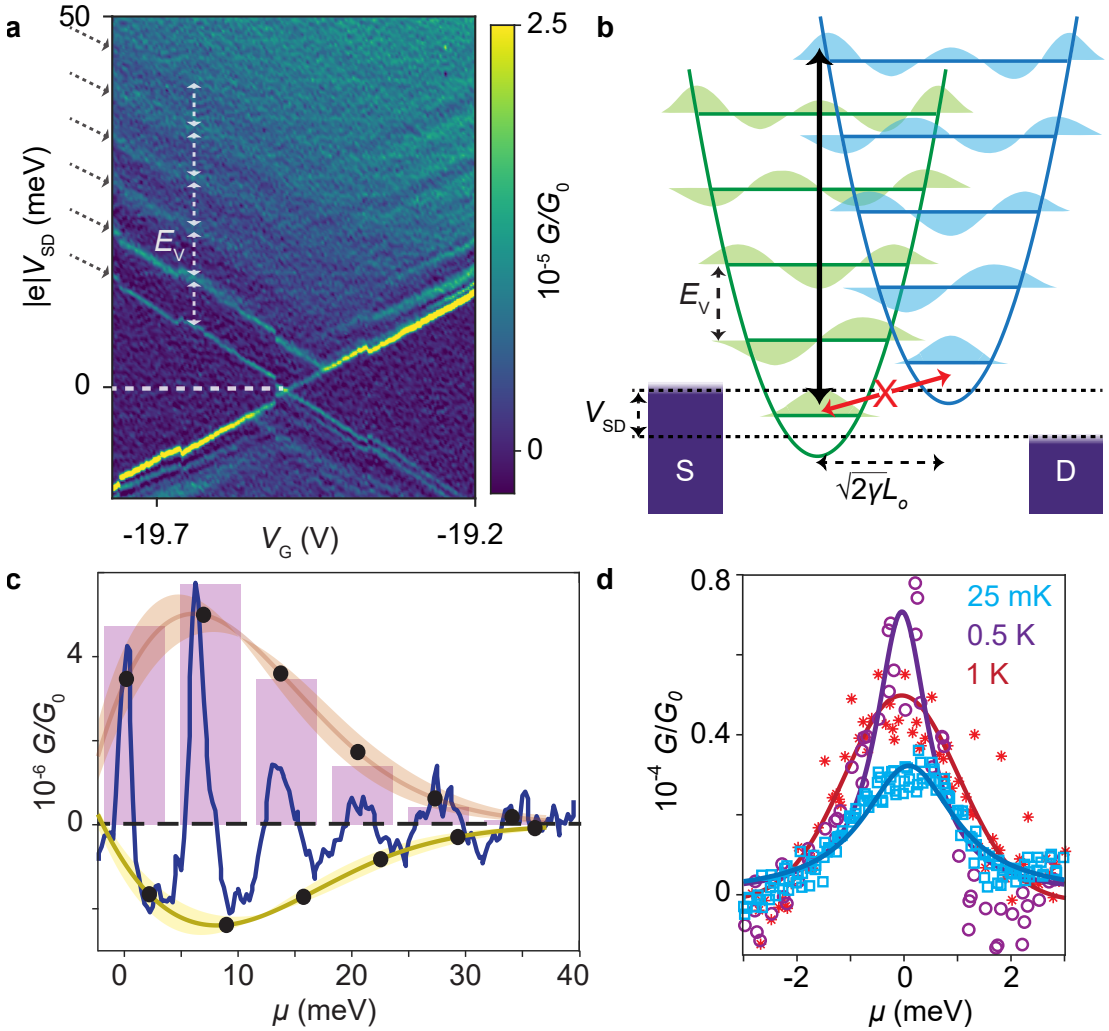


Figure 6.3: **a,** Detail of vibrational state suppression in the differential conductance G, in units of quantum conductance G_0 versus V_{SD} and V_G. Arrows indicate the excited states, which I assign to vibrational given the equal spacing between them. $T = 20\,\mathrm{mK}$. **b,** The Frank–Condon blockade in the transport properties of nanodevices is depicted schematically, with the equilibrium coordinates for two adjacent charge states (green and blue) represented horizontally. Strong vibronic coupling suppresses ground-to-ground transitions exponentially, whereas ground-to-excited-state transitions become viable at higher bias. **c,** Blockade peaks as a function of the chemical potential μ as experimentally observed (blue line) and as expected by Frank–Condon theory for maxima (orange) and minima (yellow). Poisson histogram for the vibrational quanta (puple) is superimposed. **d,** Lifting of the Frank–Condon blockade for a transmission channel upon increasing the temperature from 25 mK (blue) to 1 K (red), together with Lorentzian fits to the data (solid lines).

Franck–Condon theory predicts that the peak conductance of the vibronic transitions, $G_n^{\max}$, follows a Poisson distribution in terms of the vibron quantum number n,

$$G_n^{\max} = \frac{\gamma^n}{n!} e^{-\gamma}, \tag{6.1}$$

By fitting the averaged conductance trace within a Coulomb cone with Eq. 6.1 I extract an electron–vibron coupling $\gamma = 1.5 \pm 0.2$. Fig. 6.3c shows the progression of the vibronic peaks, which arise when an electron tunnels through a molecular orbital and simultaneously excites a molecular vibrations [289].

A hint of Franck-Condon suppression apparent from Figure Fig. 6.3d where an increase in T from 25 mK to 0.5 K is followed by an increase in G. A further increase to 1 K decreases G due to significant temperature broadening. The same figure was used to calculate the electrode–MGNR coupling energy $\Gamma \simeq (185 \pm 30)\,\mu\text{eV}$, in line with the estimate detailed in the previous chapter.

6.4 Simulation of the Stability Diagram

I shall now try to validate our conclusions exposed in the previous section about the possibility of having a Franck–Condon suppression of the conductance by reproducing the experimental observation with a simulated model. I shall use, to this end, the model exposed in Sec. 2.3.2, and assume that the molecular energy level, $\mu = C_S V_{SD} - C_G V_G$, shifts with both bias and gate voltages. The calculated conductance G (Tab. 6.1 reports the simulation parameters) is plotted as a function of V_{SD} and V_G, and is displayed next to an experimental stability diagram in Fig. 6.4.

The calculated and experimental stability diagrams match each other extremely well. Importantly, the calculated diagram shows that the single-mode–environment model reproduces the main features of our data, i.e. conductance lines equally spaced by $E_v \simeq 7.5\,\text{meV}$, a significant contribution from the phonon bath and conductance asymmetry with bias. The calculated stability diagram contains additional conductance sidebands in the blocked regions that are not present in the experimental diagram. I explain the increase of background conductance at high bias as the result of the coupling with an increasing number of phonon modes in the

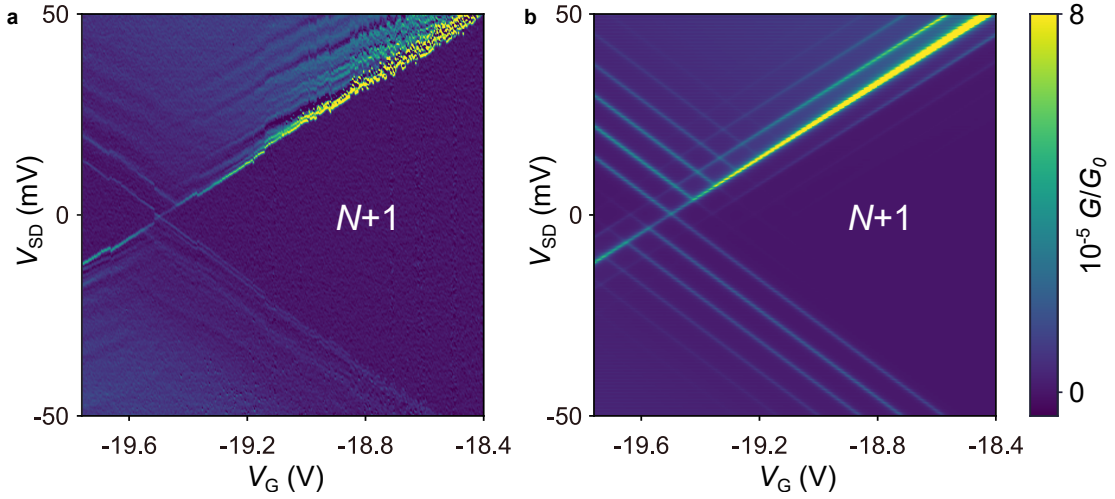


Figure 6.4: Maps of the conductance for the same transition as in Fig. 6.3a, plotted on identical colour scale. **a,** Experimental conductance map for the same charge transition of Fig. 6.3a. **b,** Simulated conductance using Eq. 2.19–2.26 and the parameters from Tab. 6.1. Integrals were evaluated using the Simpson's rule as implatemented in Numpy.

Table 6.1: Simulation parameter for the vibrational electron transport model

T (mK)	$\hbar\omega_q$ (meV)	$\hbar\omega_c$ (meV)	$\hbar g_q$ (meV)	λ (meV)	Γ_S (meV)	Γ_D (meV)	C_S (fF)	C_G (fF)
25	7	8.5	20	150	1.2×10^{-3}	0.5	0.54	2.25×10^{-2}

bath. This hypothesis would also explain the different tunnelling rates I had to use to reproduce the spectrum, which are the reason for the observed V_{SD} asymmetry, and may be caused by larger contact length L_c between the MGNR and the drain than the source lead. The model does not take into account the slanted conductance lines originating from the leads and does therefore not reproduce these.

6.5 Role of the Maleimide Groups: *Ab-Initio* and Statistical Analysis

Since our MGNRs are synthesised with molecular precision through bottom-up synthesis, I deem appropriate to calculate from *ab-initio* the vibrational properties of a simplified MGNR structure and to attempt elucidating the origin of the Franck–Condon blockade and the nature of the vibrational mode I identified through

the conductance measurements.

DFT calculations were performed using the GGA–PBE functional as implemented in the Siesta package [118, 290]. One structure was calculated with edges terminated by hydrogen atoms, another with anthracene groups, and the third with maleimide groups (Fig. 6.5 and Fig. 6.6). Along the non-periodic directions an adequate number of vacuum states were added in order to avoid unwanted interactions. An energy cut-off of 400 Ry was used together with a $20 \times 1 \times 1$ Monkhorst–Pack grid constructed along the three Cartesian directions. The structure was optimized until the maximum force on the atoms was less than $0.01\,\mathrm{eV\,\AA^{-1}}$. The dispersion relation is calculated with a supercell size of $3 \times 1 \times 1$, where 3 represents 3 unit cells along the periodic direction, and atomic displacements of the Γ phonon mode are visualised with the software XCrySDen. The phonon disperions were calculated using the same numerical constraints.

Firstly, Fanmiao Kong calculated the effect the anthracene groups have on the atom displacements compared to the base case (Fig. 6.5). I can qualitatively assess the emergence of new phonon modes, the majority of which are exclusive to the anthracene groups, and a few of which correlate to the MGNR backbone. In addition, the three acoustic phonons combine with optical phonons, resulting in the constant dispersion of new hybrid phonons throughout the Brillouin zone. Particularly, the dispersion relation reveals that the phonon mode at $\hbar\omega_\nu = 7.50\,\mathrm{meV}$ is robust at the Γ point and experiences mode mixing at certain wavevectors.

In addition, at the Γ point one mode is reduced from 7.86 meV to 7.48 meV, matching the experimental value (Sec. 6.3) much more accurately. I conclude, using the visualisation tool, that this phonon mode may be responsible for the MGNR backbone bending as well as the quenching of the amplitude oscillation of the atoms along the edges.

Secondly, I looked at how the inclusion of maleimide groups on the phonon dispersion following the introduction of the maleimide groups (Fig. 6.6). Compared to the anthracene, the acoustic mode at $\hbar\omega = 7.48\,\mathrm{meV}$ induce a stronger ribbon backbone bending (Fig. 6.6d), as also put in evidence by the greater mode

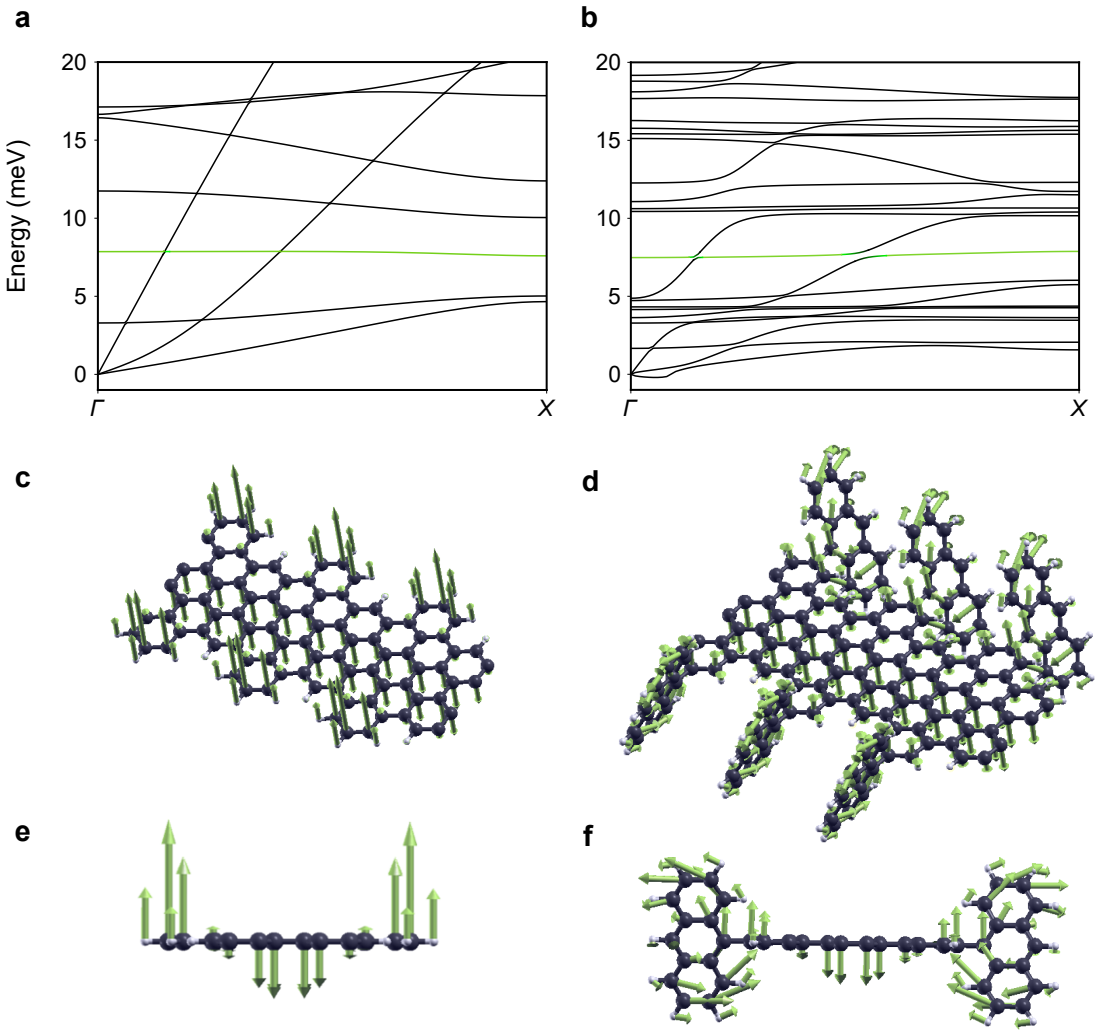


Figure 6.5: a, b, Energy dispersion of the lowest vibrational modes when anthracene groups are attached to the edges, with the one at 7.5 meV highlighted in green. **c, d,** Relative displacement of the atoms for the 7.5 meV vibrational mode at Γ point. **e, f,** Side view of the relative displacement for the 7.5 meV vibrational mode at Γ point.

amplitude. Furthermore, I note that the displacement of core-backbone atoms remains approximately constant, whereas cove-edge atoms become more rigid. This qualitative observation seems to suggest that bending will be primarily confined to the backbone centre when 3D side groups are introduced.

Despite being rigorous, our analysis may be incomplete. In fact, while DFT is commonly regarded as the *de facto* standard for calculating molecular and physical properties in a reasonable amount of time, issues sometime arise when accurate

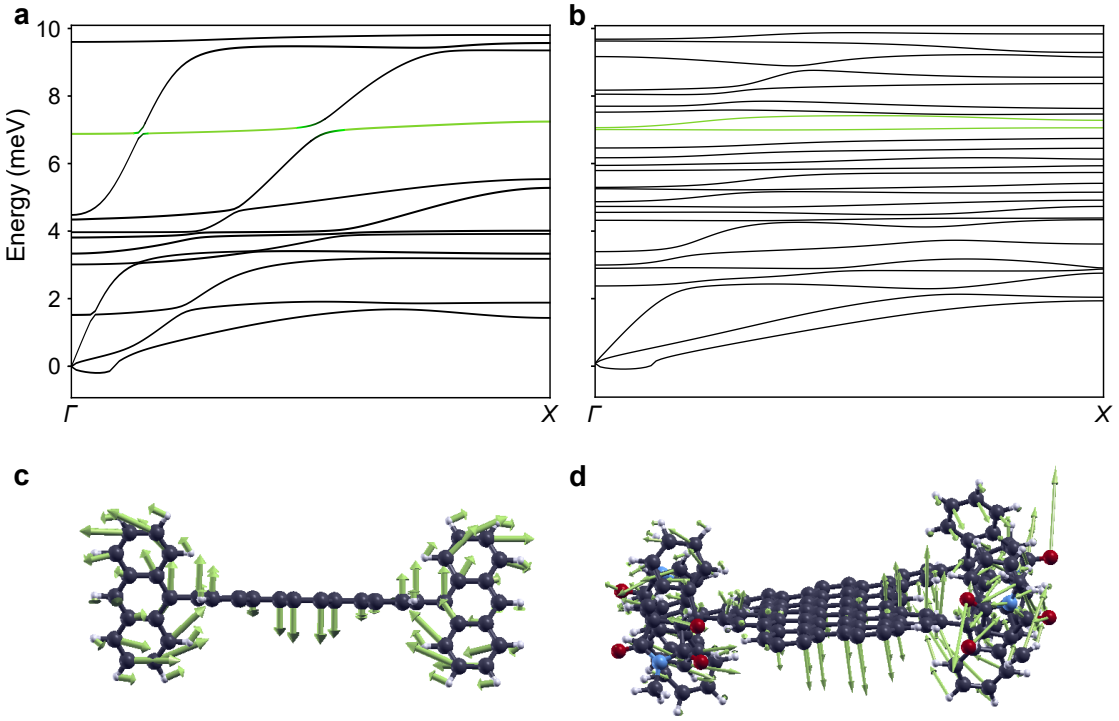


Figure 6.6: a, b, Energy dispersion of the lowest vibrational modes when maleimide groups are attached to the edges, with the one at 7.5 meV highlighted in green. **c, d,** Side view of the relative displacement of the atoms for the 7.5 meV vibrational mode at Γ point.

estimates are required. Because our system includes not only the ribbon but also the graphene leads, the question of whether maleimide groups promotes or not the dispersability of MGNRs in a solvent, thus boosting the chances to have ultra-clean SETs may still arise. In order to answer this question, I will use a simple yet powerful idea from standard statistics.

In order to exclude the possibility that the observed number of SETs (see also Appendix A) are produced merely by chance, I shall use statistics to test if out of the total number of devices the SET formation probabilities when either MGNR**1** or MGNR**2** are employed are generated from the same statistical process (null hypothesis, H_0). By setting the p-value threshold at the common value $p = 0.05$ means that I have a 5% chance of falsely concluding that 3D bulky groups do not promote the formation of ultra-clean SETs, meaning that the SET formation probability are generated by the same statistical process.

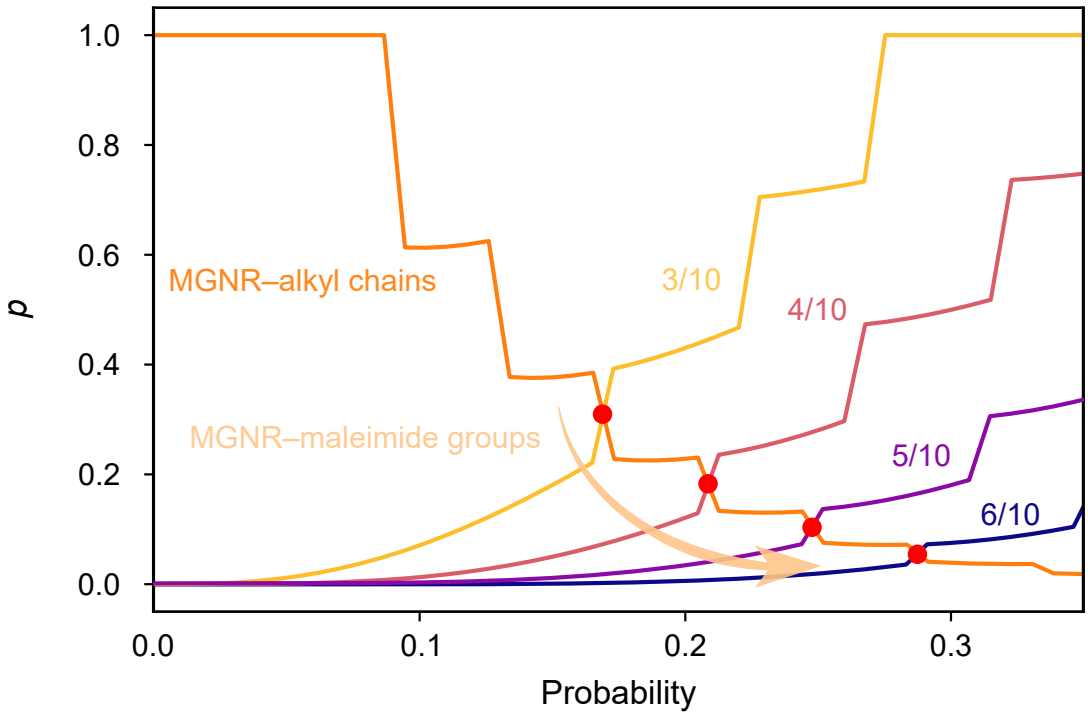


Figure 6.7: p-value as a function of the likelihood of obtaining a SET (probability, for short) when using MGNR**2**. The numerical figures represent the number of observed SETs relative to the overall number of survived at the thermal schock when loaded in the fridge. The p-value decreases by more than an order of magnitude as the number of observed SETs increases by 2 units.

Table 6.2: Statistics of the SET formation probability of all the measured devices.

MGNR Type	**1**	**2**	**2**	**2**
Number of Devices Cooldown	10	10	10	10
Number of SETs per chip	0/10	3/10	4/10	6/10
p value	—	0.307	0.182	0.056

I made one chip by depositing MGNR**1** on top of GTJs and three by dropcasting MGNR**2**. I then wirebonded 10 devices on each chip and cooled them down at 25 mK. I counted the number of SETs for each chip by measuring high-resolution full-range stability maps and selecting whether or not to include a device based on visual inspection.

Assuming I can pick up a SET with equal chance by dropcasting either MGNR**1** or MGNR**2**, I can run a binomial test to get the p-value of obtaining 0/10 SETs when MGNR**1** is dropcasted. The results are stored in Tab. 6.2 and shown in Fig. 6.7.

The observations from the study suggest that, with 95% confidence, the statistical test does not definitively ascertain whether the SETs obtained using the 3D bulky groups occurred by chance. This conclusion warrants further elucidation. Primarily, the validity of the statistical analysis rests upon the repetition of the experiment under identical conditions. However, in this scenario, the number of detected SETs across different measured chips is contingent on the total number of devices that withstood the thermal shock transitioning from 50 Kelvin to cryogenic temperatures. This condition does not eliminate the possibility that additional SETs were produced but remained unmeasured due to the interference of this secondary process with our statistical analysis.

Secondly, the volume of data accumulated may not be adequate for a comprehensive statistical analysis. Specifically, smaller samples, those comprising less than ten observations, are prone to underestimate the population standard deviation and their means often deviate from the true population mean. This phenomena is well documented in the statistical literature [291, 292]. Consequently, I cannot definitively dismiss the hypothesis that maleimide groups are integral to the fabrication of ultra-clean SETs. However, from a statistical perspective, I also cannot confirm it based on the current data. Future research may consider employing a cryogenic multiplexer to enhance the number of devices that can be measured with a single cooldown by an order of magnitude. This approach would expand the sample size, thereby strengthening the statistical robustness and accuracy.

6.6 Discussion

A close inspection of the low-temperature Coulomb oscillations has revealed the presence of conductance suppression for small eV_{SD}, which we explained within the Franck–Condon conductance-blockade mechansim. When compared to γ values reported for in-situ generated suspended CNTs, our findings are lower for some but higher for others (Tab. 6.3), and suggest enhanced electron–vibron coupling in graphene nanoribbons [293].

Table 6.3: Electron–vibron coupling has been described in the literature for a variety of devices.

Material type	γ	Reference
C_{60}	$\ll 1$	[295]
CNT	0.5–1.1	[294]
C_{140}	$\simeq 1.4$	[296]
MGNR	1.5 ± 0.2	This work
C_{60} (graphene junctions)	3	[297]
CNT	3.3	[131]
Fe_4 SMM	4.2	[298]

Remarkably, our values are equivalent to those obtained in molecular junctions comprising C_{140}, but far greater than those observed in base C_{60}. We can hypothesise that low-energy modes in the substrate phonon bath may facilitate transport near the diamond edges, so suppressing the true magnitude of the Franck–Condon effect. Decoupling the nanoribbon from the substrate environment via suspension should therefore result in higher γ values than for nanotubes [294]. Furthermore, first-principles studies have suggested the existence of edge-localised nonlinear modes in AGNRs with energies 6.8–8.7 meV [299], which would encompass our experimental and DFT findings. Based on these, we conclude that the electronic wave function of GNR have a large non-zero overlap with the bending mode at $\hbar\omega_\nu \simeq 7.5\,\text{meV}$, resulting in high electron–vibron coupling which would explain the larger conductance compared to lower-lying vibrons [300].

As we saw in Ch. 2, the nanotube electronic structure is heavily dependent on the tube chirality, length, and radius, which are difficult to control and may greatly vary across devices. On the other hand, MGNRs can now be engineered with molecular accuracy, thus allowing the production of devices with more uniform performance. Currently, one of the biggest challenge is the synthesis of nanoribbons of with length spanning several hundreds of nanometer, which should lead to a higher control when positioned on top of devices.

6.7 Outlook and Perspectives

The presence of sterically-hindred chemical functionalisations grated onto the edges has enabled GNRSETs where vibrational states can be probed through transport spectroscopy, revealing level of details comparable with ultra-clean CNT embedded in a SET [130, 294]. Investigations of mechanical and quantum vibrations are paramount when excitations in the MHz–GHz range are sent to excite and manipulate spins [112, 301, 302]. We therefore consider this work a starting point in that direction, which might lead to the first the manipulation of qubits embedded in all-carbon molecular structure, similar to those proven in semiconductor quantum dots [303, 304].

By reducing the lattice vibrations by rationally design MGNR, one could, in principle, increase the spin–phonon coupling, leading to precited long coherence times [305]. This platform could be realised, for example, by either grafting onto the edges porphyrin rings where the metal ion is a single-molecule magnets, or direct substitutional inclusion within the graphene lattice.

Theoretical and numerical estimates have also suggested several reasons why MGNRs may be an appealing class for spintronic devices. In particular, spin–relaxation time between 10–1000 ms have been predicted, when the dechorence mechanisms are limited to only single-phonon processes [306]. Albeit these predictions are very encouraging, experimental evidences reported that a single-phonon process is unrealistic and that two-phonon processes should also be studied, which may be lead to lower spin–lattice relaxation times [195]. Moreover, spin-diffusion-length calculations suggested values of approximately 17 µm in presence of an extrinsic spin–orbit coupling, and that hot-spot processes could futher increase these values [307]. Both spin-lattice relaxation times and spin-diffusion lengths have been linked to the $l_{\mathrm{GNR}}/w_{\mathrm{GNR}}$ ratio, suggesting increments for larger ratios. Even though it cannot be excluded that longer GNRs will pose more questions, we believe atomically-precise long ribbons ($l_{\mathrm{GNR}} \geq 100\,\mathrm{nm}$) could be a suitable platform for addressing all these challenges.

6.8 Project Overview

MGNRs**1** were supplied by the group of Akimitsu Narita, whereas MGNRs**2** were synthesised in Dresden by the group of Xinliang Feng. The Franck–Condon analysis was undertaken by Dr Simen Sopp (see also [231]), whereas I acquired temperature data, and Fanmiao Kong calculated the phonon dispersion. Dr Alex Gee supported me in fabricating the devices when I was compelled to stay out of the lab for more than a month owing to covid-19 infection and subsequent health issues that necessitated medical care.

7

Chemical Doping of Graphene Nanostructures

Contents

7.1 Introduction 141
7.2 Numerical Study of the Edge Doping 143
7.3 Methoxy-Edge-Decorated MGNRFETs 147
7.4 Heteroatoms-Doping-Embedment in MGNRs 151
7.5 Discussion 163
7.6 Outlook and Perspectives 164

7.1 Introduction

The idea of using chemical functionalisations to induce a preferential doping in carbon nanostructures is not new. Several proposals have indeed demonstrated the possibility to tune the conductance of ropes [95] and individual [96, 308] carbon nanotubes by introducing dopants onto the structure, thus leading to p–n junctions and Esaki diodes.

When atoms with different number of valence electrons are placed into the honeycomb lattice of graphene nanoribbons, a charge transfer occurs based on the relative position of the MGNRs Fermi level with the HOMO and LUMO of the

dopant atom. For example, if a dopant HOMO is greater than the Fermi level of the ribbon, a charge transfer from the dopant to the ribbon occurs, and the dopant acts as a donor. On the other hand, when the LUMO is less than the Fermi level of GNR, a charge transfer in the opposite direction occurs, and the dopant acts as an acceptor.

Graphene can be doped to be p-type or n-type through chemical strategies by adsorbing dopant atoms onto the honeycomb lattice. When graphene is p-doped, the Dirac points are elevated above the Fermi level, whereas n-type doping lowers the Dirac points. In general, molecules having electron-withdrawing groups result in p-type doping, while molecules with donating groups result in n-type doping.

One of the most appealing aspects of graphene nanoribbons is that, thanks to bottom-up synthesis, substitutional doping, i.e. the substitution of carbon atoms with atoms carrying a different number of valence electrons, would enable chemically controlling electronic properties at a very fundamental level, overcoming a major limitation of solid-state semiconductors. Frontier-crystal-orbitals wave functions are predicted to be fully delocalized across the ribbon width, with electronic bandgap of cove-edged GNRs infinite ribbon settling around 1.70 eV, and mobilities values in the order of thousands $\mathrm{cm\,V^{-2}\,s^{-1}}$ for both electrons and holes [139].

This chapter examines the impact of introducing several chemical functionalisations from both a numerical and experimental standpoint. Specifically, DFT simulations will be used to analyse different functional groups and make predictions regarding the ensuing electrical characteristics. Then, we will examine a completely innovative method for introducing chemical functionalisations within MGNRs, namely the insertion of porphyrin units bearing transition-metal ions via the formation of heterojunctions.

The supply of porphyrin–GNRs (pGNRs) was courteously provided by Dr Qiang Chen and Professor Harry Anderson. My colleague, Fanmiao Kong, provided assistance in setting up the electronic computations on the ARC supercomputing centre. We extend our gratitude to the centre for their continued cooperation

and assistance, particularly when we encountered issues with jobs not executing as planned.

7.2 Numerical Study of the Edge Doping

Collaborators from the Feng group in Dresden and the Müllen group in Mainz provided graphene nanoribbons with different functional groups along the edges. These ribbons share the same aromatic core and have widths ranging from $w_{\mathrm{GNR}} \simeq$1.1–1.2 nm with lengths which follow a gaussian distribution (Fig. 7.1). This last point comes from that the separation between ribbons having different length is carried out by size-exclusion chromatography means, where the average residence time in the pores created by the column packing depends on the effective size of the analyte molecules. MGNRs larger than the average pore size of the packing are excluded and thus suffer essentially no retention; such species are the first to be eluted and are ribbons with longer lengths. On the other hand, ribbons having diameters significantly smaller than the pores may penetrate or permeate throughout the pore network and are thus retained inside the column for the greatest time. Unfortunately these ribbon featured very poor solubility, even after several sonication and dilution cycles in most of the common organic solvents. Since it was not possible to carry out a thorough experimental study at the device level, we have investigated the structural and electronic properties of GNR–H and compared them with the ones of GNR–OMe, GNR–Br, GNR–Cl, and GNR–Anthracene through DFT simulations. Ab-initio calculations were performed by using the local-density approximation (LDA)-CA and the generalised-gradient approximation (GGA)-PBE exchange–correlation functionals as implemented in Siesta [118, 290]. To simplify the geometry, alkyl chains were removed and replaced with hydrogen atoms. Sufficient vacuum distance is added along the non-periodic directions to avoid unwanted interactions. Numerical atomic pseudopotential was used together with an energy cut-off of 400 Ry. Monkhorst Pack k-point-grid was chosen to be

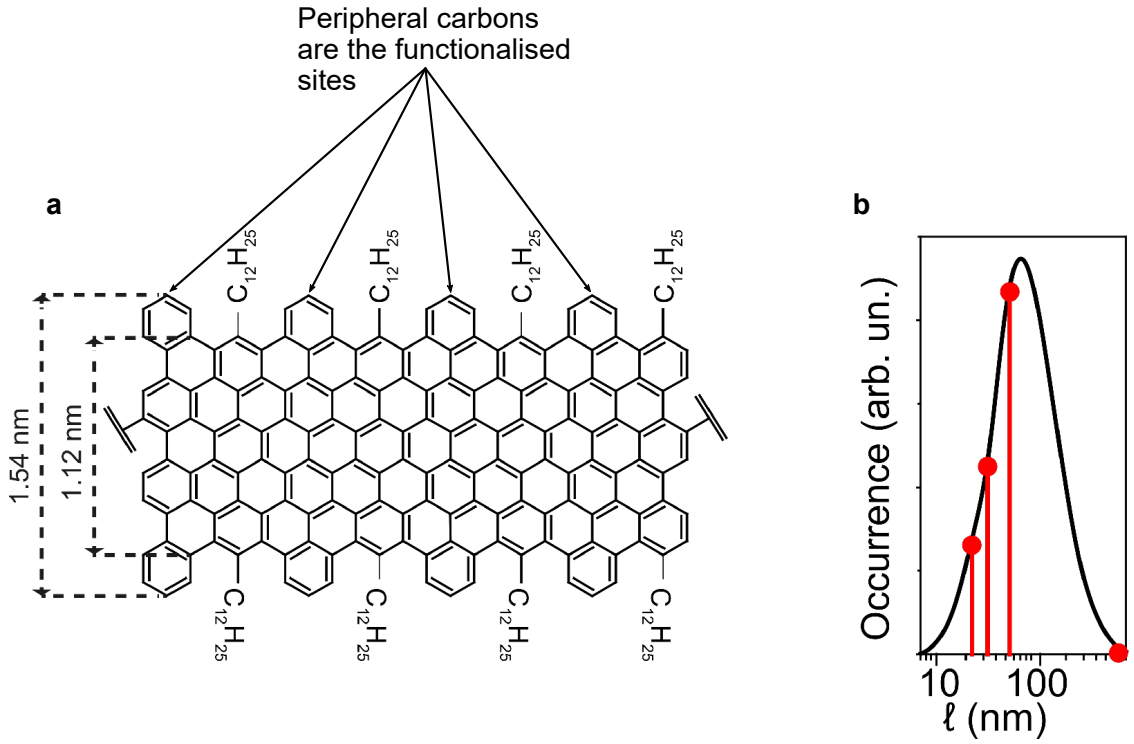


Figure 7.1: a, Structure of a 4-Cove graphene nanoribbon. Highlighted are the carbon sites where dopant atoms are introduced through chemical synthesis. **b,** Distribution of MGNR lengths l as obtained from size-exclusion chromatography on the polymerized molecular precursor (black). Red dots and vertical lines identify various length obtainable with different elution curves. Adapted from [309].

$(20 \times 1 \times 1)$ along the three Cartesian directions. The structure is optimized until the maximum force on the atoms is less than $0.01\,\mathrm{eV\,\AA^{-1}}$.

Fig. 7.2 shows the comparison between the base case and the same ribbon functionalised with anthracene along the edges. Compared to the base case, the introduction of anthracene groups introduces sharpe features in the DOS in correspondence of flat lines in the band structure, which can be assigned to a more discrete energy spectrum. This observation could be combined with NEGF estimates about the reactivity of MGNRs, in particular about the even–odd conductance effect [310]: for functional groups with an odd number of rings, the local density of states shoudl reside on the site of the guest molecule, which is bound convalently to the nanoribbon, resulting in a non-negligible interaction between the continuum of states in GNR and the localised state on the edge-attached adduct.

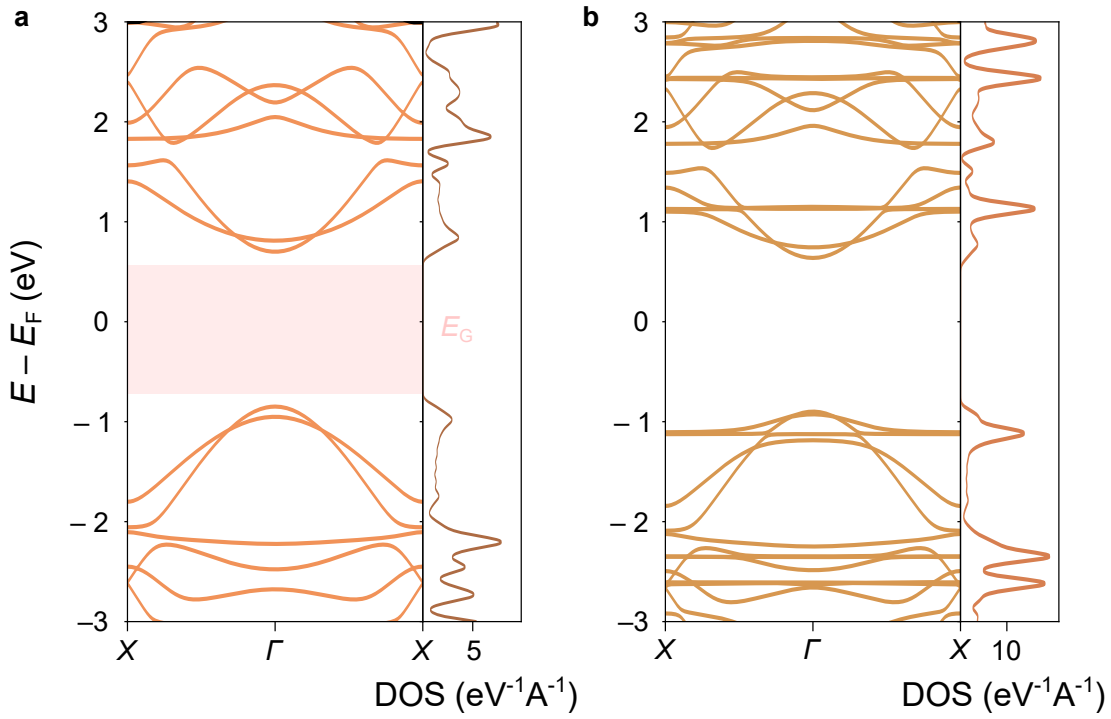


Figure 7.2: **a,** Band structure and density of states for a 4-Cove GNR–H and **b,** a 4-Cove GNR–Anthracene calculated with the exchange–correlation functional GGA-PBE.

Furthermore, at this level of theory it appears that, when anthrance groups are introduced along the edges, the particle–hole symmetry is broken for low excitation energies, as the band structure spectrum is no longer symmetric with respect to the Fermi energy. Fig. 7.3 compares the band structures and DOS between GNR–H (top-left) and other chemical dopants. In the case of GNR–OMe, four electron-donating methoxy groups per repeating unit have been considered, while six negative inductive Clorine groups were considered for GNR–Cl and GNR–Br.

Firstly, it is possible to observe the frontier bands in case of GNR–OMe are $\simeq 0.5\,\text{eV}$ higher than those of GNR–H, likely due to charge redistribution induced by the methoxy groups. Despite the fact that both the bromine and chlorine substitutions share electrons with the ribbon preferentially via σ-bond, GNR–Cl exhibits a more pronounced bandgap contraction (Tab. 7.1) and a decrease in effective mass m^* at the Γ point of the conduction band, as demonstrated by the more steep curvature. The same holds true for the case of methoxy substitution. As the

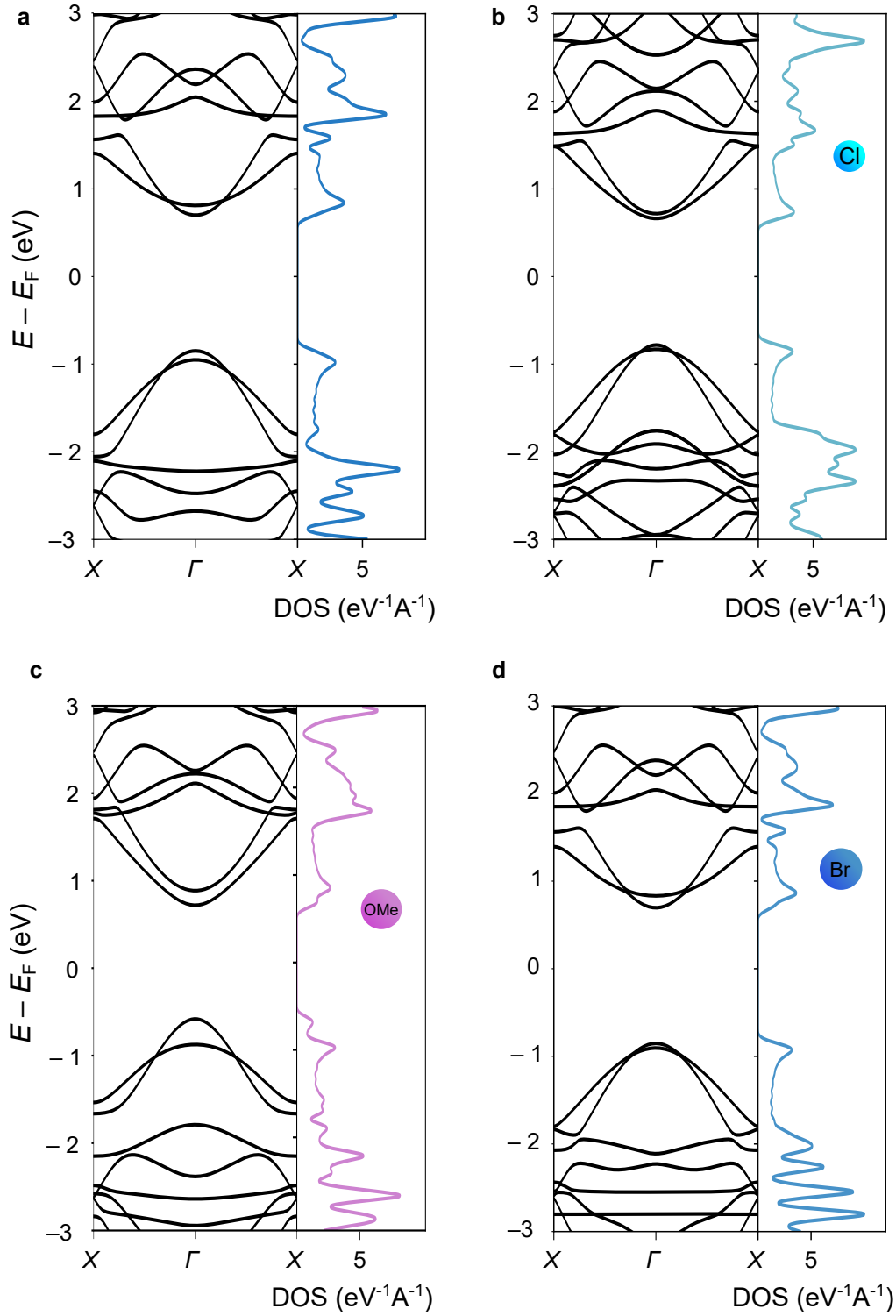


Figure 7.3: Band structure and density of states for graphene nanoribbons decorated with various electron donors or acceptors resulted after applying the GGA approximation for the exchange–correlation energy term.

Table 7.1: Calculated bandgaps using different exchange–correlation implementations.

Edge functionalisation	LDA − CA (eV)	GGA − PBE (eV)	ΔE_g(CA) (%)	ΔE_g(PBE) (%)
–H	1.57	1.55	–	–
–Anthracene	1.55	1.54	−0.96	−0.77
–Br	–	1.55	–	−0.04
–Cl	1.45	1.44	−7.62	−6.77
–OMe	1.31	1.3	−16.21	−16.1
–CH3	1.56	1.55	−0.44	−0.25
–CN	1.58	1.56	+0.62	+0.74
–NH2	1.36	1.35	−13.03	−12.9
–COOH	1.55	1.53	−0.84	−0.98
–NO2	1.47	1.47	−6	−5.24
–OH	1.47	1.46	−5.82	−5.82

charge-carriers effective mobility μ_{eff} is proportional to the inverse of their effective mass, GNR–OMe could display higher mobilities, leading to an increase in the output current and possibly to better device performance. On the other hand, no appreciable deviation from the base case is observed for the ribbon functionalized with –Br groups, which could be explained by a lower electronegativity and consequently a lower ability to induce charge rearrangements of the ribbon frontier orbitals.

7.3 Methoxy-Edge-Decorated MGNRFETs

In order to test the idea of chemically-induced doping, we fabricated tw FETs using GNR–H (base case) and GNR–OMe (methoxy). As reported in Tab. 7.1, methoxy groups are expected to induced the largest relative change in the bandgap compared to the base case.

GNR–OMe were provided by Dr Alicia Götz and prof. Akimitsu Narita from the Okinawa Institute of Science and Technology. The ribbons have a structure similar to the one reported in Fig. 7.1a, where the peripheral carbons are functionalised with methoxy groups. The Hammett equation classifies a methoxy substituent in the para positions of a benzene ring as an electron-donating group, but it will behave as an electron-withdrawing group if placed at the meta position [311]. The methyl free rotation is expected to induce a considerable change in the Hammett prediction

becuase of the steric effect, leading to a change in the ortho position reactivity, which otherwise follows the same trend as the para position [312]. GNRFETs were

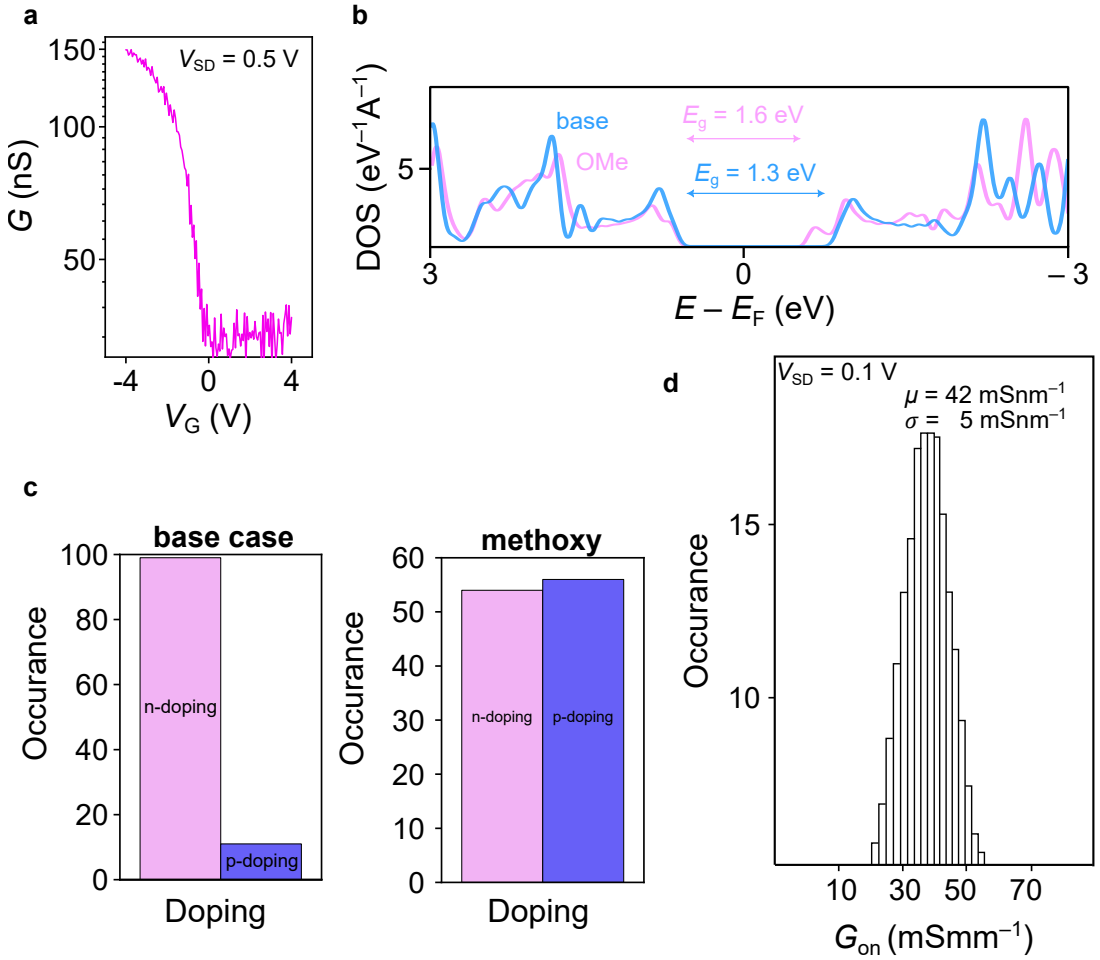


Figure 7.4: a, Typical transfer G–V_G curve of a p-type methoxy-functionalised GNRFET with 0.5 V of biase applied. **b,** Calculated electron states density at DFT–PBE level for GNR–H (base case) and GNR–OMe. **c,** Compared to the base case, when methoxy decorations are introduced there is a significant increase in the number GNRFETs displaying p-type doping. **d,** Histogram for the on-state conductance normalised by the channel width W_{ch}.

fabricated as detailed in Ch. 3. Fig. 7.4a shows a typical transfer characteristics curve with $I_{on}/I_{off} \simeq 10^1$, that is about three order of magnitude below digital application requirements [35]. Numerical DFT calculations using the PBE pseudopotential suggest that the bandgap could shrink by a $\simeq 16\%$ (Fig. 7.4b) but because we are not including many-body corrections [313], this estimate is likely to be an

overestimate of the true value.

Albeit the quantification of how many functionalisations per ribbon length is challenging, we tried to establish the effctiveness of the methoxy groups by measuring the position of the charge neutrality point (CNP) in approximately hundred devices (Fig. 7.4c), as this reflects the graphene type of doping. For the base case, GNRFETs display almost exclusively n-type of doping (CNP at negative voltages), which confirms the observation of a larger bandgap for hydrogen-terminated GNR [314]. On the other hand, methoxy groups increased significantly the number of devices with p-type doping. We advanced two explanations for this observation. First, as we can see from Fig. 7.4b the valence band is more affected than the bottom of the conduction band, since it is upshifted compared to the base (blue) case. This effect has also been reported when GNR edges are decorated with electron-withdrawing groups [315, 316]. Second, the methoxy groups could introduce holes more efficiently thanks also to the reduced effective mass, which would correspond to a higher tunnelling probability, but also introduce p-type impurities in the transistor channel [30, 317].

We evaluated performance metrics after the introduction of the methoxy groups, namely the on-state conductance G_{on} (Fig. 7.4d) and the subthreshold swing SS (Fig. 7.5). Because surface techniques like as AFM could not be used, we estimated the number of graphene nanoribbons in the conduction channel as follows. Since graphene nanogaps produced through electroburning are $d \simeq 5\,\mathrm{nm}$, and the ribbons width is $w_{\mathrm{GNR}} = 1.12\,\mathrm{nm}$ (Fig. 7.1) we estimate that the channel width W_{ch} contains about 5 nanoribbons, thus $W_{\mathrm{ch}} \simeq 5\,\mathrm{GNR/nm}$. This number is supported also by similar estimates from Monte Carlo and STM [188, 213, 225]. The on-state conductance $G_{\mathrm{on}} = G_{\mathrm{sat}}/(w_{\mathrm{GNR}} W_{\mathrm{ch}}) = 0.03\,\mathrm{S\,mm^{-1}}$ and conductivity $\sigma = Gl_{\mathrm{GNR}}/w_{\mathrm{GNR}} = 1.4\,\mu\mathrm{S}$ is approximately two orders of magnitude lower compared to values from carbon nanotubes ($\sim 500\,\mu\mathrm{A\,\mu m^{-1}}$).

To quantify the concentrations of chemically-induced charge carries control over the number of functional groups along is necessary, but unfortunately our colleagues could not achieved it yet. Furthermore, one interesting hypothesis to test would be

to check if there is an edge-selectivity of the process, for example by adding chemical decorations on ribbons of varying width, and look for a width-dependent response: intuitively, narrower ribbons should yield an increased response, being the number of edge sites relative to ribbon basal plane sites higher. At room temperature, we

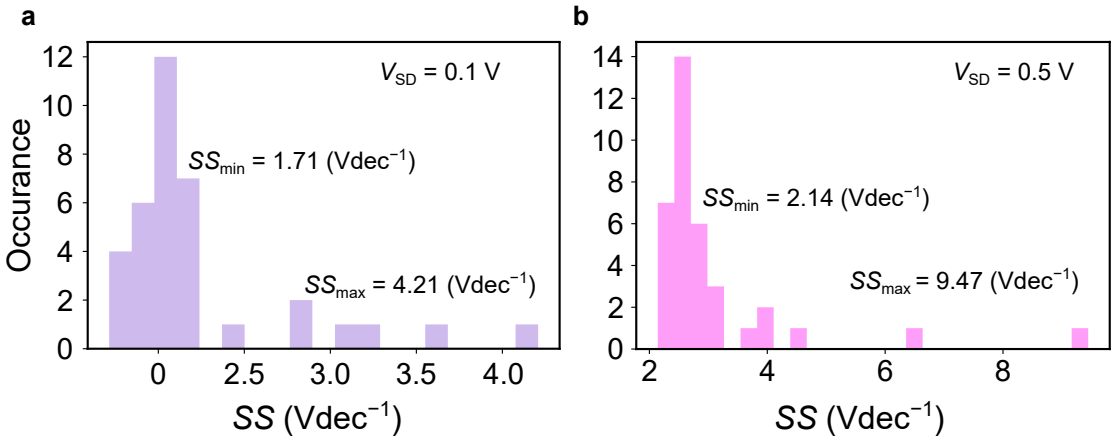


Figure 7.5: a, Switching histograms at low ($V_{SD} = 0.1\,V$) and **b,** medium ($V_{SD} = 0.5\,V$) drain voltages in ambient conditions.

see no fast switching behaviour (Fig. 7.5). The experimental values we measured are at least three orders of magnitude lower than the most competitive CNTFETs (Tab. 2.2 in Ch. 2). We also measured degrading performance upon increasing the source–drain bias (Fig. 7.5b). We do not have, at this stage, a reasonable explanation for this observation, but it might due to the higher concentration of holes injected through the methoxy groups [318].

We would like want to point out, however, that the conductive channel in our devices is poorly defined, as we do not have exact control over the structural arrangement of the nanoribbons on top of the leads due to dropcasting. The addition of 3D bulky groups that suppress the π–π interactions between individual ribbons (see also Ch. 6) might further increase the performance of transistors like these. Future research should compare the device performance of GNR–OME with and without maleimide groups.

7.4 Heteroatoms-Doping-Embedment in MGNRs

Over the past half-decade, significant efforts have been invested into integrating nanographenes as substituents to the periphery of porphyrin rings, with the aim of creating hybrid structures possessing tunable photophysical properties [179, 319]. Porphyrins, macrocyclic heterostructures that coordinate well with most transition metals, are of great significance in biological systems and medicine [320, 321], and exhibit intriguing electrical properties for molecular transport applications [322].

In more recent studies, covalently-bonded Hexa-peri-hexabenzocoronene (HBC)–porphyrin adducts demonstrated electron transfer from the HBC to the porphyrin unit [323]. Additionally, triply-fused porphyrin-nanographene conjugates have displayed significantly π-extended systems with tunable $\Delta E_{\text{HOMO-LUMO}}$ values [319]. In light of these promising developments, and through our collaboration with Harry Anderson's group, we are excited to present the first FET measurements ever made of pGNRs.

Suspensions were prepared by sonicating a dry powder of the pGNRs in toluene ($0.02\,\text{mg}\,\text{mL}^{-1}$) for 60 min. Several cycles of the electroburning protocol were performed, up to three different gate voltages for each device (Sec. 3.4), and each time scanning in gate voltage at fixed bias to check for residual graphene quantum dots. For all devices, the resistance limit was set at $2.3\,\text{G}\Omega$. Devices which show an increase in current post-deposition are selected for wire bonding and further measurements. A possible junction geometry formed between the graphene leads and pGNR is reported in Fig. 7.7a, whereas Fig. 7.7b reports the device with the electrical connections. Transport measurements were performed both room temperature (Fig. 7.7c) using the probe station setup (Sec. 3.3) and at low temperature (Fig. 7.7d) in our Oxford Instruments Triton 200 dilution refrigerator (Sec. 3.7).

Field-Effect Transistor Measurements

Fig. 7.8a shows a pGNR-based FET. The transfer curves at different biases show clearly p-type doping and on-state channel conductance G normalised by the width of the GNR ($w_{\text{GNR}} = 1.2\,\text{nm}$) increases from $0.05\,\text{S}\,\text{mm}^{-1}$ at $V_{\text{SD}} = 0.1\,\text{V}$ to

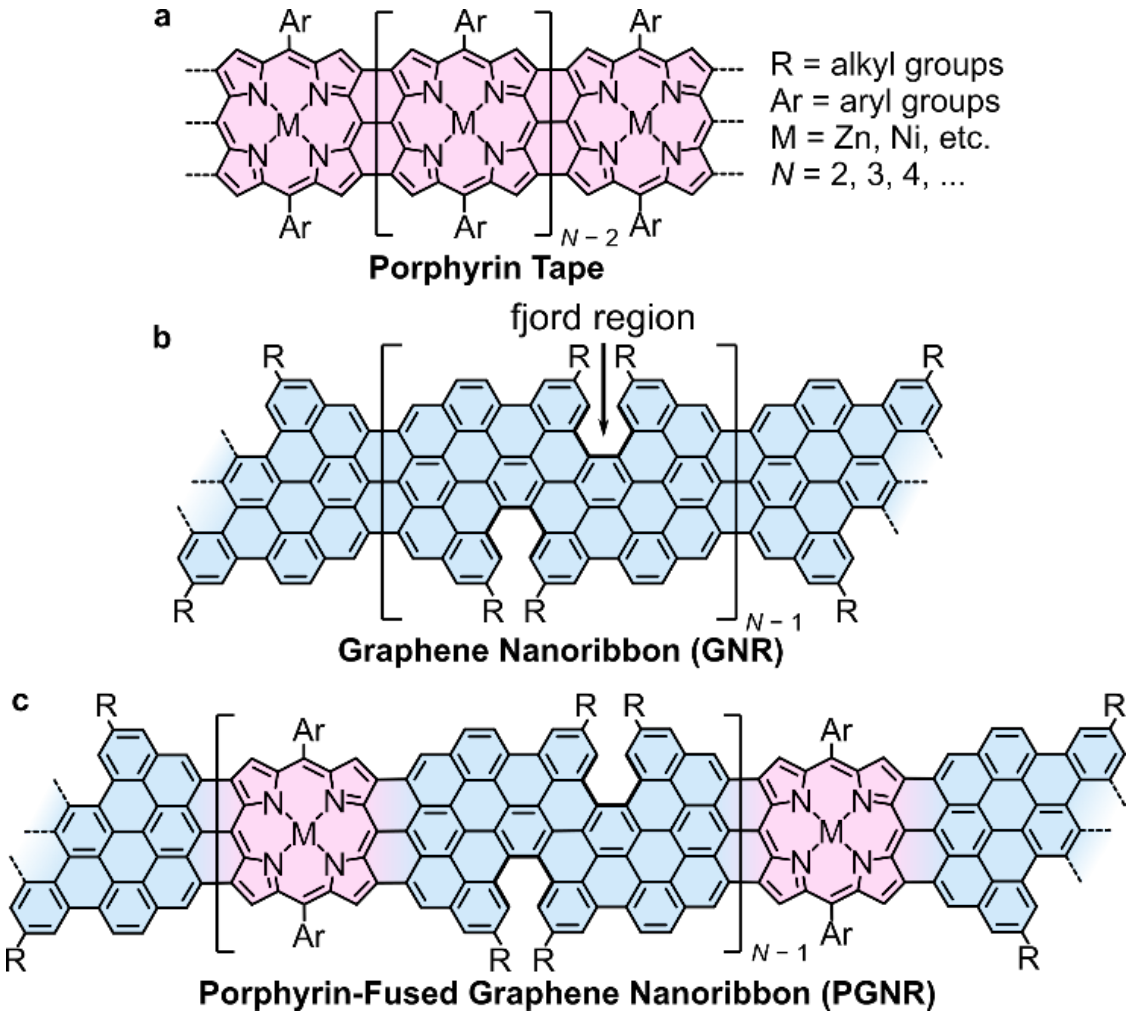


Figure 7.6: **a**, Edge-fused porphyrin tape. **b**, Graphene nanoribbon with fjord-type edges (R = ^{t}Bu–). **c**, Porphyrin-fused fjord-edged graphene nanoribbon (R = ^{t}Bu–). The focus of my measurements was narrowed to pGNRs carrying Ni Heteroatoms as metal centers. Spatial distance between two porphyrin centers is $d_{\mathrm{M–M}} \approx 2.5\,\mathrm{nm}$, whereas the theoretical unit cell size was calculated to be $a \approx 5.8\,\mathrm{nm}$.

$0.1\,\mathrm{S\,mm^{-1}}$ when V_{SD} is increased to 0.5 V. We estimate an on-state conductivity $\sigma = GL/w_{\mathrm{GNR}} = 3.73\,\mu\mathrm{S}$ for a channel length $L \simeq 40\,\mathrm{nm}$[§]. The device was switched off when the gate voltage V_{G} was larger than 0.5 V and had good $I_{\mathrm{on}}/I_{\mathrm{off}} \simeq 10^3$ at $V_{\mathrm{SD}} = 0.1\,\mathrm{V}$. Off-state conductance was estimated around $G_{\mathrm{off}} \simeq 6\,\mathrm{pS\,nm^{-1}}$ at $V_{\mathrm{SD}} = 0.1\,\mathrm{V}$ and increasing as the V_{SD} was increased, despite exhibiting consistent switching behaviour of about $SS \simeq 400\,\mathrm{mV\ dec^{-1}}$ which indicates stable control of the gate over the conduction channel.

[§]The channel length is estimated through low-temperature data. See next subsection.

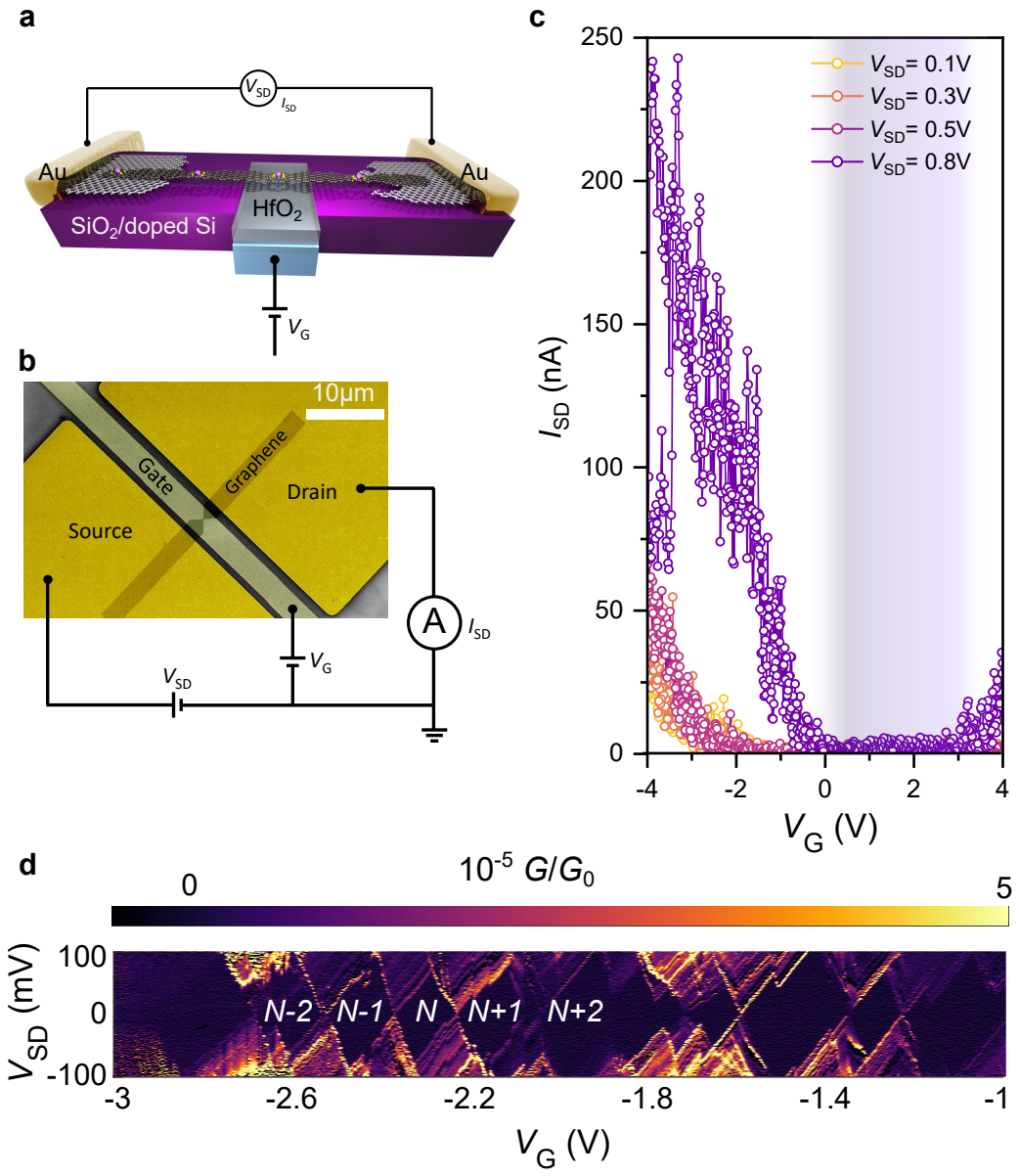


Figure 7.7: **a**, Cartoon of the device schematic and the electrical wiring. **b**, False-scale SEM image of a device, highlighting the Au pads, HfO_2 gate, graphene leads, and the electrical connections for biasing the device. **c**, Room-temperature FET response of a device under different applied biases. Upon increasing V_G, a drastically-reduced conductance is measured, demonstrating p-doping effect. The estimated for this device is $E_g \simeq 2\,\text{eV}$. **d**, SET behaviour for pGNR when measured at cryogenic temperatures ($T = 20\,\text{mK}$). The leftmost Coulomb diamond was progressively charged through the injection of electrons from the source lead, eventually resulting in a stable, closed charge state that contained two more electrons than in the neutral case.

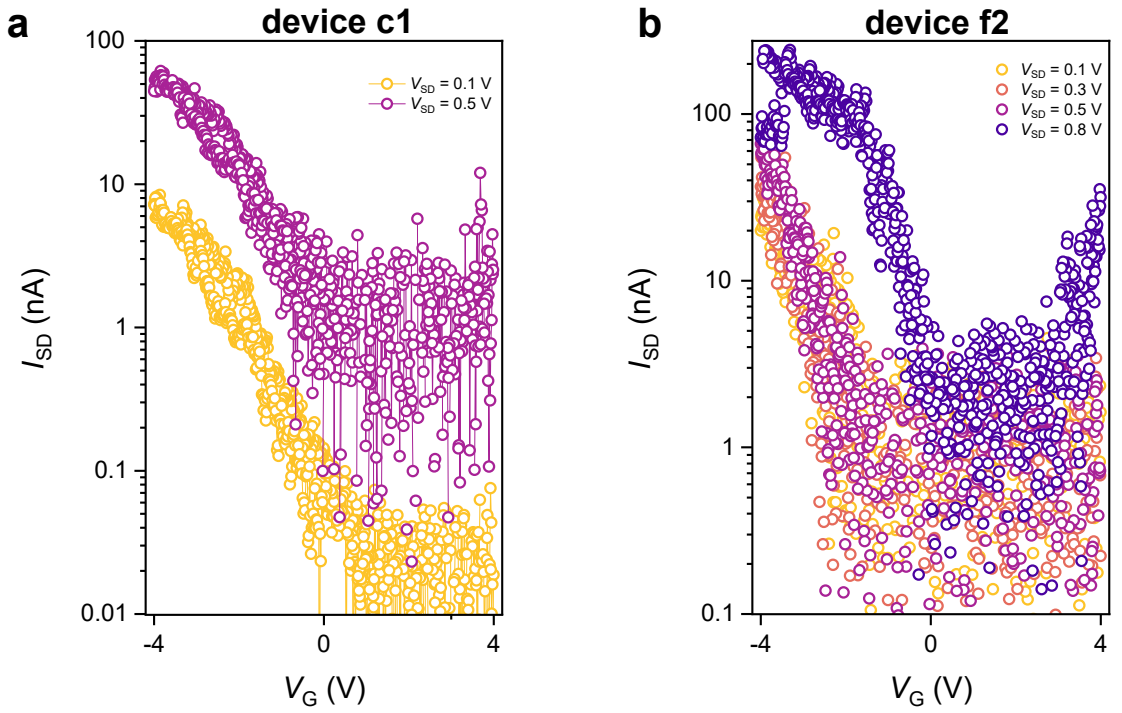


Figure 7.8: **a**, Semi-log plot of the transfer curves for a p-type FET device obtained with pGNR acquired at low and medium biases. **b**, Another p-type device with the transfer curves acquired under equispaced V_{SD} voltages.

On top of that, almost no hysteresis was measured under ambient conditions. The hydrophobic nature of the sandwich established by the ribbon and graphene leads considerably minimises the undesired hysteresis in the transfer characteristics of the transistors, which could be caused by the presence of water close at the GNR–dielectric interface (gate-voltage sweep rate was $44\,\mathrm{mV\,s^{-1}}$). Although we saw mild hysteresis in a few of our devices (device **c4** in Fig. 7.9 and device **c6** in Fig. 7.10), we believe this represents already a great step forward compared to early CNTFET [67].

While the on-state current is not directly related to the bandgap energy E_g, the off-state current depends on the tunnelling current and on E_g [39]. Assuming the synthesised pGNR is an intrinsic semiconductor, and its band structure has a mid-gap alignment with the source–drain contacts, it is possible to provide a lower-bound estimate of E_g from the on–off ratio, which in case of device **c1** is:

$$2k_{\mathrm{B}}T \ln\left(\frac{I_{\mathrm{on}}}{I_{\mathrm{off}}}\right) = E_g \simeq 350\,\mathrm{meV}, \tag{7.1}$$

Since it is typically difficult to establish the threshold voltage in transfer characteristics without ambiguity, conventional FETs are frequently compared using the so-called field-effect mobility. This is device-specific rather than material-specific, and includes effects such as contact resistances and surface effects [324]. We have estimated both the linear and the saturation FET mobilities for several devices (Tab. 7.2). The conduction channel is pinched-off when $V_{SD} = V_G - V_{Th}$, where V_{Th} is

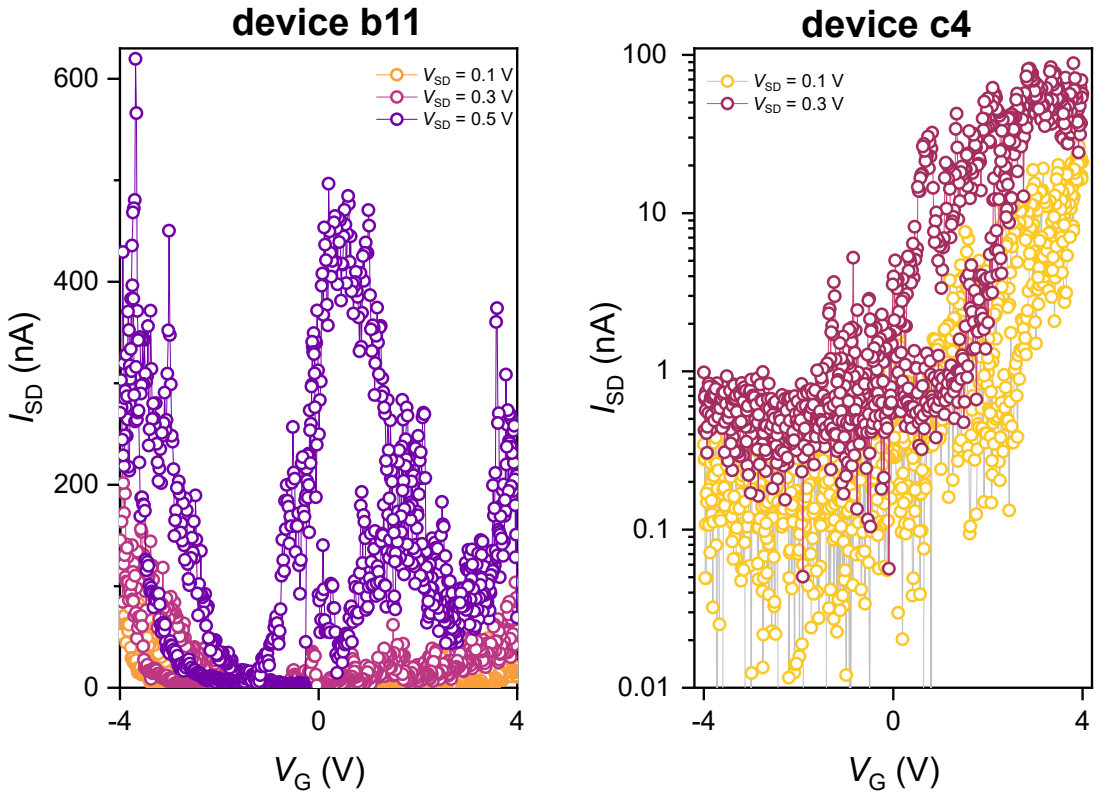


Figure 7.9: left, FET characteristics: $I_{on}/I_{off} \simeq 10^2$ at $V_{SD} = 0.1\,V$, ambipolar behaviour at $V_{SD} = 0.5\,V$, $SS \simeq 430\,mV\ dec^{-1}$ at $V_{SD} = 0.5\,V$.
right, FET characteristics: $I_{on}/I_{off} \simeq 10^2$ at $V_{SD} = 0.3\,V$, small hysteresis present in the $V_{SD} = 0.3\,V$ transfer characteristics, $SS \simeq 435\,mV\ dec^{-1}$ at $V_{SD} = 0.3\,V$ for the forward sweep, degrades down to $SS \simeq 870\,mV\ dec^{-1}$ for the backward sweep, $\mu_{lin} = 11\,cm^2\,V^{-1}\,s^{-1}$, $\mu_{sat} = 4.3\,cm^2\,V^{-1}\,s^{-1}$

the threshold voltage at which the device switches on. In this condition, the current cannot increase substantially anymore and saturates to a value $I_{SD,sat}$ identifiable as a plateau by either plotting the semi-logarithmic plot of the transfer characteristics or by simply visualising the output characteristics. If channel-shortening effects

caused by the depletion region at the drain are neglected, the saturation current can be obtained by substituting V_{SD} with $V_{\mathrm{G}} - V_{\mathrm{Th}}$, and within the gradual-channel approximation the drain-saturation current may be written as [325]

$$I_{\mathrm{SD,sat}} = \frac{w_{\mathrm{GNR}}}{2L}\mu_{\mathrm{sat}} C_{\mathrm{G}}(V_{\mathrm{G}} - V_{\mathrm{Th}})^2, \tag{7.2}$$

where C_{G} is the gate capacitance per unit area. From the capacitance measurments detailed in the next section, we recovered a value for $C_{\mathrm{G}} = 1.4 \times 10^{-2}\,\mathrm{F\,m^{-2}}$. We estimate a saturation mobility (also called field-effect mobility) for this particular device to be $0.8\,\mathrm{cm^2\,V^{-1}\,s^{-1}}$. We further estimate the field-effect mobility in the linear regime ($V_{\mathrm{G}} \gg V_{\mathrm{SD}}$) by extracting the gradient of I_{SD} versus V_{G} at constant $V_{\mathrm{SD}} = 0.1\,\mathrm{V}$:

$$\mu_{\mathrm{lin}} = \frac{\partial I_{\mathrm{SD}}}{\partial V_{\mathrm{G}}}\frac{L}{w_{\mathrm{GNR}} C_{\mathrm{G}} V_{\mathrm{SD}}} = \frac{g_m L^2}{C_{\mathrm{GS}} V_{\mathrm{SD}}}, \tag{7.3}$$

where C_{GS} is the capacitance between the nanoribbon segment that spans across the gate and the gate itself. Therefore, we have estimated that the capacitance per unit area for a ribbon of $L \simeq 40\,\mathrm{nm}$ and $w_{\mathrm{GNR}} = 1.2\,\mathrm{nm}$ placed on top of a gate of thickness $d \simeq 10\,\mathrm{nm}$ is:

$$C_{\mathrm{GS}} = \frac{\varepsilon_0 \varepsilon_r A}{d} = 0.7\,\mathrm{aF}, \tag{7.4}$$

For device **c1**, we estimate a linear FET mobility $\mu_{\mathrm{lin}} \simeq 4\,\mathrm{cm^2\,V^{-1}\,s^{-1}}$. Device **f2** in Fig. 7.8 reproduces qualitatively a similar behaviour. In comparison with device **c1**, this device exhibits $I_{\mathrm{on}}/I_{\mathrm{off}} \simeq 10^2$, which then would correspond to a $E_g \simeq 220\,\mathrm{meV}$ by using Eq. 7.1. The peculiarity of this device is that a current saturation limit is reached only at $V_{\mathrm{SD}} = 0.8\,\mathrm{V}$, with a $\Delta V_{\mathrm{gap}} \simeq 3\,\mathrm{V}$, and the off-state current tends to increase with increasing bias. The gate has good control ($SS \simeq 400\,\mathrm{mV\ dec^{-1}}$) over the conductive channel at small biases, and excellent control $SS \simeq 160\,\mathrm{mV\ dec^{-1}}$ at $V_{\mathrm{SD}} = 0.8\,\mathrm{V}$, which is amongst the highest values measured across our devices. Furthermore, the on-state channel conductance G normalised by the channel width reaches values as high as $0.2\,\mathrm{S\,mm^{-1}}$ and on-state conductivity $\sigma \simeq 6\,\mu\mathrm{S}$. We report slightly higher values for the mobility of this device as we extracted $\mu_{\mathrm{sat}} = 3.5\,\mathrm{cm^2\,V^{-1}\,s^{-1}}$ and $\mu_{\mathrm{lin}} = 16\,\mathrm{cm^2\,V^{-1}\,s^{-1}}$.

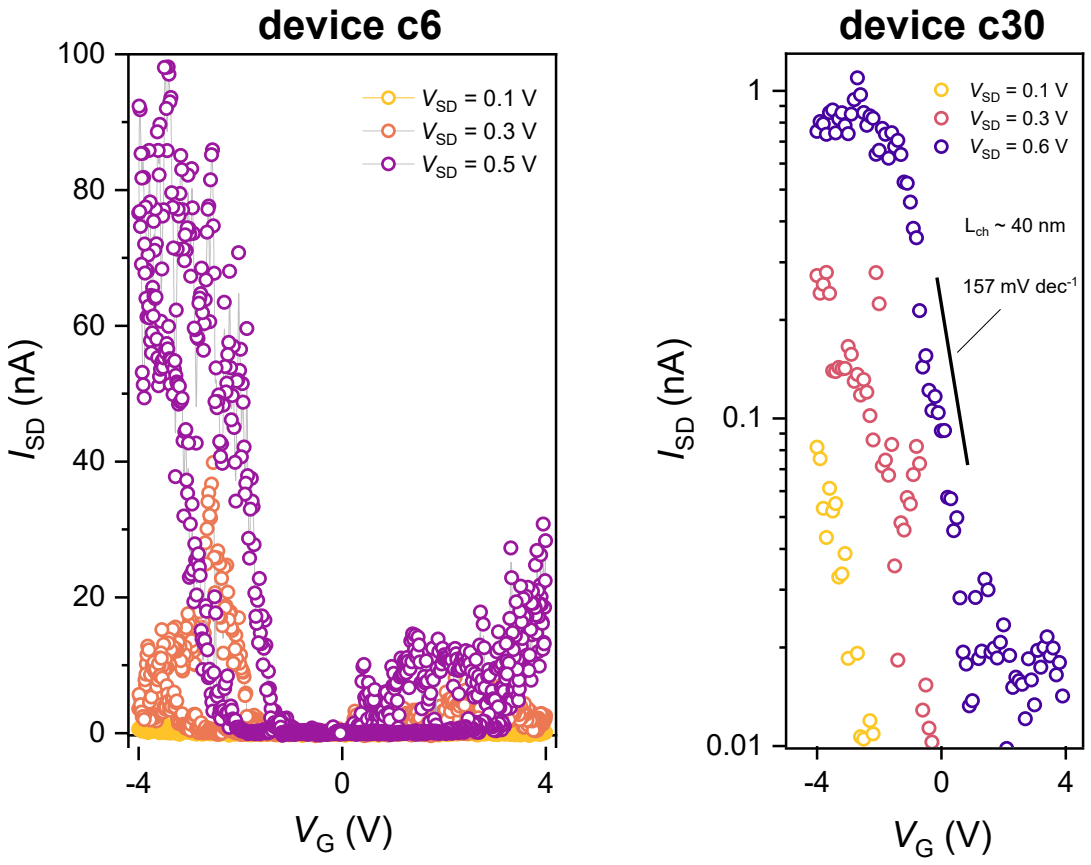


Figure 7.10: left, FET characteristics: $I_{on}/I_{off} \simeq 10^2$ at $V_{SD} = 0.3\,V$, small hysteresis present in the $V_{SD} = 0.3\,V$ transfer characteristics, gap is a negative gates (slight n-doping), $SS \simeq 860\,mV\ dec^{-1}$ at $V_{SD} = 0.5\,V$ for the forward sweep, degrades down to $SS \simeq 925\,mV\ dec^{-1}$ for the backward sweep, $\mu_{lin} = 39\,cm^2\,V^{-1}\,s^{-1}$, $\mu_{sat} = 4\,cm^2\,V^{-1}\,s^{-1}$. **right**, FET characteristics: $I_{on}/I_{off} \simeq 10^2$ at $V_{SD} = 0.1\,V$, $SS \simeq 157\,mV\ dec^{-1}$ at $V_{SD} = 0.6\,V$, estimated channel length $L_{ch} \simeq 40\,nm$, $\mu_{lin} = 28\,cm^2\,V^{-1}\,s^{-1}$, $\mu_{sat} = 6\,cm^2\,V^{-1}\,s^{-1}$

Table 7.2: Linear and saturation mobilities extracted from the transfer characteristics of several devices.

Device name	μ_{lin} ($cm^2\,V^{-1}\,s^{-1}$)	μ_{sat} ($cm^2\,V^{-1}\,s^{-1}$)
E5	5	1
C1	4	0.8
F2	16	3.5
C6	39	4
C4	11	4.3

Further pGNR-FETs are showed in Fig. 7.9 and Fig. 7.10, and in Appendix. B. In Tab. 7.2, we present the linear and saturation mobilities for a variety of devices. Since our pGNR has molecularly defined edges, we explain these values by assuming that the effective mobility decreases as the ribbon width approaches sub-5 nm. The linear-mobility values correlate well with those expected by theoretical estimation [165], but the saturation-mobility values have not yet been found. At room temperature, the effective mobilities are predicted to be limited by acoustic phonons. Nonetheless, if the surface-impurity density is large, this may become the major scattering mechanism, and values in the range of 10–1000 $\mathrm{cm^2\,V^{-1}\,s^{-1}}$ are expected [326], which is consistent with the values we measured.

Low-Temperature Data

The full charge-stability diagram of a typical device cooled down to 25 mK is shown in Fig. 7.7d. Yellow colours indicate regions of higher differential conductance while darker colours indicate lower regions of differential conductance. At gate voltages below $-1\,\mathrm{V}$ clear signs of Coulomb blockade diamonds are present. Outside this gate voltage range, the level of current is close to the noise limit of the current-to-voltage converter used in our transport setup. In the absence of a discernible repeating pattern, it is possible that the faint diamonds visible at higher gate voltages are caused by spurious charges injected possibly through the gate oxide or surface states.

From Fig. 7.11 we can read the addition energies for the different charge states by reading the height of each diamond, within the assumption that only one electron is exchanged for each charge transition. Across all the diamonds, we can extract the gate coupling which measures the effectiveness of the gate voltage to change the chemical potential of the ribbon. We found $\alpha_\mathrm{G} \simeq 0.65\,\mathrm{eV\,V^{-1}}$ averaged across all the measurable charge states, with a slight asymmetric coupling with the drain lead for this particular device. Furthermore, two peaks at $V_\mathrm{G} \simeq -2.5\,\mathrm{V}$ and $V_\mathrm{G} \simeq -1.5\,\mathrm{V}$ are closed, so we can extract their lifetime broadening by fitting a low-bias ($V_\mathrm{SD} \simeq 2.6\,\mathrm{mV}$) gate trace with a Breit–Wigner resonance (Tab. 7.13). The tunnelling couplings with the graphene leads are one order of magnitude stronger

than the majority of tunnelling coupling reported for devices fabricated with normal graphene nanoribbons, confirming the hypothesis of about the origin of the reduced hysteresis observed in pGNRs-FETs A possible explanation for the observed values

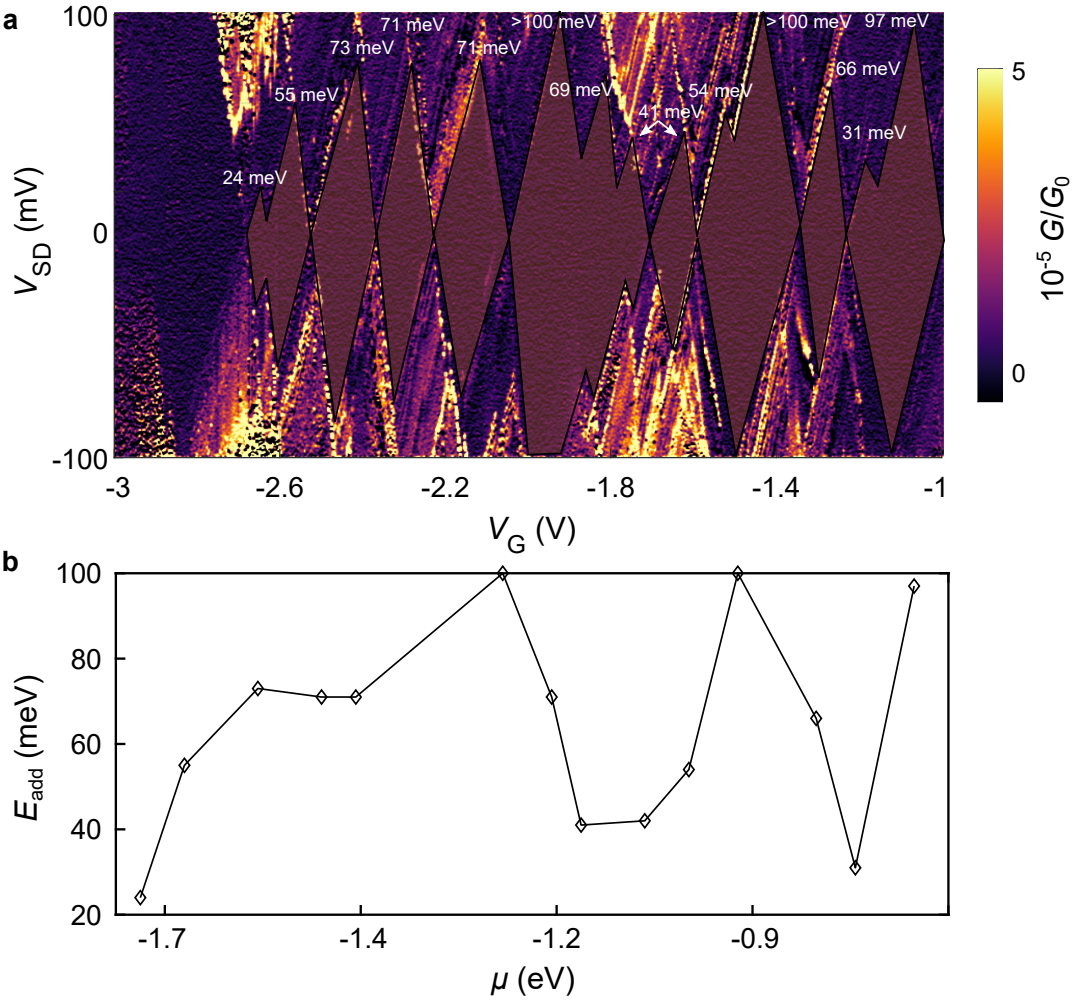


Figure 7.11: a, Low-temperature stability map demonstrating Coulomb blockade and well-defined charge states. **b,** We extract the addition energies from the diamond height and plot them as a function of the chemical potential felt by the ribbon as a result of the application of a gate voltage, assuming a constant gate coupling of $\alpha_G \simeq 0.65\,\mathrm{eV\,V^{-1}}$ for all charge states.

for the tunnelling coupling might be the different length of the pGNR compared to the bottom-up ribbons studied in in the last two chapters. Since the thickness of the HfO_2 oxide on top of the gate is approximately 10 nm, we had to experimentally measure the capacitance of the the oxide in order to extract a more accurate value.

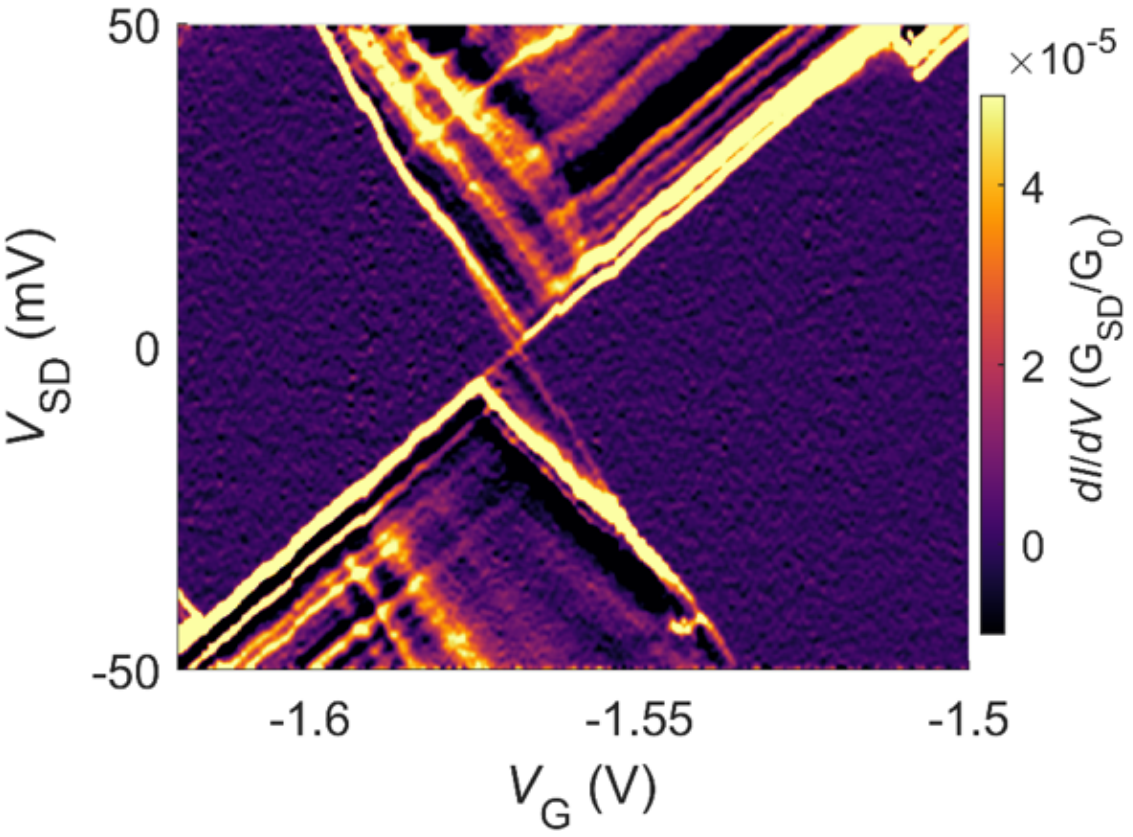


Figure 7.12: Enlargement of a single diamond in the stability diagram. The well-defined structure of ribbon hybrid allows us to resolve several excited lines within a single diamond at low temperatures, which we attribute to vibrational and electronic excitations.

From Fig. 7.12 there are several approximately equally spaced states. By following a harmonic oscillator mode, we can tentatively attribute these states to vibrational modes of the PGNRb (Supplementary Table 3). In particular the 42 meV level corresponds to the 350 cm^{-1} energy of Ni-N A^* out-of-plane vibration modes[23], while the B^* Ni-N, in plane vibration mode is observed at 20 meV[24]. The remaining 35, 28, 10, and 8 meV modes are also all reported in the literature for Ni-porphyrins as carbon-carbon bending modes[24]. This shows excellent agreement between quantum transport signal and the structural features of the PGNR hybrids.

A parameter needed to determine the length of pGNRs is the relative permittivity of the gate oxide. Because of the ultra-thin nature of the oxide used in these devices, it is not possible to rely on the bulk value for HfO_2 and it must be experimentally determined [327]. firstlkong

Figure 7.13: Tables Lorentzian fit parameters and vibrational modes.

(a) Lorentzian fit parameters extracted by fitting a low-bias gate trace.

Peak Position (eV)	Lifetime Broadening (meV)	$G_{\max}$ (G0)
-1.64	2.5±0.2	$(4.5\pm0.2)\times10^{-7}$
-1.04	2.8±0.2	$(2.8\pm0.1)\times10^{-7}$

(b) Assignment of mode frequencies.

Number	Energy Level (meV)	Frequency (cm^{-1})	Assignment
1	42	339	A_{1g} ν(Ni-N)
2	35	282	A_{1g} δ(C-C)$_{sym}$
3	28	226	A_{2g} δ(C-C)$_{asym}$
4	20	161	B_{1g} δ(Ni-N)
5	10	81	B_{2g} δ(C-C)

This was achieved by microfabricating capacitors on the devices using the following approach. A chip is selected from the same wafer used to fabricate devices 1, 2 and 3. The substrate is O_2-plasma etched to remove the CVD graphene layer and prepare the surface for lithography (20 minutes, 25 sccm and 100 percent power). An array of top electrodes is patterned using electron-beam lithography, metal deposition and lift-off. The design consists of overlapping top electrode of varying areas with the gate contact pad separated by the ALD-deposited HfO2 dielectric layer as shown in Fig. 7.14. A small region is removed from the top electrode allowing a W probe to make contact through the oxide and electrically contact the bottom electrode.

An Andeen–Hagerling 2550A ultra-precision capacitance bridge is used to measure the capacitance between the top electrode and the bottom-gate electrode. The measurement is carried out at room temperature in a probe station. The stray capacitance of the probe station and experimental wiring is measured and is found to be insignificant when compared to the values obtained from the microfabricated capacitors. The excitation voltage applied by the bridge is limited to 1 V RMS to

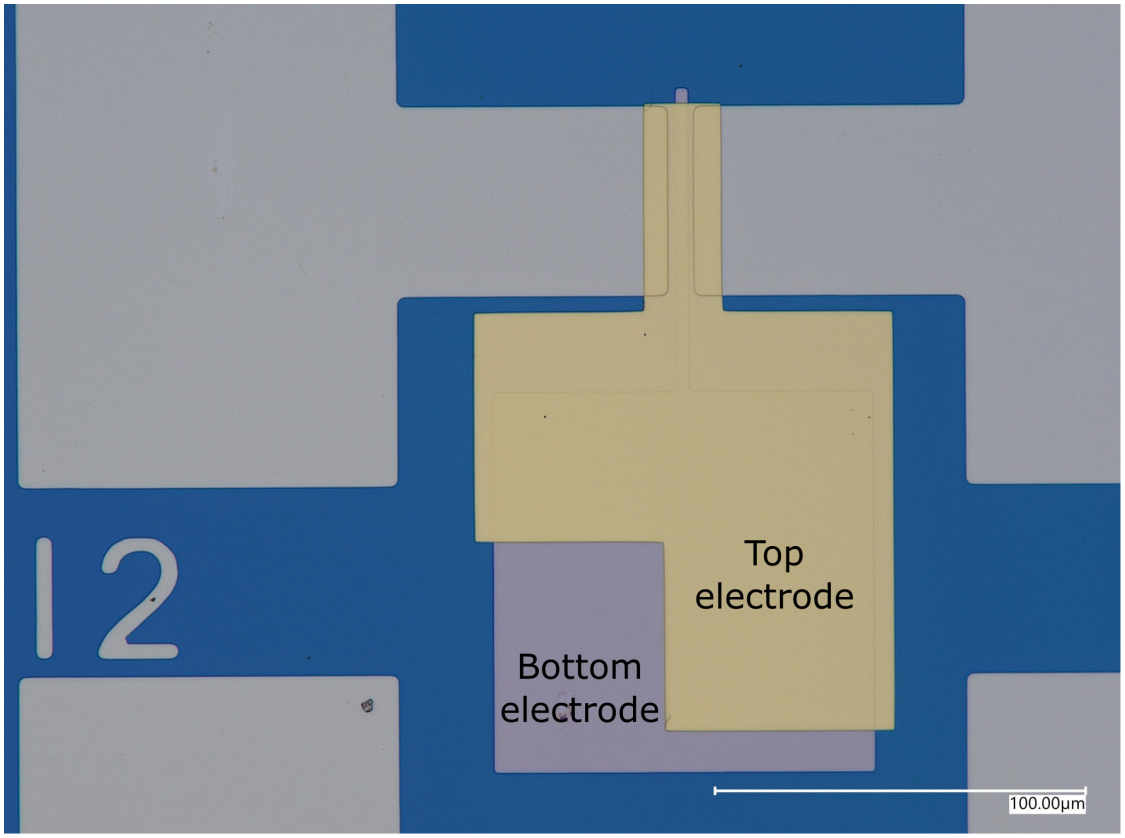


Figure 7.14: Capacitors fabricated through electron-beam photolithography showing top and bottom electrodes.

reduce the risk of dielectric breakdown. ε_r is thus determined by:

$$\varepsilon_r = \frac{Cd}{\varepsilon_0 A}, \tag{7.5}$$

where $d = 10\,\text{nm}$ is the oxide thickness, ε_0 is the permittivity of free space, and A is overlapping area of the top and bottom electrode measured using microscopy. The obtained values are shown in Table 1. An average value of $\varepsilon_r = 15.41$ is used in all length calculations. Since the distance between the ribbon and the gate is comparable to the ribbon width we would need to employ the general formula for retrieving the length from the charging energy [274], i.e.

$$l = \frac{e^2\left(8d\arctan\left(\frac{w}{4d}\right) + w\log\left(1+\frac{16d^2}{w^2}\right)\right)}{4\pi E_C \epsilon_r \epsilon_0}, \tag{7.6}$$

where e is the electron charge, ϵ_0 is the vacuum permittivity, w is the PGNR width and d is the HfO_2 thickness. In our devices, we detected PGNRs of lengths of

Table 7.3: Measured values of electrode area, capacitance and ε_r for several capacitors. These are consistent across various randomly selected points onto a single chip. Errors for ε_r were found to be at the third decimal place.

Device name	Electrode Area (μm^2)	Measured Capacitance (pF)	ε_r
A1	7455	101.1 ± 1.0	15.3 ± 0.02
A2	4542	62.4 ± 0.6	15.51 ± 0.02
C3	2402	32.5 ± 0.3	15.26 ± 0.02
E1	7438	100.6 ± 1.0	15.3 ± 0.02
I1	7433	103.3 ± 1.0	15.7 ± 0.02

$L = 40 \pm 3$, 35 ± 3, and 10 ± 3 nm, respectively (see also Appendix).

7.5 Discussion

We attempted two things in this chapter. To begin, we simulated the engineering of the MGNR electronic band structure using DFT, when various chemical functionalisations, acting both as donors and acceptors of electrons, are inserted along the lateral edges onto the ribbon.

The energy shifts produced by the insertion of dopant atoms appear to have a weak effect on the bandgap at the level of accuracy we simulated. We did not examine how the bandgap shrinkage can be influenced by increasing the ribbon width while maintaining the chemical group, and as such, we encourage further research in the future. For decreasing ribbon widths, we expect to detect negligible impacts of the dopant atom, although out predictions could be skewed by progressively high many-body correlations taking over. In particular, by considering a $\Delta E_g \simeq 300\,\text{meV}$, which is roughly the variation observed in Tab. 7.1 for the methoxy groups, I expect that doping effect should become visible widths as large as $\simeq 30\,\text{nm}$.

The role of chemically-induced doping in GNRFETs is still an open problem. We have seen in Sec. 7.3 that methoxy functionalisations could be responsible for the doping observed through the shift of the CNP. However, the bare shift of the CNP is a controversial, and often molecules adsorbed onto the surface or contaminations left from the photoresists can induce shift too. In order to have

a more strong experimental evidence these measurements should be repeated in controlled atmospheres, such as vacuum and nitrogen.

In addition, we could not test MGNRs with different functional groups but GNR–OME. To test the presence or not of a real doping effect from the substituents, two possible experiments can be undertaken. First, groups that subtract electron density from the ribbon must be used. However, after discussions with our collaborators, this experiment might be non-trivial since n-type functionalisations decrease the edge reactivity to Diels–Alder polimerisation reactions. Second, these measurements should be repeated in various gas atmospheres, including vacuum and nitroge.

We also reported the first FETs devices realised with a new class of hybrid porphyrin–MGNR molecules. We verfied this by measuring the room-temperature output and transfer characteristics. The devices we obtained showed good performance, with on–off ratio up to 1×10^3 and subthreshold swings as low as $SS \simeq 160\,\mathrm{mV\ dec^{-1}}$ at $V_{\mathrm{SD}} = 0.6\,\mathrm{V}$. Furthermore, the devices displayed a reduced hysteresis which we attribute to the strong hydrophobic interactions active between the ribbon and the graphene leads. A few of the devices we report shows n-type of doping, an encouraging result towards the of building p–n heterojuction in these systems. We were able to measure mobilities values comparable with other carbon-based devices and conductive polymers [325, 326]. In order to extract important device parameter informations, we then progressed by measuring also the conductivity at mK temperatures, highlighting individual charge states. We also estimated the coupling between the ribbon and the graphene leads $\Gamma \simeq\simeq (2.8 \pm 0.2)\,\mathrm{meV}$ to be stronger than the one reported between normal graphene and MGNRs. Finally, our results prove that we can use the pGNR to investigate both field-effect and single-electron behaviour, offering a valid alternative to substitutional doping grafted onto the edges.

7.6 Outlook and Perspectives

The difficulty of carrying out edge-doping is addressed by measuring another class of very promising emerging materials, i.e. pGNRs, where the dopant atoms is

introduced thorugh a porphyrin directly into the honeycomb lattice of the MGNR. The motivations come from the fact that (1) fused porphyrin oligomers (also called *tape*) have displayed an increase in the conductance for longer tapes, an observation rationalised with the bandgap shrinkage [328], and (2) that magnetic porphyrins attached toGNRs are able to retain their magnetic fingerprint [329], not compromising those topological states intensively sought-after for the creation of robust molecular qubits. The results are encouraging: the porphyrin embedded in the MGNR topology results in FET where both n and p-doping can be induced, fast switching behaviour can be observed, and field-effect mobilities are in line with what expected from FETs at ambient condition.

8

Conclusions and Perspectives

In the realm of carbon nanostructures, extensive efforts have been dedicated towards their integration into IC, giving rise to the pioneering first a central processing unit made entirely of carbon nanotubes [330]. Despite the promising potential of CNTs to reduce power consumption in silicon circuits, their processability remains a formidable challenge.

A new generation of carbon nanomaterials, howeve, shaped by bottom-up synthetic methods, may offer solutions to some of the nanotube difficulties. This work has been devoted to examining the challenges these emergent materials present, and the strategies I employed to mitigate or entirely resolve them.

Firstly, I explored the integration of molecularly defined graphene nanoribbons into the structure of single-electron transistors (SETs). These SETs are critical components in low-power logic applications: a CMOS inverter dissipates approximately 70 µW, whereas a SET only dissipates about 13 pW [331]

One of the cornerstone achievements of this thesis was the development of a new temperature protocol for performing electron transport experiments, as detailed in Ch. 4. Upon implementing this protocol, we presented groundbreaking evidence of an MGNR-based SET capable of functioning at near room temperature. The charging energy E_C was observed to effectively overcome the thermal fluctuations

even at room temperature, resulting in the observation of persistent Coulomb oscillations, a key aspect of the behaviour of SETs.

Through the investigation of low-energy excitations, three transport regimes were identified, which shed light on the fundamental mechanisms dictating the SET operation. At cryogenic temperatures, the heights of Coulomb oscillations remain virtually invariant, in a pure Coulomb-blockade regime. Power-law scaling in temperature of the Coulomb-oscillation heights was found from $T = 1\,\mathrm{K}$ to approximately $T = 80\,\mathrm{K}$, while Coulomb-oscillation widths were proportional to T. Similar scalings for the Coulomb profile have been documented in the literature and attributed to the presence of finite-range Coulomb interactions in 1D systems. Since I did not observe an exponential decay of the conductance $G \sim T^{-\beta\phi_\mathrm{B}}$, I ruled out thermally activated processes [275].

The power-law scaling analysis implies that tunnelling events occur via a Tomonaga–Luttinger-liquid phase, and interpreted through a correlated-sequential-tunnelling framework where– when an electron transfer occurs–plasmon modes are excited, and their experimental fingerprints can be associated with the power-law exponents for each charge transition.

To validate this hypothesis, I calculated an average tunnelling exponent from the impedance of a plasmon oscillation-associated ideal transmission line, yielding a value near the experimental observation, $\alpha_\mathrm{end} \simeq 0.5$. High temperatures initiate flexural phonon scattering in graphene, disrupting the Tomonaga-Luttinger-liquid phase. These findings generally align with a non-linear dispersion of low-energy excitations, in contrast with metallic carbon nanotubes.

In an effort to seek an explanation for the ultra-clean Coulomb diamonds features observed for several devices, I experimented with two graphene nanoribbons, where varying functionalisations were grafted onto the edges to improve dispersion in solution. The ribbons decorated with alkyl chains resulted in p-doped FETs, whereas the graphene nanoribbons carrying sterically hindered groups were systematically

associated with SET devices. There is substantial experimental evidence supporting this claim.

I was also able to observe a significant suppression of the tunnelling current at low bias, combined with vibron-assisted excitations, using millikelvin-transport spectroscopy. This observation was explained within the Franck–Condon conductance blockade model. Additionally, the conductance suppression was supported by *in silico* experiments, where the phonon dispersions of graphene nanoribbon with and without maleimide groups were calculated.

The results suggest that the vibrational modes in graphene nanoribbons are more strongly coupled to the electric charge than that of suspended carbon nanotubes in similar devices. I therefore suggest that understanding mechanical and quantum vibrations is crucial when frequencies in the MHz–GHz range are used to excite and manipulate spins [112, 301, 302].

In the final section of this thesis, I evaluated the chemical engineering of the bandgap in graphene nanoribbons by modifying the electronic band structure using DFT, with edge decorations serving as electron donors or acceptors. Simulation results suggested that the introduction of dopant atoms induced only minimal bandgap shifts. The influence of ribbon width changes on bandgap shrinkage, however, was not explored and should be a focal point of future investigations. I predict minor effects of dopant atoms for smaller ribbon widths, but many-body interactions may contradict this prediction.

The minimal impact of dopant atoms on the bandgap was partially confirmed through experimental testing of edge-doped graphene nanoribbons. Despite no overall change in device performance, p-type doping was suggested by a likely decrease in conductance with more positive gate voltages upon the introduction of methoxy groups. Further testing, potentially in controlled environments, is required to attribute this effect to the functional groups.

The issues related to doping were addressed by investigating porphyrin-fused graphene nanoribbons, with porphyrin serving as a direct carrier of dopant atoms into the graphene nanoribbon lattice. The findings are promising.

The optical bandgap (1.0 eV) of porphyrin-fused graphene nanoribbons, estimated from absorption spectra, is among the lowest for solution-synthesised graphene nanoribbons. High charge carrier mobilities ($\mu_{\mathrm{dc}} \approx 32 \pm 4\,\mathrm{cm^2V^{-1}s^{-1}}$), appealing room temperature FET characteristics ($SS \simeq 400\,\mathrm{mV/dec}$), and clear single-electron-transistor behaviour at millikelvin temperatures were revealed by charge-transport experiments. Moreover, the sub-400 mV minimum voltage of negative differential conductance regions suggests potential for low-power operations.

Considering their inherent properties and capacity to bind a plethora of metal ions, porphyrin-integrated graphene nanoribbons unveil new possibilities in fields such as magnetism, molecular electronics, spintronics, and memory technology. Through the integration of magnetic porphyrins into graphene nanoribbon structures, we could see the emergence of an exciting field in the sphere of spintronics. This method could potentially increase electron-spin coherence times, playing a vital role in crafting resilient molecular qubits.

One of the key challenges in achieving a fully GNR-based CPU revolves around the fabrication process. The accurate alignment and positioning of GNRs at a large scale presents a complex puzzle to solve. Given that the properties of GNRs vary considerably based on their edge structure and width, perfecting the fabrication processes is a critical goal that appears achievable only with bottom-up GNRs. Additionally, ensuring the long-term stability and reliability of GNR-based devices under a wide range of operational conditions is another area that demands attention. Moreover, the existing semiconductor industry is firmly rooted in silicon-based technology, and a shift to a radically different material such as graphene would necessitate significant technological and financial advancements.

In conclusion, we have simultaneously developed several research avenues focused on the study of electron transport in graphene nanoribbons. With this

approach, the experimental results have (1) offered a direction for the synthetic design of the materials toward novel compounds with improved properties, such as the addition of 3D groups grafted onto the ribbon edges; (2) developed new instrumentation and new measurement protocols to deepen our knowledge of the fundamental properties of molecularly-made systems; and (3) realised two first-of-their-kind electronic devices.

The findings of this thesis provide insights into transport physics, offer initial guidance for overcoming longstanding obstacles that have hindered the advancement of carbon-based electrical devices, and will have an appreciable influece on the development of the first graphene nanoribbon-based microprocessor.

Appendices

A

Graphene Nanoribbons Single-Electron Transistors

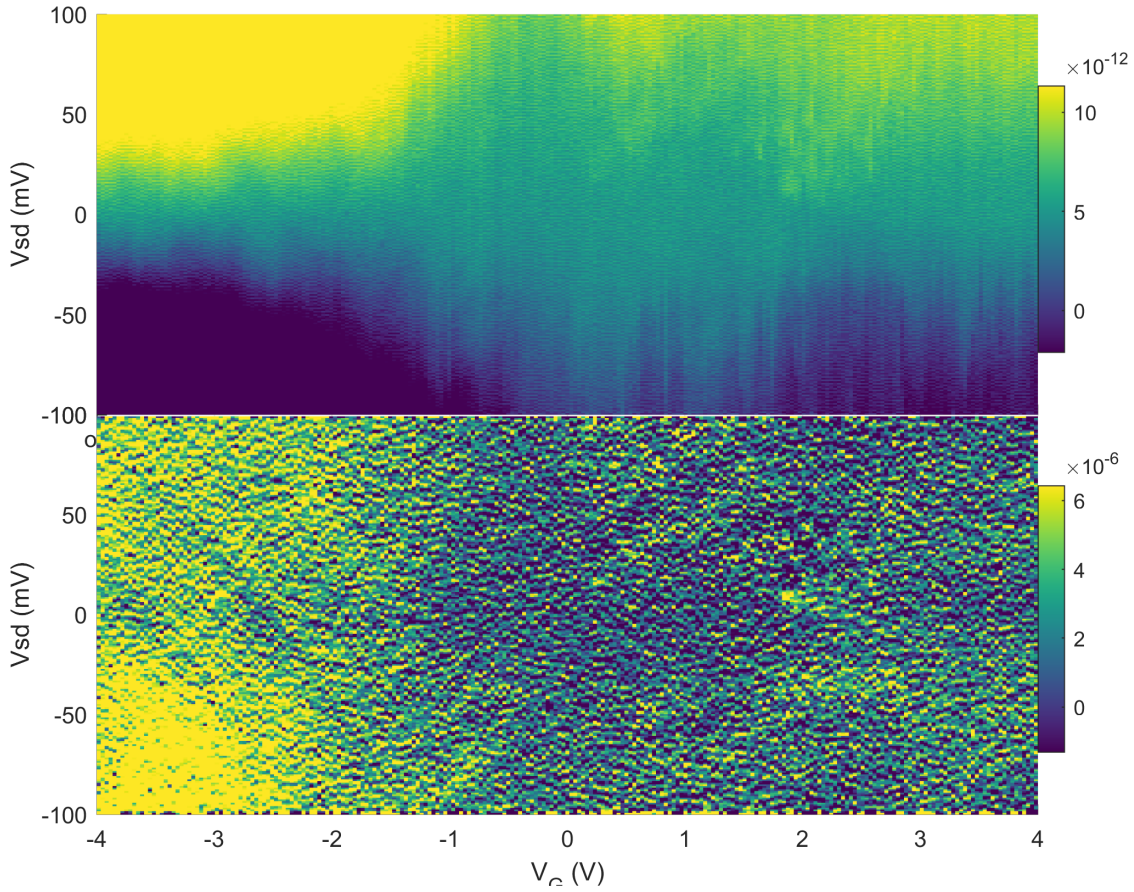
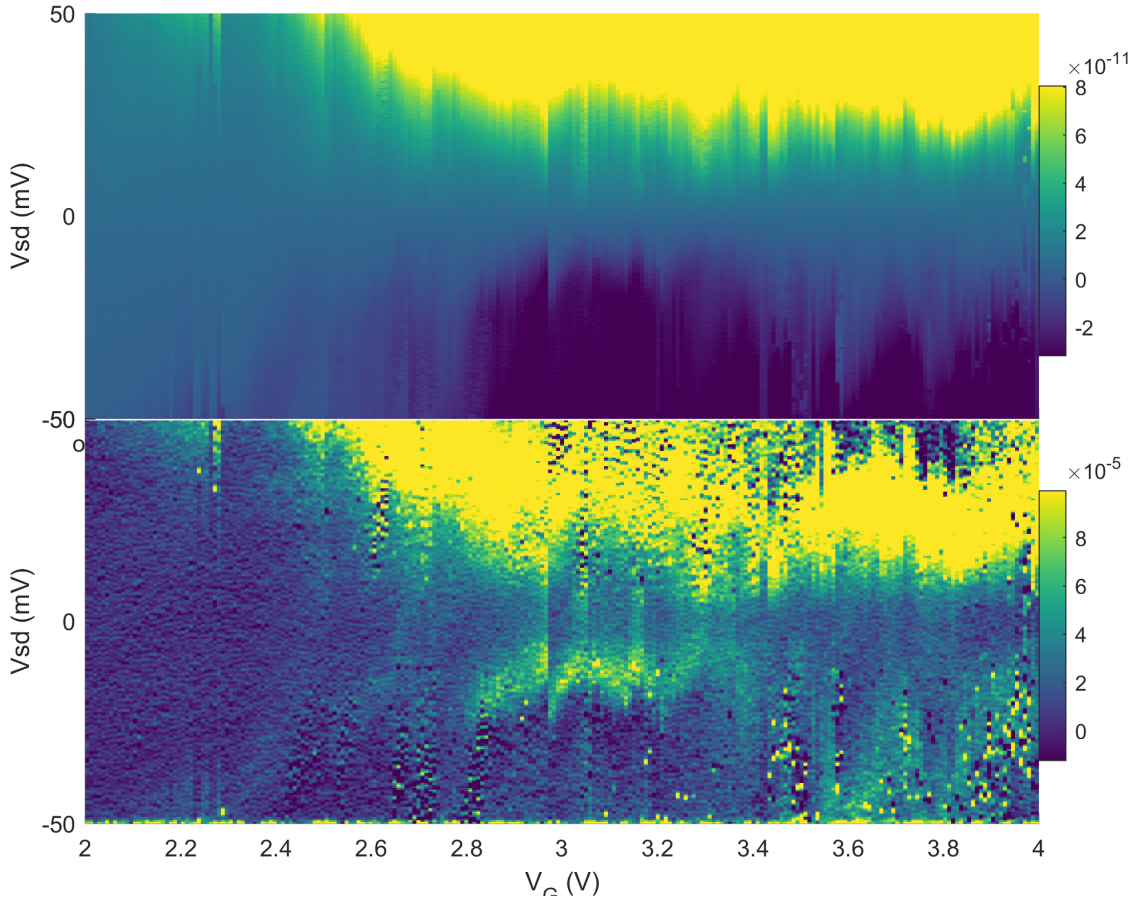
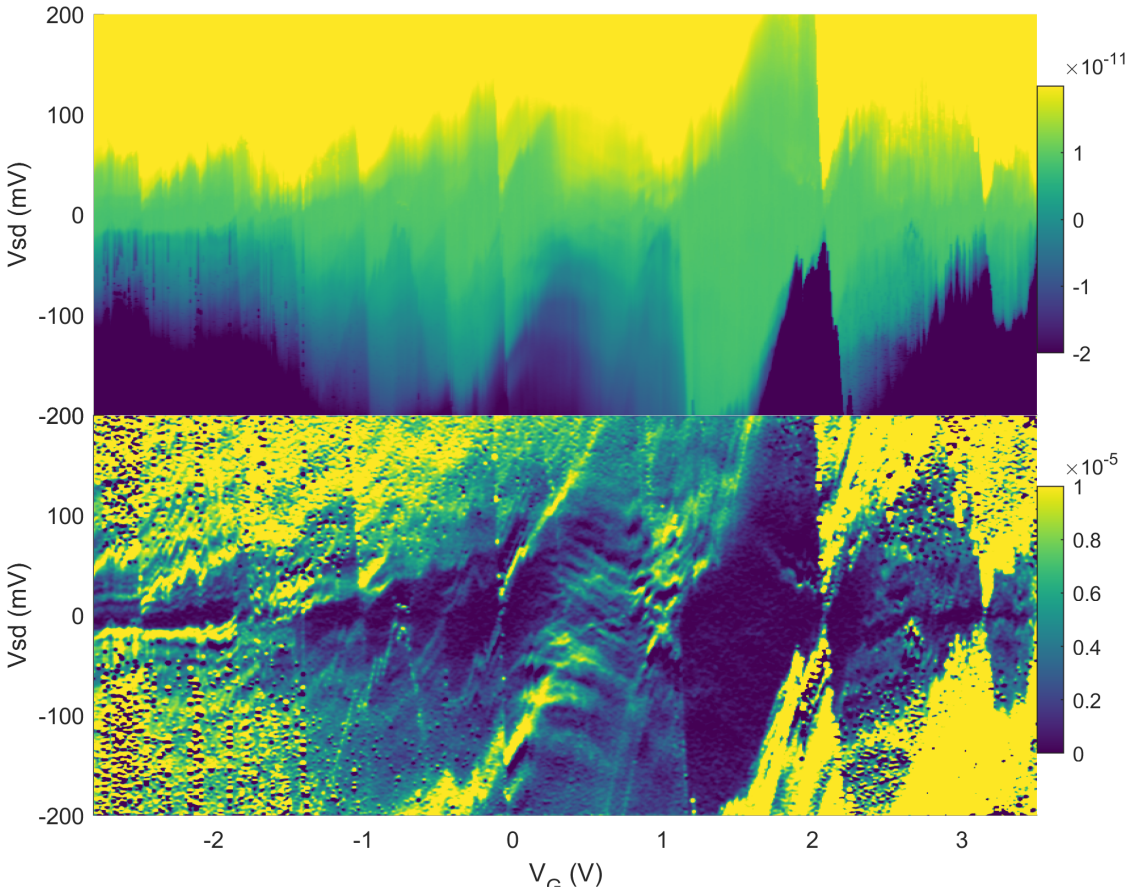


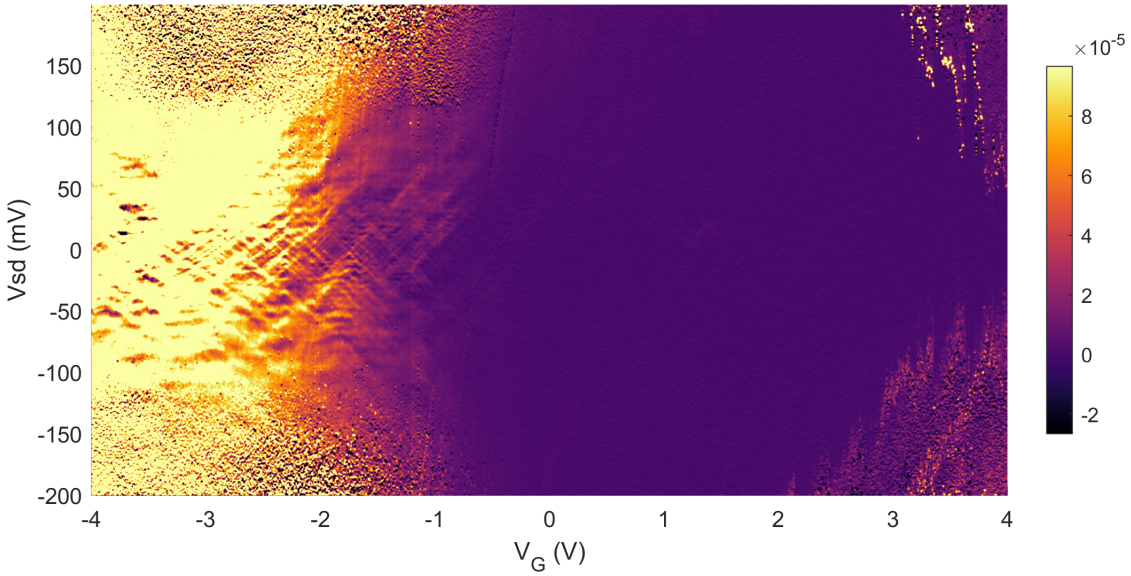
Figure A.1: Device MGNR**1**-d.



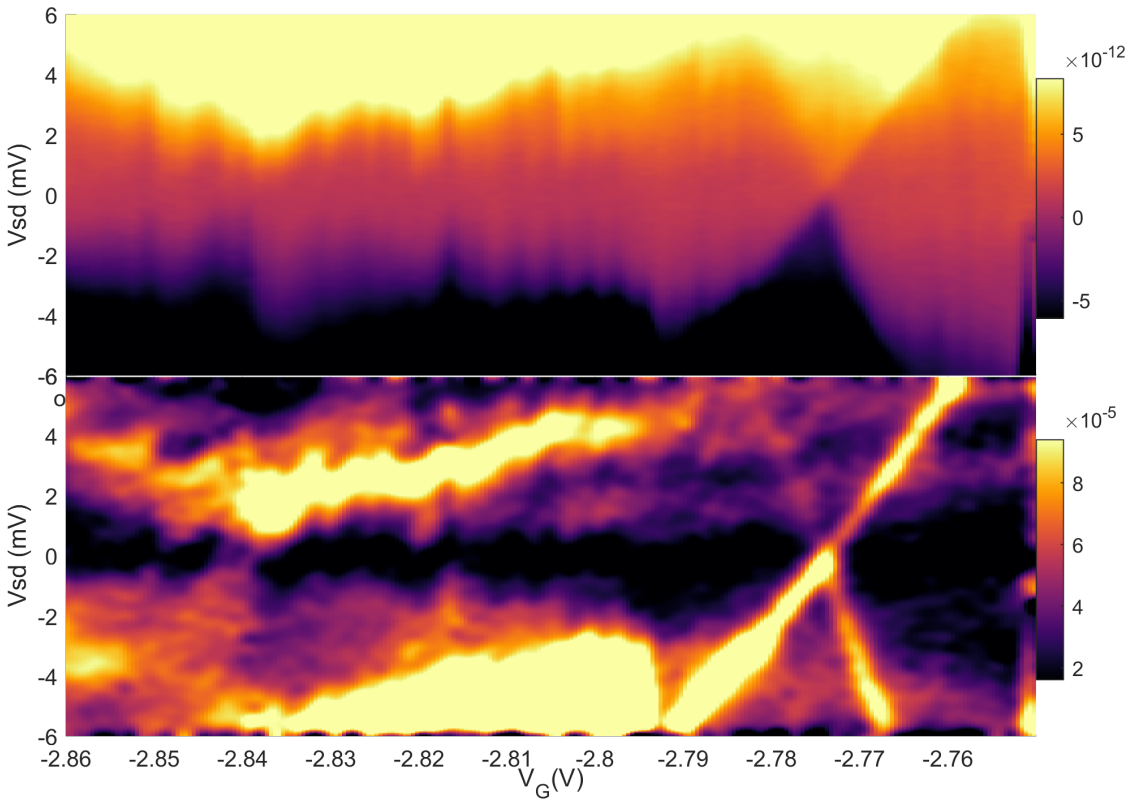
Device MGNR**1**-e.



Device MGNR**1**-f.



Device MGNR**1**-g.



Device MGNR**1**-h.

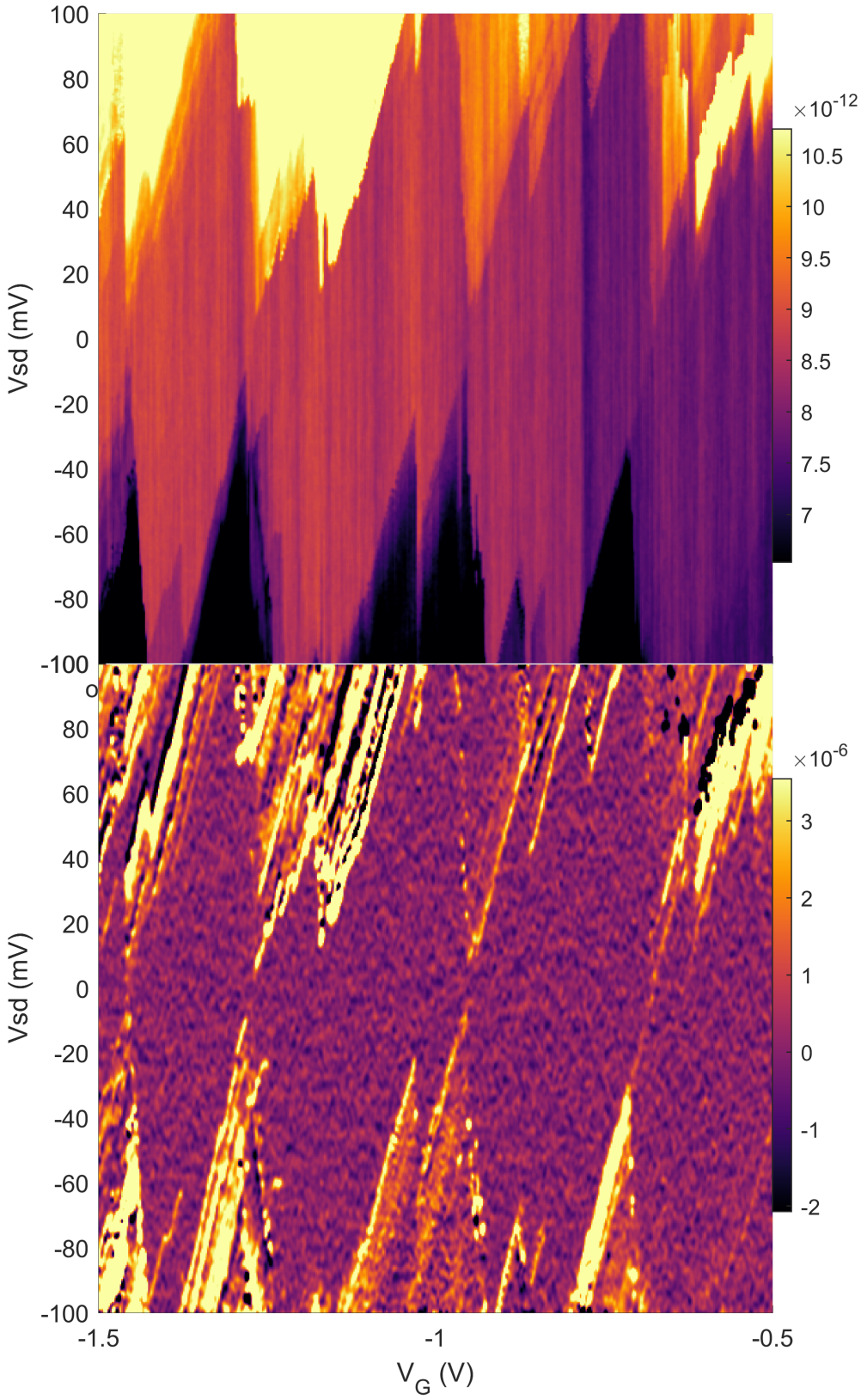
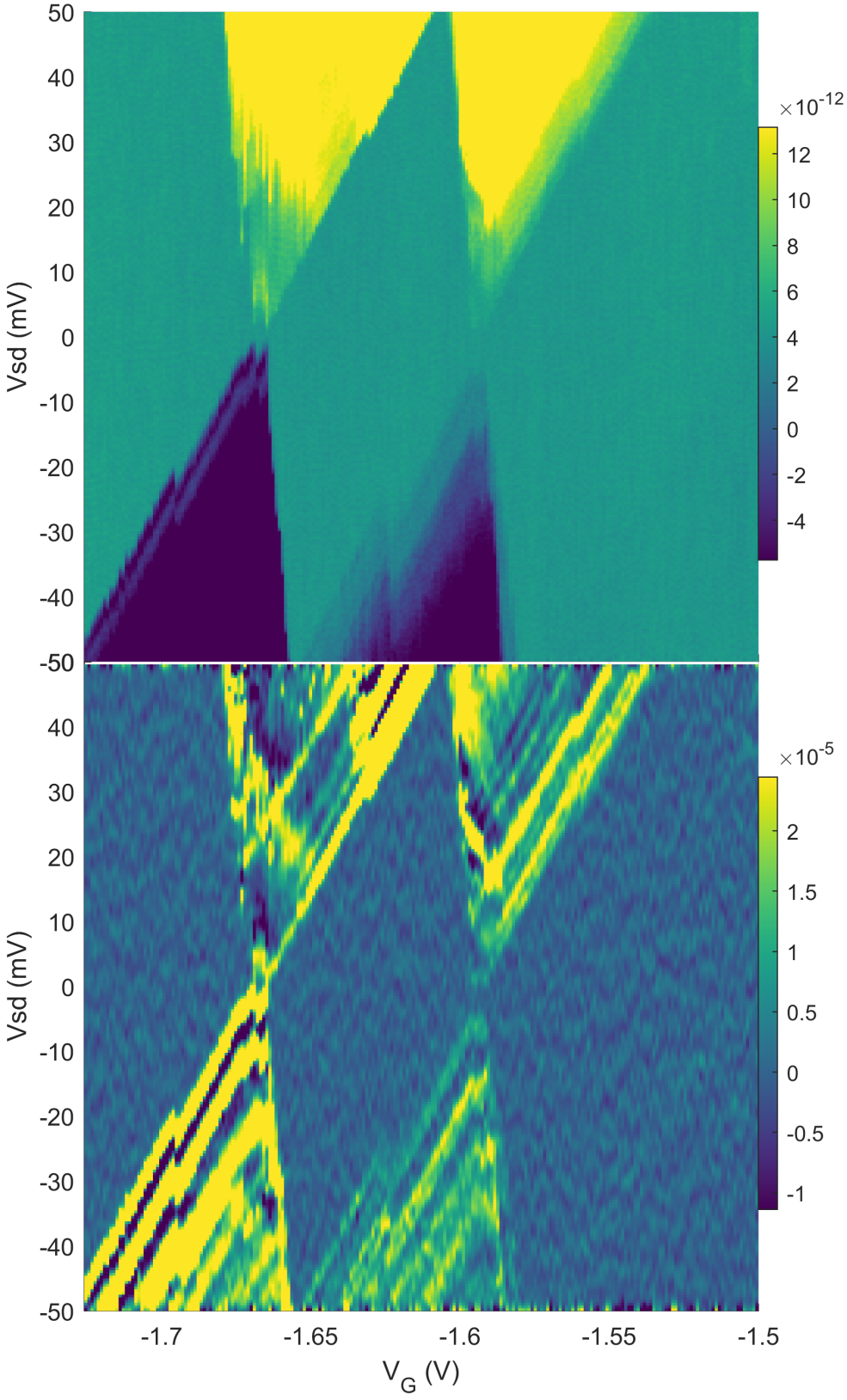
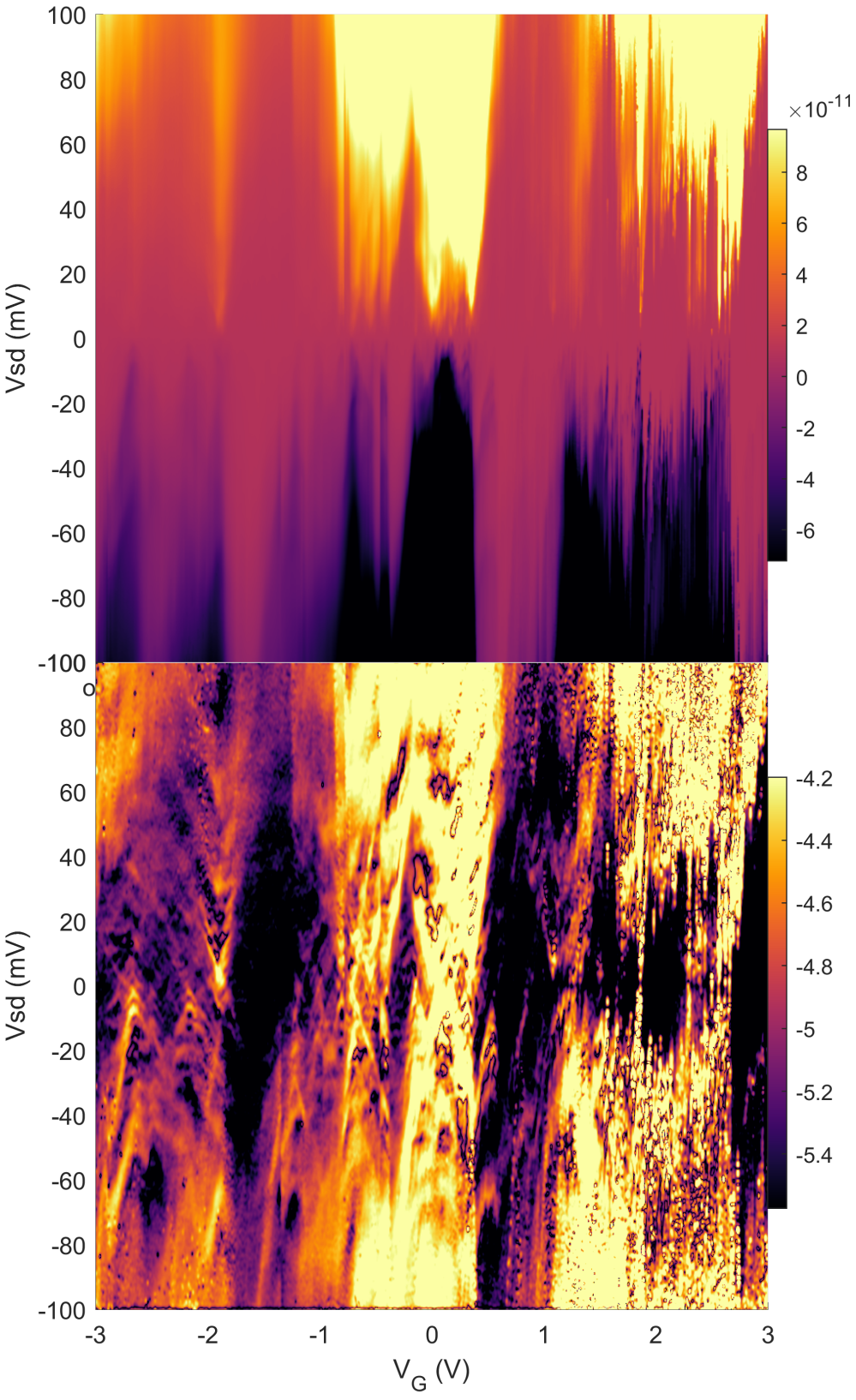


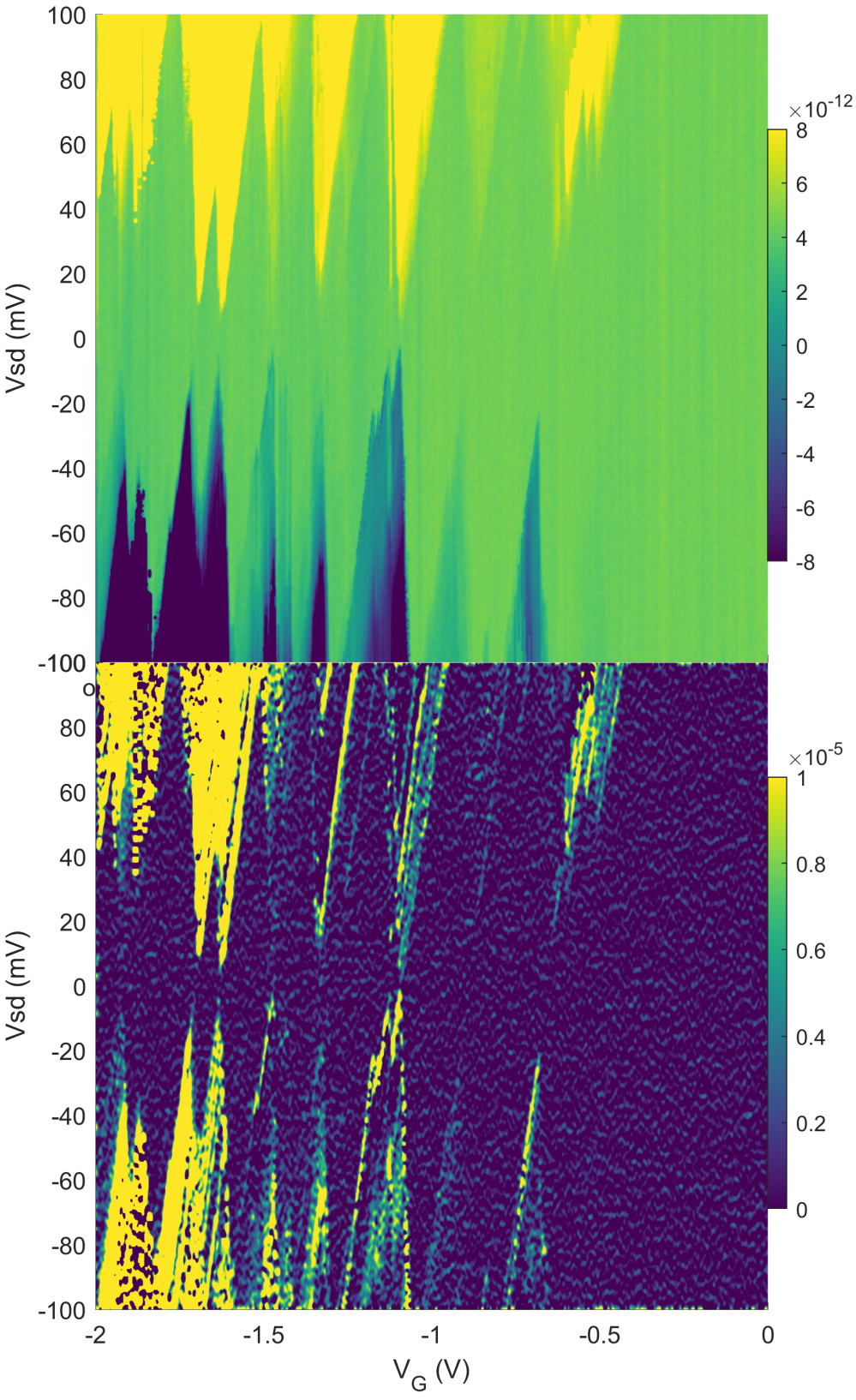
Figure A.2: Device MGNR**2**-d.



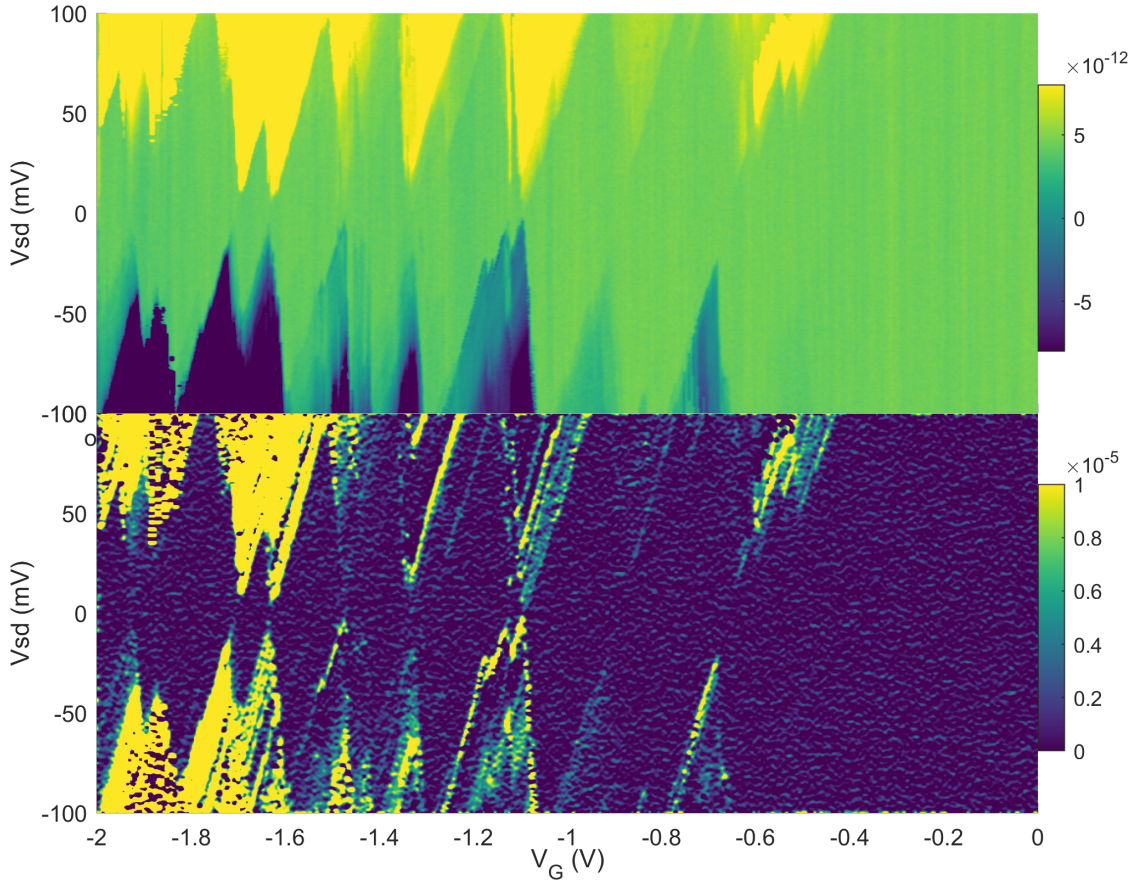
Device MGNR**2**-e.



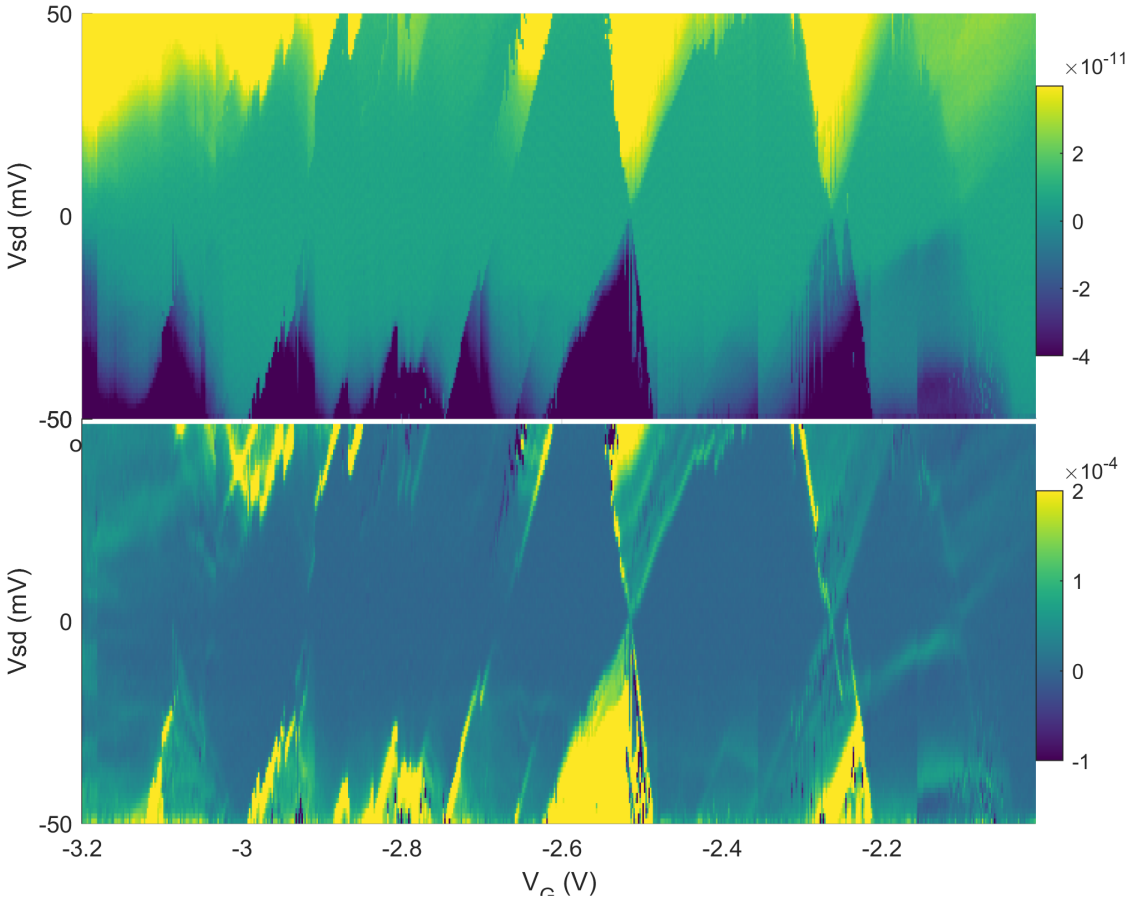
Device MGNR**2**-e.



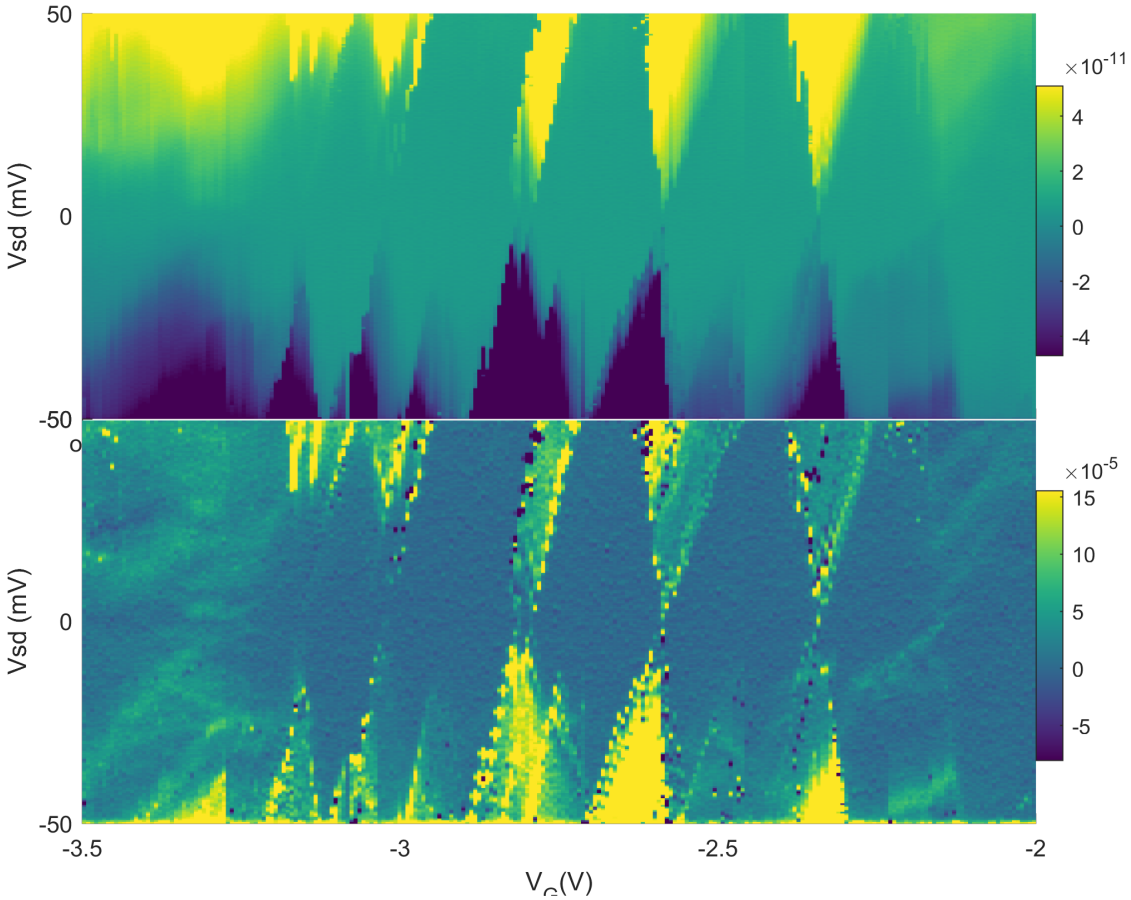
Device MGNR**2**-f.



Device MGNR**2**-g.



Device MGNR**2**-h.



Device MGNR**2**-i.

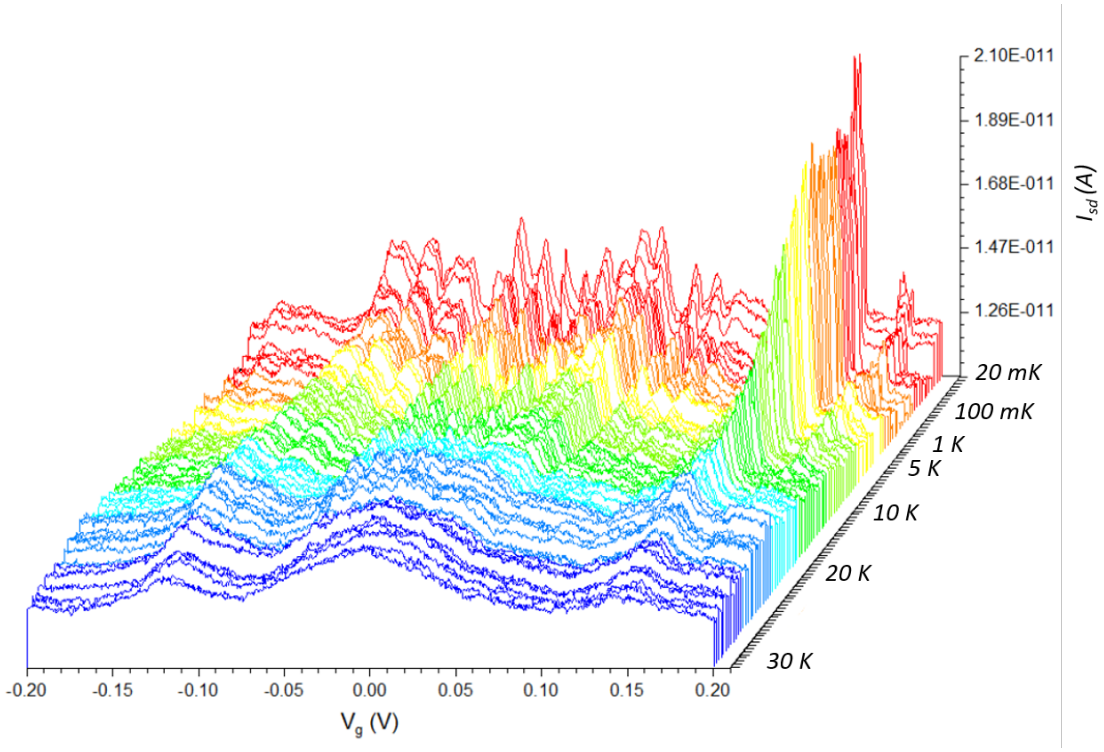


Figure A.3: Temperature dependence for a gate voltage range of device b3. The temperature trend for the transition close to $V_G \simeq 0.15\,V$ exhibits a $G \propto e^{-T}$, suggesting a thermally-activated kind of tunnelling.

B

Porphyrin-Fused Graphene Nanoribbons: Single-Electron and Field-Effect Transistors

Contents

B.1 Additional Data 184

B.1 Additional Data

Here below we report additional data for the pGNRs

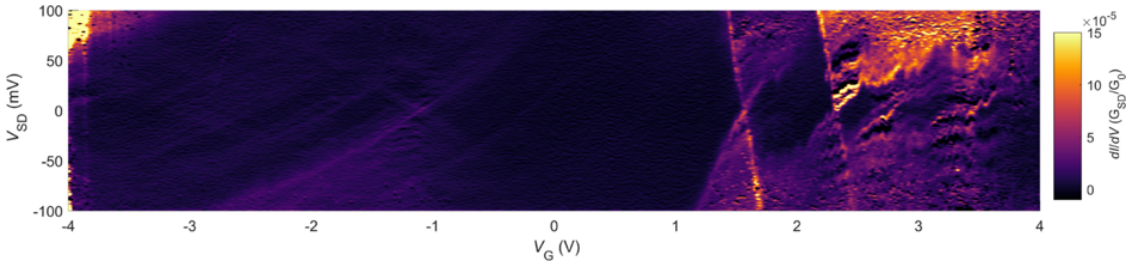


Figure B.1: Conductance map at 0.025 K for device 2. Lines are visible within the conducting regions which run non-parallel to the diamond edges. These are probably graphene lead states which are due to an electrostatic variation in the density of states in the graphene leads[25]. Analysis of the diamond between the two clearest Coulomb peaks at a gate voltage $V_G \approx 2$ V gives values for $E_{\text{add}} = 93$ meV and $\alpha = 0.125$ eV/V.

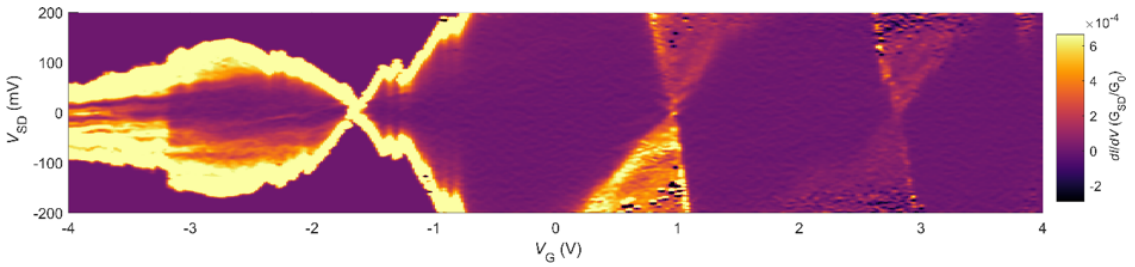


Figure B.2: Conductance map at 0.025 K for device 2. Analysis of the diamond between the two clearest Coulomb peaks at a gate voltage $V_G \approx 2$ V gives values for $E_{\text{add}} = 390$ meV and $\alpha = 0.125$ eV/V. Some signatures of cotunneling are visible especially around the charge degeneracy of the peak at $V_G = 0.97$ V. Current in the regions of the stability diagram at $V_G < -1$ V are not measured as the current exceeded the limit of the current to voltage converter and the dI/dV appears flat in these regions.

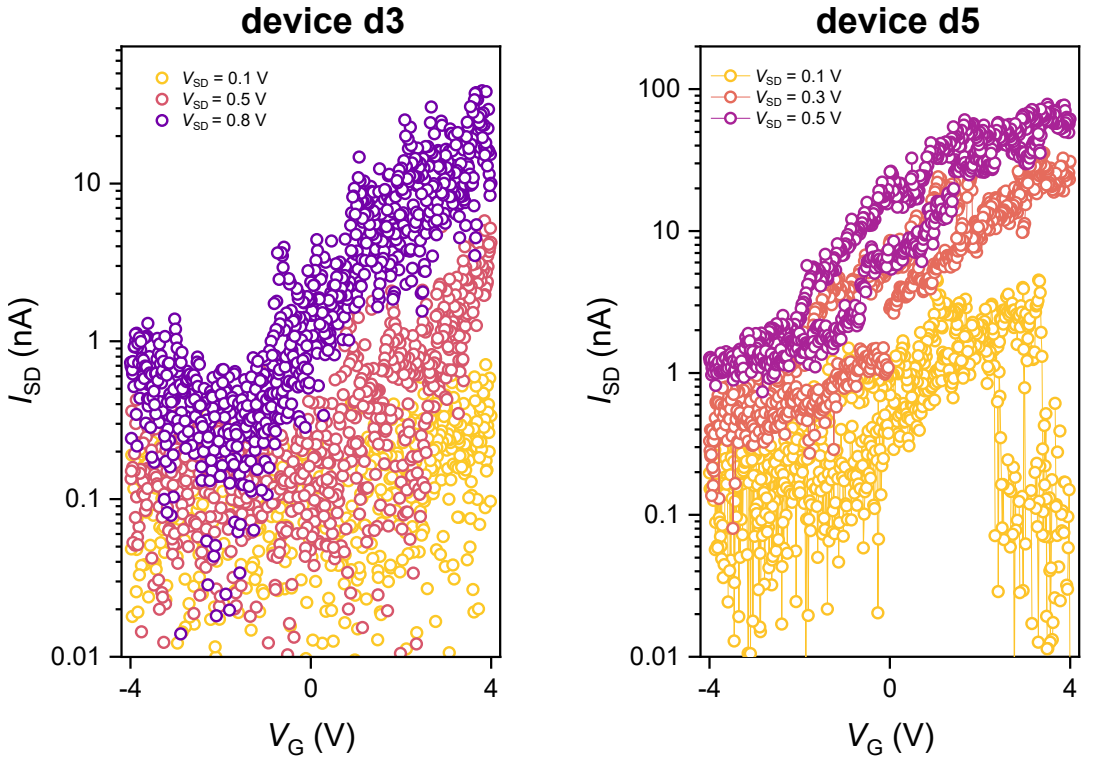


Figure B.3: left, FET characteristics: $I_{on}/I_{off} \simeq 10^1$ at $V_{SD} = 0.1\,V$, $SS \simeq 3\,V\ dec^{-1}$ at $V_{SD} = 0.6\,V$, slightly n-doped, poor off ($I_{off} \simeq 0.1\,nA$) and on ($I_{on} \simeq 5\,nA$) currents. **right,** FET characteristics: $I_{on}/I_{off} \simeq 10^2$ at $V_{SD} = 0.5\,V$, $SS \simeq 1.5\,V\ dec^{-1}$ at $V_{SD} = 0.3\,V$, n-doped, poor off ($I_{off} < 1\,nA$) and on ($I_{on} \simeq 15\,nA$) currents.

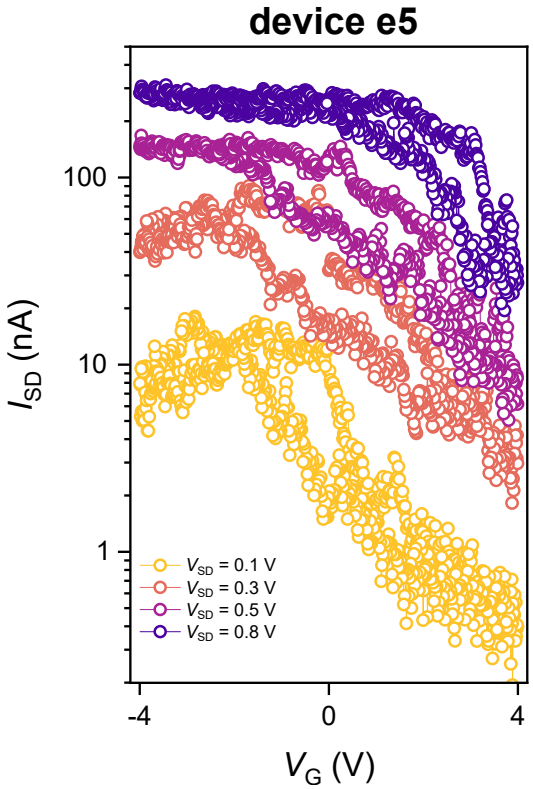


Figure B.4: FET characteristics: $I_{on}/I_{off} \simeq 10^2$ at $V_{SD} = 0.1\,V$ ($I_{on}/I_{off} \simeq 10^1$ at $V_{SD} = 0.8\,V$), small hysteresis present in all the transfer characteristics, $SS \simeq 400\,mV\ dec^{-1}$ at $V_{SD} = 0.8\,V$, $\mu_{lin} = 5\,cm^2\,V^{-1}\,s^{-1}$, $\mu_{sat} = 1\,cm^2\,V^{-1}\,s^{-1}$

References

[1] Wenhui Niu et al. “Exceptionally clean single-electron transistors from solutions of molecular graphene nanoribbons”. In: *Nature Materials* 22.2 (2023), pp. 180–185.

[2] Qiang Chen et al. “Porphyrin-Fused Graphene Nanoribbons”. In: (2023).

[3] Ian King, Adrian Leung, and Pogkas Demetrios. *The Chip Shortage Keeps Getting Worse. Why Can’t We Just Make More?* Ed. by Bloomberg. May 2021. URL: https://www.bloomberg.com/graphics/2021-chip-production-why-hard-to-make-semiconductors/.

[4] Antonio Veras et al. *Strengthening the Global Semiconductor Supply Chain in an Uncertain Era*. Ed. by Semiconductor Industry Association BCG. Apr. 2021. URL: https://www.semiconductors.org/wp-content/uploads/2021/05/BCG-x-SIA-Strengthening-the-Global-Semiconductor-Value-Chain-April-2021_1.pdf.

[5] William Shockley. “The path to the conception of the junction transistor”. In: *IEEE Transactions on Electron Devices* 31.11 (1984), pp. 1523–1546.

[6] Andrea Gemma and Bernd Gotsmann. “A roadmap for molecular thermoelectricity”. In: *Nature Nanotechnology* 16.12 (2021), pp. 1299–1301.

[7] Mildred S Dresselhaus et al. “New directions for low-dimensional thermoelectric materials”. In: *Advanced materials* 19.8 (2007), pp. 1043–1053.

[8] Fu-Liang Yang et al. “5nm-gate nanowire FinFET”. In: *Digest of Technical Papers. 2004 Symposium on VLSI Technology, 2004.* IEEE. 2004, pp. 196–197.

[9] JJ Gu et al. “First experimental demonstration of gate-all-around III–V MOSFETs by top-down approach”. In: *2011 International Electron Devices Meeting*. IEEE. 2011, pp. 33–2.

[10] Daniel Neumaier, Stephan Pindl, and Max C Lemme. “Integrating graphene into semiconductor fabrication lines”. In: *Nature Materials* 18.6 (2019), pp. 525–529.

[11] Anurag Chaudhry and M Jagadesh Kumar. “Controlling short-channel effects in deep-submicron SOI MOSFETs for improved reliability: a review”. In: *IEEE Transactions on Device and Materials Reliability* 4.1 (2004), pp. 99–109.

[12] Qian Xie, Jun Xu, and Yuan Taur. “Review and critique of analytic models of MOSFET short-channel effects in subthreshold”. In: *IEEE transactions on electron devices* 59.6 (2012), pp. 1569–1579.

[13] Pedro C Feijoo, David Jiménez, and Xavier Cartoixà. “Short channel effects in graphene-based field effect transistors targeting radio-frequency applications”. In: *2D Materials* 3.2 (2016), p. 025036.

[14] Frank Schwierz. “Graphene transistors”. In: *Nature Nanotechnology* 5.7 (2010), p. 487.

[15] SA Thiele, JA Schaefer, and Frank Schwierz. "Modeling of graphene metal-oxide-semiconductor field-effect transistors with gapless large-area graphene channels". In: *Journal of Applied Physics* 107.9 (2010), p. 094505.

[16] Mildred S Dresselhaus, Gene Dresselhaus, and Ado Jorio. *Group theory: application to the physics of condensed matter*. Springer Science & Business Media, 2007.

[17] Philip Richard Wallace. "The band theory of graphite". In: *Physical Review* 71.9 (1947), p. 622.

[18] A. H. Castro Neto et al. "The electronic properties of graphene". In: *Rev. Mod. Phys.* 81.1 (Jan. 2009), pp. 109–162. URL: http://link.aps.org/doi/10.1103/RevModPhys.81.109.

[19] RS Deacon et al. "Cyclotron resonance study of the electron and hole velocity in graphene monolayers". In: *Physical Review B* 76.8 (2007), p. 081406.

[20] Edward L Wolf. *Graphene: a new paradigm in condensed matter and device physics*. 2014.

[21] Kostya S Novoselov et al. "Electric field effect in atomically thin carbon films". In: *Science* 306.5696 (2004), pp. 666–669.

[22] Cristina Bena and Steven A Kivelson. "Quasiparticle scattering and local density of states in graphite". In: *Physical Review B* 72.12 (2005), p. 125432.

[23] Kirill I Bolotin et al. "Temperature-dependent transport in suspended graphene". In: *Physical Review letters* 101.9 (2008), p. 096802.

[24] J-H Chen et al. "Charged-impurity scattering in graphene". In: *Nature Physics* 4.5 (2008), pp. 377–381.

[25] Zhigang Jiang et al. "Quantum Hall states near the charge-neutral Dirac point in graphene". In: *Physical Review Letters* 99.10 (2007), p. 106802.

[26] Barbaros Özyilmaz et al. "Electronic transport and quantum Hall effect in bipolar graphene p- n- p junctions". In: *Physical Review Letters* 99.16 (2007), p. 166804.

[27] Mark Neisser. "International Roadmap for Devices and Systems lithography roadmap". In: *Journal of Micro/Nanopatterning, Materials, and Metrology* 20.4 (2021), p. 044601.

[28] Frank Schwierz, Hei Wong, and Juin J Liou. *Nanometer CMOS*. Pan Stanford Publishing, 2010.

[29] EH Hwang, S Adam, and S Das Sarma. "Carrier transport in two-dimensional graphene layers". In: *Physical Review Letters* 98.18 (2007), p. 186806.

[30] Fredrik Schedin et al. "Detection of individual gas molecules adsorbed on graphene". In: *Nature Materials* 6.9 (2007), pp. 652–655.

[31] SV Morozov et al. "Giant intrinsic carrier mobilities in graphene and its bilayer". In: *Physical Review Letters* 100.1 (2008), p. 016602.

[32] Gianluca Giovannetti et al. "Substrate-induced band gap in graphene on hexagonal boron nitride: Ab initio density functional calculations". In: *Physical Review B* 76.7 (2007), p. 073103.

[33] Yuan Cao et al. “Unconventional superconductivity in magic-angle graphene superlattices”. In: *Nature* 556.7699 (2018), pp. 43–50.

[34] Anna M Seiler et al. “Quantum cascade of new correlated phases in trigonally warped bilayer graphene”. In: *arXiv preprint arXiv:2111.06413* (2021).

[35] Frank Schwierz. “Graphene transistors: status, prospects, and problems”. In: *Proceedings of the IEEE* 101.7 (2013), pp. 1567–1584.

[36] Andrea F Young and Philip Kim. “Quantum interference and Klein tunnelling in graphene heterojunctions”. In: *Nature Physics* 5.3 (2009), pp. 222–226.

[37] MI Katsnelson, KS Novoselov, and AK Geim. “Chiral tunnelling and the Klein paradox in graphene”. In: *Nature Physics* 2.9 (2006), pp. 620–625.

[38] Antonio Di Bartolomeo. “Graphene Schottky diodes: An experimental review of the rectifying graphene/semiconductor heterojunction”. In: *Physics Reports* 606 (2016), pp. 1–58.

[39] Kinam Kim et al. “A role for graphene in silicon-based semiconductor devices”. In: *Nature* 479.7373 (2011), pp. 338–344.

[40] Dharmendar Reddy et al. “Graphene field-effect transistors”. In: *Journal of Physics D: Applied Physics* 44.31 (2011), p. 313001.

[41] Inanc Meric et al. “RF performance of top-gated, zero-bandgap graphene field-effect transistors”. In: *2008 IEEE International Electron Devices Meeting*. IEEE. 2008, pp. 1–4.

[42] Inanc Meric et al. “Current saturation in zero-bandgap, top-gated graphene field-effect transistors”. In: *Nature Nanotechnology* 3.11 (2008), p. 654.

[43] Ivo Colmiais et al. “Towards RF graphene devices: a review”. In: *FlatChem* (2022), p. 100409.

[44] Lei Liao and Xiangfeng Duan. “Graphene for radio frequency electronics”. In: *Materials Today* 15.7-8 (2012), pp. 328–338.

[45] Yu-Ming Lin et al. “Operation of graphene transistors at gigahertz frequencies”. In: *Nano letters* 9.1 (2009), pp. 422–426.

[46] Yu-Ming Lin et al. “Development of graphene FETs for high frequency electronics”. In: *2009 IEEE International Electron Devices Meeting (IEDM)*. IEEE. 2009, pp. 1–4.

[47] Mi Jang et al. “Improved performance and stability of field-effect transistors with polymeric residue-free graphene channel transferred by gold layer”. In: *Physical Chemistry Chemical Physics* 16.9 (2014), pp. 4098–4105.

[48] Y-M Lin et al. “100-GHz transistors from wafer-scale epitaxial graphene”. In: *Science* 327.5966 (2010), pp. 662–662.

[49] Yang Xu et al. “Contacts between two-and three-dimensional materials: ohmic, Schottky, and p–n heterojunctions”. In: *ACS Nano* 10.5 (2016), pp. 4895–4919.

[50] Lei Liao et al. “High-speed graphene transistors with a self-aligned nanowire gate”. In: *Nature* 467.7313 (2010), p. 305.

[51] Simon M Sze, Yiming Li, and Kwok K Ng. *Physics of semiconductor devices*. John wiley & sons, 2021.

[52] Rui Cheng et al. "High-frequency self-aligned graphene transistors with transferred gate stacks". In: *Proceedings of the National Academy of Sciences* 109.29 (2012), pp. 11588–11592.

[53] Yanqing Wu et al. "State-of-the-art graphene high-frequency electronics". In: *Nano Letters* 12.6 (2012), pp. 3062–3067.

[54] S Sonde et al. "Electrical properties of the graphene/4 H-SiC (0001) interface probed by scanning current spectroscopy". In: *Physical Review B* 80.24 (2009), p. 241406.

[55] Zelei Guo et al. "Record maximum oscillation frequency in C-face epitaxial graphene transistors". In: *Nano letters* 13.3 (2013), pp. 942–947.

[56] K.L. Tan et al. "94-GHz 0.1- mu m T-gate low-noise pseudomorphic InGaAs HEMTs". In: *IEEE Electron Device Letters* 11.12 (1990), pp. 585–587.

[57] I. Post et al. "A 65nm CMOS SOC Technology Featuring Strained Silicon Transistors for RF Applications". In: *2006 International Electron Devices Meeting*. 2006, pp. 1–3.

[58] R Lai et al. "Sub 50 nm InP HEMT device with Fmax greater than 1 THz". In: *2007 IEEE International Electron Devices Meeting*. IEEE. 2007, pp. 609–611.

[59] Mildred S Dresselhaus et al. "Carbon nanotubes". In: *The physics of fullerene-based and fullerene-related materials*. Springer, 2000, pp. 331–379.

[60] G Dresselhaus, Mildred S Dresselhaus, and Riichiro Saito. *Physical properties of carbon nanotubes*. World scientific, 1998.

[61] GA Steele et al. "Large spin-orbit coupling in carbon nanotubes". In: *Nature communications* 4.1 (2013), pp. 1–7.

[62] Edward A Laird et al. "Quantum transport in carbon nanotubes". In: *Reviews of Modern Physics* 87.3 (2015), p. 703.

[63] Luis EF Foa Torres, Stephan Roche, and Jean-Christophe Charlier. *Introduction to graphene-based nanomaterials: from electronic structure to quantum transport*. Cambridge University Press, 2014.

[64] Sander J Tans, Alwin RM Verschueren, and Cees Dekker. "Room-temperature transistor based on a single carbon nanotube". In: *Nature* 393.6680 (1998), pp. 49–52.

[65] Aaron D Franklin et al. "Sub-10 nm carbon nanotube transistor". In: *Nano Letters* 12.2 (2012), pp. 758–762.

[66] Aaron D Franklin and Zhihong Chen. "Length scaling of carbon nanotube transistors". In: *Nature Nanotechnology* 5.12 (2010), p. 858.

[67] Ralf Thomas Weitz et al. "High-performance carbon nanotube field effect transistors with a thin gate dielectric based on a self-assembled monolayer". In: *Nano letters* 7.1 (2007), pp. 22–27.

[68] Yu-Ming Lin et al. "High-performance carbon nanotube field-effect transistor with tunable polarities". In: *IEEE Transactions on Nanotechnology* 4.5 (2005), pp. 481–489.

[69] Ali Javey et al. "High-field quasiballistic transport in short carbon nanotubes". In: *Physical Review Letters* 92.10 (2004), p. 106804.

[70] N Chimot et al. “Gigahertz frequency flexible carbon nanotube transistors”. In: *Applied Physics Letters* 91.15 (2007), p. 153111.

[71] Michael Schröter et al. “CNTFET-based RF electronics—State-of-the-art and future prospects”. In: *2016 IEEE 16th Topical Meeting on Silicon Monolithic Integrated Circuits in RF Systems (SiRF)*. IEEE. 2016, pp. 97–100.

[72] Ali Javey et al. “High-κ dielectrics for advanced carbon-nanotube transistors and logic gates”. In: *Nature Materials* 1.4 (2002), p. 241.

[73] Vladimir Derenskyi et al. “Carbon nanotube network ambipolar field-effect transistors with 108 on/off ratio”. In: *Advanced Materials* 26.34 (2014), pp. 5969–5975.

[74] A Le Louarn et al. “Intrinsic current gain cutoff frequency of 30 GHz with carbon nanotube transistors”. In: *Applied physics letters* 90.23 (2007), p. 233108.

[75] Ali Javey et al. “High performance n-type carbon nanotube field-effect transistors with chemically doped contacts”. In: *Nano letters* 5.2 (2005), pp. 345–348.

[76] Yuchi Che et al. “T-gate aligned nanotube radio frequency transistors and circuits with superior performance”. In: *ACS nano* 7.5 (2013), pp. 4343–4350.

[77] Yu Cao et al. “Radio frequency transistors using aligned semiconducting carbon nanotubes with current-gain cutoff frequency and maximum oscillation frequency simultaneously greater than 70 GHz”. In: *ACS nano* 10.7 (2016), pp. 6782–6790.

[78] Fumiyuki Nihey et al. “A top-gate carbon-nanotube field-effect transistor with a titanium-dioxide insulator”. In: *Japanese journal of applied physics* 41.10A (2002), p. L1049.

[79] Pak Heng Lau et al. “Fully printed, high performance carbon nanotube thin-film transistors on flexible substrates”. In: *Nano letters* 13.8 (2013), pp. 3864–3869.

[80] Ali Javey and Jing Kong. *Carbon nanotube electronics*. Springer Science & Business Media, 2009.

[81] Amandeep Singh, Mamta Khosla, and Balwinder Raj. “Comparative analysis of carbon nanotube field effect transistors”. In: *2015 IEEE 4th Global Conference on Consumer Electronics (GCCE)*. IEEE. 2015, pp. 552–555.

[82] Otto F Sankey, Roland E Allen, and John D Dow. “Si/transition-metal Schottky barriers: Fermi-level pinning by Si dangling bonds at interfacial vacancies”. In: *Solid state communications* 49.1 (1984), pp. 1–5.

[83] Adrian Bachtold et al. “Logic circuits with carbon nanotube transistors”. In: *Science* 294.5545 (2001), pp. 1317–1320.

[84] Johannes Svensson et al. “The dependence of the Schottky barrier height on carbon nanotube diameter for Pd–carbon nanotube contacts”. In: *Nanotechnology* 20.17 (2009), p. 175204.

[85] François Léonard and J Tersoff. “Role of Fermi-level pinning in nanotube Schottky diodes”. In: *Physical Review Letters* 84.20 (2000), p. 4693.

[86] Seong Chu Lim et al. “Contact resistance between metal and carbon nanotube interconnects: Effect of work function and wettability”. In: *Applied Physics Letters* 95.26 (2009), p. 264103.

[87] Li Ding et al. “Y-contacted high-performance n-type single-walled carbon nanotube field-effect transistors: scaling and comparison with Sc-contacted devices”. In: *Nano Letters* 9.12 (2009), pp. 4209–4214.

[88] Lian-Mao Peng, Zhiyong Zhang, and Chenguang Qiu. “Carbon nanotube digital electronics”. In: *Nature Electronics* 2.11 (2019), pp. 499–505.

[89] Adrian M Ionescu and Heike Riel. “Tunnel field-effect transistors as energy-efficient electronic switches”. In: *nature* 479.7373 (2011), pp. 329–337.

[90] Ahmed MM Hammam et al. “Sub-10 nm graphene nano-ribbon tunnel field-effect transistor”. In: *Carbon* 126 (2018), pp. 588–593.

[91] Wan Sik Hwang et al. “Room-temperature graphene-nanoribbon tunneling field-effect transistors”. In: *npj 2D Materials and Applications* 3.1 (2019), pp. 1–7.

[92] Brett Lee Allen, Padmakar D Kichambare, and Alexander Star. “Carbon nanotube field-effect-transistor-based biosensors”. In: *Advanced Materials* 19.11 (2007), pp. 1439–1451.

[93] Yosuke Nosho et al. “n-type carbon nanotube field-effect transistors fabricated by using Ca contact electrodes”. In: *Applied Physics Letters* 86.7 (2005), p. 073105.

[94] Liam Brownlie and Joseph Shapter. “Advances in carbon nanotube n-type doping: Methods, analysis and applications”. In: *Carbon* 126 (2018), pp. 257–270.

[95] Marc Bockrath et al. “Chemical doping of individual semiconducting carbon-nanotube ropes”. In: *Physical Review B* 61.16 (2000), R10606.

[96] Chongwu Zhou et al. “Modulated chemical doping of individual carbon nanotubes”. In: *Science* 290.5496 (2000), pp. 1552–1555.

[97] Choongho Yu et al. “Air-stable fabric thermoelectric modules made of N-and P-type carbon nanotubes”. In: *Energy & Environmental Science* 5.11 (2012), pp. 9481–9486.

[98] Aaron D Franklin and Zhihong Chen. “Length scaling of carbon nanotube transistors”. In: *Nature Nanotechnology* 5.12 (2010), p. 858.

[99] Jose M Marulanda and Ashok Srivastava. “Carrier density and effective mass calculations in carbon nanotubes”. In: *Physica Status Solidi (b)* 245.11 (2008), pp. 2558–2562.

[100] Phaedon Avouris et al. “Carbon nanotube electronics”. In: *Proceedings of the IEEE* 91.11 (2003), pp. 1772–1784.

[101] MP Anantram and F Leonard. “Physics of carbon nanotube electronic devices”. In: *Reports on progress in physics* 69.3 (2006), p. 507.

[102] Max M Shulaker et al. “Carbon nanotube computer”. In: *Nature* 501.7468 (2013), pp. 526–530.

[103] Artem Fediai, Dmitry A Ryndyk, and Gianaurelio Cuniberti. “Electron transport in extended carbon-nanotube/metal contacts: Ab initio based Green function method”. In: *Physical Review B* 91.16 (2015), p. 165404.

[104] Fabian Teichert et al. “An improved Green’s function algorithm applied to quantum transport in carbon nanotubes”. In: *Computational Materials Science* 169 (2019), p. 109014.

[105] Artem Fediai et al. “Towards an optimal contact metal for CNTFETs”. In: *Nanoscale* 8.19 (2016), pp. 10240–10251.

[106] Lijun Liu et al. “Scaling down contact length in complementary carbon nanotube field-effect transistors”. In: *Nanoscale* 9.27 (2017), pp. 9615–9621.

[107] Vivek Saraswat, Robert M Jacobberger, and Michael S Arnold. “Materials science challenges to graphene nanoribbon electronics”. In: *ACS Nano* 15.3 (2021), pp. 3674–3708.

[108] Meninder S Purewal et al. “Scaling of resistance and electron mean free path of single-walled carbon nanotubes”. In: *Physical Review Letters* 98.18 (2007), p. 186808.

[109] Johannes Svensson and Eleanor EB Campbell. “Schottky barriers in carbon nanotube-metal contacts”. In: *Journal of Applied Physics* 110.11 (2011), p. 16.

[110] Supriyo Datta. *Electronic transport in mesoscopic systems*. Cambridge university press, 1997.

[111] Kathleen M McCreary et al. “Magnetic moment formation in graphene detected by scattering of pure spin currents”. In: *Physical Review Letters* 109.18 (2012), p. 186604.

[112] Luis Escalera-Moreno et al. “Spin states, vibrations and spin relaxation in molecular nanomagnets and spin qubits: a critical perspective”. In: *Chemical science* 9.13 (2018), pp. 3265–3275.

[113] Dmitri K Efetov and Philip Kim. “Controlling electron-phonon interactions in graphene at ultrahigh carrier densities”. In: *Physical Review Letters* 105.25 (2010), p. 256805.

[114] G Zimmerli et al. “Noise in the Coulomb blockade electrometer”. In: *Applied Physics Letters* 61.2 (1992), pp. 237–239.

[115] Pascal Gehring, Jos M Thijssen, and Herre SJ van der Zant. “Single-molecule quantum-transport phenomena in break junctions”. In: *Nature Reviews Physics* 1.6 (2019), pp. 381–396.

[116] Rocco Gaudenzi et al. “Transport mirages in single-molecule devices”. In: *The journal of chemical physics* 146.9 (2017), p. 092330.

[117] Stefan Thiele. *Read-Out and Coherent Manipulation of an Isolated Nuclear Spin: Using a Single-Molecule Magnet Spin-Transistor*. Springer, 2015.

[118] José M Soler et al. “The SIESTA method for ab initio order-N materials simulation”. In: *Journal of Physics: Condensed Matter* 14.11 (2002), p. 2745.

[119] R Frisenda and HSJ Van Der Zant. “Transition from strong to weak electronic coupling in a single-molecule junction”. In: *Physical Review Letters* 117.12 (2016), p. 126804.

[120] Jakub K Sowa et al. “Beyond Marcus theory and the Landauer-Büttiker approach in molecular junctions: A unified framework”. In: *The Journal of chemical physics* 149.15 (2018), p. 154112.

[121] DV Averin and Yu V Nazarov. “Virtual electron diffusion during quantum tunneling of the electric charge”. In: *Physical Review Letters* 65.19 (1990), p. 2446.

[122] R Schleser et al. “Cotunneling-mediated transport through excited states in the Coulomb-blockade regime”. In: *Physical Review letters* 94.20 (2005), p. 206805.

[123] HW Liu et al. “Pauli spin blockade in cotunneling transport through a double quantum dot”. In: *Physical Review B* 72.16 (2005), p. 161305.

[124] James O Thomas et al. “Understanding resonant charge transport through weakly coupled single-molecule junctions”. In: *Nature communications* 10.1 (2019), pp. 1–9.

[125] Jakub K Sowa et al. “Beyond Marcus theory and the Landauer–Büttiker approach in molecular junctions. II. A self-consistent Born approach”. In: *The Journal of Chemical Physics* 152.6 (2020), p. 064103.

[126] Johannes S Seldenthuis et al. “Vibrational excitations in weakly coupled single-molecule junctions: a computational analysis”. In: *ACS Nano* 2.7 (2008), pp. 1445–1451.

[127] Massimiliano Esposito and Michael Galperin. “Self-consistent quantum master equation approach to molecular transport”. In: *The Journal of Physical Chemistry C* 114.48 (2010), pp. 20362–20369.

[128] Matthew D Todd et al. “Electron transfer rates from time-dependent correlation functions. Wavepacket dynamics, solvent effects, and applications”. In: *Journal of Photochemistry and Photobiology A: Chemistry* 82.1-3 (1994), pp. 87–101.

[129] Konstantin K Likharev. “Single-electron devices and their applications”. In: *Proceedings of the IEEE* 87.4 (1999), pp. 606–632.

[130] S Sapmaz et al. “Electronic excitation spectrum of metallic carbon nanotubes”. In: *Physical Review B* 71.15 (2005), p. 153402.

[131] Renaud Leturcq et al. “Franck–Condon blockade in suspended carbon nanotube quantum dots”. In: *Nature Physics* 5.5 (2009), pp. 327–331.

[132] DV Averin and KK Likharev. “Coulomb blockade of single-electron tunneling, and coherent oscillations in small tunnel junctions”. In: *Journal of low temperature physics* 62.3-4 (1986), pp. 345–373.

[133] Bernhard Stojetz et al. “Effect of band structure on quantum interference in multiwall carbon nanotubes”. In: *Physical Review Letters* 94.18 (2005), p. 186802.

[134] Pablo Jarillo-Herrero et al. “Orbital Kondo effect in carbon nanotubes”. In: *Nature* 434.7032 (2005), pp. 484–488.

[135] Jens Koch and Felix Von Oppen. “Franck-Condon blockade and giant Fano factors in transport through single molecules”. In: *Physical Review Letters* 94.20 (2005), p. 206804.

[136] Jens Koch, Felix Von Oppen, and AV Andreev. “Theory of the Franck-Condon blockade regime”. In: *Physical Review B* 74.20 (2006), p. 205438.

[137] Xinran Wang et al. “Room-temperature all-semiconducting sub-10-nm graphene nanoribbon field-effect transistors”. In: *Physical Review Letters* 100.20 (2008), p. 206803.

[138] Akimitsu Narita et al. “Synthesis of structurally well-defined and liquid-phase-processable graphene nanoribbons”. In: *Nature chemistry* 6.2 (2014), pp. 126–132.

[139] Junzhi Liu et al. "Toward cove-edged low band gap graphene nanoribbons". In: *Journal of the American Chemical Society* 137.18 (2015), pp. 6097–6103.

[140] Thierry Giamarchi. *Quantum Physics in One Dimension*. Vol. 121. Clarendon press, 2003.

[141] MA Cazalilla et al. "One dimensional bosons: From condensed matter systems to ultracold gases". In: *Reviews of Modern Physics* 83.4 (2011), p. 1405.

[142] Thierry Giamarchi. "One-dimensional physics in the 21st century". In: *Comptes Rendus Physique* 17.3-4 (2016), pp. 322–331.

[143] Erminald Bertel. "Physics in One Dimension". In: *European Journal of Physics Education* 4.1 (2017), pp. 58–77.

[144] Sin-itiro Tomonaga. "Remarks on Bloch's method of sound waves applied to many-fermion problems". In: *Progress of Theoretical Physics* 5.4 (1950), pp. 544–569.

[145] JM Luttinger. "An exactly soluble model of a many-fermion system". In: *Journal of mathematical physics* 4.9 (1963), pp. 1154–1162.

[146] Daniel C Mattis and Elliott H Lieb. "Exact solution of a many-fermion system and its associated boson field". In: *Bosonization*. World Scientific, 1994, pp. 98–106.

[147] FDM Haldane. "'Luttinger liquid theory'of one-dimensional quantum fluids. I. Properties of the Luttinger model and their extension to the general 1D interacting spinless Fermi gas". In: *Journal of Physics C: Solid State Physics* 14.19 (1981), p. 2585.

[148] Jan Von Delft and Herbert Schoeller. "Bosonization for beginners—refermionization for experts". In: *Annalen der Physik* 7.4 (1998), pp. 225–305.

[149] Yiqing Jin. "Measurement of electron-electron interactions in one dimension with tunnelling spectroscopy". PhD thesis. University of Cambridge, 2020.

[150] Thierry Giamarchi. "Strong correlations in low dimensional systems". In: *AIP Conference Proceedings*. Vol. 846. 1. American Institute of Physics. 2006, pp. 94–129.

[151] Bella Lake et al. "Quantum criticality and universal scaling of a quantum antiferromagnet". In: *Nature Materials* 4.4 (2005), pp. 329–334.

[152] Martin Mourigal et al. "Fractional spinon excitations in the quantum Heisenberg antiferromagnetic chain". In: *Nature Physics* 9.7 (2013), pp. 435–441.

[153] Pedro Vianez, Oleksandr Tsyplyatyev, and Christopher Ford. "Semiconductor nanodevices as a probe of strong electron correlations". In: *Frontiers of Nanoscience*. Vol. 20. Elsevier, 2021, pp. 31–66.

[154] Reinhold Egger and Alexander O Gogolin. "Effective low-energy theory for correlated carbon nanotubes". In: *Physical Review Letters* 79.25 (1997), p. 5082.

[155] Reinhold Egger. "Luttinger liquid behavior in multiwall carbon nanotubes". In: *Physical Review Letters* 83.26 (1999), p. 5547.

[156] Charles Kane, Leon Balents, and Matthew PA Fisher. "Coulomb interactions and mesoscopic effects in carbon nanotubes". In: *Physical Review Letters* 79.25 (1997), p. 5086.

[157] Bitan Roy, Malcolm P Kennett, and S Das Sarma. "Chiral symmetry breaking and the quantum Hall effect in monolayer graphene". In: *Physical Review B* 90.20 (2014), p. 201409.

[158] Ann E Mattsson, Sebastian Eggert, and Henrik Johannesson. "Properties of a Luttinger liquid with boundaries at finite temperature and size". In: *Physical Review B* 56.24 (1997), p. 15615.

[159] Michele Fabrizio and Alexander O Gogolin. "Interacting one-dimensional electron gas with open boundaries". In: *Physical Review B* 51.24 (1995), p. 17827.

[160] Marc Bockrath et al. "Luttinger-liquid behaviour in carbon nanotubes". In: *Nature* 397.6720 (1999), p. 598.

[161] Henk W Ch Postma et al. "Carbon nanotube single-electron transistors at room temperature". In: *Science* 293.5527 (2001), pp. 76–79.

[162] M Thorwart et al. "Correlated tunneling in intramolecular carbon nanotube quantum dots". In: *Physical Review Letters* 89.19 (2002), p. 196402.

[163] Wentao Xu and Tae-Woo Lee. "Recent progress in fabrication techniques of graphene nanoribbons". In: *Materials Horizons* 3.3 (2016), pp. 186–207.

[164] Melinda Y Han et al. "Energy band-gap engineering of graphene nanoribbons". In: *Physical Review Letters* 98.20 (2007), p. 206805.

[165] Zhansong Geng et al. "Graphene Nanoribbons for Electronic Devices". In: *Annalen der Physik* 529.11 (2017), p. 1700033.

[166] Philip Kim et al. "Graphene nanoribbon devices and quantum heterojunction devices". In: *2009 IEEE International Electron Devices Meeting (IEDM)*. IEEE. 2009, pp. 1–4.

[167] Xiaolin Li et al. "Chemically derived, ultrasmooth graphene nanoribbon semiconductors". In: *science* 319.5867 (2008), pp. 1229–1232.

[168] Zhihong Chen et al. "Graphene nano-ribbon electronics". In: *Physica E: Low-dimensional Systems and Nanostructures* 40.2 (2007), pp. 228–232.

[169] Li Yang et al. "Quasiparticle energies and band gaps in graphene nanoribbons". In: *Physical Review Letters* 99.18 (2007), p. 186801.

[170] Martin Evaldsson et al. "Edge-disorder-induced Anderson localization and conduction gap in graphene nanoribbons". In: *Physical Review B* 78.16 (2008), p. 161407.

[171] Jinming Cai et al. "Atomically precise bottom-up fabrication of graphene nanoribbons". In: *Nature* 466.7305 (2010), p. 470.

[172] Akimitsu Narita, Xinliang Feng, and Klaus Müllen. "Bottom-up synthesis of chemically precise graphene nanoribbons". In: *The Chemical Record* 15.1 (2015), pp. 295–309.

[173] Yunbin Hu et al. "Bandgap engineering of graphene nanoribbons by control over structural distortion". In: *Journal of the American Chemical Society* 140.25 (2018), pp. 7803–7809.

[174] Liang Ma, Jinlan Wang, and Feng Ding. "Recent Progress and Challenges in Graphene Nanoribbon Synthesis". In: *ChemPhysChem* 14.1 (2013), pp. 47–54.

[175] Dmitry V Kosynkin et al. "Longitudinal unzipping of carbon nanotubes to form graphene nanoribbons". In: *Nature* 458.7240 (2009), pp. 872–876.

[176] Sujit S. Datta et al. "Crystallographic Etching of Few-Layer Graphene". In: *Nano Letters* 8.7 (2008), pp. 1912–1915. URL: http://arxiv.org/pdf/0806.3965v1.pdf.

[177] Melinda Y Han, Juliana C Brant, and Philip Kim. "Electron transport in disordered graphene nanoribbons". In: *Physical Review Letters* 104.5 (2010), p. 056801.

[178] Federico Lombardi et al. "Synthetic tuning of the quantum properties of open-shell radicaloids". In: *Chem* 7.5 (2021), pp. 1363–1378.

[179] Federico Lombardi et al. "Quantum units from the topological engineering of molecular graphenoids". In: *Science* 366.6469 (2019), pp. 1107–1110.

[180] Katsunori Wakabayashi et al. "Electronic states of graphene nanoribbons and analytical solutions". In: *Science and technology of advanced materials* 11.5 (2010), p. 054504.

[181] Young-Woo Son, Marvin L Cohen, and Steven G Louie. "Energy gaps in graphene nanoribbons". In: *Physical Review Letters* 97.21 (2006), p. 216803.

[182] Arlenciu Celis et al. "Graphene nanoribbons: fabrication, properties and devices". In: *Journal of Physics D: Applied Physics* 49.14 (2016), p. 143001.

[183] Verónica Barone, Oded Hod, and Gustavo E Scuseria. "Electronic structure and stability of semiconducting graphene nanoribbons". In: *Nano Letters* 6.12 (2006), pp. 2748–2754.

[184] Jens Baringhaus et al. "Exceptional ballistic transport in epitaxial graphene nanoribbons". In: *Nature* 506.7488 (2014), pp. 349–354.

[185] Li Yang et al. "Quasiparticle energies and band gaps in graphene nanoribbons". In: *Physical Review Letters* 99.18 (2007), p. 186801.

[186] Kyoko Nakada et al. "Edge state in graphene ribbons: Nanometer size effect and edge shape dependence". In: *Physical Review B* 54.24 (1996), p. 17954.

[187] Amina Kimouche et al. "Ultra-narrow metallic armchair graphene nanoribbons". In: *Nature communications* 6.1 (2015), pp. 1–6.

[188] Dimas G de Oteyza et al. "Substrate-independent growth of atomically precise chiral graphene nanoribbons". In: *ACS nano* 10.9 (2016), pp. 9000–9008.

[189] Eduard Carbonell-Sanroma et al. "Electronic properties of substitutionally boron-doped graphene nanoribbons on a Au (111) surface". In: *The Journal of Physical Chemistry C* 122.28 (2018), pp. 16092–16099.

[190] Yousuke Kobayashi et al. "Edge state on hydrogen-terminated graphite edges investigated by scanning tunneling microscopy". In: *Physical Review B* 73.12 (2006), p. 125415.

[191] Young-Woo Son, Marvin L Cohen, and Steven G Louie. "Half-metallic graphene nanoribbons". In: *Nature* 444.7117 (2006), pp. 347–349.

[192] Sudipta Dutta, Arun K Manna, and Swapan K Pati. "Intrinsic half-metallicity in modified graphene nanoribbons". In: *Physical Review Letters* 102.9 (2009), p. 096601.

[193] Oleg V Yazyev, Rodrigo B Capaz, and Steven G Louie. "Theory of magnetic edge states in chiral graphene nanoribbons". In: *Physical Review B* 84.11 (2011), p. 115406.

[194] Hosik Lee et al. "Magnetic ordering at the edges of graphitic fragments: Magnetic tail interactions between the edge-localized states". In: *Physical Review B* 72.17 (2005), p. 174431.

[195] Michael Slota et al. "Magnetic edge states and coherent manipulation of graphene nanoribbons". In: *Nature* 557.7707 (2018), pp. 691–695.

[196] YU Peter and Manuel Cardona. *Fundamentals of semiconductors: physics and materials properties*. Springer Science & Business Media, 2010.

[197] Christoph Stampfer et al. "Tunable Coulomb blockade in nanostructured graphene". In: *Applied Physics Letters* 92.1 (2008), p. 012102.

[198] Jian Sun et al. "Lateral plasma etching enhanced on/off ratio in graphene nanoribbon field-effect transistor". In: *Applied Physics Letters* 106.3 (2015), p. 033509.

[199] Lingxiu Chen et al. "Oriented graphene nanoribbons embedded in hexagonal boron nitride trenches". In: *Nature communications* 8 (2017), p. 14703.

[200] Wan Sik Hwang et al. "Graphene nanoribbon field-effect transistors on wafer-scale epitaxial graphene on SiC substrates". In: *APL materials* 3.1 (2015), p. 011101.

[201] Wan Sik Hwang et al. "Transport properties of graphene nanoribbon transistors on chemical-vapor-deposition grown wafer-scale graphene". In: *Applied Physics Letters* 100.20 (2012), p. 203107.

[202] Liying Jiao et al. "Facile synthesis of high-quality graphene nanoribbons". In: *Nature nanotechnology* 5.5 (2010), pp. 321–325.

[203] Changxin Chen et al. "Sub-10-nm graphene nanoribbons with atomically smooth edges from squashed carbon nanotubes". In: *Nature Electronics* (2021), pp. 1–11.

[204] Kyuhyun Bang et al. "Effect of ribbon width on electrical transport properties of graphene nanoribbons". In: *Nano convergence* 5.1 (2018), p. 7.

[205] Denis A Areshkin, Daniel Gunlycke, and Carter T White. "Ballistic transport in graphene nanostrips in the presence of disorder: Importance of edge effects". In: *Nano Letters* 7.1 (2007), pp. 204–210.

[206] Ivar Martin and Ya M Blanter. "Transport in disordered graphene nanoribbons". In: *Physical Review B* 79.23 (2009), p. 235132.

[207] Zhihong Chen et al. "Graphene nano-ribbon electronics". In: *Physica E: Low-dimensional Systems and Nanostructures* 40.2 (2007), pp. 228–232.

[208] Leonid A Ponomarenko et al. "Chaotic Dirac billiard in graphene quantum dots". In: *Science* 320.5874 (2008), pp. 356–358.

[209] Carlo WJ Beenakker. "Theory of Coulomb-blockade oscillations in the conductance of a quantum dot". In: *Physical Review B* 44.4 (1991), p. 1646.

[210] Patrick B Bennett et al. "Bottom-up graphene nanoribbon field-effect transistors". In: *Applied Physics Letters* 103.25 (2013), p. 253114.

[211] Fengnian Xia et al. “The origins and limits of metal–graphene junction resistance”. In: *Nature nanotechnology* 6.3 (2011), pp. 179–184.

[212] Xiao-Ye Wang, Akimitsu Narita, and Klaus Müllen. “Precision synthesis versus bulk-scale fabrication of graphenes”. In: *Nature Reviews Chemistry* 2.1 (2017), pp. 1–10.

[213] Juan Pablo Llinas et al. “Short-channel field-effect transistors with 9-atom and 13-atom wide graphene nanoribbons”. In: *Nature communications* 8.1 (2017), p. 633.

[214] Oliver Braun et al. “Optimized graphene electrodes for contacting graphene nanoribbons”. In: *Carbon* 184 (2021), pp. 331–339.

[215] Maria El Abbassi et al. “Controlled quantum dot formation in atomically engineered graphene nanoribbon field-effect transistors”. In: *ACS Nano* 14.5 (2020), pp. 5754–5762.

[216] Ji Won Suk et al. “Transfer of CVD-grown monolayer graphene onto arbitrary substrates”. In: *ACS Nano* 5.9 (2011), pp. 6916–6924.

[217] Yi Chen, Xiao-Lei Gong, and Jing-Gang Gai. “Progress and challenges in transfer of large-area graphene films”. In: *Advanced science* 3.8 (2016), p. 1500343.

[218] Sami Ullah et al. “Graphene transfer methods: A review”. In: *Nano Research* 14.11 (2021), pp. 3756–3772.

[219] AA Houck et al. “Kondo effect in electromigrated gold break junctions”. In: *Nano Letters* 5.9 (2005), pp. 1685–1688.

[220] Regina Hoffmann et al. “Conductance of gold nanojunctions thinned by electromigration”. In: *Applied Physics Letters* 93.4 (2008), p. 043118.

[221] CS Lau et al. “Nanoscale control of graphene electrodes”. In: *Physical Chemistry Chemical Physics* 16.38 (2014), pp. 20398–20401.

[222] Bart Limburg et al. “Anchor Groups for Graphene-Porphyrin Single-Molecule Transistors”. In: *Advanced Functional Materials* 28.45 (2018), p. 1803629.

[223] Gabriele de Boo. *QTLab*. `https://github.com/ggdeboo/QTLab`. 2013.

[224] James Victor Uspensky. “Introduction to mathematical probability”. In: (1937).

[225] Yuxuan Lin et al. “Scaling and Statistics of Bottom-Up Synthesized Armchair Graphene Nanoribbon Transistors”. In: *arXiv preprint arXiv:2201.09341* (2022).

[226] Nisachol Nerngchamnong et al. “The role of van der Waals forces in the performance of molecular diodes”. In: *Nature nanotechnology* 8.2 (2013), pp. 113–118.

[227] Jurriaan Huskens et al. “A model for describing the thermodynamics of multivalent host- guest interactions at interfaces”. In: *Journal of the American Chemical Society* 126.21 (2004), pp. 6784–6797.

[228] E Mostaani, ND Drummond, and VI Fal’Ko. “Quantum Monte Carlo calculation of the binding energy of bilayer graphene”. In: *Physical Review Letters* 115.11 (2015), p. 115501.

[229] Mindy D Bishop et al. “Fabrication of carbon nanotube field-effect transistors in commercial silicon manufacturing facilities”. In: *Nature Electronics* 3.8 (2020), pp. 492–501.

[230] Robert D Deegan et al. “Capillary flow as the cause of ring stains from dried liquid drops”. In: *Nature* 389.6653 (1997), pp. 827–829.

[231] Simen Olav Njaa Sopp. “Investigation of Magnetic States in Molecular Systems in Cryogenic Environments”. PhD thesis. University of Oxford, 2021.

[232] Guanzhong Wang, Jouri Bommer, and Michiel de Moor. *Notes on Transport Measurements Using a Lock-In*. `http://homepage.tudelft.nl/q40r9/lockin-meas-guide-v20200603.pdf`. 2020.

[233] Reuben Harding. “Endohedral fullerenes as standards for portable atomic clocks”. PhD thesis. University of Oxford, 2019.

[234] Raymond Schouten. *Personal Website*. `https://qtwork.tudelft.nl/~schouten/ivvi/doc-mod/docs3b.htm`. 2021.

[235] Eugenio Coronado. “Molecular magnetism: from chemical design to spin control in molecules, materials and devices”. In: *Nature Reviews Materials* 5.2 (2020), pp. 87–104.

[236] Eugenio Coronado et al. “Coexistence of superconductivity and magnetism by chemical design”. In: *Nature chemistry* 2.12 (2010), pp. 1031–1036.

[237] Lapo Bogani and Wolfgang Wernsdorfer. “Molecular spintronics using single-molecule magnets”. In: *Nature materials* 7.3 (2008), pp. 179–186.

[238] Christian Cervetti et al. “The classical and quantum dynamics of molecular spins on graphene”. In: *Nature materials* 15.2 (2016), pp. 164–168.

[239] Chiu-Chun Tang et al. “Characteristics of a sensitive micro-Hall probe fabricated on chemical vapor deposited graphene over the temperature range from liquid-helium to room temperature”. In: *Applied Physics Letters* 99.11 (2011), p. 112107.

[240] David Collomb, Penglei Li, and Simon J Bending. “Nanoscale graphene Hall sensors for high-resolution ambient magnetic imaging”. In: *Scientific Reports* 9.1 (2019), pp. 1–10.

[241] JE Huffman, ML Snodgrass, and FJ Blatt. “Magnetoresistance of copper, gold, and indium”. In: *Physical Review B* 23.2 (1981), p. 483.

[242] John Sydney Dugdale. *The electrical properties of disordered metals*. Cambridge University Press, 1995.

[243] David Collomb, Penglei Li, and Simon Bending. “Frontiers of graphene-based Hall-effect sensors”. In: *Journal of Physics: Condensed Matter* 33.24 (2021), p. 243002.

[244] Andreas Candini. “Hall Probes Magnetometry For The Study of Molecular Nanomagnets”. PhD thesis. University of Modena and Reggio Emilia, 2007.

[245] Guibin Song, Mojtaba Ranjbar, and Richard A Kiehl. “Operation of graphene magnetic field sensors near the charge neutrality point”. In: *Communications Physics* 2.1 (2019), pp. 1–8.

[246] Adam Januszko et al. “CVD-graphene-based flexible, thermoelectrochromic sensor”. In: *Journal of Nanomaterials* 2017 (2017).

[247] Bogdan Karpiak, André Dankert, and Saroj P Dash. "Gate-tunable Hall sensors on large area CVD graphene protected by h-BN with 1D edge contacts". In: *Journal of Applied Physics* 122.5 (2017), p. 054506.

[248] S Sonusen et al. "Single layer graphene Hall sensors for scanning Hall probe microscopy (SHPM) in 3–300 K temperature range". In: *Applied surface science* 308 (2014), pp. 414–418.

[249] Zhenxing Wang et al. "Encapsulated graphene-based Hall sensors on foil with increased sensitivity". In: *Physica Status Solidi (b)* 253.12 (2016), pp. 2316–2320.

[250] André Dankert, Bogdan Karpiak, and Saroj P Dash. "Hall sensors batch-fabricated on all-CVD h-BN/graphene/h-BN heterostructures". In: *Scientific Reports* 7.1 (2017), pp. 1–7.

[251] Jan Dauber et al. "Ultra-sensitive Hall sensors based on graphene encapsulated in hexagonal boron nitride". In: *Applied Physics Letters* 106.19 (2015), p. 193501.

[252] Silke Paschen and Qimiao Si. "Quantum phases driven by strong correlations". In: *Nature Reviews Physics* 3.1 (2021), pp. 9–26.

[253] Kyounghwan Kim et al. "Tunable moiré bands and strong correlations in small-twist-angle bilayer graphene". In: *Proceedings of the National Academy of Sciences* 114.13 (2017), pp. 3364–3369.

[254] Matthew Yankowitz et al. "Tuning superconductivity in twisted bilayer graphene". In: *Science* 363.6431 (2019), pp. 1059–1064.

[255] Valeri N Kotov et al. "Electron-electron interactions in graphene: Current status and perspectives". In: *Reviews of Modern Physics* 84.3 (2012), p. 1067.

[256] Chuyao Tong et al. "Pauli Blockade of Tunable Two-Electron Spin and Valley States in Graphene Quantum Dots". In: *Physical Review Letters* 128.6 (2022), p. 067702.

[257] Xinran Wang et al. "Graphene nanoribbons with smooth edges behave as quantum wires". In: *Nature nanotechnology* 6.9 (2011), pp. 563–567.

[258] Pablo Jarillo-Herrero et al. "Electron-hole symmetry in a semiconducting carbon nanotube quantum dot". In: *Nature* 429.6990 (2004), pp. 389–392.

[259] Liying Jiao et al. "Narrow graphene nanoribbons from carbon nanotubes". In: *Nature* 458.7240 (2009), pp. 877–880.

[260] Oliver Gröning et al. "Engineering of robust topological quantum phases in graphene nanoribbons". In: *Nature* 560.7717 (2018), pp. 209–213.

[261] Daniel J Rizzo et al. "Topological band engineering of graphene nanoribbons". In: *Nature* 560.7717 (2018), pp. 204–208.

[262] Yinjuan Huang et al. "Intrinsic properties of single graphene nanoribbons in solution: synthetic and spectroscopic studies". In: *Journal of the American Chemical Society* 140.33 (2018), pp. 10416–10420.

[263] Wenhui Niu et al. "Synthetic engineering of graphene nanoribbons with excellent liquid-phase processability". In: *Trends in Chemistry* 1.6 (2019), pp. 549–558.

[264] Raymond T Tung. "The physics and chemistry of the Schottky barrier height". In: *Applied Physics Reviews* 1.1 (2014), p. 011304.

[265] Eduardo R Mucciolo, AH Castro Neto, and Caio H Lewenkopf. "Conductance quantization and transport gaps in disordered graphene nanoribbons". In: *Physical Review B* 79.7 (2009), p. 075407.

[266] C Stampfer et al. "Energy gaps in etched graphene nanoribbons". In: *Physical Review Letters* 102.5 (2009), p. 056403.

[267] S Fahlvik Svensson et al. "Nonlinear thermovoltage and thermocurrent in quantum dots". In: *New Journal of Physics* 15.10 (2013), p. 105011.

[268] Jian Zhang et al. "Room-Temperature Carbon Nanotube Single-Electron Transistors with Mechanical Buckling–Defined Quantum Dots". In: *Advanced Electronic Materials* 4.5 (2018), p. 1700628.

[269] Vishva Ray et al. "CMOS-compatible fabrication of room-temperature single-electron devices". In: *Nature nanotechnology* 3.10 (2008), pp. 603–608.

[270] Tian Pei et al. "Exchange-induced spin polarization in a single magnetic molecule junction". In: *Nature communications* 13.1 (2022), pp. 1–8.

[271] Daniel J Rizzo et al. "Rationally designed topological quantum dots in bottom-up graphene nanoribbons". In: *ACS nano* 15.12 (2021), pp. 20633–20642.

[272] Pascal Gehring et al. "Complete mapping of the thermoelectric properties of a single molecule". In: *Nature Nanotechnology* 16.4 (2021), pp. 426–430.

[273] H Van Houten et al. "Thermo-electric properties of quantum point contacts". In: *Semiconductor Science and Technology* 7.3B (1992), B215.

[274] AA Shylau, JW Kłos, and IV Zozoulenko. "Capacitance of graphene nanoribbons". In: *Physical Review B* 80.20 (2009), p. 205402.

[275] F Sols, F Guinea, and AH Castro Neto. "Coulomb blockade in graphene nanoribbons". In: *Physical Review Letters* 99.16 (2007), p. 166803.

[276] Zhen Yao et al. "Carbon nanotube intramolecular junctions". In: *Nature* 402.6759 (1999), pp. 273–276.

[277] Eros Mariani and Felix Von Oppen. "Flexural phonons in free-standing graphene". In: *Physical Review Letters* 100.7 (2008), p. 076801.

[278] L Lindsay, DA Broido, and Natalio Mingo. "Flexural phonons and thermal transport in graphene". In: *Physical Review B* 82.11 (2010), p. 115427.

[279] Henk W Ch Postma et al. "Carbon nanotube single-electron transistors at room temperature". In: *Science* 293.5527 (2001), pp. 76–79.

[280] A Bachtold et al. "Suppression of tunneling into multiwall carbon nanotubes". In: *Physical Review Letters* 87.16 (2001), p. 166801.

[281] Junjie Liu et al. "Quantum coherent spin–electric control in a molecular nanomagnet at clock transitions". In: *Nature Physics* 17.11 (2021), pp. 1205–1209.

[282] Simone Calvello et al. "CERES: An ab initio code dedicated to the calculation of the electronic structure and magnetic properties of lanthanide complexes". In: *Journal of computational chemistry* 39.6 (2018), pp. 328–337.

[283] IL Kurland, IL Aleiner, and BL Altshuler. "Mesoscopic magnetization fluctuations for metallic grains close to the Stoner instability". In: *Physical Review B* 62.22 (2000), p. 14886.

[284] Mikhail Shekhirev et al. “Interfacial self-assembly of atomically precise graphene nanoribbons into uniform thin films for electronics applications”. In: *ACS Applied Materials & Interfaces* 9.1 (2017), pp. 693–700.

[285] Hyeong Taek Ham, Yeong Suk Choi, and In Jae Chung. “An explanation of dispersion states of single-walled carbon nanotubes in solvents and aqueous surfactant solutions using solubility parameters”. In: *Journal of Colloid and Interface Science* 286.1 (2005), pp. 216–223.

[286] Linda Vaisman, H Daniel Wagner, and Gad Marom. “The role of surfactants in dispersion of carbon nanotubes”. In: *Advances in colloid and interface science* 128 (2006), pp. 37–46.

[287] Kyle L Grosse et al. “Nanoscale Joule heating, Peltier cooling and current crowding at graphene–metal contacts”. In: *Nature nanotechnology* 6.5 (2011), pp. 287–290.

[288] Stoyan Karabunarliev et al. “Rigorous Franck–Condon absorption and emission spectra of conjugated oligomers from quantum chemistry”. In: *The Journal of Chemical Physics* 113.24 (2000), pp. 11372–11381.

[289] Joost Van Der Lit et al. “Suppression of electron–vibron coupling in graphene nanoribbons contacted via a single atom”. In: *Nature communications* 4.1 (2013), pp. 1–6.

[290] Alberto Garcia et al. “Siesta: Recent developments and applications”. In: *The Journal of chemical physics* 152.20 (2020), p. 204108.

[291] William F Reus et al. “Statistical tools for analyzing measurements of charge transport”. In: *The Journal of Physical Chemistry C* 116.11 (2012), pp. 6714–6733.

[292] Matthew G Reuter et al. “Signatures of cooperative effects and transport mechanisms in conductance histograms”. In: *Nano letters* 12.5 (2012), pp. 2243–2248.

[293] Guoqing Zhou et al. “Electron–phonon scattering is much weaker in carbon nanotubes than in graphene nanoribbons”. In: *The Journal of Physical Chemistry Letters* 10.22 (2019), pp. 7179–7187.

[294] S Sapmaz et al. “Tunneling in suspended carbon nanotubes assisted by longitudinal phonons”. In: *Physical review letters* 96.2 (2006), p. 026801.

[295] Hongkun Park et al. “Nanomechanical oscillations in a single-C60 transistor”. In: *Nature* 407.6800 (2000), pp. 57–60.

[296] AN Pasupathy et al. “Vibration-assisted electron tunneling in C140 transistors”. In: *Nano Letters* 5.2 (2005), pp. 203–207.

[297] Chit Siong Lau et al. “Redox-dependent Franck–Condon blockade and avalanche transport in a graphene–fullerene single-molecule transistor”. In: *Nano letters* 16.1 (2016), pp. 170–176.

[298] Enrique Burzurí et al. “Franck–Condon blockade in a single-molecule transistor”. In: *Nano Letters* 14.6 (2014), pp. 3191–3196.

[299] AV Savin and Yu S Kivshar. “Localized vibrations of graphene nanoribbons”. In: *Low Temperature Physics* 42.8 (2016), pp. 703–710.

[300] Matthias Droth and Guido Burkard. "Acoustic phonons and spin relaxation in graphene nanoribbons". In: *Physical Review B* 84.15 (2011), p. 155404.

[301] Romain Vincent et al. "Electronic read-out of a single nuclear spin using a molecular spin transistor". In: *Nature* 488.7411 (2012), pp. 357–360.

[302] Alejandro Gaita-Ariño et al. "Molecular spins for quantum computation". In: *Nature chemistry* 11.4 (2019), pp. 301–309.

[303] Ronald Hanson et al. "Spins in few-electron quantum dots". In: *Reviews of Modern Physics* 79.4 (2007), p. 1217.

[304] Guido Burkard et al. "Semiconductor spin qubits". In: *arXiv preprint arXiv:2112.08863* (2021).

[305] András Pályi et al. "Spin-orbit-induced strong coupling of a single spin to a nanomechanical resonator". In: *Physical review letters* 108.20 (2012), p. 206811.

[306] Matthias Droth and Guido Burkard. "Electron spin relaxation in graphene nanoribbon quantum dots". In: *Physical Review B* 87.20 (2013), p. 205432.

[307] Wudmir Y Rojas, Cesar EP Villegas, and Alexandre R Rocha. "Ab initio modelling of spin relaxation lengths in disordered graphene nanoribbons". In: *Physical Chemistry Chemical Physics* 21.47 (2019), pp. 26027–26032.

[308] CP Ewels and M Glerup. "Nitrogen doping in carbon nanotubes". In: *Journal of Nanoscience and Nanotechnology* 5.9 (2005), pp. 1345–1363.

[309] Nicola Dotti. "Electronic Transport in Magnetic Materials at Different Dimensionalites". PhD thesis. University of Oxford, 2018.

[310] Kristiāns Čerņevičs, Michele Pizzochero, and Oleg V Yazyev. "Even–odd conductance effect in graphene nanoribbons induced by edge functionalization with aromatic molecules: basis for novel chemosensors". In: *The European Physical Journal Plus* 135.8 (2020), pp. 1–11.

[311] Eric V Anslyn and Dennis A Dougherty. *Modern physical organic chemistry*. University science books, 2006.

[312] Alicia Götz et al. "Band structure modulation by methoxy-functionalization of graphene nanoribbons". In: *Journal of Materials Chemistry C* 10.11 (2022), pp. 4173–4181.

[313] Giovanni Onida, Lucia Reining, and Angel Rubio. "Electronic excitations: density-functional versus many-body Green's-function approaches". In: *Reviews of modern physics* 74.2 (2002), p. 601.

[314] Hongtao Liu, Yunqi Liu, and Daoben Zhu. "Chemical doping of graphene". In: *Journal of materials chemistry* 21.10 (2011), pp. 3335–3345.

[315] Eduard Carbonell-Sanromà et al. "Doping of graphene nanoribbons via functional group edge modification". In: *ACS nano* 11.7 (2017), pp. 7355–7361.

[316] Manabu Ohtomo et al. "Interpolymer self-assembly of bottom-up graphene nanoribbons fabricated from fluorinated precursors". In: *ACS applied materials & interfaces* 10.37 (2018), pp. 31623–31630.

[317] Naeyoung Jung et al. "Charge transfer chemical doping of few layer graphenes: charge distribution and band gap formation". In: *Nano letters* 9.12 (2009), pp. 4133–4137.

[318] Kenji Tokunaga and James C Sturm. "Substrate bias dependence of subthreshold slopes in fully depleted silicon-on-insulator MOSFET's". In: *IEEE transactions on electron devices* 38.8 (1991), pp. 1803–1807.

[319] Qiang Chen et al. "Synthesis of triply fused porphyrin-nanographene conjugates". In: *Angewandte Chemie International Edition* 57.35 (2018), pp. 11233–11237.

[320] Karl M Kadish, Roger Guilard, and Kevin M Smith. *Handbook Of Porphyrin Science: With Applications To Chemistry, Physics, Materials Science, Engineering, Biology And Medicine (Volumes 6-10)*. Vol. 2. World Scientific, 2010.

[321] Maria da GH Vicente and Kevin M Smith. "Syntheses and functionalizations of porphyrin macrocycles". In: *Current organic synthesis* 11.1 (2014), pp. 3–28.

[322] Victor Posligua et al. "Band structures of periodic porphyrin nanostructures". In: *The Journal of Physical Chemistry C* 122.41 (2018), pp. 23790–23798.

[323] Jan M Englert et al. "HBC–porphyrin–close contact chromophores". In: *Chemical Communications* 49.42 (2013), pp. 4827–4829.

[324] T Dürkop et al. "Extraordinary mobility in semiconducting carbon nanotubes". In: *Nano letters* 4.1 (2004), pp. 35–39.

[325] Jana Zaumseil and Henning Sirringhaus. "Electron and ambipolar transport in organic field-effect transistors". In: *Chemical reviews* 107.4 (2007), pp. 1296–1323.

[326] Tian Fang et al. "Mobility in semiconducting graphene nanoribbons: Phonon, impurity, and edge roughness scattering". In: *Physical Review B* 78.20 (2008), p. 205403.

[327] John Robertson. "High dielectric constant oxides". In: *The European Physical Journal-Applied Physics* 28.3 (2004), pp. 265–291.

[328] Edmund Leary et al. "Bias-driven conductance increase with length in porphyrin tapes". In: *Journal of the American Chemical Society* 140.40 (2018), pp. 12877–12883.

[329] Yuanqin He et al. "Fusing tetrapyrroles to graphene edges by surface-assisted covalent coupling". In: *Nature chemistry* 9.1 (2017), pp. 33–38.

[330] Gage Hills et al. "Modern microprocessor built from complementary carbon nanotube transistors". In: *Nature* 572.7771 (2019), pp. 595–602.

[331] Brijendra Mishra, Vivek Singh Kushwah, and Rishi Sharma. "Power consumption analysis of MOSFET and Single electron transistor for inverter circuit". In: *Materials Today: Proceedings* 47 (2021), pp. 6600–6604.